UNIVERSITAT DE BARCELONA

Beam secondary shower acquisition design for the CERN high accuracy wire scanner

Jose Luis Sirvent Blasco

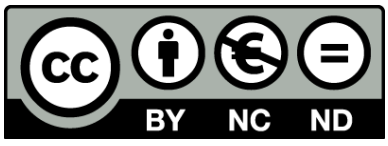

Beam secondary shower acquisition design for the CERN high accuracy wire scanner

Memoria presentada para optar al grado de
Doctor por la Universidad de Barcelona

Programa de Doctorado en Ingeniería y Ciencias Aplicadas

Autor:
Jose Luis Sirvent Blasco

Director:
Dr. Federico Roncarolo

Tutor:
Dr. Ángel Diéguez Barrientos

Departamento de Electrónica y Bioingeniería
Facultad de Física, Universidad de Barcelona

Septiembre 2018

UNIVERSITAT DE BARCELONA

Beam secondary shower acquisition design for the CERN high accuracy wire scanner

Memoria presentada para optar al grado de
Doctor por la Universidad de Barcelona

Programa de Doctorado en Ingeniería y Ciencias Aplicadas

Autor:
Jose Luis Sirvent Blasco

Director:
Dr. Federico Roncarolo

Tutor:
Dr. Ángel Diéguez Barrientos

Departamento de Electrónica y Bioingeniería
Facultad de Física, Universidad de Barcelona

Septiembre 2018

UNIVERSITAT DE BARCELONA

Abstract

The LHC injectors upgrade (LIU) project aims to boost the LHC luminosity by doubling the beam brightness with the construction of the new LINAC4, the first linear accelerator on the LHC chain. The brighter beams require upgrades on the full injector chain to deliver low emittance beams for the future High-Luminosity LHC (H-LHC). Thus, new and more precise beam instrumentation is under development to operate on this new scenario. These upgrades include the development of a new beam wire scanners generation (LIU-BWS), interceptive beam profile monitors used for the beam emittance calculation. Wire scanners determine the transverse beam profile by crossing a carbon wire (30 µm) through the particle beam. The beam profile is inferred from the intensity of the shower of secondary particles, scattered from beam-wire interaction, and the wire position.

The current BWS generation features high operational complexity and its performance is partly limited by their secondary shower detectors and acquisition systems. They are traditionally based on scintillators attached to a Photo-Multiplier tube (PMT) through optical filters. These detectors require tuning according to the beam energy and intensity prior to a measurement to not saturate the readout electronics, located on the surface buildings. Under these circumstances, many configurations lead to a poor SNR and very reduced resolution, directly affecting the measurement reliability. In addition, bunch-by-bunch profile measurements are degraded by the use of long coaxial lines, which reduce the system bandwidth leading to bunch pile-up.

This thesis covers the design of an upgraded secondary shower acquisition system for the LIU-BWS. This includes the study of a novel detector technology for BWS, based on polycrystalline Chemical Vapour Deposited (pCVD) diamond, and the implementation of two acquisition system prototypes.

This work reviews operational acquisition systems to identify their limitations and shows advanced particle physics simulations with FLUKA for better understanding of the secondary particles shower behaviour around the beam pipe. Simulations, along with a study of the different beams in each machine, leaded to the estimation of the required dynamics per accelerator, and an optimised placement of the upgraded detectors.

To cope with the injectors working points, the acquisition systems implemented performed high dynamic range signal acquisition and digitisation in the tunnel with a radiation-hard front-end nearby the detector, digital data is afterwards transmitted to the counting room through a 4.8Gbps optical link. This novel schema not only allowed low-noise measurements, but also avoided the bandwidth restrictions imposed by long coaxial lines, and greatly simplified the scanner operation.

The upgraded design investigates two approaches to cover a dynamic of about 6 orders of magnitude: a single-channel system, with logarithmic encoding, and a multi-channel system, with different gains per channel. Prototypes of both schemes were fully developed, characterised on laboratory and successfully tested on SPS and PSB under different operating conditions.

The evaluation of the acquisition systems during beam tests allowed the study of the LIU-BWS mechanical performance and comparative the measurements with operational systems.

pCVD diamond detectors, with a typical active area of $1cm^2$, were systematically evaluated as BWS detectors. This document analyses the results from several measurement campaigns on SPS over its energy and intensity boundaries ($5 \cdot 10^9 - 1.1 \cdot 10^{11}$ protons per bunch and 26 - 450 GeV). The SPS results suggest a potential application on LHC beam wire scanners.

Acknowledgements

This thesis wouldn't have been possible without the help, advice, collaboration and support of many people who directly or indirectly have contributed on its development.

Firstly I'd like to express my gratitude to **Bernd Dehning**, he gave me the opportunity to join CERN as a engineering technical student, on the BE-BI-BL section, and trusted me as doctoral student to undertake this project. Tireless and friendly supervisor, he always had a gap for discussions and was willing to help on the accelerators interventions independently of his work load. His wise advice and support were essential in many points of this thesis. Unfortunately, Bernd passed away during the thesis development.

A very special thanks goes to **Federico Roncarolo**, who kindly took over the project supervision and the revision of this document. He welcomed me on the BE-BI-PM section and followed closely the progress of this theis always with good suggestions. A great thanks to **Angel Dieguez** for accepting the academic supervision of this work and being my link with the University of Barcelona, I really appreciate his help with the university paperwork, which eased a lot the development of a thesis done abroad.

Everyday work wouldn't be the same without the implication of many colleagues from BE-BI-PM and BE-BI-BL, that in some way are a source of inspiration. Thanks **Jonathan Emery** who followed the project very closely and always provided good advice (and suggestions to improve the quality of the research carried out), also to **Patrik Andersson** for his help on installations and to **Georges Trad** for his great ideas and visits to my office. Lots of thanks to **Sune Jacobsen** for his help on the detectors design and construction, I had the chance to learn a lot from our conversations. Many thanks to **Emiliano Piselli**, without him many of the first measurements wouldn't had been possible, he operated wire scanners until very late in the night for data taking. In general, I would like to thank all members of both sections (PM and BL) who really made me feel like at home from the very first day and made daily work a delight.

Many thanks to **Tullio Grassi and Stephen Groadhouse** from CMS for their collaboration on the GBT implementation on Igloo2 FPGAs, it was great to work with them. Here, I would like to acknowledge as well **Manoel Barros** and **Sophie Baron** for their advice during our long conversations about the GBT code migration and constant support.

I had the opportunity to contact some institutes in search of collaboration, I want to thank Prof. **Ulrich Heintz** and his Fermilab contacts for providing some QIE10 samples, also to **Eduardo Picatoste and David Gascon** the ICECAL designers, and my link with the LHCb collaboration. They kindly provided ICECAL samples and received me as a member of their team while fixing of one of the ICECAL mezzanine boards in the UB.

I'd like to thank **Raymond Veness, William Andreazza, Dmitry Gudkov and Morad Hamani** from BE-BI-ML for their commitment on the procurement of mechanical components required for the detectors construction and their advice for its installation.

On the personal side, my biggest thanks goes to my girlfriend **Angela**, companion during this adventure working at CERN, who did not hesitated in being with me from the very first day (and it's been 7 years since then...). She was always there on those frustrating periods cheering me and and giving the extra kick (many actually) of motivation needed to complete this document. I need to thank her infinite patience in the difficult task of living with a grumpy doctoral student. I also appreciate a lot her help formatting in LaTeXa big part of the present document. But above all, thanks for that smile and her daily complicity.

I couldn't forget to acknowledge **my parents** who, during my lifetime, gave me the values and encouraged me to give the best of myself when facing a challenge, they always provide unconditional support no matter the distance. Finally, a big thanks goes to all those **relatives** (Angela's and mine) and **friends** who supported me during the project.

Contents

Chapter 1

Introduction

CERN, the European Organisation for Nuclear Research (Conseil Europèen pour la Recherche Nucléaire, in french), located in the Franco-Swiss border near Geneva is one of the leading institutes in particle physics worldwide. It was founded in 1954 with the mandate of establishing a world-class fundamental physics research organisation in Europe. This was one of the Europe's first joint ventures, originally founded with 12 countries nowadays it counts with 22 member states. Since its foundation it has been an example of international collaboration and has achieved major contributions to fundamental questions of physics, including the remarkable discovery of the Higgs-Bosson announced on July 2012.

CERN provides the particle accelerators and other infrastructures required for high energy physics research, including its flagship accelerator, the Large Hadron Collider (LHC), the largest accelerator ever built with 27 Km of circumference, which lies 100 metres underground. The LHC is designed to provide high energy (7 TeV) protons or heavy ions collisions on its interaction points, where the experiments ATLAS, CMS, LHCb and ALICE are located. The purpose of the LHC and its experiments is to analyse the products of the collisions in order to answer unresolved fundamental particle physics questions such as the determination of the primary building blocks of the matter and the origin of the particles mass.

The CERN accelerator complex (see Fig.1.1) counts with several linear and circular accelerators employed to gradually accelerate the particles prior to injection on the LHC. These are the linears LINAC2, LINAC3 and soon LINAC4, and circulars Low Energy Ion Ring (LEIR), Proton Synchrotron Booster (PSB), Protron Synchrotron (PS) and Super Proton Synchrotron (SPS).

The injector chain apart of feeding the LHC is also used to deliver particles to a number of other experiments carried out at CERN, including:

- Antimatter research with experiments hosted on the Antiproton Decelerator (AD) and Extra Low ENergy Antiproton (ELENA) decelerator rings.
- Radioactive ion beams research with experiments hosted on the Isotope Separator On-Line Device (ISOLDE).
- Research on neutron-nucleus interaction for a wide range of neutron energies on the Neutron Time-of-Flight (N_TOF) facility.
- Research on radiation induced damage on materials in the High-radiation to Materials (HiRadMat) facility.
- Study on the use of proton-driven plasma wakefields for charged particles acceleration in the Advanced WAKefield Experiment (AWAKE).

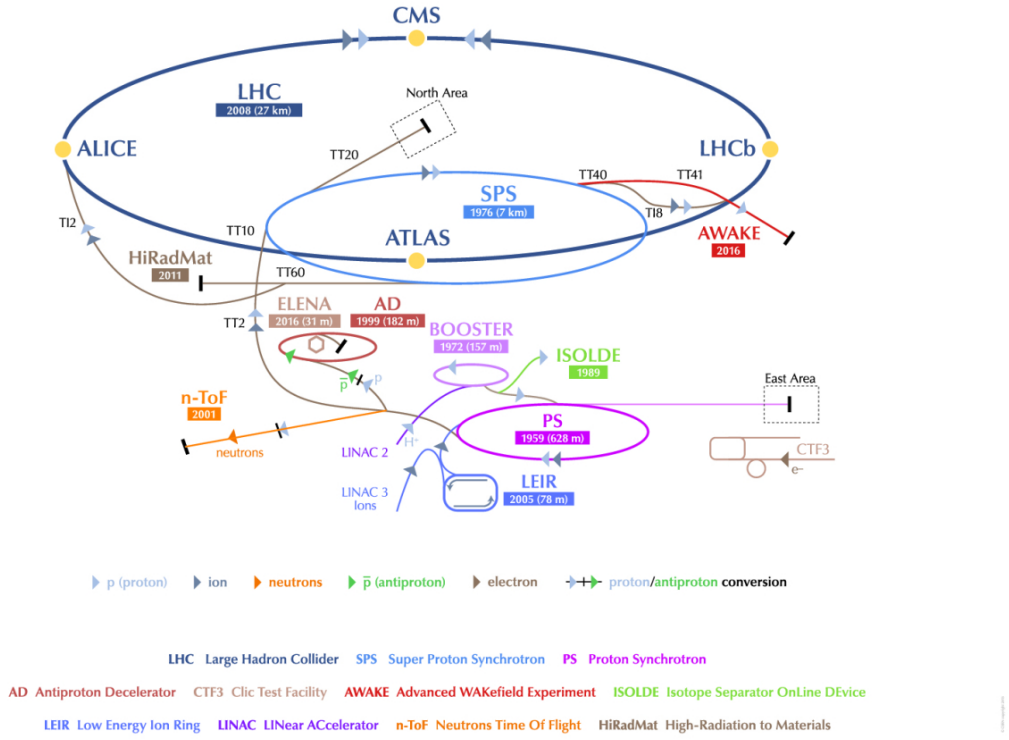

Figure 1.1 – LHC injector chain and experiments at CERN [1].

1.1. LHC and injectors chain

In order to reach the nominal collision energies at LHC, the proton beam must travel throughout the injector chain progressively acquiring energy. This chain is comprised by the LINAC2, PSB, PS, SPS and finally the LHC itself. This section describes the different stages of the proton acceleration for a standard 25 ns LHC fill [2].

The proton source consists in hydrogen gas injected into a plasma chamber. A strong electric field ionises the gas atoms and strips off its electrons, leaving only protons at 100 KeV to enter the LINAC2 accelerator.

LINAC2 is an 80 m long linear accelerator that compresses the protons into packets often labeled as "bunches" and accelerates them to 50 MeV kinetic energy, at this point particles travel at about one third of the speed of light (c). LINAC2 delivers high intensity proton bunches to the first circular accelerator, the PSB.

The PSB is the first, and smallest, circular accelerator at CERN (50 m diameter) and it is composed by four superimposed synchrotron rings. The particle bunches are accelerated from 50 MeV to 1.4 GeV (91.6% of c). This process lasts about 530 ms and the beam revolution period varies from 1 µs to 0.6 µs. Each PSB ring is capable of hosting up to 2 bunches, meaning that up to 8 bunches can be accelerated simultaneously. For a nominal LHC filling only 3 rings are used, a total of 6 PSB bunches. All the 4 rings can be operated in parallel for other LHC filling schemes or to feed the ISOLDE experiments.

The protons are then transferred to the PS (628 m of circumference) and accelerated up to an energy of 26 GeV (99.9% of c). During the energy ramp in the PS, the particles undergo the so-called "γ-transition", after which the added energy on the protons by the accelerating electrical field is not translated into increase of velocity but into an increase of mass.

Throughout different RF cavities manipulations, the 6 long and high intensity PSB bunches are split into 72 shorter and lower intensity bunches, thus defining the ultimate LHC longitudinal structure with 25 ns bunch spacing. The PS cycle and RF manipulations take about 1.1 s. Once the beam reaches the extraction energy, it is transferred to the SPS for further energy increase. When not serving the SPS, the PS can deliver beams to the EAST area, n_TOF and AD.

The SPS is the second largest machine in the CERN accelerator complex with nearly 7 Km of circumference. It requires 4 PS injections of 72 bunches to accumulate 288 bunches in the ring, each injection corresponds to a batch (group of bunches). Once completed, the 26 GeV beams are then accelerated to the LHC injection energy (450 GeV), during 4.3 s. At this point particles are highly relativistic, the nominal 23 μs revolution period on this machine only varies by 800 parts per million (ppm) during the cycle. The beam is delivered to the LHC through two different transfer lines that allow to fill each of the LHC rings in clockwise and anticlockwise direction. In the past, the SPS was used as a proton/anti-protons collider and as electrons/positrons injector for the Large Electron Positron collider (LEP). Nowadays, apart from feeding the LHC, it is used to deliver beams to the North Area fix target experiments, to the HiRadMat facility and to the AWAKE experiment.

A nominal LHC fill consists of 39 batches of 72 bunches each (a total of 2808 bunches per ring), that corresponds to 12 SPS injections according to the 234 334 334 334 schema shown on Fig. 1.2. The LHC filling can take more than 30 minutes. Afterwards, the LHC itself provides the last energy boost, accelerating the beam in each ring from 450 GeV up to its top energy (6.5 TeV today, the design 7 TeV is expected to be reached in 2020). After a short period at top energy necessary to prepare the LHC optics parameters and the LHC experiments, the LHC collision physics starts and the experiments record data. If not stopped by unexpected accelerator faults, the physics period is kept as long as considered efficient, which depends on many factors, like the beam intensity deterioration by the collisions themselves (also named *burnout*).

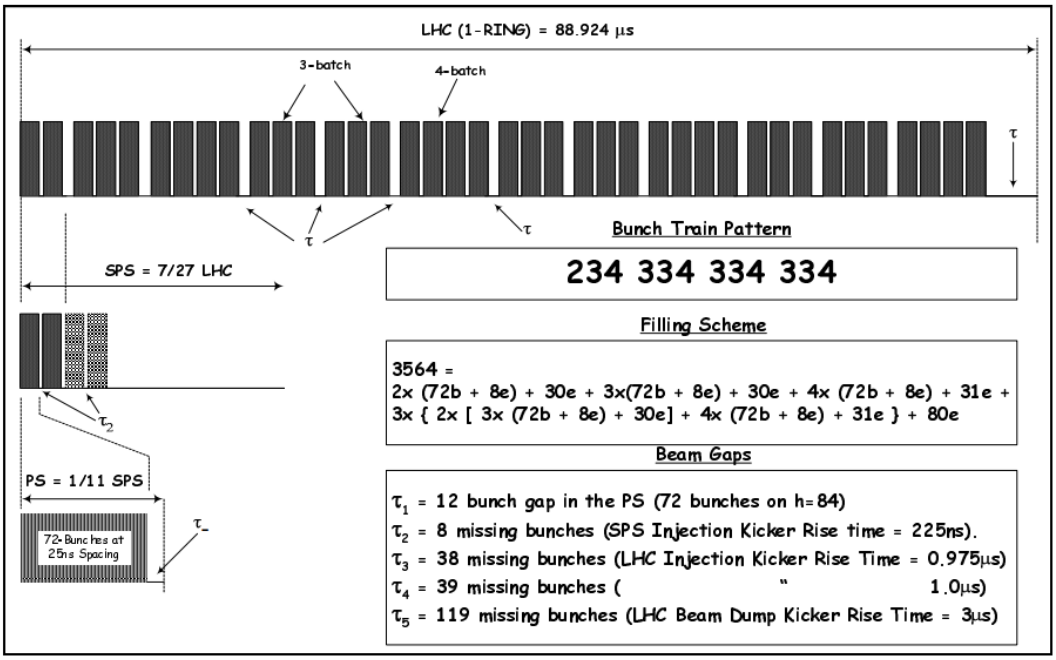

Figure 1.2 – Nominal LHC filling with 25ns separation bunches [2].

The LHC operates in "Runs" lasting several years. During a Run, and on the long shut down periods (1-2 years) that are normally scheduled between runs, the LHC and the injectors smoothly increase their performance. During Run 1 (2010-2013), the LHC was operated only up to 3.5 and 4 TeV (being 7 TeV the design top energy), with bunch spacing decreasing

from 150 to 50 ns (w.r.t the nominal design for 25 ns). Despite this, the LHC achieved many records, in terms of maximum beam intensity, energy stored and luninosity, never reached in the world before. The Run 1 yielded to the historical discovery of the Higgs boson and to the first measurement of its mass, around 126 GeV, consistent with the Standard Model.

During the first long shutdown (LS1 2013-2014), intended for maintenance and consolidation, the accelerators were prepared to reach 6.5 TeV per beam, thus for collisions at the unprecedented energy of 13 TeV, and for operation at the nominal 25ns bunch structure. Run 2 (2015-2018) opens a new frontier for high energy physics research, where the LHC keeps accumulating records. The 26th June 2016 the LHC reached its design luminosity for the first time in a fill that was kept on the machine during 37 hours. Table 1.1 shows how key parameters of the LHC accelerator now approach the design values.

Table 1.1 – Overview of the LHC performance parameters during the LHC Run 1 and 2

Parameter		**2011**	**2012**	**2015**	**2016**	**Design**
Beam Energy	[TeV]	3.5	4	6.5	6.5	7
Bunch Spacing	[ns]	150	75/50	50	25	25
β^* IP	[m]	1.5/1.0	0.6	0.8	0.4	0.55
ϵ^* at Injection	[mm mrad]	2.4	2.5	3.5	2.0	3.75
Bunch Population	[10^{10} p/bunch]	1.45	1.6	1.15	1.15	1.15
Max num of bunches		1380	1380	2244/2232	2220/2208	2808
Max Stored Energy	[MJ]	110	140	270	265	362
Peak Luminosity	[$cm^{-2}s^{-1}$]	$3.7 \cdot 10^{33}$	$7.7 \cdot 10^{33}$	$5 \cdot 10^{33}$	$1.4 \cdot 10^{34}$	10^{34}

1.2. Accelerator physics overview

1.2.1. Particle accelerator basic concepts

The acceleration and guiding (bending and focusing) of a particle beam in High Energy Physics (HEP) is in first instance governed by the Lorentz force experienced by charged particles travelling through electromagnetic fields. Lorentz law is expressed as on Eq. 1.1:

$$\vec{F} = q[\vec{E} + (\vec{v} \times \vec{B})] \tag{1.1}$$

where q is the charge of a particle with velocity $\vec{v}$ passing through an electric field $\vec{E}$ and a magnetic field $\vec{B}$.

The first term in the equation correspond to the effect of the electric field, providing acceleration, and the second to the magnetic force, providing bending or focusing.

A charged particle, with a defined initial velocity, in the presence of a magnetic field perpendicular to the velocity itself, experiences a transverse kick, while keeping its tangential velocity unchanged. This principle is used in particle accelerators to guide and contain particle beams around a reference trajectory. A practical example of this principle are cyclotrons, where the circular trajectory of the particles is defined by a well controlled perpendicular magnetic field (see Fig. 1.3). Cyclotrons accelerate their beams through the application of an alternating electric field in synchronisation with the particles passage in-between its two D shaped sectors. As a consequence, particles acquire kinetic energy and become heavier, thus requiring of a stronger magnetic field to keep a circular trajectory. This effect is used in cyclotrons to make particles travel in spiral as they acquire energy until they reach the extraction point.

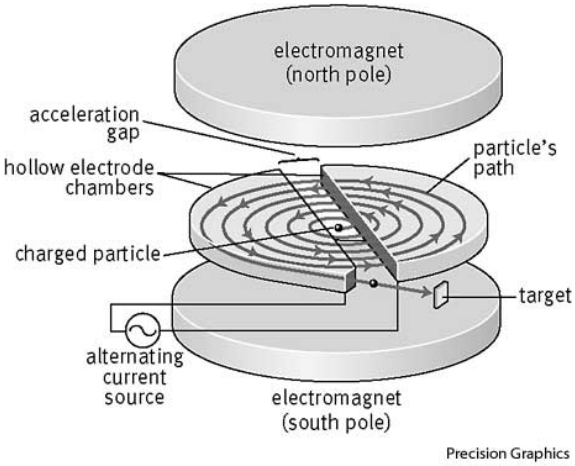

Figure 1.3 – Cyclotron working principle [3].

In larger circular accelerators, such as those at CERN, the particles acceleration is provided by RF cavities, whereas dipoles and quadruples guide and confine the beam through a reference orbit.

RF cavities are a series of hollow structures and gaps that feature alternating electric fields that change polarity as charged particles go through. The sinusoidal and synchronised modulation of the RF cavities with respect to the revolution frequency and the particles passage, allow the creation of stationary trap regions used to group particles in well defined time slots. These are known as buckets that could (or could not) be filled with particles. Filled buckets are known as bunches.

Dipole magnets, featuring a magnetic field B_y normal to the beam direction, are used to bend the beam trajectory and guide it along the accelerator. The radius of curvature ρ of a particle with charge q and momentum $p = mv$ travelling in the horizontal plane is derived from the equilibrium between the centrifugal force and the centripetal Lorentz force:

$$\rho = \frac{p}{qB_y} \tag{1.2}$$

To keep the same trajectory along the acceleration cycle, dipole magnets are "ramped" (raising their supply current) as the beam is accelerated to increase the strength of their magnetic field.

When two particles go through the same dipole magnet with different initial angles, they experience the same deflection, but each of them exits with a different trajectory. This is illustrated on Fig. 1.4, which also shows the case of two particles immersed in a uniform magnetic field.

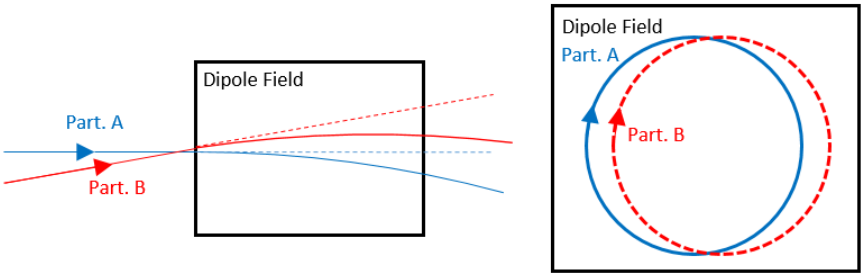

Figure 1.4 – Trajectory of particles with different initial conditions through a dipole magnet (left) and when immersed in a uniform magnetic field (right).

Normally, in circular accelerators the dipole magnets are designed to curve the particle beam in the horizontal plane whereas no force is experienced on the vertical plane. Quadrupoles are required to confine the beam and compensate for the dipoles exit angle difference, i.e. they are used for beam focusing in both horizontal and vertical planes.

The force that a particle experiences when traversing a quadrupole magnet depend on the particle position (being stronger for the particles with higher offset from the quadrupole centre) and its momentum. The focusing capability of a quadrupole only applies on one transverse plane, whereas on the other particles experience a defocusing effect (see Fig. 1.5). The focusing effect of a quadrupole can be seen as the one of a focal lens in optics.

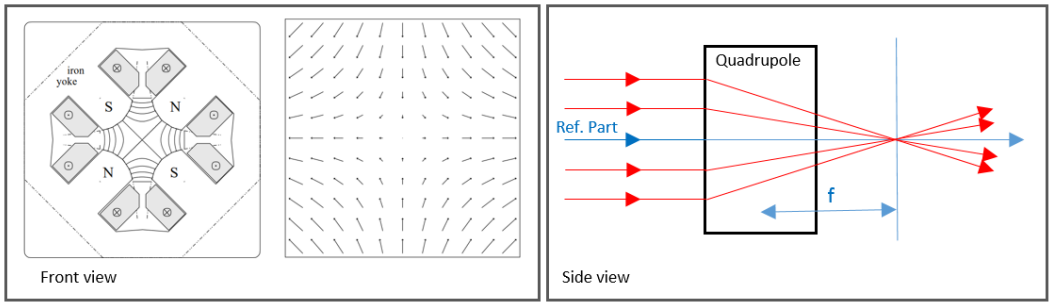

Figure 1.5 – Quadrupole configuration and force vectors experienced by charged particles on front view [4] (left) and one plane focusing effect on side view (right).

For a net focusing in both transverse planes, consecutive quadrupoles with opposite polarities are required. Structures based on this concept are known as FODO cells, and they consist in a horizontal focusing quadrupole (F), a drift space (O), a vertical focusing quadrupole (D) and another drift space (O). The configuration of dipoles and quadrupoles in a circular accelerator is what defines the accelerator "optics" (or lattice) in both transverse planes. "Chromatic" focusing effects derived by particles momentum dispersion are compensated with higher order magnetic elements such as sextupole magnets.

1.2.2. Transverse beam dynamics

As a particle travels along the accelerator it perform oscillations (as a pendulum) around a reference circular orbit as a consequence of its passage through dipoles and quadrupoles. These oscillations (known as Betatron oscillations) are experienced in both transverse planes and are characterised by the instantaneous offset from the central path (x) and its angle (x') (see Fig. 1.6). The number of Betatron oscillations per turn in each plane is defined as tune (Q_h, Q_v).

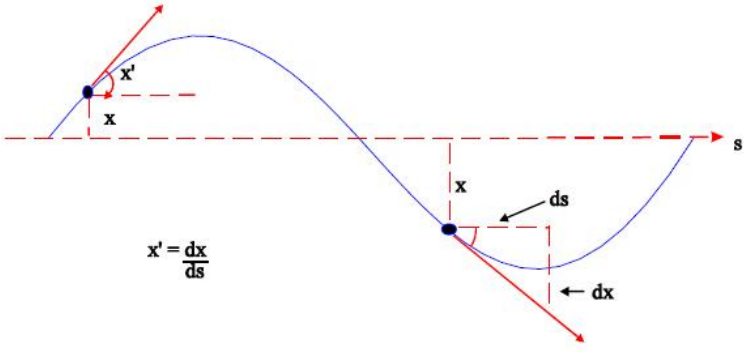

Figure 1.6 – Transverse position and angle displacement for a circulating particle in an accelerator [5].

The transverse motion of particles in a storage ring is described by Hill's equation [6]:

$$\frac{d^2x}{ds} + K(s)x = 0 \tag{1.3}$$

that defines the particles transverse dynamics as a pseudo harmonic oscillator with a harmonic constant $K(s)$ varying with the quadrupoles magnetic fields strength, dependent on the ring position (s).

The general solution for Hill's equation is:

$$\begin{aligned} x &= \sqrt{\epsilon\beta(s)}\cos\left(\Psi(s) + \Phi\right) \\ x^{'} &= \sqrt{\frac{\epsilon}{\beta(s)}}\sin\left(\Psi(s) + \Phi\right) \end{aligned} \tag{1.4}$$

where ϵ (defined later) and Φ are constants dependent on the particle's initial conditions, $\beta(s)$ is the amplitude of the modulation due to changing focusing strength (beta function). $\Psi(s)$ is the phase advance experienced by particles along the trajectory, dependent on the focusing strength and therefore on β as:

$$\Psi(s) = \int_0^s \frac{1}{\beta(s)} ds \tag{1.5}$$

The tune is obtained by calculating the phase advance of the particles in a complete revolution ($\Delta\Psi$) (i.e number of complete oscillations).

$$Q = \frac{\Delta\Psi}{2\pi} \tag{1.6}$$

The particles transverse dynamics is often described by their distribution in phase space (position x and angle $x^{'}$) at each location on the ring s. By passing turn after turn at the location s, each particle describes a phase space ellipse. Liouville's theorem states that under the influence of conservative forces, the shape and orientation of the ellipse varies for each location s, but it's area remains constant.

The ensemble of particles (populating a particle beam) is normally described by an envelope ellipse containing a well defined fraction of the single particle ones. For Gaussian distributed particles (in position and angle) it is conventional to set such a fraction to 68 %, correspondent to considering all particles within $\pm 1\,\sigma$ of the Gaussian distribution.

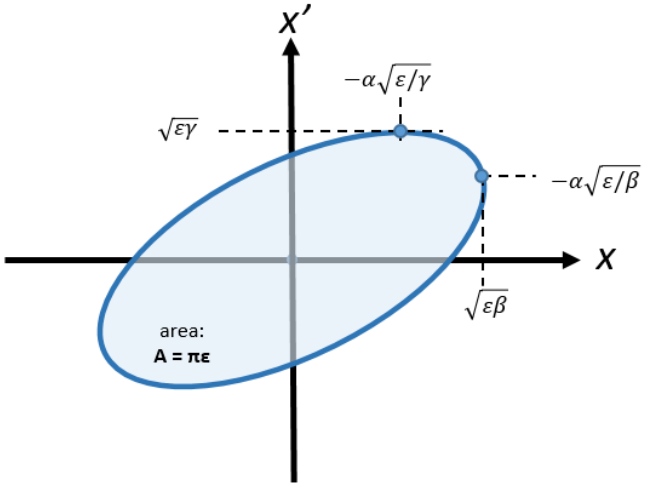

Figure 1.7 – Beam Phase-Space ellipse.

The area of the beam ellipse in phase-space, linked with the constant factor π, is defined as the transverse beam emittance ϵ:

$$\int_{ellipse} dx dx^{'} = \pi\epsilon \tag{1.7}$$

The beam emittance can also be expressed as:

$$\epsilon = \gamma x^2 + 2\alpha x x^{'} + \beta x^{'2} \tag{1.8}$$

where γ, α and β (Betatron function) are the ellipse parameters (also known as Twiss or Courant-Snyder parameters) that determine its shape and orientation, while also satisfying the following mathematical dependencies:

$$\alpha = -\frac{\beta^{'}}{2}, \gamma = \frac{1+\alpha^2}{\beta} \tag{1.9}$$

Through the knowledge of Twiss parameters variation along the accelerator ring it is possible to predict the shape and orientation of the beam phase-space ellipse in every location of the machine.

1.2.3. Transverse emittance and beam size

The beam size and its divergence can be extracted from the beam emittance and the Twiss parameters as:

$$\begin{aligned} \sigma_{x,y} &= \sqrt{\epsilon_{x,y}\beta_{x,y}(s)} \\ \sigma_{x^{'},y^{'}} &= \sqrt{\epsilon_{x,y}\gamma_{x,y}(s)} \end{aligned} \tag{1.10}$$

where $\sigma_{x,y}$ is defined as horizontal/vertical beam size and $\sigma_{x^{'},y^{'}}$ is its divergence. These are essentially the projected values of the beam phase-space ellipse on the space axis (x) and on the phase axis ($x^{'}$) (see Fig. 1.7). Typically particles in the accelerator have a Gaussian distribution in position and angle, thus the beam size and divergence are defined as their Gaussian sigma values.

As the beam crosses focusing and defocusing quadrupoles, its dimension in horizontal and vertical planes is being modulated by the corresponding Betatron function ($\beta_x(s)$ or $\beta_y(s)$). The transverse linear motion on both planes is considered decoupled and without cross talk, however, as the beam is focused in one plane it is being defocused on the other (see Fig. 1.8).

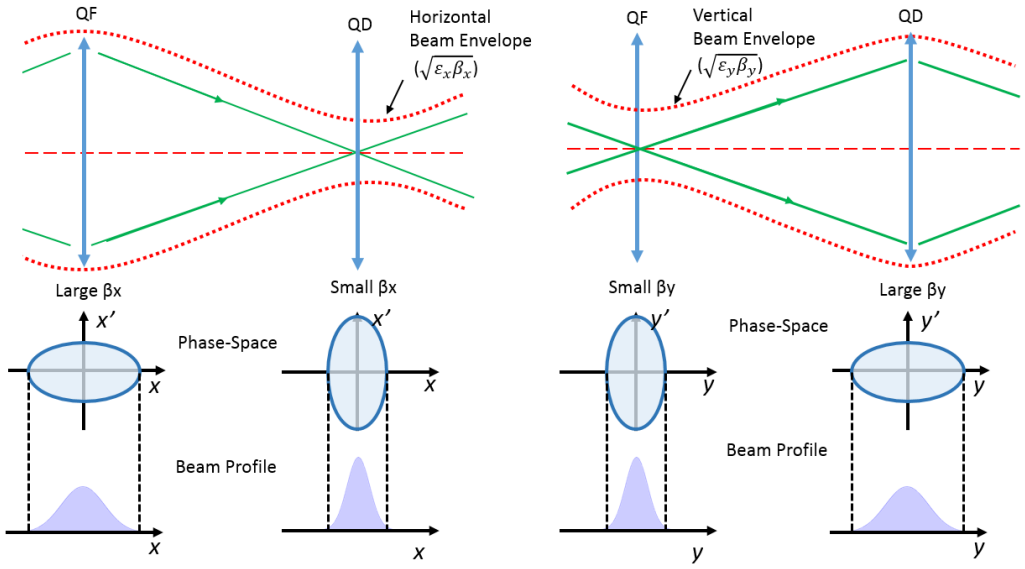

Figure 1.8 – Horizontal (left) and Vertical (right) beam size variations through quadrupoles along with their corresponding phase ellipse. QF and QD stands for focusing and defocusig quadrupoles.

The transverse size of the beam experiences a shrinking inversely proportional to the momentum increase since the beam emittance varies with energy. This phenomenon is known as adiabatic damping. In high energy physics, normalized emittance (ϵ^*) is widely used to account for emittance variation with beam momentum [7]:

$$\begin{aligned} \epsilon^*_{x,y} &= (\gamma_L\beta_r)\epsilon_{x,y} \\ \epsilon^*_{x,y} &= (\gamma_L\beta_r)\frac{\sigma^2_{x,y}}{\beta x, y} \end{aligned} \tag{1.11}$$

where $(\gamma_L\beta_r)$ are relativistic functions dependent on the beam energy.

The Lorentz factor (γ_r) is the ratio between the particles energy and their rest mass, and the relativistic factor β_r scales with their velocity to the speed of light.

$$\gamma_L = \frac{E}{m_0c^2},\ \beta_r = \frac{v}{c} \tag{1.12}$$

The normalized emittance is invariant at every location of the ring and independent from the beam energy. This provides a great advantage for beam diagnostics, where one can evaluate the beam emittance at collision energy and estimate its impact on the accelerator luminosity, described in following sections.

1.2.3.1. Momentum spread

In a particle beam, off-momentum particles follow shifted trajectories with respect to the nominal path. In a dipole field, heavier (higher energy) particles follow a bigger radius of curvature than those particles with a lower energy.

The dynamics of the off-momentum particles result in shifted transverse phase-space ellipses that ultimately contribute to an effective beam profile widening, as shown in Eq. 1.13:

$$\sigma^2 = \sigma^2_\beta + \sigma^2_D = \epsilon^*\beta(s) + (\delta D(s))^2 \tag{1.13}$$

The first term of the beam size definition correspond to the accelerator optics and the beam emittance, the second is the beam widening due to momentum dispersion. $D(s)$ is the

dispersion function, dependent on the ring position and created by the dipole and quadrupole magnets.

The beam momentum spread is defined as:

$$\delta = \frac{p - p_0}{p_0} \tag{1.14}$$

Momentum spread and the dispersion function must be carefully taken into consideration when reconstructing the beam emittance from a beam profile measurement. In general, this effect is more significant on the horizontal plane and usually neglected on the vertical plane.

1.2.4. Luminosity

The figure of merit of particle colliders is their event production capability (proton-proton collisions on the LHC) and the frequency at which those events are produced. A very high event rate is required to observe rare events and increase the machines discovery potential. The luminosity is considered as one of the most important parameters of a collider, since it defines its ability to produce a required number of interactions when colliding two particle beams. The luminosity ($\mathcal{L}$) is a proportionality factor, used to calculate the event rate $\frac{dR}{dt}$ (number of events per second) from the interaction cross section σ_{int}.

$$\frac{dR}{dt} = \mathcal{L}\sigma_{int} \tag{1.15}$$

The luminosity of two head-on colliding Gaussian beams is dependent on the number of particles per bunch and the transverse beam size at the interaction point:

$$\mathcal{L} = f\frac{N_1 N_2 N_b}{4\pi\sigma_H\sigma_V} \tag{1.16}$$

where f is the collider revolution frequency, N_1 and N_2 are the number particles in each colliding bunch, N_b the total number of bunches on the ring and $\sigma_{H,V}$ the horizontal and vertical transverse beam dimensions at the collision point.

Given the impossibility to measure the beam size at the interaction point (IP), the beam width at this location is derived from the calculated beam emittance, provided by beam profile monitors (i.e. wire scanners), and the known Betatron function on the IP, see Eq. 1.17.

$$\mathcal{L} = f\frac{N_1 N_2 N_b}{4\sqrt{\epsilon_H\beta^*_H\epsilon_V\beta^*_H}} \tag{1.17}$$

where $\beta^*_{H,V}$ are the horizontal and vertical Betatron function values on the IP, defined by the collider optics. Design parameters on the LHC specify $\beta^*_{H,V} \approx 50cm$ at the IP which, together with the design normalized emittance, leads to colliding beams with a nominal transverse RMS size in the order of 10 µm.

The maximum number of bunches in the LHC ring and its revolution frequency are fixed by design. Therefore, to achieve maximum performance, the LHC injector chain needs to produce high intensity beams with a very small normalized emittance. In addition, these conditions must be preserved during the acceleration cycle.

The luminosity might be affected afterwards by a number of effects that contribute on its reduction, such as the crossing angle, offset between the colliding beams and the hourglass factor [8].

1.3. Transverse beam profile monitors

This section aims to provide a general overview of beam profile monitors used in high energy physics, with special focus on those employed at the CERN circular accelerator chain. Beam profile monitors are categorised into two types, interceptive and non-interceptive in function of their measurement technique.

1.3.1. Non-Interceptive devices

These monitors require of no interaction (or minimal) with the beam. However given the nature of their detecting mechanism, they require of an absolute calibration or correcting parameters. They feature, in general, lower accuracy than interceptive methods. Measurement campaigns in parallel with interceptive devices (i.e, wire scanners) are usually performed for calibration purposes.

Synchrotron light monitors (BSRT)

These monitors profit from the light produced on dipole magnets when highly relativistic particles are deflected by a magnetic field. Synchotron monitors are usually placed to make use of this parasitic light after a dipole and behind an "undulator" magnet, where the beam is deflected several times to enhance the photon emission. A total of three synchrotron light monitors are installed at CERN, two in the LHC (one per beam) and one on SPS. To obtain beam profile information, from synchrotron radiation, direct imaging with intensified cameras are typically used with traditional optics and a mirrors system [9], see Fig.1.9.

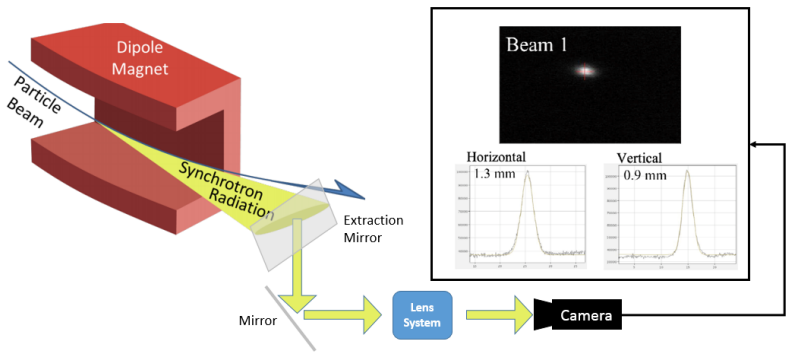

Figure 1.9 – Simplified schematic of the BSRT monitor with direct beam imaging. [9]

The resolution of such systems is mainly limited by optical diffraction given the small size of the beam for high energies (200-300 µm in LHC at 7TeV). For this reason, different methods based on interferometry are under investigation [10] [11].

Beam Gas Ionisation Profile Monitor (BGI)

These beam profile monitors are also known as Ionisation Profile Monitors (IPM). Their working principle consists on the ionisation of the rest gas (or injected gas) on the vacuum chamber, the electrons generated by ionisation are accelerated by a strong electric field towards one side of the chamber, where they are detected. The footprint of the electron distribution on the detector represents the beam dimensions in one plane. Traditional BGI monitors use a multi-channel plate (MCP) to provide electron multiplication and a phosphor screen, where the electrons distribution is illuminated, an optical system directs the image from the phosphor to a CCD camera [12], see Fig. 1.10 left. This architecture is currently being used on SPS and LHC. Both spatial and temporal resolution are limited by the performance of the camera to tens of micrometers and tens of nanoseconds. A new BGI generation was evaluated on the PS ring by using pixelated silicon detectors placed directly into the chamber [13], see Fig. 1.10 right. This approach ensures a higher electron detection efficiency and enhanced performance.

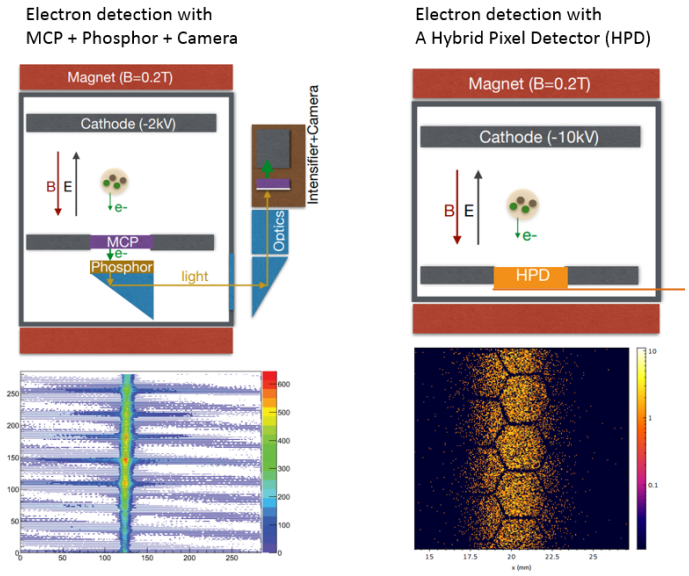

Figure 1.10 – Simplified schematics of Beam Gas Ionisation Profile Monitors at SPS and LHC (left). Upgraded architecture tested on PS shown (right) [13].

Beam Gas Vertex Detector (BGV)

The BGV is a beam-gas interaction device, its beam profile measurement method is based on reconstructing the track of secondary particles, produced by inelastic beam-gas collisions, exiting the beam pipe. Through the track reconstruction, the position of the interaction (vertex), and therefore the beam size, can be determined. This method was firstly used at LHCb and currently a demonstrator set-up is installed on the LHC [14], it employs several matrices of scintillating fibres (250µm diameter) with silicon photo-multiplier (SiPM) readout to obtain bi-dimensional information of the interactions. The expected accuracy of this device is <10%, however it requires of long integration times (>5minutes).

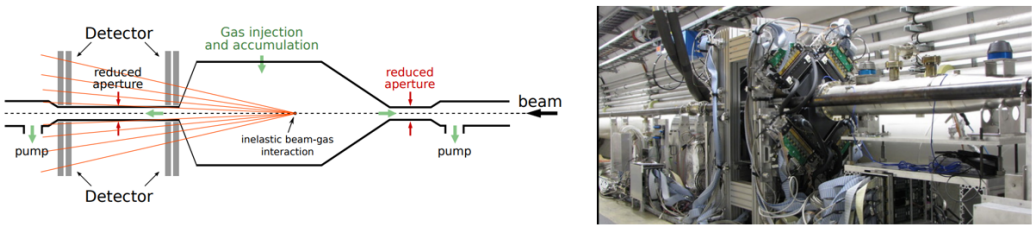

Figure 1.11 – Schematic of the Beam Gas Vertex detector (left) and picture of installation on LHC (right) [14].

1.3.2. Interceptive devices

These monitors use methods requiring of a direct interaction with the beam, which could potentially degrade its properties, i.e emittance blow-up. They are subject to deterioration or critical failure due to direct energy deposition on the materials exposed to the beam. On the other hand, they offer high accuracy in the absolute beam profile measurement.

Secondary Emission Grids (SEM-Grids)

SEM-grids consists on a series of thin filaments arranged in parallel. Typical wire diameters are 40µm if made of tungsten or 30µm if made of carbon. On their construction, the wire spacing can vary from 300µm to 500µm [15]. A pneumatic mobile mechanism allows to place the grid directly onto the beam. When the beam crosses the grid, a current is generated in each of its filaments by secondary electron emission. The current in each filament is proportional to the beam intensity in the wire position, thus each wire requires a dedicated acquisition

channel. By combining the information of all wires, the beam dimensions in one plane can be determined with a single shot. Their measurable beam intensities are limited by the wires heating, and their measurement resolution is linked to the number of wires used (channels) and the space between them.

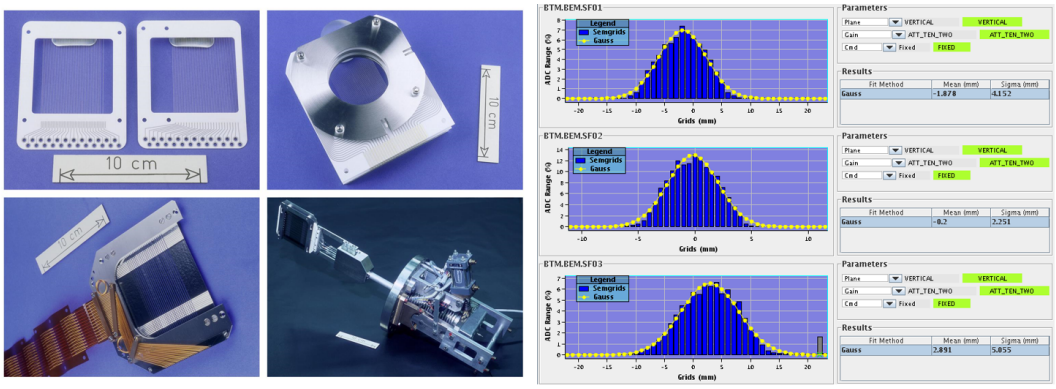

Figure 1.12 – SEM Grids used at CERN (left) and beam profiles with SEM-grids on the CERN's BTM transfer line from PSB [15].

With an arrangement of three consecutive SEM-grids, and knowing the lattice of the elements in-between, one can fully characterise the normalised emittance in phase-spacs. This is known as the three-profiles method it is also applied in LINAC4 [16].

Given their simple construction, radiation hardness and single shot measuring capability SEM-grids are widely used for beam diagnostics on linear accelerators and transfer lines. A similar approach is currently being implemented on new beam profile monitors for the SPS experimental areas, consisting on an arrangement of parallel plastic scintillating fibres with multi-channel readout based on silicon photomultipliers (SiPM) [17].

Optical Transition Radiation (OTR) screens

These monitors are also known as "betatron matching monitors". Their detection method is based on optical transition radiation (OTR) produced in thin screens, directly exposed into the primary beam with an angle of 45 degrees. OTR is emitted when a charged particle beam goes through an interface with different dielectric constant. A luminous image with the footprint of the beam is generated on the material, thus, offering bi-dimensional information of the beam in a single shot. The beam footprint is captured with a CCD camera through an image intensifier and a system of lenses (see Fig. 1.13). These screens are typically made of Alumina, Titanium or Carbon depending the beam intensity to measure, the usual configuration of an OTR monitor features the three materials to cover a wide dynamic range, either by switching between screens or building a hybrid screen. The fast timing response of OTR also allows bunch length measurements, limited in many cases by the performance of the cameras.

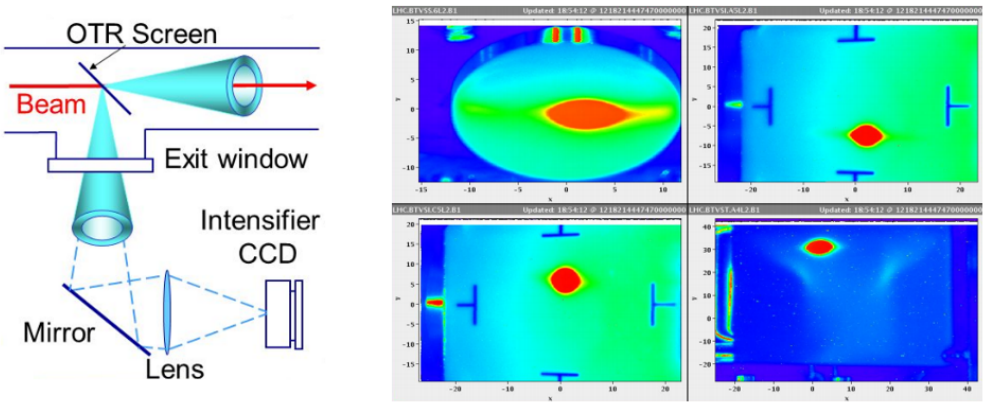

Figure 1.13 – OTR monitor working principle (left) and first beam observations with OTRs on the LHC (right) [18]

The attractiveness of such method resides in its simplicity. However, the radiation hardness of the cameras used is a major concern, research is ongoing to provide alternative digitalization strategies, such as the use of linear CMOS image sensors [19].

Wire Scanners

These are the beam profile monitors on the scope of this work. The working principle of wire scanners consists on the passage of a very thin carbon wire (≈30µm) through the circulating particle beam. A shower of secondary particles is generated by the beam/wire interaction. The secondaries shower is detected outside of the beam pipe, with a scintillator, and transformed into an electrical current through a photo-multiplier tube. During the measurement, the wire position is monitored. Since the shower intensity is proportional to the beam intensity at a given wire position, the beam profile in a single plane can be obtained by correlating the wire position with the secondaries shower intensity, see Fig. 1.14.

For low energy machines where very few secondaries escape the beam pipe (i.e. PSB at injection energy), the beam profile amplitude is acquired from the secondary electron emission on the wire (as SEM-grids). A detailed description of operational scanner mechanics and acquisition systems is provided on Chapter 2.

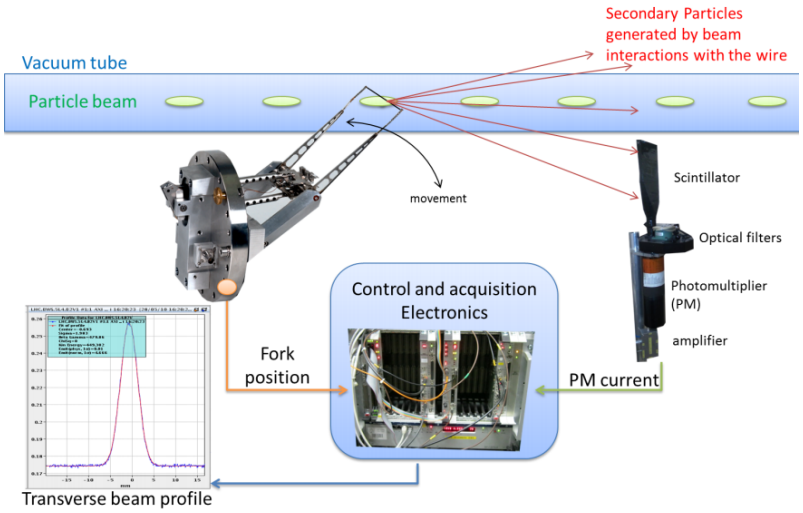

Figure 1.14 – Schematic of the wire scanner working principle.

This method is capable of bunch by bunch beam profile monitoring on cyclic machines, however the bunch profile measurement resolution is determined by the accelerator revolution frequency and the scanner speed.

Chapter 2

CERN beam wire scanners and upgrade programme

The beam wire scanners upgrade is part of the LHC injectors upgrade (LIU) program, meant to provide higher luminosity beams for collision in the HL-LHC. This chapter defines the wire scanners upgrade requirements, by identifying the operational systems performance limits and, consequently, the items to address for a successful upgrade. A detailed description of the existing wire scanners at CERN, as well as their related acquisition electronics, is provided for understanding. The requirements and general specifications for the upgraded secondaries acquisition systems are detailed. The upgraded prototypes mechanical designs are presented, including a detailed description of its optical position sensor.

2.1. Operational systems

Fast wire scanners are installed in all CERN synchrotrons and are based on different mechanical designs for both historical reasons and different requirements for different machines. They are typically considered as the most accurate beam profile monitors and used for the calibration of other instruments, such as synchrotron light or beam-gas monitors. Wire scanners are used on a daily basis to diagnose the beams emittance, for which their accuracy and availability are a key factor for the accelerators operation. At the moment of writing, a total of 31 scanners are installed at CERN, distributed as shown in Table 2.1.

Table 2.1 – Operational beam wire scanners installed at CERN

Operational CERN Beam Wire Scanners: Location and Types (2016)			
Location	**# of Scanners**	**Type**	**Max. Speed (m/s)**
PSB	4H + 4V	Rotational Fast	15
PS	3H + 2V	Rotational Fast	15
SPS	5H + 5V	Linear, Rotational	1, 6
LHC	2H + 2V (B1) 2H + 2V (B2)	Linear	1

2.2. Mechanical designs

The operational scanner mechanics can be categorised into two main families, *linear* and *rotational*. Both types share a similar working principle, based on bellows for the movement transfer from air to vacuum and potentiometers for position measurement.

The architecture of linear scanners (installed in the SPS and LHC) limits their scan speed to 1 m/s, which also limits the intensity of safely scanned beams [20]. The direct linear move-

ment transmission and measurement allows a relatively precise wire position determination (mainly limited by electronic noise on the potentiometer reading).

There are two rotational operational architectures. The first is commonly known as purely "rotational" (SPS) in which the scanner shaft is shared with the motor, the second is known as "rotational fast" (PS and PSB), and uses a lever arm mechanism. These models can reach speeds of 6 and 15m/s respectively due to the low mass of the mobile parts. "Rotational fast" type feature a more complex mechanics for motion transfer, which generates in some cases mechanical play [21]. Furthermore, the strong acceleration at which the system is exposed generate vibrations on the moving elements, which increases the measurement incertitude [22]. Figure 2.1 gives an overview of the scanner types used at CERN.

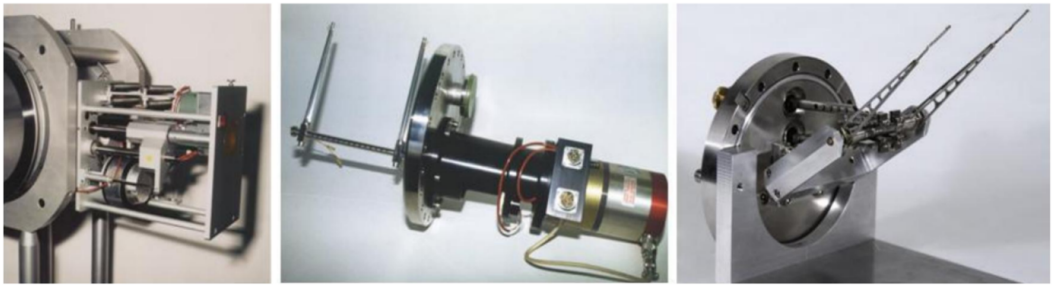

Figure 2.1 – Beam wire scanners architectures at CERN: Linear (left), Rotational (centre) and Rotational fast (right).

As mentioned above, air to vacuum motion transfer is ensured by bellows. A thin flexible metallic structure preserves vacuum, allowing to move an object in vacuum from the outside. Due to the extensive usage of beam wire scanners, bellows age relatively quickly and an exchange might be required every few years of operation. The breakage of one of these components might compromise the accelerator vacuum. The mechanical design of the "rotating fast" scanners is shown in Fig. 2.2.

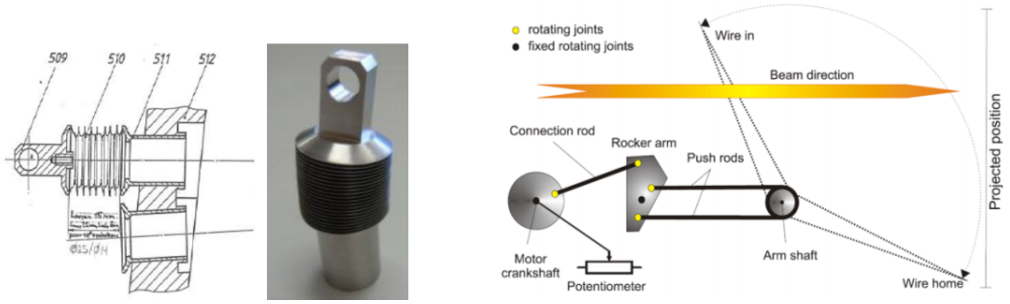

Figure 2.2 – Rotational Fast mechanics schematic (right) and bellows detail (left).

2.3. Wire scanners calibration

Rotational wire scanners need to be periodically calibrated in order to correct any potential system non-linearity and infer the accurate projected wire position from the angular information provided by the potentiometer [23].

The calibration process is based on a laser beam that emulates the proton beam. The laser system is mounted on precise micrometric mobile stages that displace the beam on the scan axis, this makes the wire to interact with the laser beam at different locations on the calibration region (100 mm). Each laser-wire crossing results in a missing laser power as measured by a photodiode. The potentiometer position corresponding to such laser power dips is correlated to the mobile stages position at the different interaction points and a calibration

table is generated. Different tables are generated for each operating speed. Each set of data is fitted with a polynomial function reproducing the transverse wire position versus the angular fork position, as expected by the system geometry (see Fig. 2.3). The fit residuals can be used to assess the level of accuracy/reproducibility.

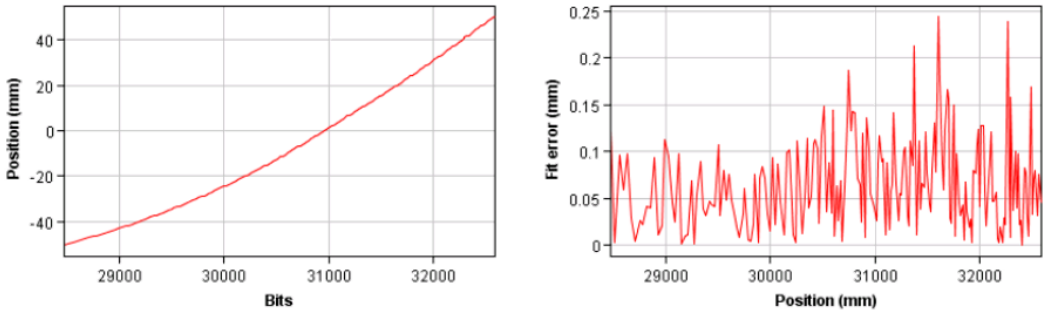

Figure 2.3 – Calibration curve of obtained for a PS BWS (left) and residuals of a 9th order polynomial fit (right).

Figure 2.4 shows the PS and PSB calibration systems working principle. In the PS case there are two mobile stages for the displacement of the laser and photodiode systems, this allows the calibration of scanners in a single plane. For the PSB scanners, there is a single mobile stage hosting optics, a mirror is placed on the opposite side of the tank and a beam splitter is used to direct the reflected light to the photodiode. The PSB calibration tank allows the installation of beam wire scanners on vertical and horizontal position (as they are mounted during normal operation), this last design allows the optics to rotate by 90 degrees to select the calibration plane.

The alignment of the optics is a critical factor, a small misalignment during calibration can introduce a measurement offset on the proton beam position and a scaling error on the beam size determination [24].

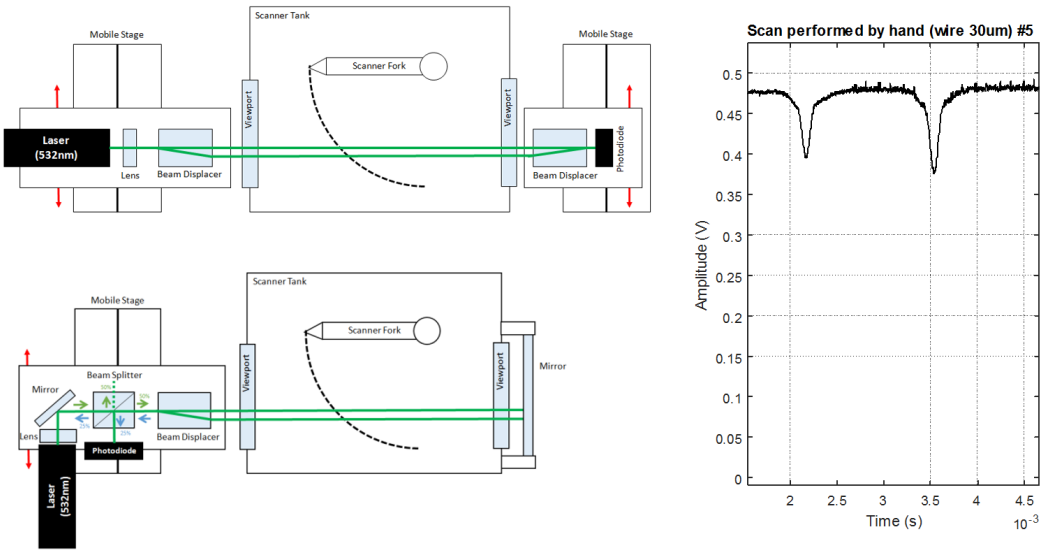

Figure 2.4 – PS (top) and PSB (bottom) calibration benches schematics and PD signal detected in a scan (right).

2.4. Operational secondary particles acquisition system

Although different scanner mechanics are used in each machine, in all cases an organic scintillator is used to detect the secondary particle shower. The light produced by the scintillating material is transported by a lightguide and attenuated with a settable neutral density filter from a wheel of filters. The scintillator light is detected with a photomultiplier tube (PMT) and transformed into a current signal. Finally the detector signal is transported through long coaxial cables and digitised on surface. Figure 2.5 shows an operational detector system in SPS.

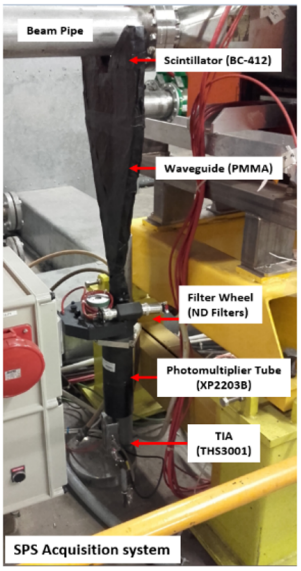

Figure 2.5 – Operational SPS secondaries acquisition system.

Filter selection and PMT gain are set by operators according the beam characteristics present on the machine prior to a measurement, in order not to saturate the acquisition electronics. Very often several scans are required to set properly the system working point. The geometry of the scintillator and light guide, the size of the PMT and the filters placed on the wheel are specific of each machine. Table 2.2 collects details of the assemblies for each specific machine.

Table 2.2 – Detailed description of scintillators and PMT systems used at CERN

Scintillator and PMT systems details for the BWS used at CERN				
	PSB	**PS**	**SPS**	**LHC**
Scintillator	BC-408 (EJ-200)		BC-412 (NE110)	
Geometry	Cilindrical (30x30mm)		Flat(250x150x20mm)	
Waveguide	Cylindrical tube with reflective walls		Wrapped PMMA Fishtail	
Photocathode	8 mm		40mm	
Dinodes	8 Metal Channel		10 Focused	6 Focused
Typical Gain	6e3 to 3e6		2e4 to 2e6	1e3 to 1e6
HV Range	400-1000V		800-1700V	800-2250V

PMT readout and digitalization electronics are also common in all systems. The signals coming from the detectors can be read in two different modes. In "turn mode" (low bandwidth), the scan signal is low pass filtered to obtain the general profile of the beam containing all bunches, low bandwidth cables are used for this mode. In "bunch by bunch" mode (high bandwidth), a transimpedance amplifier (TIA), with a fixed gain, attached at the end of the

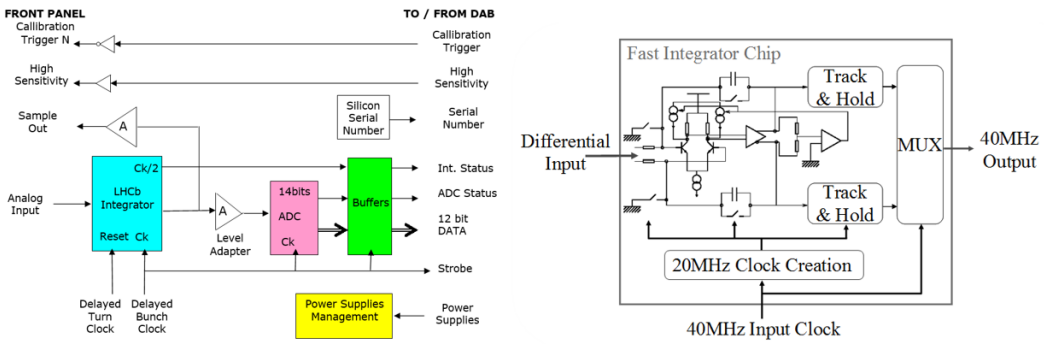

Figure 2.6 – IBMS Mezzanine simplified schematic (left) and fast integrator ASIC detail (right)[26].

PMT is used for fast current to voltage signal conversion and line impedance matching. The analog signal is transported to surface with long CK50 coaxial cables (distance vary depending scanner location from approximately 70 m to 250 m). Bunch by bunch mode allows single bunch profile measurements.

The digitization electronics are placed on surface, they are based on a VME digital carrier board (DAB64x) [25] and a digitization mezzanine board (IBMS) [26].

The **IBMS** mezzanine allows the integration of individual bunch signals at 40 MHz (21 ns integration windows with 4 ns dead time). This board uses a fast integration ASIC originally developed for LHCb preshower detector [27] and a 14bits ADC working at 40 MSPS(AD8138). The integrator ASIC accepts bipolar voltage signals (±2.5 V max) and contains 8 channels. Each channel is composed of two independent integrators followed by track and hold circuitry working at 20 MHz, as one integrator integrates the other discharges in alternating cycles. The track and hold outputs of each sub-channel are multiplexed, providing an effective integration frequency of 40 MHz. The input impedance is matched to 50 Ω and the input swing is ±3 nVs. Figure 2.6 shows schematics of the IBMS board and its main ASIC.

Given the unipolar nature of PMT signals, only half of the ASIC input range is actually being used. In addition, characterisation studies have demonstrated the need of electronics calibration prior to operation [28]. Calibration parameters include linear correction and offset compensation between the two sub-channels. Calibrated performance shows a linearity error below 1% and a spurious free dynamic range (SFDR) of 54 dB. The digital acquisition noise of this system results in 5 ADC bins, which translates to a relative error of 0.25% in amplitude for full scale signals.

The **DAB64x** is a standard digital board used on the different systems managed by the CERN Beam Instrumentation (BI) group. Beam loss monitors (BLMs), fast beam current transformers (FBCTs), and beam wire scanners (BWS) among other systems use this board to store and pre-process data. All logic is compiled in a large Altera Stratix EP1S40 FPGA, the board features the VME64 specifications for bus interface communications, a SRAM (512k x 32bit), timing interfaces for synchronisation with the accelerator and GPIO connectors for two mezzanines. The storage capability of the memory limits the amount turns that can be stored for a whole LHC fill (2808 bunches) to a total of 512k/2808 = 182 turns. A typically large LHC25ns beam at injection with beam $\sigma = 1.7$ mm scanned at 1 m/s it would require about 76 turns (89 us per turn) to acquire 4σ. To properly capture the full beam profile the acquisition gate has to be synchronised accurately (within the millisecond range).

Secondary shower acquisitions must be performed with beam synchronous timing (BST) to properly resolve bunch profiles. Machines synchronisation is provided by the CERN timing trigger and control (TTC) distribution network, which delivers the required 40MHz bunch clocks (SPS and LHC) and the orbit turn clocks for the different accelerators. The beam synchronous timing receiver interface for the beam observation system (BOBR) is a VME

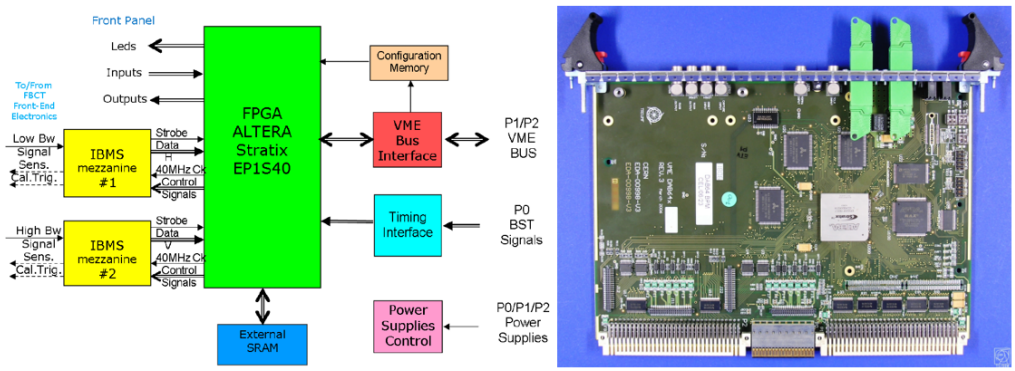

Figure 2.7 – DAB64x simplified schematic (left) and board picture (right).

board required to translate the TTC signals (distributed through optical fiber to the monitor location) into TTL clock signals.

2.5. Ugrade motivations

The requirements of the LIU [29], in terms of beam profile monitoring, highlights the need of upgraded beam wire scanners to overcome the limitations of current systems.

2.5.1. Mechanical point of view

Linear scanners such as LHC and SPS type feature a strong limitation on beam intensity measurement. Due to the speed of linear scanners (1 m/s), the carbon wire may sublimate when measuring nominal beams (1e11p/bunch) by RF heating and beam energy transfer. Studies on wire/beam interaction determined a limit of 2-3e13 charges/mm as threshold for wire sublimation. This approximation would correspond to around 240 LHC nominal bunches at 450 GeV (a total of 2.7e13 p crossing the wire), or around 2 nominal bunches at 6.5 TeV (a total of 1.2e12p crossing the wire) while scanning at 1 m/s [30]. Loses produced by BWS on LHC should also be limited nearby super-conducting magnets to avoid magnets quench [31]. In practical terms, only low intensity beams are used to measure the beam emittance evolution during the acceleration cycle with such scanners.

Concerning accuracy, repeatability studies on linear SPS scanners (BWS517V-BWS521V) yielded to 6-10 µm uncertainty on beam size for TOTEM beams at 26GeV (<1.5% uncertainty on emittance)[32]. Studies on the LHC linear scanners showed around 4.5% systematic error on beam profile measurement which would be translated into $\approx 9\,\%$ in emittance, these studies shown that a statistical error $\approx 6\,\%$ on emittance remained independently of the beam size and correction techniques employed [33].

The position precision of current systems is strongly influenced by electronic noise on the potentiometer reading. Position uncertainty only by electronic noise was determined to be ± 18 µm for linear scanners (after applying correction algorithms), ±33 µm for SPS rotational and ±90 µm for PS rotational [34]. The wire position incertitude of PSB "fast rotational" scanners was studied on a calibration bench, these systems featured a wire measurement precision of ±100 µm which is a combined effect of potentiometer noise, mechanical play and vibrations [23] [24].

For LHC, the number of nominal bunches measurable by current systems would be strongly reduced with the higher intensity post-LIU beams. A factor 10 increase on nominal scanning speed is therefore required to minimise the wire/beam interaction to be able to measure full LHC nominal fills of 2080 bunches at injection, while at the same time reducing the losses per scan (thus the risk of a quench).

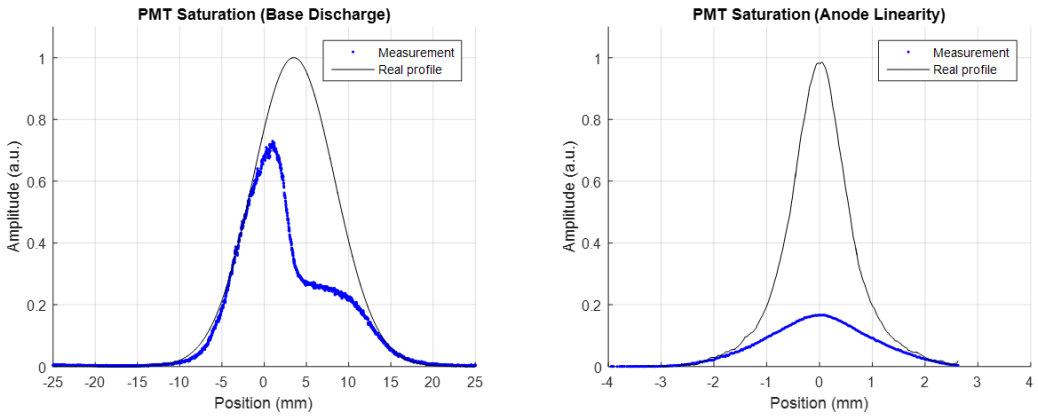

Figure 2.8 – Wire Scanner profile measurements showing two typical cases of degraded measurements.

The required emittance measurement incertitude for upgraded systems is specified to $<5\,\%$. For the most critical location at LHC this translates into a required position incertitude of 1-5µm.

2.5.2. Secondaries acquisition system point of view

One of the most complicated tasks for the operators when performing wire scanner measurements is to define the settings of the secondaries acquisition system. The different beam conditions in the accelerators (width, intensity and energy) strongly impacts on the secondary shower fluence, thus the detector signal amplitude. This situation obliges the operators to set a popper working point according the beam present on the machine to adapt the PMT output range to the acquisition electronics input range.

The main limitation of the detector assembly is that under certain circumstances, the PMT is forced to work out of its specifications. A very high photon flux in its cathode per bunch might compromise the anode linearity due to space-charge effects, this effect can be present on measurements before it becomes evident on the beam profile, by slightly distorting the Gaussian shape (providing a beam size measurement systematically wider). This effect, dependent on the input photon flux (cathode linearity) and output current (anode linearity), in practice places a limit on the maximum output pulsed current amplitude for a given configuration.

In other cases, even if the PMT is operating on its pulsed linear region and no space-charge effects are present, it may happen that the local charges available on the PMT base are not enough for the formation of the full scan signal. This effect, known as "PMT saturation" (base discharge), it leads to an unbalance on the dynodes voltage distribution and changes on the whole PMT gain during the measurement. Profiles highly affected by PMT saturation feature a sudden drop on amplitude. This type of saturation is linked to the total charge per scan demanded to the PMT.

The Fig. 2.8 shows measurements with both effects discussed previously. On the left (base discharge), the sudden signal drop can be easily identified. On the right (anode linearity), the PMT signal is not able to follow the beam profile due to space-charge effects. In general both effects are palliated with a change of ND filter (to attenuate the incoming light) or by reducing the PMT gain (to reduce the output current pulses amplitude).

PMT base discharge palliation was a topic under research during the last few years, this effect has been identified as a stopper in some beam measurement campaigns [35]. Previous contributions have deeply investigated on the topic [36] [37], and experimental knowledge have leaded the usage of custom PMT bases, including bigger capacitors on the last dynode stages [38] to allow the PMTs provide the required charge during a scan.

In addition to the inherent limitations of PMTs, beam profile measurements are degraded by the use of long coaxial cables for analog signal transmission. Such a long copper link (up to 250m) limits the system bandwidth inducing bunch pile-up in 25 ns structures, thus compromising the bunch by bunch beam profile measurement reliability. Given the harsh electro-magnetic (EM) environment of tunnel areas, these long transmission lines also expose the signal to a high RF and EM noise coupling, reducing the measurement SNR and directly affecting the beam profile determination.

The main topic of this work is to investigate on upgraded secondaries detector and acquisition systems for the LIU-BWS. It is required to cover a very high dynamic range to cope with the different machine configurations and allow Gaussian far-tail visualisation avoiding, where possible, the need of configurable parameters to ease operation. On the context of this work, an alternative detection mechanism, based on solid state pCVD diamond detectors will be evaluated to overcome the limits of PMTs.

2.6. LIU-BWS Design

Given the various issues discussed above for the present scanners, the development of a new scanner type for the LIU is motivated by the need to provide a faster, more robust, reliable and accurate instrument, featuring a high dynamic range for the secondary showers acquisition. The expected need to measure smaller beam sizes at higher beam intensities in the future is another driving reason for the upgrade. The basic concept is to combine a high scan velocity, nominally $20ms^{-}1$ to avoid wire damage, with an accurate and direct wire position determination. The specified precision on the wire position measurement is set to $\pm$2-5µm based on the LIU requirements.

The upgraded system places all mobile parts in vacuum and is developed around a frameless permanent magnet synchronous motor (PMSM). The rotor is placed in vacuum whereas the stator is outside the chamber. A thin non-magnetic stainless-steel wall between both parts preserves the vacuum. The motion transfer is performed through magnetic coupling, avoiding the need of bellows. The scanner shares the motor shaft for all components, including the forks, a high accuracy optical position sensor, a solid rotor resolver and a magnetic brake. Such a design avoids any mechanical play and offers a direct fork angular position measurement.

The motor is controlled through PWM by using position information from a resolver. Custom electronics were developed to drive the motor control from the surface [39]. As a safety feature, a passive magnetic brake is included on the design to allow the fork to return to a safe position in case of a power cut or control loss [40]. Finally, the position information from a high accuracy optical position sensor is used to precisely obtain the wire position during the scan for the beam profile reconstruction [41].

Wire vibrations during a scan are a source of uncertainty, IN and OUT scans must be performed with a specific movement profile divided in three phases (acceleration, constant speed and deceleration) during the 180 degrees stroke of a scan. To minimise wire vibrations, a careful tuning speed/acceleration profile is required [22], as well as optimisation of the different mechanical parts [42].

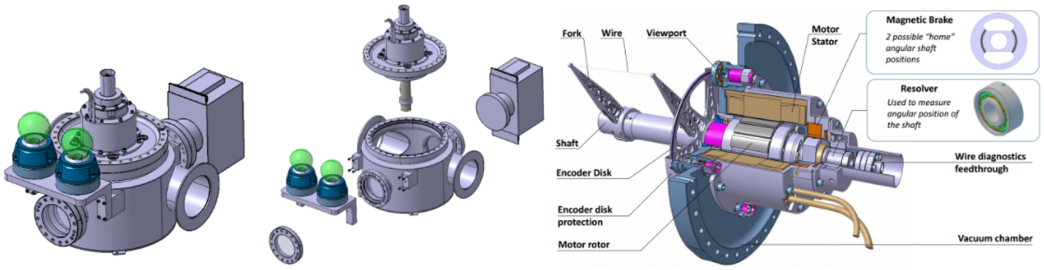

Figure 2.9 – PSB Beam Wire Scanner prototype for LIU.

The BWS upgrade for LIU at the moment of this work resulted in two mechanical designs. The first design iteration, shown on [43], was installed in the SPS on January 2015. The second iteration, motivated by integration challenges in the PSB, resulted in a lighter and more compact system. The last was installed in the PSB on March 2017 and is the baseline design for the rest of the accelerators, see Fig. 2.9.

2.6.1. Optical position sensor

The optical position sensor for the wire position determination, schematically shown in Fig. 2.10, is a critical part of the LIU-BWS design. It consist of a custom passive detector based on fibre optic incremental encoders. Surface electronics drive a laser diode and photodiode. The laser is operated in continuous mode and connected to an optical circulator. The continuous laser signal is transmitted through a radiation hard single mode optical fibre (SMF) to the tunnel, where the scanner is located. A couple of aspheric lenses focus the light, exiting the fibre, on a disk attached to the scanner shaft. Such a disk contains a track with a pattern composed by alternating slits of reflective and non-reflective areas. As the disk rotates, the reflections from the reflective areas are collected by lenses and coupled back onto the fibre. The "pseudo-sinusoidal" signal from the disk rotation is then directed to the photodiode by the optical circulator.

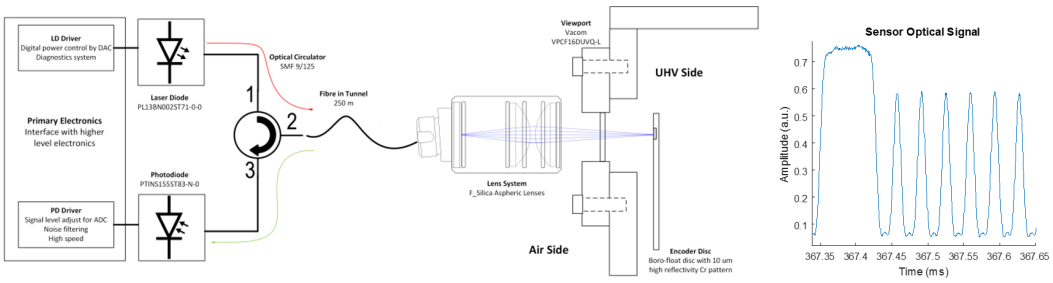

Figure 2.10 – LIU-BWS optical system schematic (left) and signal example showing a counting reference (right).

The fibre used is a SMF 9/125µm designed for 1310 nm (laser operating wavelength), the fibre output beam can be considered as a Gaussian with 9.2µm mode field diameter (MFD). The source divergence is defined by the fibre numerical aperture (NA=0.14). The focusing lenses apply a magnification factor of 2 (M=2) on the focal plane, i.e. the disk surface, meaning that the disk track is scanned with a Gaussian spot of 20µm $1/e^2$ diameter. The encoder disk consists of a glass substrate with a highly reflective chrome pattern applied by photolithography, the pattern pitch 20µm, with 10µm of chrome and 10µm of glass areas. Longer reflective slits are placed on strategic locations so that the sensor detects one counting reference at the beginning of the scan and another one at the end. Investigations are ongoing to include metallic discs.

Details of the optical sensor design on the first LIU-BWS iteration can be found in [41] and [44]. The final design is detailed in [45].

2.6.1.1. Optical signal stability

Optical signal amplitude is desired as constant as possible, any change on signal amplitude could potentially lead to position errors, i.e. loss counts. If the disk surface displaces axially respect to the focal point during the rotation, the optical signal can be affected by two effects: modulation by interferometry and coupling efficiency loss.

The interferometry modulation is produced by two wavefronts travelling on the same direction with a variable phase relationship. The first wavefront is produced by the back-reflection on the interface silica-air on the tip of the fibre (with a fixed phase), the second comes from the disk reflections. Little axial movements that vary the distance fibre-disk and produce a phase the shift between these two waveforms, leading to constructive and destructive interferences on the light signal travelling to the PD according. These interferences are explained by Eq. 2.1:

$$I = I_0[R_1 + R(1-R_1)^2 + 2(1-R_1)\sqrt{RR_1}\frac{sin(\epsilon)}{\epsilon}cos(4\pi\frac{x_0}{\lambda})] \tag{2.1}$$

where I_0 is the laser diode radiation, R_1 is the reflectivity at the end of the fibre, R the reflectivity of the disk reflective areas, x_0 the wavefronts path difference, λ the light wavelength and ϵ considers the effect of the coherence length.

Axial displacements on the order or half of the laser wavelength (1310nm/2 = 655nm) change the path length difference by 2π, which modulates the optical signal with a sinusoidal complete period. This effect makes the system very sensitive to vibrations, even if $R_1 << R$. Angled physical contact (APC) fibre ending is used on the fibre connector to minimise R_1, and therefore reduce the depth of the interferometry modulation. APC ending palliates the sensitivity to vibrations and enhances the robustness of the system, see Fig. 2.11.

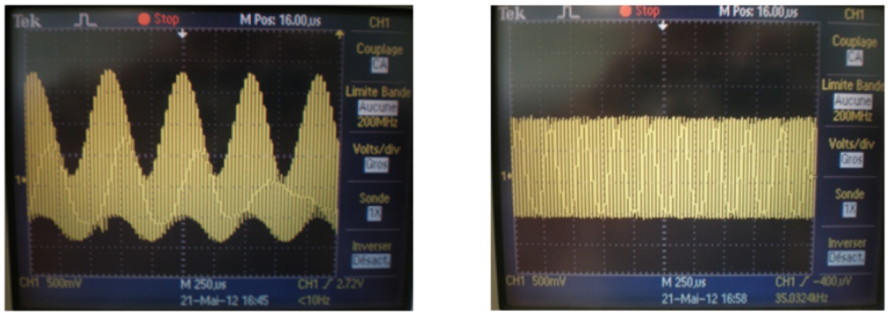

Figure 2.11 – Optical signal envelope produced by interferometry due to small disk-lens variation during the disk rotation, signals using PC (left) and APC (right) fibre termination are compared.

Coupling efficiency loss occurs when the disk surface is displaced w.r.t the system focal point, in this case the optical signal is not properly coupled back on the fibre, leading to optical signal loss. Optical simulations, as well as practical verification, determined an optical power loss of 20% for focal distance variations of ±100µm, see Fig. 2.12.

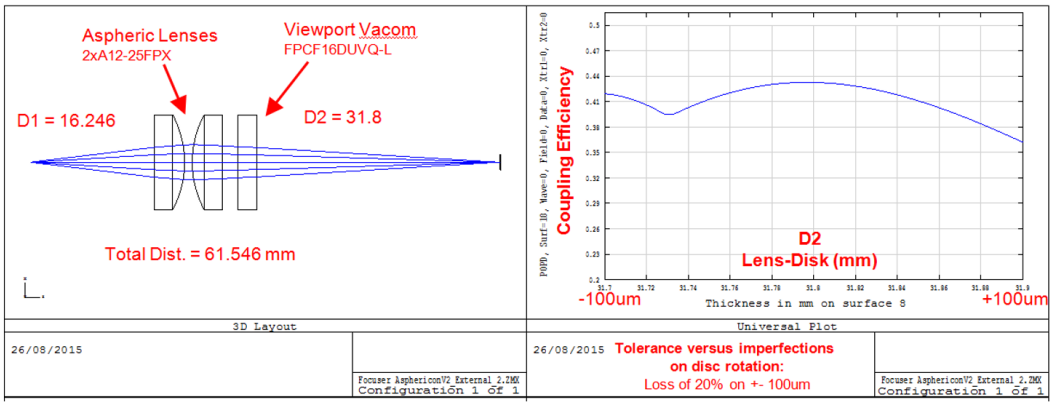

Figure 2.12 – Optical simulation schematic and tolerance for PSB.

By changing the lens configuration to bigger magnifications, the focal distance tolerance can be increased, however since the scanning dot is also increased, signal transitions are smoother. See practical tolerance measurements with different magnifications in Fig. 2.13).

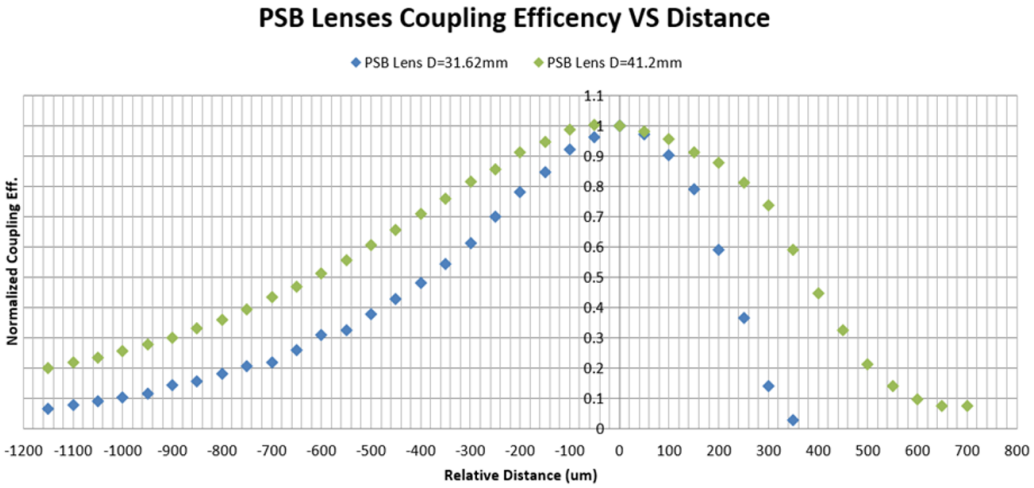

Figure 2.13 – Measured normalised coupling efficiency VS distance from focal point for different magnification factors.

2.6.1.2. Resolution and accuracy

According to the geometrical considerations (see Fig. 2.14). The encoder angular resolution and uncertainty can be approximated as on Eq. 2.2:

$$\Delta\alpha \pm \sigma_\alpha = \frac{2\pi}{(\frac{2\pi R_t}{P_t \pm \sigma_{pt}})} = \frac{P_t \pm \sigma_{pt}}{R_t} \tag{2.2}$$

which translated into projected position:

$$\Delta P_y \pm \sigma_{py} = F_L(\Delta\alpha \pm \sigma_\alpha cos(\alpha_c)) \tag{2.3}$$

where $\Delta\alpha \pm \sigma_\alpha$ and $\Delta P_y \pm \sigma_{py}$ are the angular and projected resolutions with their respective accuracy, R_t is the track diameter, $P_t \pm \sigma_{pt}$ represent the track pitch and its accuracy, α_c is the fork-beam crossing angle respect to the horizontal and F_L is the fork length.

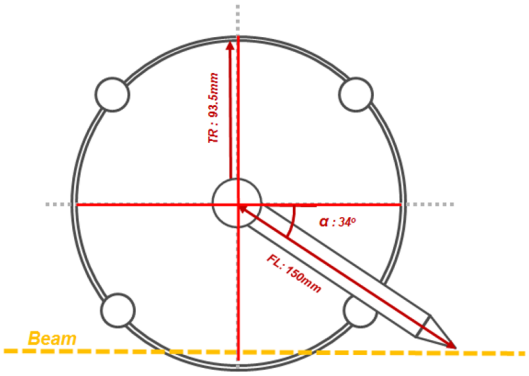

PSB Optical position Sensor Resolution				
Fork Length (FL)	150			mm
Impact Angle (α)	34			deg
Track Radius (TR)	93.5			mm
Slits Pitch	20	30	40	µm
# of slits on disk	29374	19583	14687	slits
Disc angular Resolution	213.9	320.8	427.8	µrad
Linear Resolution (ΔP)	32.09	48.13	64.17	µm
Projected Resolution (ΔY)	**26.6**	**39.9**	**53.2**	**µm**

Figure 2.14 – Schematic of the geometry for PSB scanner and optical position sensor, showing beam crossing angle (left) and resolution for different track pitch (right).

The disk provider specifies 10 µm reflective slits with 20 µm pitch and a placement incertitude of 1 µm in 100 mm. Wire/beam crossing angle is set to 34 degrees respect to the horizontal axis. The main specifications of SPS and PSB LIU-BWS are summarised in Table 2.3

Table 2.3 – Main parameters of SPS and PSB BWS optical position sensors

Main characteristics of the optical position sensor for the different prototypes								
System	**Fork Length (mm)**	**Track Diameter (mm)**	**Track Pitch (um)**	**Crossing Angle (deg.)**	**Agular Res. (urad)**	**Error (urad)**	**Projected Res. (µm)**	**Error (µm)**
SPS	182.5	135.5	21± 1	34	314	14.7	47.5	2.22
PSB	150.0	187.0	20±1	34	214	10.7	26.6	1.33

On encoder systems, the position error is determined by the quality of the encoder disk and by graduation tolerances, detection errors, and ultimately installation misalignment.

Installation errors are the dominant uncertainty source on the LIU-BWS optical position systems. Due to a number of design constraints, it is not possible use traditional optical aliment techniques. A metallic holder fix the glass disk in the scanner shaft. The misalignment of the track centre with respect to the scanner centre of rotation leads to a sinusoidal angular position error (eccentricity error). This error is cyclic in each revolution, see Fig. 2.15.

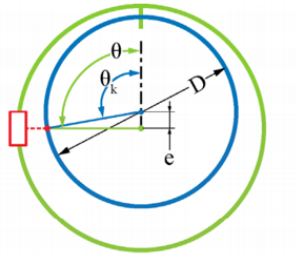

Eccentricity position error (in radians):

$$\theta_e = \theta - O_k = \frac{2e \sin\theta}{D}$$

Figure 2.15 – Position error induced by disk mounting eccentricity.

It is important to note that a mounting eccentricity of only 100µm leads to systematic angular errors up to ±1 mRad (resulting in a projected systematic beam position error up to ± 124µm). This error would also induce a systematic beam width error. Such position incertitude is unacceptable given the system specifications and mounting errors must be compensated by self-calibration.

2.6.1.3. On-axis self-calibration and performance

Self-calibration of optical encoders is possible through several reading heads [46]. Such a calibration technique is suitable to correct eccentricity errors and other systematic position errors linked to the disk graduation lines arrangement. The technique used to cancel LIU-BWS encoder mounting error is based on the use of two detectors displaced by π radians. The sinusoidal position error seen by each of the sensors is also displaced by π radians.

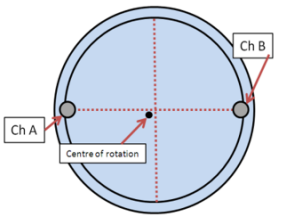

$$\Delta\theta_A = \Delta\theta + \frac{2e\sin(\theta)}{D} + \ldots$$

$$\Delta\theta_B = \Delta\theta + \frac{2e\sin(\theta+\pi)}{D} + \ldots$$

$$\frac{\Delta\theta_A - \Delta\theta_B}{2} = \frac{2e\sin(\theta)}{D}$$

Figure 2.16 – On-axis calibration strategy for eccentricity error compensation

The position measured by each sensor contains the real position $\Delta\theta$ (relative to a reference) plus an error of eccentricity with a different sign on each sensor (Fig. 2.16). The resulting error introduced by assembly misalignment is obtained by subtracting and dividing by two he position information of both sensors. This information is used afterwards to remove eccentricity error from the position reading.

The performance of this calibration method and its repeatability was tested for the SPS prototype resulting in 18μrad incertitude. An improved processing algorithm was employed for evaluation on PSB prototype to compensate the optical signal modulation produced by residual interferometry, out-of-focus disk displacements and impurities on the surface. The processing algorithm detects the local signal peaks and valleys, determines the amplitude at those local regions and applies a threshold on the 50% of the amplitude for each transition. The position information is extracted by counting only the signal threshold crossing points on the rising edges after a reference is detected (see Fig. 2.17).

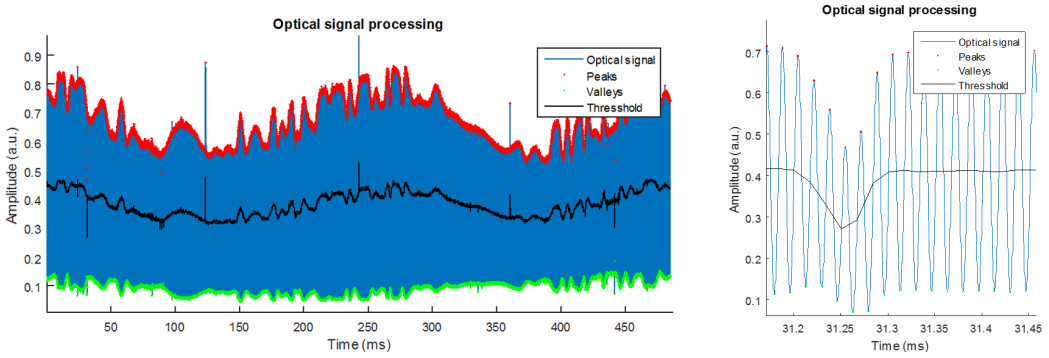

Figure 2.17 – On-axis calibration strategy for eccentricity error compensation

The PSB BWS optical disk and holder were placed in a test bench with the two sensors aligned as shown in Fig. 2.16 left. A DC motor rotated the disk at an approximated constant speed of 13rad/s (nominal LIU-BWS angular speed for scans at 20 m/s is $\approx$110 rad/s).

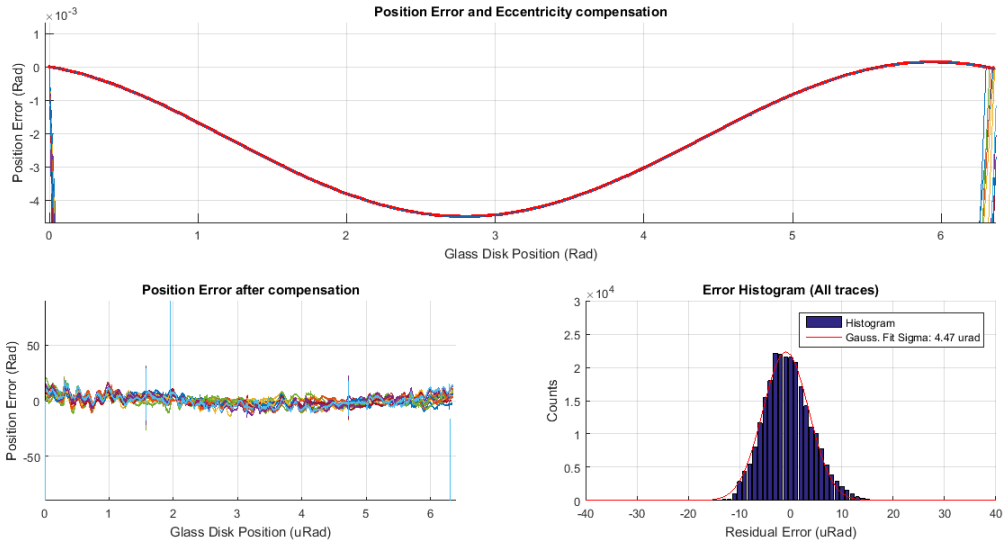

Figure 2.18 – On-axis calibration strategy for eccentricity error compensation

The Figure 2.18 shows an eccentricity error with ±2.25 mRad amplitude (disk off-centre by 210µm) this information is used as calibration look-up table for position corrections.

The repeatability of this calibration procedure can be inferred by subtracting one of these error traces to the rest of them. A Gaussian fit on the resulting residuals determines a position incertitude of 4.47 μRad (0.5 µm projected) after calibration. Different results may be obtained with nominal scans, vibrations due to strong accelerations might influence the calibration precision.

The strength of this calibration mechanism resides on the following points:

- If a single sensor is used for position recording, a single scan (or turn) with both sensors is required to extract a calibration table.
- In case of a failure of one of the sensors the system can still work with the other sensor by applying a corrected calibration table.
- On-line calibration is possible if both sensors are working in parallel during a measurement, the position information of both sensors for the same scan can be used to compensate mounting errors.
- Calibration can be performed on the device once mounted on the accelerator tank, moreover the study of different calibration curves over time can identify unexpected behaviours on the assembly.

2.6.2. Performance on calibration bench

The performance of the LIU-BWS assembly was studied with a calibration bench similar to those used on operational systems. The upgraded scanners featured a wire position precision of about 11 µm when operated at nominal speed (20 ms-1). This is close to 10 times better than operational PSB scanners, which typically feature ≈ 100 µm precision on the wire position determination.

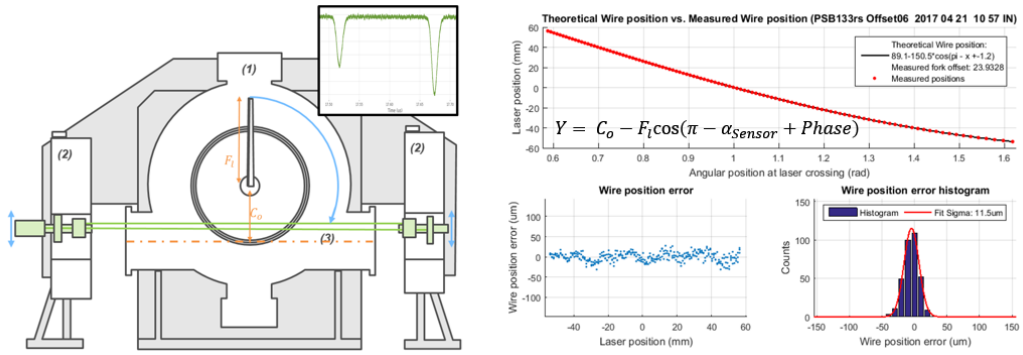

Figure 2.19 – Calibration bench schematic (left) and calibration results analysis (right)

As shown on 2.19, the scanner performance is studied from the fit residuals of the data points against the projected analytic equation. The analytic equation is determined by the scanner mechanical assembly and only three free parameters are adjusted by the fitting routine, these are: the distance from the beam centre to the rotation axis (Co), the fork length (FL) and the angle between the disk reference and the fork (Phase). Additional details on the LIU-BWS scanners characterisation can be found in [47] and [48].

Chapter 3

Radiation detection in high energy physics

The detection of particles is possible through their energy loss while crossing the detector. There is a rich variety of processes that describe this energy loss mechanism and, as consequence, a large number of detector devices are employed in high energy physics.

This chapter provides a brief introduction and theoretical background on particles interaction with matter, paying special attention to typical energy loss mechanisms of charged particles. A general review on radiation detectors and their operation theory is here provided.

3.1. The passage of particles through matter

When a charged particle pass through matter, it losses part of its energy and is deflected from its initial direction. The process underlying the energy loss of a particle is dependent on the nature of the particles, being different for electrons and positrons, heavy charged particles and neutrons (which in general barely interact). The processes causing these effects are inelastic collision with the atomic electrons of the material and elastic scattering of nuclei (Coulomb scattering), other process also cause energy loss such as Bremsstrahlung, emission of Cherenkov radiation, and nuclear reactions, the last ones have a very low probability.

3.1.1. Heavy charged particles

Heavy charged particles (elementary particles with a mass equal or greater than that of a proton) lose their energy mainly by ionising or exciting the atoms of the media. The ionising energy loss of charged particles, other than electrons or positrons, is defined by the Bethe-Bloch formula (Eq. 3.1) [49]. This is the mean rate of energy loss, or stopping power, in $MeVg^{-1}cm^2$, that a charged particle with velocity $v = \beta c$ and charge z loses on the material.

$$-\frac{1}{\rho}\frac{dE}{dx} = Kz^2\frac{Z}{A}\frac{1}{\beta^2}\left(\frac{1}{2}\ln\frac{2m_ec^2\beta^2\gamma^2T_{max}}{I^2} - \beta^2 - \frac{\delta(\beta\gamma)}{2}\right) \tag{3.1}$$

where $K \approx 0.307MeVcm^2/mol$ is a constant defined from the Abogadro's number (N_A), the electron mass (m_e), its classical radius (r_e) and the speed of light (c). Z, A and I are absorber material dependent (atomic number, atomic mass and mean excitation energy respectively). $\delta(\beta\gamma)$ is the relativistic density effect and corrects for the shielding of the particle's electric field by the atomic electrons. γ and β are relativistic quantities that can be expressed as:

$$\gamma = \frac{1}{\sqrt{1+\beta^2}} = \frac{E}{Mc^2} \tag{3.2}$$

where E is the kinetic energy of the particle and M its mass.

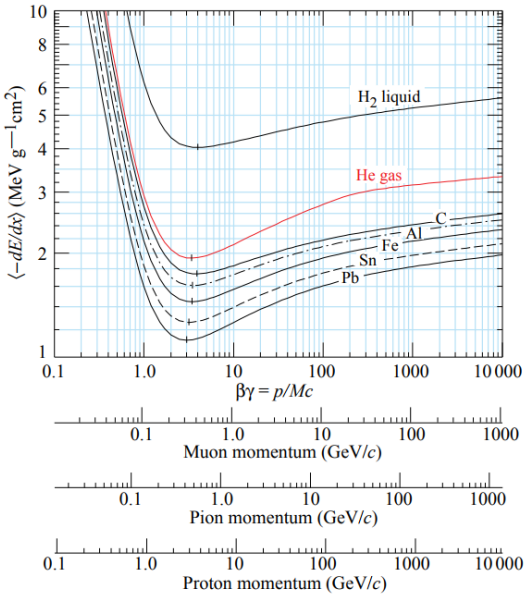

Figure 3.1 – Mean energy loss rate in liquid hydrogen, gaseous helium, carbon, aluminium, iron, tin and lead [49].

T_{max} is the maximum energy transfer in a single collision of a heavy particle with an electron of the material:

$$T_{max} = \frac{2m_e c^2 \beta^2 \gamma^2}{1 + \frac{2\gamma m_e}{M} + (\frac{m_e}{M})^2} \approx 2m_e c^2 \beta^2 \gamma^2 : M >> m_e \tag{3.3}$$

This approximation is valid for moderately relativistic particles within the region $0.1<\beta\gamma<1000$, and for intermediate Z materials. Above this region radiative effects dominate the particle energy loss. The loss rate given by Bethe-Bloch can be split in three regions in function of the particle velocity.

- $0.1 < \beta\gamma < 1$: There is a large dependency of the term β^{-2}, at this point the particle energy deposition strongly decreases with its velocity.
- $1 < \beta\gamma < 4$: Within this region there is a tendency change and the energy deposition rate reaches its minimum. Particles within this range are known as minimum ionising particles (MIPs).
- $4 < \beta\gamma < 1000$: As the particle momentum increases (β closer to 1), the term β^{-2} is almost constant and the term $\beta\gamma$ becomes dominant. This ultimately results in a slow energy deposition increase proportional to $\ln \beta\gamma$, this slope is known as "relativistic rise" and the density effect correction is applicable at this point.

In practical terms, slow particles deposit more energy, and as the particle momentum increases, with its maximum velocity saturating at c, $\frac{dE}{dx}$ flattens its behaviour, reaching the MIP threshold. From this point, the relativistic rise hardly exceeds 50%, hence, particles with velocities corresponding to $\beta\gamma>3$ are usually considered MIPs. Figure 3.1 hows an example of energy loss rate for Muons, Pions and Protons at different energies for different materials.

3.1.2. Electrons and Positrons

As heavy charged particles, electrons and positrons also loss energy due to ionisation at low energies. Their ionisation loss is explained with a modified version of the Bethe-Bloch formula, where incident and target electrons have the same mass. Since the scattering of

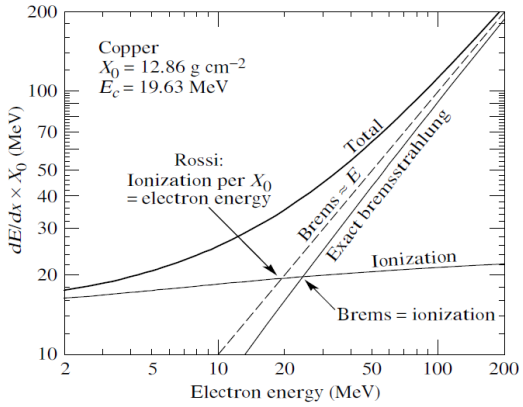

Figure 3.2 – Critical energy definition for electrons traversing Copper [49].

target and projectile particles are the same, they are considered as indistinguishable particles. For ionisation loss, the mean energy transfer for a single electron-electron collision is defined as half of the projectile electron energy ($T_{max} = \frac{m_e c^2 \gamma}{2}$) [50].

Ionisation loss is dominant for low electron/positron energies along with minor contributions of other processes such as Moller and Bhabha scattering and Positron annihilation. At high energies, Bremsstrahlung (Brems) emission is the main energy loss contribution. The boundary energy between these two mechanisms is normally within $E \approx 10 - 30MeV$, and is defined as the point where the differential energy deposition per unit of length by Ionisation and Brems is equal. The transition point is known as critical energy (E_c) and it is material dependent (see Eq. 3.4).

$$-\frac{dE}{dx}(E_c)\Big\rangle_{ionisation} = -\frac{dE}{dx}(E_c)\Big\rangle_{bremsstrahlung} \tag{3.4}$$

Figure 3.2 shows the transition between ionisation and Bremsstrahlung on copper and the contribution of both processes.

Bremsstrahlung (or braking radiation) is produced when charged particles loss energy by interactions with the coulomb field of the nuclei of the traversed medium. As the charged particles are decelerated in the Coulomb field, a fraction of their kinetic energy is emitted as photons, thus satisfying the law of conservation of energy. It can be described by:

$$\frac{dE}{dx} = 4\alpha N_a \frac{z^2 Z^2}{A}\left(\frac{1}{4\pi\epsilon_0}\frac{e^2}{mc^2}\right)E \ln\frac{183}{Z^{\frac{1}{3}}} \tag{3.5}$$

Bremsstrahlung is especially important for light particles, such as electrons and positrons, since the energy loss is proportional to $\frac{1}{m^2}$. For the specific case of electrons the Eq. 3.5 can be re-formulated in terms of radiation length as:

$$-\frac{dE}{dx} = \frac{dE}{X_0} \tag{3.6}$$

where E is the energy of the incident particle and X_0 is the radiation length, defined as:

$$X_0 = \frac{A}{4\alpha N_A Z(Z+1) r_e{}^2 \ln 183 Z^{\frac{-1}{3}}} \tag{3.7}$$

The radiation length is the mean distance over which a high energy electron loses all but $\frac{1}{e}$ of its initial energy. In contrast with ionisation loss, that features a logarithmic dependence on the energy beyond the MIP threshold, the energy loss by Bremsstrahlung shows a proportionality with energy.

3.1.3. Fluctuations on energy loss

The energy loss mechanisms previously detailed are statistical processes, the energy loss equations only describe the average value. The amount of energy that a particle losses on a material fluctuates with the number of collisions that the incident particle performs with the atomic structure of the detector material as the particle goes through. The Landau distribution describes the probabilistic distribution of energy loss for particles with same momentum through thin detectors. On this case the particle loses very few energy, and fluctuations are present around the calculated value (this would be the case of a single MIP). As the absorber gets thicker ($\frac{dE}{dx}x \gg 2m_e c^2\beta^2\gamma^2$), the probability distribution turns into a Gaussian-like form. For thin detectors, corrections are applied on the general formulas for the calculation of the most probable energy loss.

3.2. Light based detectors

The detection of ionising radiation by scintillation or Cherenkov light is one of the oldest techniques on record. These detectors transform the energy deposited in the materials into a proportional detectable photon yield. The scintillation process remains one of the most useful methods available for the detection and spectrometry of a wide assortment of radiations.

3.2.1. Organic scintillators

Organic scintillators can be found as polymerised plastics, liquids or crystals. Plastic scintillators are the most widely used detectors in high energy physics (HEP)[51] given their low cost, shape versatility, fast response and light yield. The most distinguishing feature of organic plastic scintillators is a very fast decay time, in the order of ns with a much faster rise time. This fast response allows the possibility of sub-ns timing resolution.

The process underlying on light production of organic scintillators is fluorescence. This process arises in organics from transitions in the energy level (vibrational status) on the structure of a single molecule. On this structure, the kinetic energy loss of charged particles through the scintillator bulk (ionisation) leads to a quick excitation of the electronic structure, changing the vibrational status to superior excited states. The primary scintillation photons (or prompt fluorescence) are emitted in the natural transition between an excited status to the ground electronic state through de-excitation [51]. Primary photons are emitted in the UV range, where the plastic absorption length is typically a few mm. For improving transmission efficiency and match the maximum-sensitivity-wavelength range of photodetector systems, fluorescent agents are added to the material acting as wavelength shifters. In these compounds, the photons generated by the primary scintillator are absorbed by the first fluor agent, the de-excitation of this fluorescent compound produces photons isotropically at a longer wavelength, for further wavelength shift, a second fluorescent agent may be added [50]. Figure 3.3 shows the different processes involved on the final light emission in organic scintillators due to ionising radiation.

Plastic scintillators densities vary from 1.03 to 1.2 g/cm^{-3} and typical photon yields are about 1 photon per 100 eV of deposited energy [49].

With the previous considerations, a one-cm-thick plastic scintillator traversed by a MIP would yield about $2x10^4$ photons. This photon yield is subject later to the wavelength shifter, material collection and transport efficiencies. In terms of linearity, all organic scintillators are characterised by a non-linear response with energy deposition at very high ionisation densities, which also depended on the particle type. In general the organic scintillators response is linear for electrons above $\approx$125 KeV, however for heavy charged particles such as protons or alpha particles, the non-linear response is still observed for higher initial energies ($\approx$ few MeV). The model describing the light output degradation at high ionisation densities ($\frac{dE}{dx}$) is explained by a semi-empirical model [53] [54] as follows:

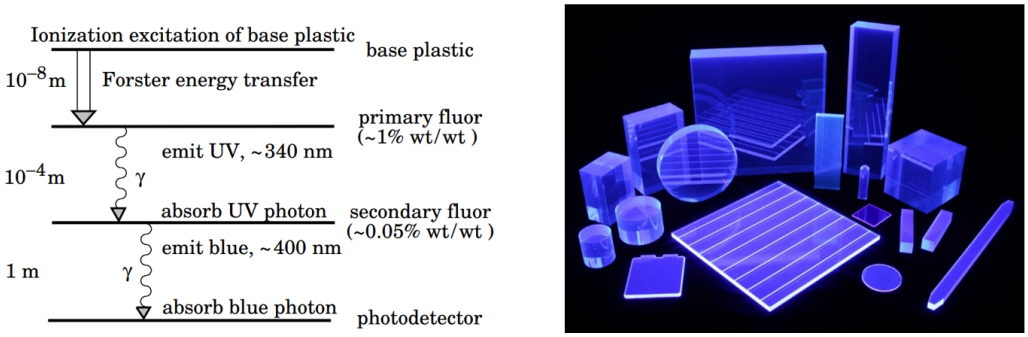

Figure 3.3 – Left: Operation mechanism of organic scintillators. Approximate fluor concentrations and energy transfer distances [49]. Right: Plastic scintillators with different sizes and geometries [52].

$$\frac{dL}{dx} = \frac{S\frac{dE}{dx}}{1 + kB\frac{dE}{dx} + C(\frac{dE}{dx})^2} \tag{3.8}$$

Where $\frac{dL}{dx}$ is the fluorescent energy emitted per unit of length, kB and C are empirically fitted parameters for specific scintillators, S is the normal scintillation efficiency and $\frac{dE}{dx}$ is the specific energy loss for the charged particle type crossing the scintillator.

The radiation-induced efficiency loss (radiation damage) on organic scintillators is a complex mechanism since it depends of many variables including the dose rate, the presence of oxygen or the nature of the radiation source. According to [55], typical plastic scintillators, such as BC-404 and BC-408 starts to show degradation (10% loss) after 0.5kGy and its properties may be completely degraded around 10kGy. On the other hand, [56], [57] show attenuations of 40-60% for TIDs ≈ 100kGy. The usage of such scintillators should be therefore limited for maximum doses 10^3 - 10^4 Gy. The optical power loss on scintillators is caused by damage to the fluorescent component, a decrease in light transport efficiency due to material darkening or the creation of optical absorption centres (colour centres), see Fig. 3.4. Timing characteristics as well as emission spectra seem to be unaffected by radiation damage.

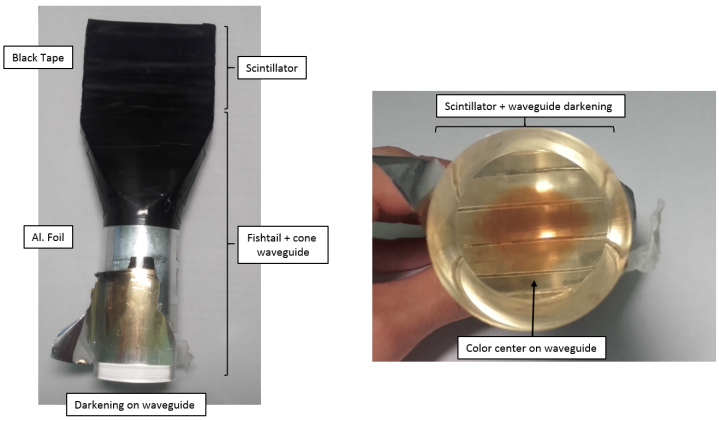

Figure 3.4 – Typical organic scintillator detector assembly (left) and detailed view of damage due to darkening and colour centre formation for long exposure to ionising radiation (right).

3.2.2. Inorganic scintillators

Inorganic scintillators are mainly crystals, pure, or doped with small amounts of other materials. The advantage of inorganic crystal scintillator lies in their greater stopping power, they have a higher density and atomic number. They feature higher light yield (better efficiency)

than organic scintillators, which is directly translated into a better energy resolution. On the other hand, their scintillation process features a slower response that could vary between tens of ns up to few µs.

Their light emission process is characteristic of the electronic band structure of the material. The absorption of energy when charged particles cross the material, results in the elevation of electrons from its nominal position in the valence band across the gap into the conduction band, leaving a hole in the valence band (electron-hole). In pure crystals, the emission of a photons during the de-excitation is an inefficient process at room temperature. To enhance the scintillator efficiency, impurities, called activators (in general Thallium, TI, or Cerium, CE), are deliberately added to modify the crystal structure, creating energy states within the forbidden gap through which an electron can be de-excited back to the valence band, this process gives rise to visible photons and therefore serve as the basis of the scintillation process [58].

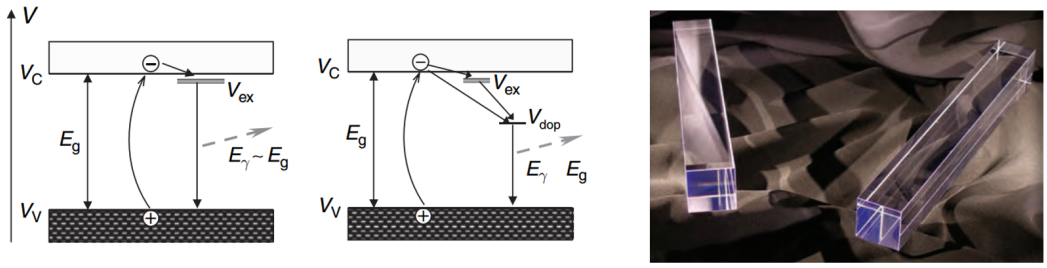

Figure 3.5 – Left: Energy bands in a pure (L) and doped (R) crystal [50]. Right: Inorganic Scintillator example [59].

Concerning scintillation efficiency, 3 times the band-gap energy of the material is required to create one electron-hole pair, in a typical inorganic scintillator based on sodium iodide, meaning that a charged particle must deposit about $20\,eV$ to generate a photon. For $1\,MeV$ of energy deposited on this crystal, around $5x10^4$ electron-hole pairs would be generated. Experimental analysis shown that the absolute scintillation efficiency of thallium-activated sodium iodide is about 12%, therefore 0.12 MeV would be translated into light energy, being about $4x10^4$ photons at $3\,eV$ ($\lambda \approx 400$nm) per $1\,Mev$ of deposited energy [51]. This represents about 4 times higher light yield than organic plastic scintillators and about 1 photon per electron-hole pair.

As organic scincillators, long exposure to ionising radiation may damage inorganic scintillators by reducing its light yield through colour centre formations and material darkening. It is widely assumed that inorganic scintillators show a better radiation tolerance than organic scintillators, however this is strongly dependent on the crystal material and the activator used. Temperature affects their scintillation light yield, and in the case of NaI(TI) also their signal timing [60], see Figure 3.6

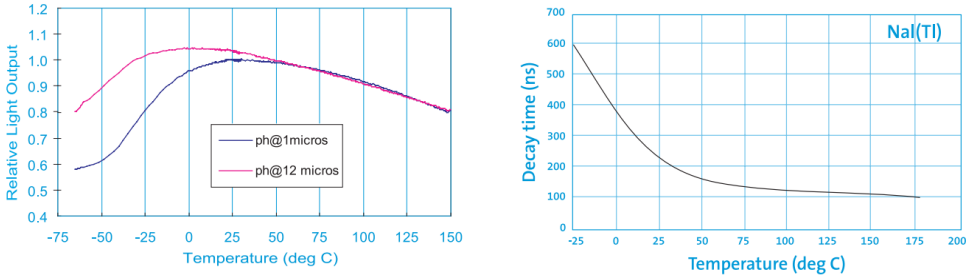

Figure 3.6 – Temperature dependence on light output and decay time for NaI (TI) [59].

3.2.3. Cherenkov detectors

Charged particles crossing a dielectric medium, with refractive index n, can reach a velocity v that exceeds the phase velocity of light into that medium $V_p = \frac{c}{n}$. When this happens, the particle emits electromagnetic radiation, known as Cherenkov radiation, visible in transparent mediums as blue glow emission.

The Cherenkov radiation is the result of the dipole field created as a charged particle polarises local atoms or molecules in the medium. When the particle velocity is slower than the local velocity of light, the dipoles are arranged symmetrically around the particle track, in this case, the resulting integrated dipole field is zero. However, when $v > \frac{c}{n}$, this symmetry is broken and there is a dipole field resulting in the emission of electromagnetic radiation (see Fig. 3.7 left). This can be defined as the creation of an electromagnetic shock wave, in analogy as sonic shock waves, created when objects travel faster than speed of sound in the air. The coherent waveform is formed in a conical shape and photons are emitted at a well-defined angle, dependent on the particle velocity (energy) and type [61].

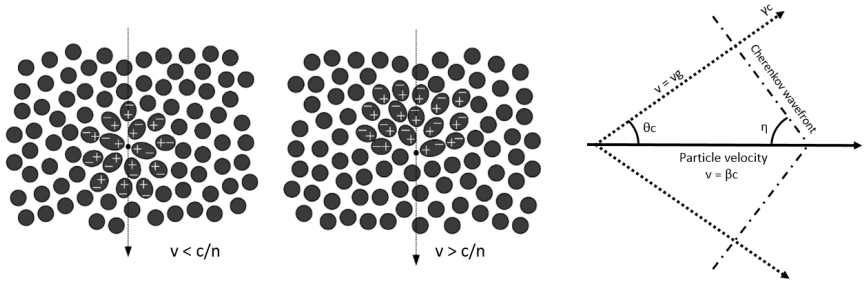

Figure 3.7 – Left: Polarisation of a medium due to charged particles traversing faster or slower than the velocity of light. Right: Direction of the emitted photons and Cherenkov wavefront respect to the particle track.

The characteristic emission angle θ_c (see Fig. 3.7 right) of the Cherenkov light with respect to the particle direction is strongly dependent on the particle energy and it is defined by the positive interference of photons at certain angle as:

$$cos(\theta_c) = \frac{1}{\beta n} \tag{3.9}$$

where $\beta = \frac{v}{c}$. The Cherenkov photons are emitted at a fixed angle with equal probability in the azimuthal direction, therefore they propagate around the direction of the charged particle in a conic distribution. The threshold value β_{th} for the production of Cherenkov radiation follows from Equation 3.9 setting the emission angle to zero, whereas the maximum emission angle θ_{cmax} takes its value at $\beta = 1$:

$$\beta_{th} = \frac{1}{n} \implies \theta_{cmax} = acos(\frac{1}{n}) \tag{3.10}$$

Due to the nature of the light emission in Cherenkov detectors, they can be built with many different materials: liquid (such water-based), gaseous (CO_2), crystals (quartz or fused silica), or as silica aerogel. The emission of Cherenkov light is in general a very small contribution to the total energy loss of a charged particle through a medium. In the case of Quartz, for a particle with $\beta \approx 1$ about 1 KeV/cm correspond to Cherenkov emission, whereas for a MIP the ionisation energy deposited would be 4.5 MeV/cm.

With regard to light yield, this type of detectors are characterised by a small number of photons per unit of length (in comparison with scintillators), but with a very large emission spectra that decays with the wavelength (normally on the 200-800 nm range). The Cherenkov photon light yield is defined as:

$$\frac{d^2N}{d\lambda dx} = \frac{2\pi z^2 \alpha}{\lambda^2}(1 - \frac{1}{\beta^2 n^2 \lambda}) \tag{3.11}$$

Where $\frac{dN}{dx}$ is the photon yield per unit of distance given in ph/cm, z is the atomic number, α is the fine structure constant ($7.297x10^{-}3$) and λ the emission wavelength. Integrating the previous equation over the typical sensitivity range of PMTs (350-550 nm) photon yield can be compared with scintillator materials.

$$\frac{dN}{d\lambda} = 2\pi z^2 \alpha (\sin\theta_c)^2 \int_{\lambda_1}^{\lambda_2} \frac{d\lambda}{\lambda^2} \; = 475 z^2 \sin^2\theta_c \tag{3.12}$$

Assuming a relativistic particle $\beta \approx 1$ crossing a quartz detector, the Cherenkov light yield would be about 2500 ph/cm, an order of magnitude less than plastic scintillators.

Cherenkov detectors are widely used for particle identification, such as RICH [62] at CERN, its use is extended as well for fast particle counters (BaBar [63]) and tracking detectors (Super-Kamiokande [64]). In recent investigations Cherenkov detectors are proposed for beam wire scanners applications [65] and for an optical fibre-based beam loss monitor system for CLIC [66].

3.2.4. Photon detection systems

Photon-detectors are used to transform the photon signal of a light-based radiation detector into a measurable current. There is a large selection of devices, especially PMT types, and technologies for such purpose in function of the application and features (timing resolution, dynamic range, position resolution ...).

3.2.4.1. Photo-Multiplier tubes (PMT)

Photo-Multiplier tubes (PMTs) are the most widely used photon-detectors for radiation monitoring. They are composed by a vacuum tube consisting of an input window, known as photo-cathode, a set of focusing electrodes, electron multipliers, and finally an anode for charge collection.

As photons impact on the photo-cathode electrons are emitted into the vacuum, this effect is known as external photoelectric effect, photo-cathode efficiency range 25-30% (i.e. about 1 e^- produced for each 3 photons impacting). The electrons generated are accelerated and focused, through an electric field, into the first dynode. When impacting the dynode, electrons are multiplied by secondary emission. Such process is repeated on successive dynode stages. The multiplied electrons emitted form the last dynode are collected on the anode for measurement. With a typical dynode electron multiplication factor, $\gamma \approx 10$, dependent on the primary electrons acceleration field and therefore the voltage between dynodes, the overall gain a PMT varies in function of the number of stages, the high voltage applied and the quantum efficiency of its elements (photo-cathode and dynodes).

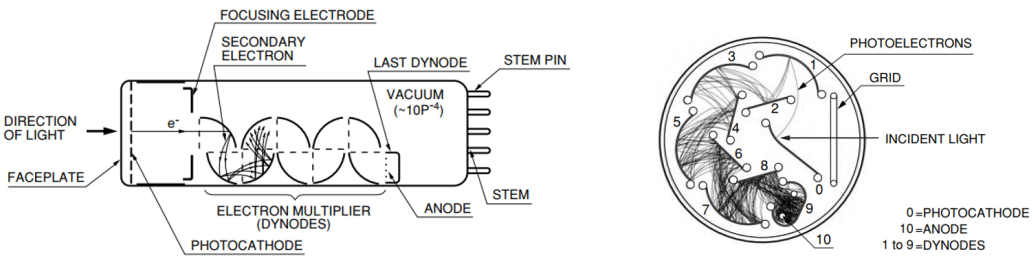

Figure 3.8 – PMT structures with main components. Linear-focused PMT (left) and Circular-cage PMT (right) [67].

PMTs are fast detectors, typical pulse width ranges 1-4ns FWHM. Timing characteristics are strongly dependent on the dynode structure type and the high voltage applied, pulses tend to be shorter at higher voltages. PMTs require a typical high voltages $\approx$ 700-2000 V for operation. Their dynamic range is limited on the low-end by dark current (thermionic emission, leakage current, field emission... etc), and in the high-end by photo-cathode linearity and by anode space-charge effects.

One can get spatial resolution from a PMT with special dynode structures and a multi-anode configuration. This is the case of metal package PMTs or Multi-Chanel Plate PMT (MCP-PMT). Metal package PMTs, features a thin dynode structure stacked in a way that allows multiplication with minimum electron trajectory spread. By using several anodes the photon impacting position on the photo-cathode can be determined. MCP-PMTs employs a two dimensional array with a great number of capillaries (channels) bundled in parallel and formed into the shape of a thin disk that substitutes the discrete chain of dynodes. In MCP-PMTs, each channel acts as an independent electron multiplier, when a primary electrons impinges the inner wall of the channel, an electric field accelerates the produced electrons to impact again the wall several times as the electrons travel through the channel, resulting in a large number of electrons released from the output end.

Given fine structure and short length of metal package PMT and MCP-PMTs, they feature a much faster response than traditional glass tube PMTs. Typical MCP-PMTs gains are $\approx 10^4$, concerning metal package PMTs, they can reach gains comparable to traditional PMTs $\approx 10^6$.

3.2.4.2. Hybrid Photo-Detectors (HPD)

Hybrid photon-detectors consist on an entry photo-cathode window (as PMTs) and a vacuum volume, were the generated photo-electrons are accelerated with a strong electrical field, and focused to impact on a semiconductor element such as PIN diodes or avalanche photo-diodes (APD). Spatial resolution is possible by using a multi-pixel detector. Their gain is about 10^3 and is defined by the electrical field applied to accelerate electrons and by the internal gain of the photo-diode (APD). The HV required to reach such gain varies in function of the silicon photo-detector used, being $\approx$ 10-20KV for PIN type and $\approx$ 4-10KV for APD type. Since this architecture is much simpler than PMTs and there are no multiplication stages (PIN type) it does not suffer from multiplicative noise intrinsic on PMTs. HPDs show a cleaner and more stable response [68]. Timing characteristics are comparable to PMTs with pulses of $\approx$ 4 ns FWHM .

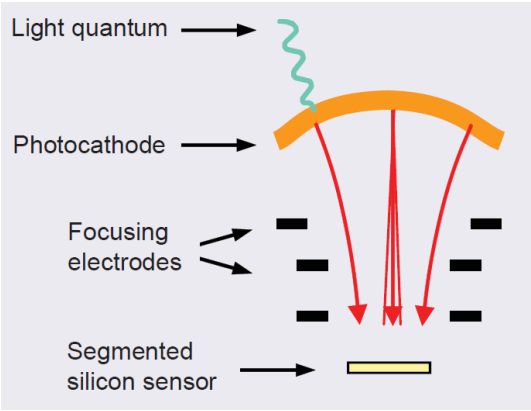

Figure 3.9 – HPD schematic and principle.

Given their low noise and dark count rate levels, they allow single photo-electron detection and feature a large dynamic range, extended up to 6 orders of magnitude, with an excellent linearity. On the other hand, their low gain requires of low noise electronics for operation.

3.2.4.3. Solid state photo detectors

This group covers standard silicon photodiodes (PIN), avalanche photodiodes (APD) and silicon photomultipliers (SiPM, also known as Multi-Pixel Photon Counters, MPPC).

PIN Photodiode: They feature a detection speed dependent on their capacitance, and therefore their size, with no amplification. A large number of photons is required for detection $> 10^4$.

APD Photodiode: Share common characteristics with the PIN photodiode but features an internal gain mechanism (up to 1000), lower light levels can be detected with such sensors but they are still far from single photon detection capabilities.

Silicon Photo-Multiplier (SiPM): They are built as a matrix of a high number of APDs pixels operated in Geiger-Mode with all cells connected in parallel to a single output. This device is capable of single photon detection with a very good resolution. When a single photon impacts on any cell it goes to breakdown and produces a well-known signal, when many cells are fired at the same time, the output signal is the sum of the single cells signal, thus featuring discrete increments. These devices provide gains ranging from 10^5 to 10^6, their dynamic range is defined by the number of pixels of the detector. As the number of received photons approaches the number of pixels, their linearity starts to saturate, this is due to the fact that when a single cell receives two or more photons at the same time, the signal produced is that of a single photon. The SiPM signals feature a fast rise time (≈1ns) with a slowly decaying tail (up to 50-70ns) characteristic of the APD diffusion process. In some applications cooling is required to avoid dark counts thermally generated.

3.3. Solid state particle detectors theory

Solid state detectors operate with the same principle as ionisation chambers, the energy absorbed by ionising radiation on the detector produces mobile charge carriers (electron-hole pairs) on the detector bulk. An electric field is induced on the material by applying a voltage difference between two electrodes to separate and collect the charges generated by the crossing particle. This process generates electrical current on the detector, detectable with an external circuit, see Figure 3.10. This re-distribution of charges on the material is seen by the electronics as a short current pulses that are typically amplified to measurable levels. The number of electron-hole pairs generated on the material is proportional to the deposited energy and therefore to the number of crossing particles.

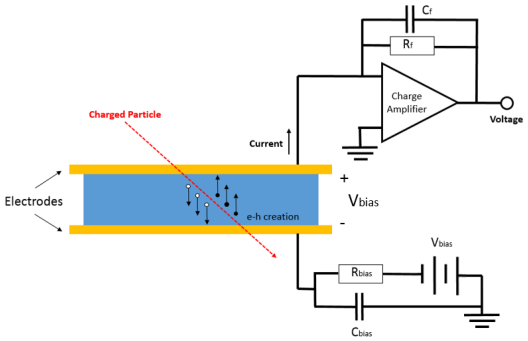

Figure 3.10 – Basic solid state detector working principle, architecture, biasing circuit and readout electronics.

Solid state detectors are usually based on Silicon (Si) Germanium (Ge), GaAs and Diamonds (C). The detector response to ionising radiation of each detector technology is linked to the electronic structure of the material and electrical properties. Table 3.1 shows a comprehensive summary of the material properties for silicon and diamond [69].

Table 3.1 – Atomic and electrical properties silicon and diamond materials for radiation detection in high energy physics.

Property	**Units**	**Silicon**	**Diamond**
Atomic Number		14	6
Mass Density	**[g/cm^3]**	2.329	3.52
Band Gap	**[eV]**	1.12	5.5
Dielectric Constant		11.9	5.7
Resistivity	**[Ω cm]**	2.3 x 10^5	10^{16}
Breackdown Field	**[V/cm]**	3 x 10^5	$10^6 - 10^7$
Electron Mobility	**[cm^2/Vs]**	1400	2200
Hole Mobility	**[cm^2/Vs]**	450	1800
Thermal Conductivity	**[W/K cm]**	1.3	6 - 20
Ionization Energy	**[eV]**	3.6	13
# of eh-pairs per MIP	**[e/µm]**	80	36
Displacement Energy	**[eV]**	13 - 20	37 - 47

The total signal charge of the detector when energy is deposited on its volume depends of the number of charges generated and is calculated as:

$$Q_s = \frac{E}{E_i} Q_e \tag{3.13}$$

Where E is the absorbed energy on the material, Q_e the electron charge ($1.6e^{-19}C$) and E_i the material ionisation energy (energy required to generate an electron-hole pair).

The signal charge (Q_s) increases with the energy deposited (E) and is inversely proportional to its ionisation energy (E_i), thus, the signal charge increases with the thickness of the detector and decreases with the material bandgap.

As an illustrative example, a 300µm thick silicon detector (E_i=3.6 eV, E_{mip}=1.66 $MeVg^{-1}cm^2$, ρ=2.32 gcm^{-3}) would exhibit about $3.2e^4$ charges per crossing MIP. A single crystal diamond detector with the same thickness, and given its higher ionisation energy, (E_i=13 eV, $E_{mip} = 1.72MeVg^{-1}cm^2$, $\rho = 3.5gcm^{-3}$) would generate about $1.3e^4$ charges for a MIP.

The ionisation energy is roughly proportional to the material bandgap energy (E_g). For the generation of mobile charges, the energy deposited must exceed E_g. The proportionality between E_g and E_i is approximated as [70]:

$$E_i \approx 2.8E_g + 0.6eV \tag{3.14}$$

This approximation shows that, for charged particles, about 30% of the energy deposited actually is dedicated to signal generation, whereas the remaining is dedicated to phonon excitation.

The timing on the signal formation is defined by the carriers velocity, which is determined by the carriers mobility and the strength of the electric field applied:

$$V(x) = \mu E(x) \tag{3.15}$$

where μ is the carrier mobility and $E(x)$ the electric field strength.

For fast responses and an efficient charge collection, a strong electric field must be applied between the electrodes. In addition, quiescent (leakage) current with such electric field must remain low, a high resistivity is therefore of interest. In solids, the resistivity depends exponentially on the bandgap and it is linked to its intrinsic carriers density. The Intrinsic carriers density is temperature dependent and calculated as:

$$n_i = \sqrt{n_v n_c} e^{-\frac{E_g}{2k_B T}} \tag{3.16}$$

where k_B is the Boltzmann constant, T the temperature in K, n_v the effective density of states in valence band and n_c the effective density of states in conduction band.

This is the number of electrons in the conduction band (and holes in the valence band) derived from thermal generation of e-h pairs, a higher carrier density increases the material conductivity.

Considering an intrinsic Silicon detector (n_i=$1.5e^{10}cm^3$) with a volume of $300e^{-}4cm^3$ (1 cm x 1 cm x 300µm) at room temperature ($\approx$ 300K) one obtains about $4.5e^8$ free carriers. Such level strongly hides the detection of a MIP event ($3.2e^4$ carriers). The power dissipation linked to the bias voltage and the material resistivity is another factor to consider. Our silicon detector example with a resistivity of $10^4\Omega cm$ and 30V bias voltage would lead to leakage currents $\approx$ 10mA and thermally dissipate about 0.3W.

On Si-based semiconductor detectors, the conductivity and carrier density is controlled through the silicon doping and the creation of PN junctions. These junctions act as diode structures and are reverse-biased, generating a depleted region that acts as the detector volume.

The crystal lattice of the detector material also defines the charge collection efficiency. Defects and impurities during the crystal growth can form trapping sites for the charge carriers. Trapping removes mobile charges available for signal formation, i.e. reduces signal amplitude. The probability of a carrier being trap is proportional to its travelling time, which leads to a carrier lifetime. If charges are swept rapidly from the crystal (with a high electric field), trapping probability is reduced. Depending the nature of the trap, the externally applied electric field can release the carrier from the trap, leading to a delayed charge collection. As a result, charge collection efficiency is generally improved with high electric fields.

The efficiency of pn-junction silicon detectors is close to 100%, virtually all charges reach the electrodes and no trapping is appreciated, this is due to high purity of the material during its fabrication process. However, after heavy irradiation, charge traps progressively emerge on the material and the mean travel distance of ionising particles shrink. In the case of diamond detectors (poly-crystalline) charge traps are always present resulting in a mean travel distance shorter than the detector thickness. The charge collection efficiency (η_c) is expressed by the mean travel distance, drift length or "charge collection distance" (CCD), divided by the detector thickness (D).

$$\eta_c = \frac{CCD}{D} \tag{3.17}$$

3.3.1. Semiconductor detectors

The traditional structures of semiconductor radiation detectors are the PN diodes reverse biased. This structure is built with silicon artificially doped with impurities to tailor its conductivity.

The PN junction is a combination on n-type and p-type silicon. Due to the gradient of electrons and holes density, charges migrate by diffusion (electrons from n- to p-region). When thermal equilibrium is reached, a potential on the junction (V_{bi}) is built-in, see Figure 3.11. This charge diffusion generates a "depletion region", virtually free of mobile charges. As in a standard diode structure, the depletion width can be artificially modified. When reverse biased the depletion region is increased as:

$$\omega = \sqrt{\frac{2\epsilon(V_b + V_{bi})}{e}(\frac{1}{N_a}\frac{1}{N_d})} \tag{3.18}$$

where N_a and N_d are dopants concentration, ϵ is the material dielectric permeability, V_{bi} the built-in voltage and V_b the applied bias voltage. When the depletion width (ω) is as big as the detector thickness (d) the detector is "fully depleted".

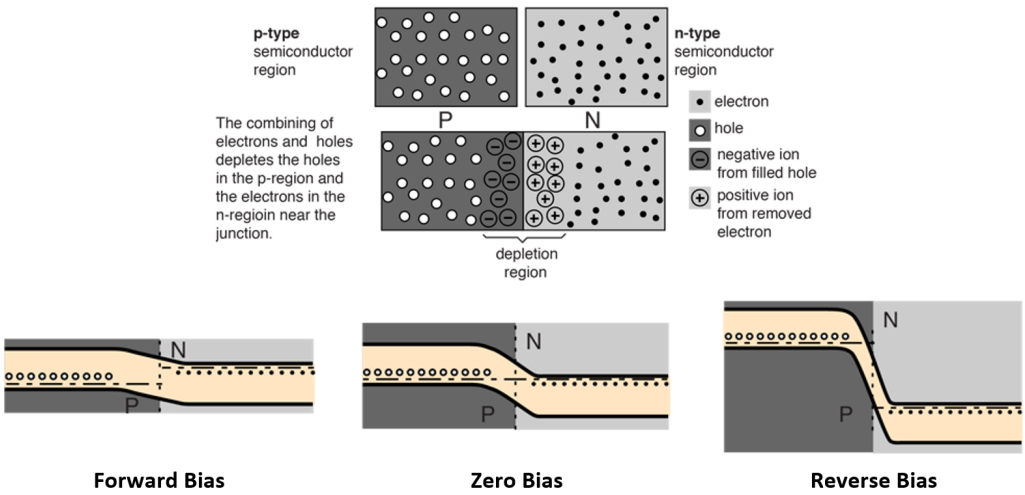

Figure 3.11 – A PN junction showing the depletion region in thermal equilibrium (top) and PN energy bands with forward, zero and reverse bias voltages [71].

The electric field in the depleted region sweep mobile carriers to the electrodes when traversed by charged particles, thus forming an ionisation chamber where the depletion region is the active detector volume. On this configuration, the detector forms a capacitor where the depleted region is considered as dielectric and the un-depleted P and N the electrodes. The detector capacitance can be calculated as:

$$C_d = \frac{\epsilon A}{\omega} \tag{3.19}$$

where A is the detector area.

When coupled to an amplifier, the capacitance of the detector influence on the signal electronic noise. Considering the noise current (I_n) negligible, by cooling the detector, the equivalent charge noise (Q_n) is calculated as:

$$Q_n \approx e_n C_d \tag{3.20}$$

Here e_n is the amplifier input voltage noise. For low noise it is desired to keep the detector capacitance (and dielectric constant) as low as possible.

Silicon is the dominant technology on particle detection, purity, cost, good understanding of the material, and availability are the main driving reasons, however they are prone radiation damage. The bibliography distinguish in two types of radiation damage [72]:

- **Bulk damage:** A traversing particle can produce defects in the lattice of the semiconductor when interacting with the material atoms. If the collision recoil energy is higher than the lattice binding energy, an atom can be displaced from its site. This displacement produces defects on the material structure and new types of atoms, which can be considered as undesired dopants.

- **Surface damage:** This term summarises all defects in produced on the oxides (pn-dopants on Si detectors). Ionising radiation on oxides is not a fully reversible process and can cause steady changes on the material properties. Surface damage affects the detectors capacity, the internal electric field and the breakdown behaviour.

On silicon detectors, based on PN junctions, the radiation damage increases the leakage current (higher noise) and changes the full depletion voltage of the detector (lower signal). The effective symptom is a decrease in the detector SNR.

3.3.2. Diamond detectors

Diamond detectors, developed and deeply investigated by the RD42 collaboration [73] from the early 1990s, are of interest on high energy physics due to their high radiation tolerance and attractive material properties in comparison to silicon detectors, see Table 3.1.

- With E_g =5.5eV it is regarded as an excellent insulator. Its very low intrinsic charge carrier concentration allows intrinsic operation without pn-junction.
- Given its high resistivity they operate with very low leakage current.
- No cooling is required due to its excellent thermal conductivity.
- Its small dielectric constant is translated into a lower detector capacitance and therefore low noise performance for subsequent electronics.
- A higher carrier mobility ensures faster signals and better temporal resolution than silicon.
- They feature a much higher radiation tolerance and with a higher displacement energy.
- Detector leakage current remains very low even after large irradiation doses.

The diamond material used for this detectors is grown in a complex Chemical Vapour Deposition (CVD) process, details can be found in [74] and [75]. Depending the substrate used for the diamond growth, these detectors can be divided in two types; single crystal (sCVD) and poly-crystalline (pCVD) diamonds. The type of diamond, as well as its size, are dependent on the seed used for its growth. Whereas for sCVD diamonds employ high pressure and high temperature (HPHT) diamond crystals as seed, pCVD diamond uses non-diamond substrates, or diamond powder. The main difference between these two types of synthetic diamond is their structural crystal purity (much better on sCVD), which has a direct impact on their charge collection efficiency. sCVD diamonds are in general fabricated in smaller sizes and at a significantly higher cost.

3.3.2.1. Signal formation

With an average energy to produce an electron/hole pair (ionisation energy) ≈13eV, the average of charges produced by a MIP per micrometre, calculated with the Bethe Bloch equation (3.1), results in $q_0 = 36e/\mu m$, a particle traversing the whole detector thickness t would produce $Q_o = tq_0$ charges. These carriers drift to the electrodes within the applied electric field. As discussed on section 3.3.1, charge traps can reduce the effective charge during the drift. The response of diamond detectors is characterised by the charge collection distance (CCD), which is defined as an equivalent detector thickness without any charge loses.

$$CCD = \frac{Q_m}{q_0} \tag{3.21}$$

where Q_m is the charge measured in the front-end electronics for a MIP. This correspond to the average drift distance of an electron (or hole) under the influence of the electric field. The quality of a diamond detector is described with the CCD and the detector thickness [69].

pCVD diamonds feature grain-boundaries which act as charge trapping centres, thus influencing the charge collection distance. pCVD detectors show optimal performance with electric field densities 1-1.5V/µm, reaching a charge collection distance smaller than the detector thickness [76]. The quality of pCVD diamond detectors has improved over the least years, their CCD is reaching 275-300µm (for 500µm thickness). sCVD diamonds feature a high purity and close to 100% charge collection efficiency (as silicon) at low electric field densities (0.2V/µm) [77]. Figure 3.12 shows the CCD evolution with bias voltage for both types of diamond detectors.

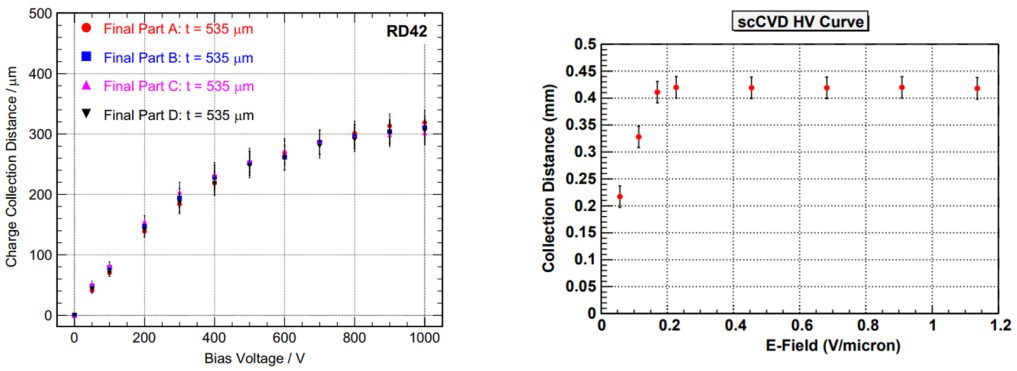

Figure 3.12 – Left: CCD for 530µm thick pCVD diamond detectors versus high voltage [76]. Right: CCD for a 440µm thick sCVD diamond detector versus electric field [77].

The better charge collection efficiency of sCVD diamond detectors (compared to pCVD) is translated into a higher signal for a MIP with a lower amplitude spread, thus better resolution. The detector response for a MIP is shown in Fig. 3.13 for both types of diamond detectors.

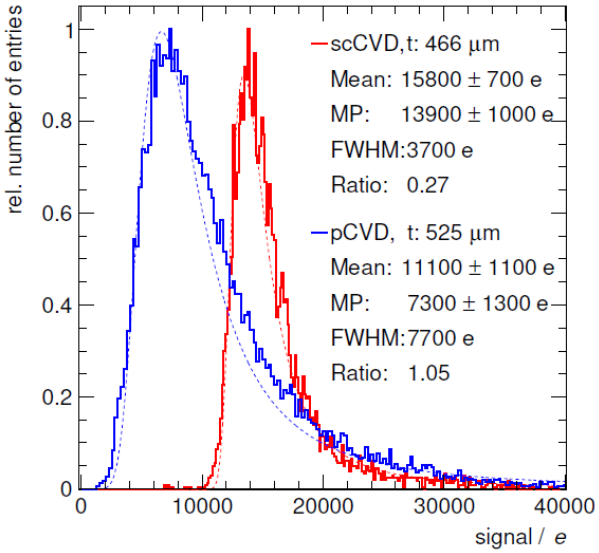

Figure 3.13 – Response of a 400um thick sCVD and 525um thick pCVD diamond detectors for a MIP [76].

Considering the charge collection distance, the approximated charge that arrives to the electrodes (Q_d) of a diamond detector can be calculated from the deposited energy (E) on its volume as:

$$Q_d = \frac{E}{E_i} Q_e \frac{CCD}{t} \tag{3.22}$$

For a MIP on a pCVD with a CCD = 300µm and 500µm thickness (t) the equivalent charge is $\approx 1.6\,\text{fC}$ [78]. The width of the current pulse (τ) is also defined by the CCD, the charges mobility and the applied electric field, this is also known as carrier lifetime.

$$\tau = \frac{CCD}{\mu \frac{V_{bias}}{t}} \tag{3.23}$$

where μ is the carriers mobility and V_{bias} the applied voltage on the electrodes. With an electric field density of 1V/µm and an electron mobility 2200 cm^2/Vs of the pulse width

observed on this detector would be about 1.5 ns. On this case, the approximated amplitude of the current pulse results $\approx 1\mu A$ and is calculated as:

$$I_d = \frac{Q_d}{\tau} \tag{3.24}$$

3.3.2.2. Pumping effect and polarisation

The charge collection distance, and signal amplitude, of a pCVD diamond detectors can increase by more than 40% after a moderate irradiation. During irradiation, the charge traps present on pCVD diamond detectors are filled and made inactive (passivated), hence they no longer absorb free electrons or holes. When the charge traps have been passivated, the detector state is called "pumped" and remains in this state for long periods of time (typically months). The detectors can return to the original "un-pumped" state if they are exposed to ultra-violet (UV) light. Diamond pumping is an extended practice to improve the pCVD diamond detectors efficiency. To fully pump a diamond detector a dose of 3-10 KRad is considered enough [79], in general irradiation is done with β particles from a ^{90}Sr source during long exposition times (10-60h).

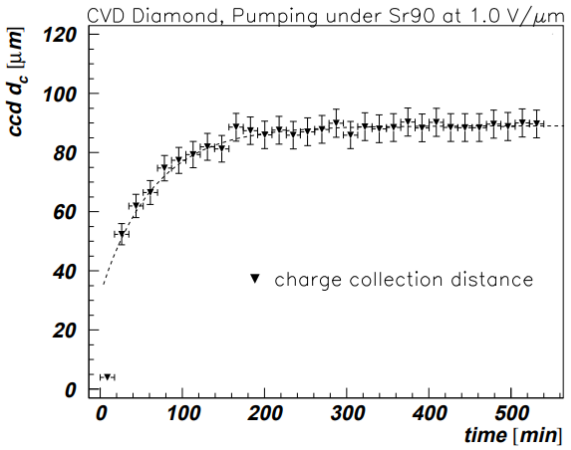

Figure 3.14 – CCD as function of exposure time to ^{90}Sr β particles of a pCVD diamond detector [73].

Pumped pCVD diamond detectors require of a stabilisation period after a bias voltage change, this effect is known as "polarization" and it is characterised as a variation on the CCD with time after a bias voltage change (see Fig. 3.15). Polarisation is strongly related to the presence of defects and charge traps on the diamond bulk. The trapped charges inside the diamond create an internal electric field that counteracts the external bias, modifying therefore the detector signal amplitude and the equivalent CCD [80]. Since this effect is linked to the presence of charge traps, its study is proposed for the characterisation of radiation-induced damage on pCVD and sCVD diamond detectors [81] [82].

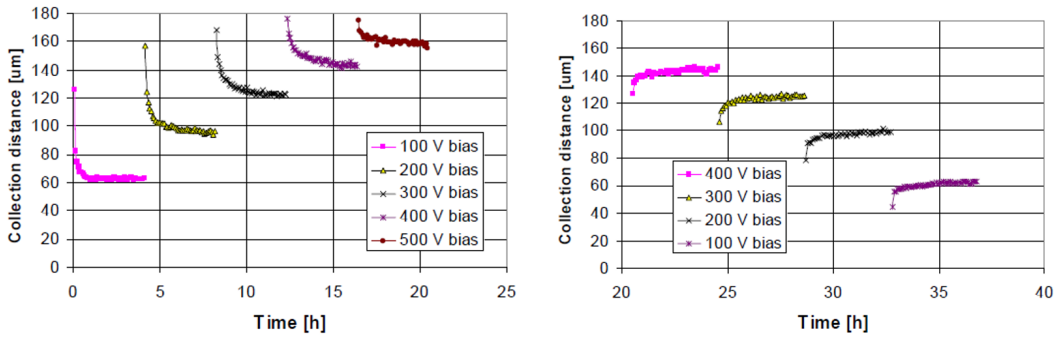

Figure 3.15 – CCD versus time showing a polarisation (left) and de-polarisation (right) each time bias is increased for a 300um thick pCVD diamond detector [80].

3.3.2.3. Radiation hardness

The performance degradation of diamond detectors with incident radiation is mainly linked to bulk damage, they feature a higher displacement energy (43eV) than silicon, thus, they are more radiation-hard. The vacancies generated by the atom displacement act as traps for mobile charges generated by ionisation. The number of displacements per atoms (DPA) of a material is a measurement of the radiation damage, it explains in average how many atoms are displaced due to impacting particles, and quantifies the crystallographic defects of the material. Recent FLUKA DPA simulations have been carried out on silicon and diamond materials with Neutrons, Protons and Pions from Kinetic energies ranging from 1MeV - 100GeV, displacement damage results about a an order of magnitude lower for diamond [83] (see Fig. 3.16).

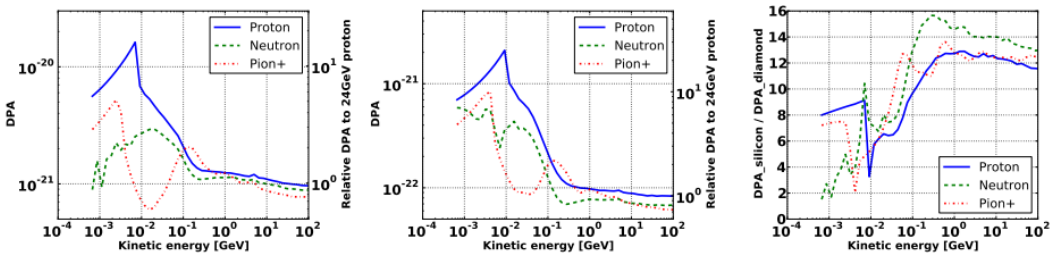

(d) DPA of Silicon (e) DPA of Diamond (f) DPA ratio: Silicon/Diamond

Figure 3.16 – Simulated DPA as a function of momentum of the impinging particle for silicon (d), diamond (e) and their ratio (f) [83].

Radiation damage on diamond detectors has been deeply investigated with irradiation campaigns using different types of particles including Pions [84], Alpha particles [85], Protons [86] and Neutrons [87] among others. Irradiations on the CERN's PS with 24 GeV protons allowed to determine an empirical model for the induced degradation of pCVD and sCVD diamond detectors in function of the Proton fluence, see Fig. 3.17)

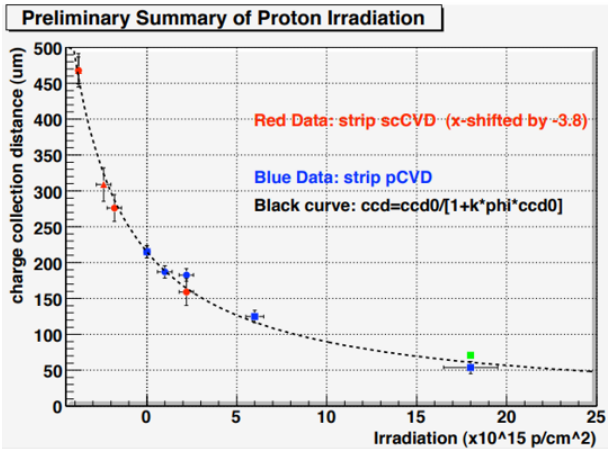

Figure 3.17 – CCD evolution for pCVD (blue) and sCVD (red) diamond detectors with 24GeV proton fluence with an analytic model (in black). All points measured with electric field density of 1 V/µm [88].

On diamond detectors, bulk damage generates charge traps that reduce the detector CCD. The data of sCVD detectors in Fig. 3.17 is shifted by $-3.8e^{15}$ p/cm^2 for parametrisation of both types with a single curve. This curve is explained with the following equation:

$$CCD = \frac{CCD_0}{1 + K\Phi CCD_0} \tag{3.25}$$

where CCD_0 is the initial charge collection distance and k is the damage constant. The data indicates that a single damage constant k properly characterises both detector types.

A 24 GeV proton irradiation fluence of $20e^{15}p/cm^2$ for CVD diamond roughly corresponds to a dose of 5 MGy, at this point signal amplitude is decreased to a 25% of its initial value [86]. In contrast to silicon detectors, were current leakage drastically increased with radiation damage, on diamonds it remained very low even after large doses of irradiation. SNR degradation on diamonds is mainly linked to a decrease on the signal amplitude and not due to noise increase.

3.3.2.4. Diamond detectors in high energy physics

The outstanding radiation hardness, dynamic range and linearity of diamond detectors makes them suitable for use under hash radiation environments such as the LHC experiments and for machine radiation protection. The HL-LHC and the next generation of particle physics with enhanced luminosity will increase the particle fluence and therefore enhance the radiation levels close to the interaction points (IP). Under this scenario, it is highly desirable the use of new technologies for monitoring and tracking detectors as alternative to silicon detectors.

Diamond detectors are now considered a mature technology and it is widely used in its simplest configuration (single pixel) as Beam Conditions Monitor (BCM). Diamond detectors are installed in LHCb [89], Atlas [90] and CMS [91]. The BCMs are machine protection devices that monitors fast increments on particle fluxes near the IPs and generates beam dump triggers in case of unexpected loses, CMS and ATLAS BCMs are also used for instantaneous luminosity monitoring. To avoid luminosity measurement saturation, Atlas BCM was upgraded with the Diamond Beam Monitor (DBM), which uses pixelated diamond detectors in a telescope configuration that allows segmentation and particle tracking (see Fig. 3.18). A similar approach was foreseen for CMS with its Pixel Luminosity Telescopes (PLT), initially implemented with Si detectors for schedule reasons [92].

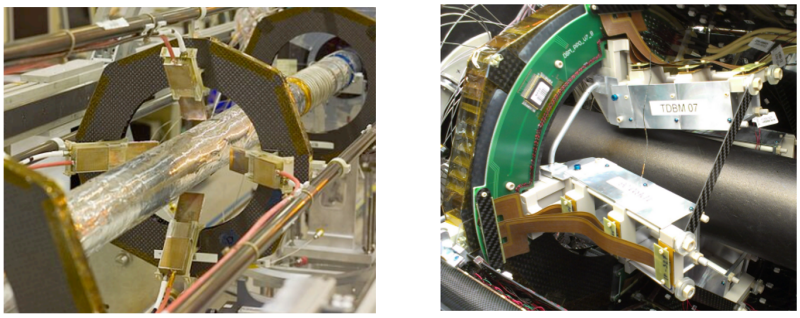

Figure 3.18 – Left: Atlas Diamond Beam Conditions Monitor (BCM) [90], Right: Atlas Diamond Bean Monitor (DBM) [92].

The Beam Loss Monitor (BLM) systems of the LHC and its injector chain are traditionally implemented with slow ionisation chambers, this is a critical protection system installed along the CERN accelerators that triggers a beam dump when the loss in a section is above a predefined threshold. The BLM system implementing commercial diamond detector modules, pCVD, for fast loss detection with ns resolution (dBLMs) [93] [94] (Fig. 3.19). Diamond detectors as BLM allow a better understanding of the loss mechanism, they allow to determine the loss structure and identify single bunch losses. The detector timing resolution and machine synchronisation also allows to use the dBLMs as beam tune measurement devices. Monolithic diamond detectors also allow operation in cryogenic temperatures, placement of into the LHC superconducting magnets is foreseen for a more reliable measurement and prevent magnet quenches [95].

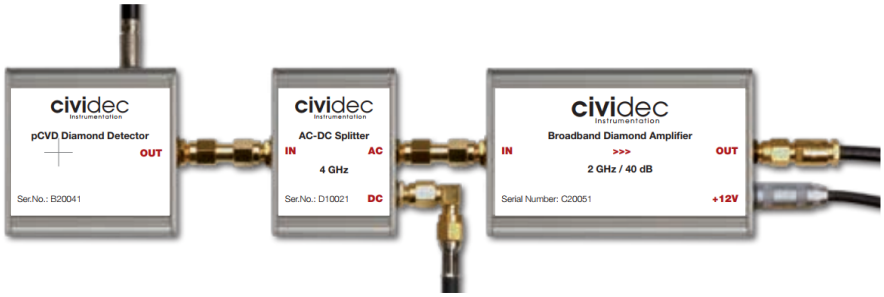

Figure 3.19 – Diamond Beam Loss Monitor (dBLM) based on commercial modules used at LHC, SPS and PS [93].

As silicon detectors, pixelated diamonds can be used as beam profile monitors when put directly into the particle beam. This concept was firstly tested for 1D ion beam profiles on TESLA with a fix diamond strip detector [96]. A similar principle was used at ATF2, evaluating a mobile diamond strip to scan electron beams and determine their profile and halo. It demonstrated a very high dynamic range (10^6) and validated the concept for other electron accelerators such as ILC or CLIC [97]. Pixelated diamond detectors are also being investigated for medical applications such x-ray detectors [98] and x-ray beam position monitors (BPM) [99].

In the search of detector operation at a lower bias voltage, the RD42 collaboration is investigating 3D diamond detectors. The idea behind this technology, is to use electrodes separations of 25-50 µm with graphitic carbon vias growth into the diamond, these pillars are alternatively biased with HV and ground. The 3D structure allows diamond detectors to operate at a much lower applied voltage. Whereas typical diamond strip detectors require ≈500V, 3D detectors can operate at 25V with an equivalent performance [69], see Fig.3.20.

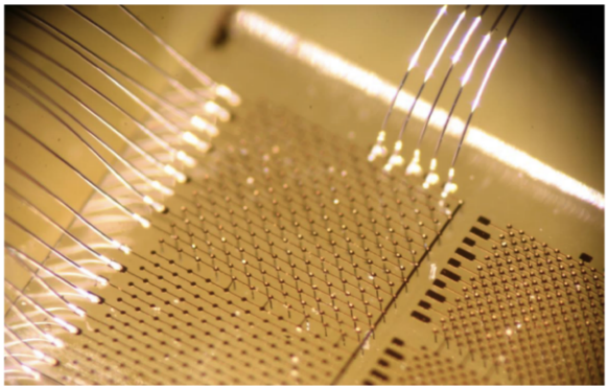

Figure 3.20 – Diamond detector tested by the RD42 collaboration with a 3D electrode structure [69].

Chapter 4

Beam wire scanner acquisition system studies

This chapter studies the acquisition dynamic range per machine from beam/wire interaction point of view by using characteristic beams, intensities and sizes. In addition, FLUKA simulations characterise the secondary particles shower fluence distribution (and energy deposition) around the beam pipe, as well as its variation with the primary beam energy. These studies will approximate the required dynamic range per machine for operational and post-LIU beams.

Operational secondaries acquisition systems transport high frequency signals from the particle detectors over long coaxial lines, which limits the system bandwidth and degrades the signal. The bandwidth reduction impact on bunch by bunch beam profile reconstruction has been evaluated by simulations and validated later by measurements. Finally, different aspects contributing on the beam width measurement error were evaluated to identify the detector system specifications, and measurement conditions, that minimise the beam profile incertitude.

4.1. Beams characteristics on the LHC and injector chain

The following subsections show the specifications of the CERN accelerators, the beams used during operation on 2016 (and the expected performance after the LHC Injectors Upgrade) and the required calculations to estimate the beam/wire interaction dynamics on operational beam wire scanner locations.

4.1.1. Beam distributions on the profile monitor locations

The maximum and minimum signal values visible by a beam profile monitor are dependent on the beam characteristics, i.e. beam intensity, energy, size and beam profile monitor location. For the calculation of the dynamic range required in each machine, horizontal and vertical bunch densities are used to estimate the scanner beam/wire interaction. Variation on bunch densities lead to variations in beam-wire interaction and therefore secondary particles production. Bunch densities are given in # protons/mm and are defined as:

$$HD_{Bunch} = \frac{N_b}{\sqrt{2\pi}\sigma_h}, VD_{Bunch} = \frac{N_b}{\sqrt{2\pi}\sigma_v} \tag{4.1}$$

Where N_b are the number of protons per bunch, and $\sigma_{(h,v)}$ is the beam width in mm.

The beam size (or beam sigma) at the monitor location can be calculated from the beam emittance and the local beta function value. Since the beam emittance, and therefore the beam width, vary inversely proportional to the particles momentum during the ramp, normalised

emittance is used to characterise the different beams of the machine. Normalized emittance remains constant with energy and is generally defined as:

$$\epsilon^*_{h,v} = \gamma_L \beta_r \epsilon_{h,v} = \gamma_L \beta_r \frac{1}{\beta_{h,v}} [\sigma^2_{h,v} (D_h \frac{dp}{p})^2] \tag{4.2}$$

$\beta_{h,v}$ and D_h are the h/v beta and dispersion functions at the monitor location respectively. $\frac{dp}{p}$ is the momentum spread. γ_L and β_r are the Lorentz factor, and the relativistic factor, defined as:

$$\gamma_L = E_0 + \frac{E_{kin}}{m_0 c^2} = \sqrt{\frac{1}{1 - \frac{u^2}{v^2}}} = \sqrt{\frac{1}{1 - \beta_r^2}} \tag{4.3}$$

Where E_0 is the protons rest energy (E_0= 938 MeV = 1.5 e^{-10} J), E_{kin} is the added energy during acceleration and m_o is the protons rest mass (m_o = 1.67e^{-27}Kg). From the previous equation, the relativistic factor β_r can be calculated as:

$$\beta_r = \frac{v}{c} = \sqrt{1 - \frac{1}{\gamma_L^2}} \tag{4.4}$$

Considering the previous factors, the transverse beam profile is finally obtained as:

$$\sigma_h = \sqrt{\frac{\epsilon^*_h \beta_h}{\gamma_L \beta_r} + (D \frac{dp}{p})^2}, \qquad \sigma_v = \sqrt{\frac{\epsilon^*_v \beta_v}{\gamma_L \beta_r}} \tag{4.5}$$

Note that, due to the momentum dispersion, there is an enlargement on the on the horizontal beam width. For the vertical plane this contribution is in general negligible, and will not be considered in our estimations.

Calculating the boundary values of the product $\gamma_L \beta_r$ it is possible to estimate, for a given beam, the transverse beam size variation during the acceleration cycle. The Fig. 4.1 and Table 4.1 show the variation with energy of the Beta Gamma product for protons and the energy boundaries of the different CERN machines.

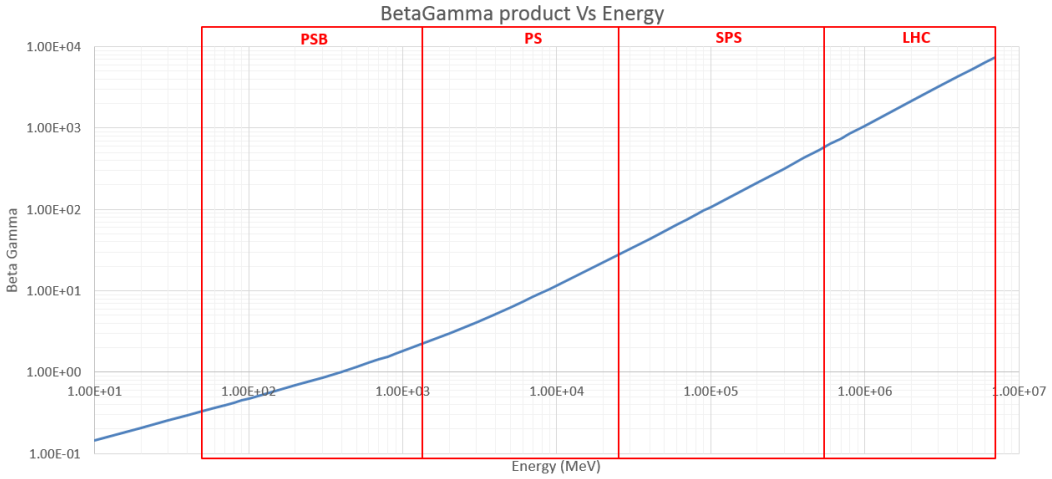

Figure 4.1 – Product $\gamma_L \beta_r$ value Vs beam energy for protons on the CERN accelerator chain.

Table 4.1 – Product $\gamma_L \beta_r$ values for LHC injector chain boundary energies

Beta Gamma product at Energies boundaries for the LHC injector Chain					
Energy	50 MeV	1.4GeV	26 GeV	450 GeV	7 TeV
$\gamma_r \beta_r$	0.33	2.28	28.65	479.47	7443.85

The following sections estimates the horizontal/vertical bunch density boundaries per machine. In each machine the beams used during 2016 are detailed [100] [101] with all their characteristics as well as the accelerator optics at the scanners location [102]. Considering the calculated horizontal and vertical beam widths for the boundary energies of each accelerator and the beam intensity values, the bunch density limits are obtained.

- **Proton Synchrotron Booster (PSB):**

Table 4.2 – PSB Operational beams on 2016 and main characteristics.

PSB BEAM OPERATIONS SPECIFICATIONS FROM 2016								
		Intensity [e^{11} p/ring]	**H.Emit.*** [mm mrad]	**V.Emit.*** [mm mrad]	**Rings Used**	**B.Lenght** [ns]	**Mom.Spread** [Δp/p] e^3	**Kin. Energy** [GeV]
ISOLDE	NORMGPS	90	15	8	1,2,3,4	230	1,10E+00	1,4
BEAMS	STAGISO	20 - 35	5	4	2,3,4	230	1,40E+00	1,4
PS	AD	40	9	5	1,2,3,4	170	1,00E+00	1,4
BEAMS	EAST1	5	1,5	1,5	3	170	1,00E+00	1,4
	EAST2	5	1,1	1,1	3	170	1,00E+00	1,4
	STFPRO	240	12	7	1,2,3,4	160	1,00E+00	1,4
	TOF	90	12	9	2	210	1,00E+00	1,4
LHC	BCM25	8,5	1,1	1,8	1,2,3,4	150	8,00E-01	1,4
BEAMS	LHC25NS	16,5	3	2	1,2,3,4	180	1,00E+00	1,4
	LHC50NS	8	1,5	1	1,2,3,4	85	1,00E+00	1,4
	LHCINDIV	0.2 - 1.2	2	1,5	3	85	5,50E-01	1,4
	LHCPROBE	0.05 - 0.2	0,8	0,8	3	70	4,50E-01	1,4

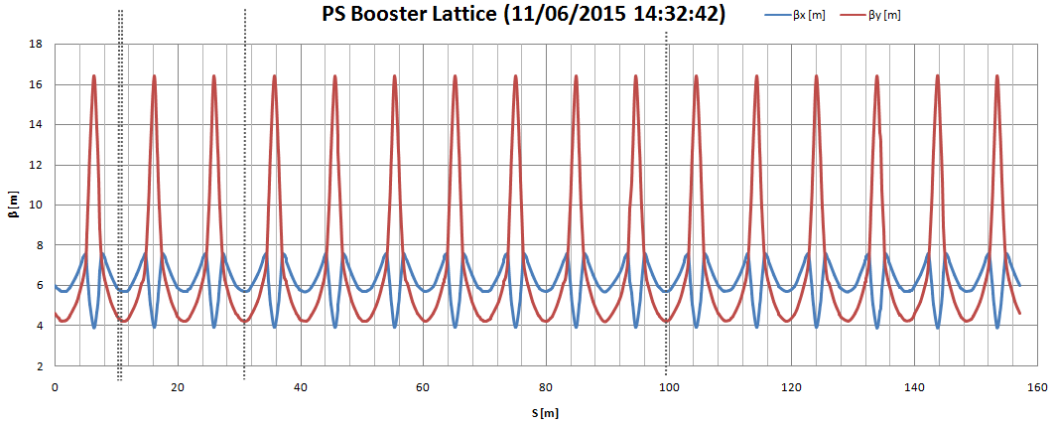

Figure 4.2 – PSB Orbit Lattice with BWS locations highlighted.

Table 4.3 – Optics parameters for the PSB beam wire scanner positions.

Optics parameters on PSB Beam Wire Scanners				
Scanner Name	**Location / s[m]**	β_h**[m]**	β_v**[m]**	**D[m]**
4 x BR.BWS.2L1.V_ROT	2L1 / 10.735	5,71	4,25	1,46
4 x BR.BWS.2L1.H_ROT	2L1 / 10.833	5,69	4,23	1,46
4 x BR.BWS.4L1.H_ROT	4L1 /30.34	5,72	4,26	1,46
4 x BR.BWS.11L1.V_ROT	11L1 / 99.06	5,71	4,25	1,46

Table 4.4 – Beam profiles and bunch intensities for PSB beam wire scanners per beam type.

Beam profiles and Bunch densities for PSB Beam Wire Scanners per Beam type									
		σ_h **[mm]**		σ_v **[mm]**		**HD Bunch** $[10^{11}/\mathbf{mm}]$		**VD Bunch** $[10^{11}/\mathbf{mm}]$	
ISOLDE	NORMGPS/HRS	6.36	13.5	3.9	8.5	2.65	5.65	4.23	9.27
BEAMS	STAGISO	4.10	8.0	2.7	6.0	0.99	3.41	1.33	5.10
PS	AD	4.98	10.5	3.1	6.7	1.52	3.20	2.38	5.21
BEAMS	EAST1	2.43	4.5	1.7	3.7	0.44	0.82	0.54	1.19
	EAST2	2.22	3.9	1.4	3.1	0.51	0.90	0.63	1.39
	STFPRO	5.69	12.1	3.6	7.9	7.90	16.82	12.06	26.43
	TOF	5.69	12.1	4.1	9.0	2.96	6.31	3.99	8.74
LHC	BCMS 25	2.03	3.8	1.8	4.0	0.89	1.67	0.84	1.85
BEAMS	LHC 25NS	3.11	6.2	1.9	4.2	1.06	2.11	1.55	3.40
	LHC50NS	2.43	4.5	1.4	3.0	0.71	1.31	1.06	2.33
	LHCINDIV	2.39	5.0	1.7	3.7	0.02	0.20	0.02	0.29
	LHCPROBE	1.57	3.2	1.2	2.7	0.01	0.05	0.01	0.07
Total Dynamics		1.57	13.5	1.2	9.0	0.01	16.82	0.01	26.43

- **Proton Synchrotron (PS)**

Table 4.5 – PS Operational beams on 2016 and main characteristics.

PS BEAMS SPECIFICATIONS FROM OPERATIONS 2016							
		Intensity [e^{11} p/bunch]	**H.Emit.*** [mm mrad]	**V.Emit.*** [mm mrad]	**B.Lenght** [ns]	**E.Spread** [Δp/p]	**Energy** [GeV]
PS	AD	40	11.6	5	180	1.56 e-3	1.4
BEAMS					33	0.74 e-3	26
	EAST 1 2	2 - 5	1.5	1	160	1.50 e-3	1.4
					Deb.	0.40 e-3	23
	EAST TOF	30	7	4.5	180	1.70	1.4
				7	25	3.80 e-1	19.4
	STFPRO MTE	20	7	5	155	1.23 e-3	1.38
							13.1
	TOF	70 - 85	14.7	8	210	1.70 e-3	1.38
			21.6	7.7	27	7.80 e-4	19.4
LHC	LHC25NS	1.2	< 2.5	< 2.5	170	1.00 e-3	1.38
BEAMS			< 3	< 3	< 4.2		25.4
	LHC25NS(BCMS)	0.7	1.4	1.1	160	0.90 e-3	1.4
		1.15	1.6	1.4	4.2	0.40 e-3	26
	LHC50NS	1.2	< 2.5	< 2.5	170	1.00 e-3	1.38
			< 3	< 3	<4.2		25.4
	LHCINDIV	0.2 - 1.5	<2	<2	90	0.50 e-3	1.38
					4	0.25 e-3	25.4
	LHCPROBE	0.1	< 1	< 1	90	0.61 e-3	1.38
			0.8	0.63	4	0.25 e-3	25.4
ION	LHC ION Early Ar11	0.24	1	1	205	4.50 e-1	0.072
BEAMS					4	3.70 e-1	5.9
	LHC ION Early Pb54	0.05	1	1	160	4.30 e-1	0.072
					3	3.70 e-1	5.9
	LHC ION Nom. Pb54	0.3	1	1	160	0.50	0.072
					4	0.50	5.9

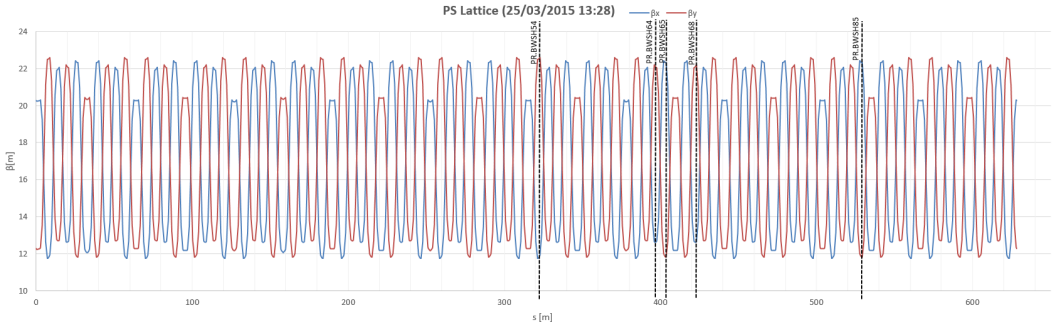

Figure 4.3 – PS Orbit Lattice with BWS locations highlighted.

Table 4.6 – Optics parameters for the PS beam wire scanners position.

Optics parameters on PS Beam Wire Scanners				
Scanner Name	**Location / s[m]**	β_h**[m]**	β_v**[m]**	D_h**[m]**
PR.BWSH54	PR.SD54 / 334.2	12.6	22.06	2.29
PR.BWSV64	PR.SD65 / 396.5	12.6	22.06	2.29
PR.BWSH65	PR.SD65 / 402.0	22.3	11.8	3.023
PR.BWSH68	PR.SD68 / 422.5	12.59	22.1	2.29
PR.BWSV85	PR.SD85 / 528.0	22.32	11.83	3.023

Table 4.7 – Beam profiles and bunch densities for PS beam wire scanners per beam type.

Beam profiles and Bunch densities for PS Beam Wire Scanners per Beam type									
		σ_h		σ_v		**HD Bunch**		**VD Bunch**	
		[mm]		**[mm]**		**[10^{11}]**		**[10^{11}]**	
PS	AD	2.8	9.2	1.4	7.0	1.73	5.65	2.29	11.12
BEAMS	EAST 1 2	1.2	5.9	0.6	3.1	0.13	1.62	0.26	3.07
	EAST TOF	2.2	9.7	1.6	6.6	1.23	5.44	1.81	7.63
	SFTPRO MTE	3.7	9.1	2.0	7.0	0.88	2.14	1.15	4.01
	TOF	4.0	13.0	2.1	8.8	2.14	8.53	3.17	16.54
LHC	LHC25NS	2.6	5.8	1.1	4.9	0.08	0.19	0.10	0.43
BEAMS	LHC50NS	2.6	5.8	1.1	4.9	0.08	0.19	0.10	0.43
	LHCINDIV	1.1	4.7	0.9	4.4	0.02	0.54	0.02	0.65
	LHCPROBE	0.8	3.6	0.5	3.1	0.01	0.05	0.01	0.08
ION	LHC ION Ear. Ar11	1.6	7.6	1.3	7.4	0.01	0.06	0.01	0.07
BEAMS	LHC ION Ear. Pb54	1.6	7.6	1.3	7.4	0.003	0.01	0.003	0.02
	LHC ION Nom. Pb54	1.7	7.6	1.3	7.4	0.016	0.07	0.016	0.09
Total Dynamics (only Pr.)		0.8	13.0	0.5	8.8	0.01	8.53	0.01	16.54
Total Dynamics (With Ions)		0.8	13.0	0.5	8.8	0.003	8.53	0.003	16.54

- **Super Proton Synchrotron (SPS)**

Table 4.8 – SPS Operational beams on 2016 and main characteristics.

SPS BEAMS SPECIFICATIONS FROM OPERATIONS 2015-2016							
		Intensity [e^{11} **p/bunch**]	**H.Emit.*** [**mm mrad**]	**V.Emit.*** [**mm mrad**]	**B.Lenght** [**ns**]	**E. Spread** [**Δp/p**]	**Energy** [**GeV**]
LHC	NOMINAL	1.3	3.0	3.0	4	1.07e-3	26
BEAMS	+		3.5	3.5	2	0.28e-3	450
	LHC25 NOMINAL	1.9	3.0	3.0	4	1.07e-3	26
	+	1.7	3.5	3.5	2	0.28e-3	450
	TOTEM	0.3	0.8	0.8	4	1.07e-3	26
	+		0.9	0.9	2	0.28e-3	450
	PILOT/LHC PROBE	0.05 - 0.2	1 - 2	1 - 2	4	1.07e-3	26
	++				2	0.28e-3	450
	LHC25 STD (2016)	1.2	2.6	2.6	4	1.07e-3	26
	++				2	0.28e-3	450
	LHC25 BCMS(2016)	1.15 - 1.7	1.3 - 1.4	1.3 - 1.4	4	1.07e-3	26
	++				2	0.28e-3	450
	LHCINDIV	0.2 - 3	<2.5	<2.5	4	1.07e-3	26
	++				2	0.28e-3	450
	SFTPRO/FT	0.2	8-12	5-7	1.25	3.05e-3	14
	+++				0.5	0.4e-3	400

* Normalized Emittance, + SPS specifications from [103]
++ From LHC Performance Workshop 2016 [104], +++ SPS Optics database

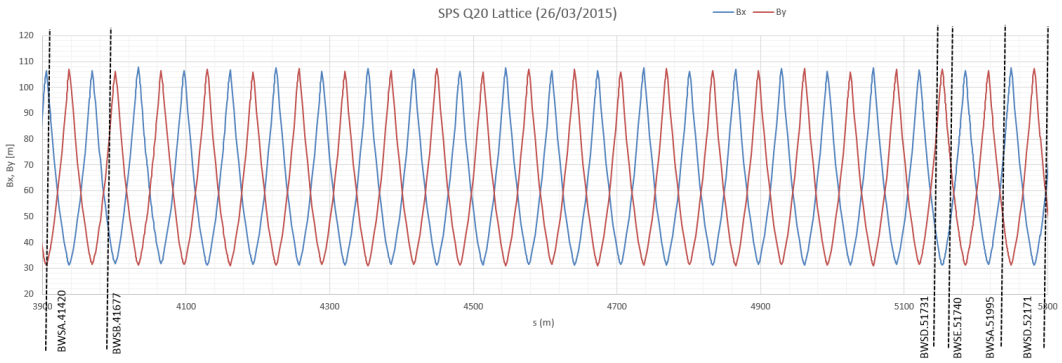

Figure 4.4 – SPS Orbit Lattice with BWS locations highlighted.

Table 4.9 – Optics parameters for the SPS beam wire scanners position.

Optics parameters on SPS Beam Wire Scanners					
Scanner Name	**Location / s[m]**	**Optics**	β_h**[m]**	β_v**[m]**	**Dh[m]**
BWSA.41420	41420 / 3907.6	LHC	100.7	33.1	3.01
		F.Target	100.1	20.9	3.5
BWSB.41677	41677 / 3989.6	LHC	49.2	71.0	-0.46
		F.Target	37.7	64.1	0.08
BWSD.51731	51731 / 5155.1	LHC	32.5	102.7	-0.49
		F.Target	21.0	103.1	-0.51
BWSE.51740	51740 / 5161.8	LHC	43.0	79.8	-0.61
		F.Target	-	-	-
BWSA.51995	51995 / 5242.5	LHC	86.79	39.6	-0.36
		F.Target	81.7	26.9	0.53
BWSD.52171	52171 / 5296.6	LHC	57.74	60.5	1.97
		F.Target	47.8	50.9	2.35

Table 4.10 – Beam profiles and bunch densities for SPS beam wire scanners per beam type.

Beam profiles and Bunch densities for SPS Beam Wire Scanners per Beam type									
		σ_h **[mm]**		σ_v **[mm]**		**HD Bunch** $[10^{11}/\mathbf{mm}]$		**VD Bunch** $[10^{11}/\mathbf{mm}]$	
LHC	NOMINAL	0.5	3.2	0.5	3.3	0.16	1.07	0.16	1.05
BEAMS	LHC25 NOMINAL	0.5	3.2	0.5	3.3	0.21	1.56	0.21	1.54
	TOTEM	0.2	1.7	0.3	1.7	0.07	0.49	0.07	0.48
	PILOT/LHC PROBE	0.3	2.7	0.3	2.7	0.01	0.31	0.01	0.30
	LHC25 STD (2016)	0.4	3.0	0.4	3.1	0.16	1.14	0.16	1.13
	LHC25 BCMS(2016)	0.3	2.2	0.3	2.2	0.21	2.29	0.20	2.25
	LHCINDIV	0.4	3.0	0.4	3.0	0.03	2.91	0.03	2.87
	SFTPRO/FT	0.8	8.7	0.6	6.7	0.01	0.10	0.01	0.13
	Total Dynamics	0.2	8.7	0.3	6.7	0.01	2.91	0.01	2.87

- **Large Hadron Collider (LHC):**

Table 4.11 – LHC beams and main characteristics.

LHC BEAMS SPECIFICATIONS FROM OPERATIONS 2015-2016							
		Intensity [e^{11} **p/bunch**]	**H.Emit*** [**mm mrad**]	**V.Emit*** [**mm mrad**]	**B.Lenght** [**ns**]	**E. Spread** [**Δp/p**]	**Energy** [**GeV**]
LHC	NOMINAL	1.15 - 1.7	3.5	3.5	1.7	0.306	450
BEAMS	+		3.75	3.75	1	0.11	7000
	LHC25NS	1.3	2.7	2.7	1.25		450
	++		3.4	3.4			6500
	LHC25NS(BCMS)	1.3	1.9	1.9	1.25		450
	++		2.4	2.4			6000
	LHCPROBE/PILOT	0.05 - 0.2	1	1	1.25		450
	+++						6500
	LHCINDIV	0.2 - 3	<2.5	<2.5	1.25		450
	+++						6500

* Normalized Emittance, +LHC specifications from [103]
++ From LHC performance workshop 2016 [105] , +++ From LHC performance workshop 2014 [106]

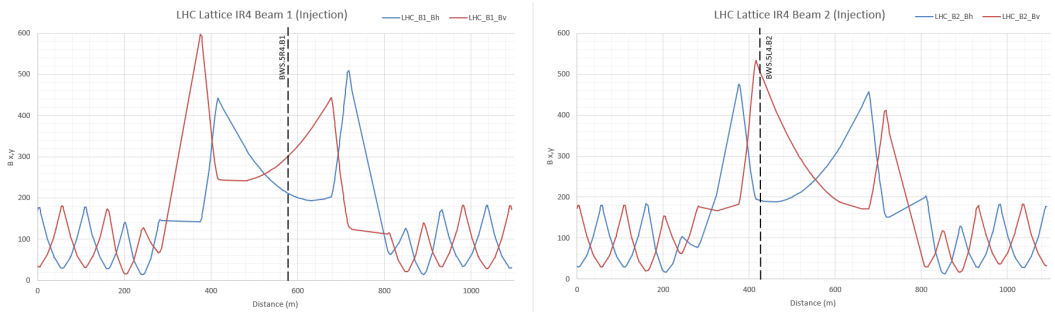

Figure 4.5 – LHC IR4 Lattice and wire scanners location for Beam 1 (left) and Beam 2 (Right).

Table 4.12 – Optics parameters for the LHC wire scanners locations.

Optics parameters on LHC Beam Wire Scanners					
Scanner Name	**Location / s[m]**	**Optics**	σ_h**[m]**	σ_v**[m]**	D_h**[m]**
BWS.5R4.B1 (V/H)	5R4.B2 / 10629.1	Injection (450GeV)	194.1	368.1	-0.027
		Collision (6.5TeV)	194.7	368.3	-0.52
BWS.5L4.B2 (V/H)	5L4.B2 / 10459.5	Injection (450GeV)	188.6	411.6	0.083
		Collision (6.5TeV)	188.9	411.4	0.4

Table 4.13 – Beam profiles and bunch densities for LHC beam wire scanners per beam type.

Beam profiles and Bunch densities for LHC Beam Wire Scanners per Beam type									
		σ_h **[mm]**		σ_h **[mm]**		**HD Bunch** [10^{11}/**mm**]		**VD Bunch** [10^{11}/**mm**]	
LHC	NOMINAL	0.31	1.19	0.43	1.79	0.385	2.176	0.256	1.574
BEAMS	LHC25NS	0.25	1.19	0.35	1.73	0.436	2.693	0.299	1.928
	LHC25NS (BCMS)	0.26	1.03	0.36	1.49	0.506	2.640	0.347	1.891
	LHC PROBE/PILOT	0.16	0.64	0.22	0.93	0.031	0.501	0.022	0.359
	LHC INDIV	0.25	1.01	0.35	1.46	0.079	4.752	0.054	3.403
	Total Dynamics	0.16	1.19	0.22	1.79	0.031	4.752	0.022	3.403

Table 4.14 – Beam sigma and bunch densities summary for the BWS on the CERN accelerators.

Beam profiles and Bunch densities for the CERN accelerators at the Beam Wire Scanners location										
	σ_h **[mm]**		σ_v **[mm]**		**HD Bunch** [10^{11}/mm]		**ΔHD Bunch**	**VD Bunch** [10^{11}/mm]		**ΔVD Bunch**
Proton Synchrotron Booster (PSB)	1.57	13.5	1.2	9.0	0.01	16.82	1.6e3	0.01	26.43	2.6e3
Proton Synchrotron (PS)	0.8	13.0	0.5	8.8	0.01	8.53	8.5e2	0.01	16.54	1.6e3
Super Proton Synchrotron (SPS)	0.2	8.7	0.3	6.7	0.01	2.91	2.9e2	0.01	2.87	2.8e2
Large Hadron Collider (LHC)	0.16	1.19	0.22	1.79	0.031	4.752	1.5e2	0.022	3.403	1.5e2

Table 4.14 shows a summary of the dynamic range estimations in terms of bunch densities for each machine. Due to the different beam types and acceleration cycle there is near four orders of magnitude variation for the PSB bunch densities. This factor is reduced to about two orders of magnitude on the LHC.

4.1.2. The LHC Injectors Upgrade (LIU) program and HL-LHC beams

The performance of the injector chain will be pushed forward to meet the requirements of the High Luminosity LHC project (HL-LHC) scheduled for the Run4 beyond 2024. The HL-LHC aims a luminosity of $5e^{34}\ cm^2s^{-1}$. To reach this target, the injected beam intensity has to be doubled, and its brightness multiplied by a factor 2.5 ($2.3e^{11}$ p/b with 25ns bunch spacing with emittances 2.1µm).

The ultimate goal of the LHC Injectors Upgrade (LIU) project is to make the injectors capable of delivering the beams required by the HL-LHC. The upgrade project includes the Linac4, PSB, PS and SPS injectors.

- **LIU-PSB:** The upgrade covers the injection ejection lines and energy regions. The injection line will be exchanged from Linac2 (50MeV) to Linac4 (160MeV). With regard to the upgrade on energy, the extraction energy to the PS would increase from 1.4GeV to 2GeV. In terms of beam intensity it is expected to be doubled, providing higher intensity beams which increases the beam brilliance for the LHC.

- **LIU-PS:** The Injection energy of the PS will be upgraded from 1.4GeV to 2Gev, the RF systems need to cope with the new beam characteristics.

- **LIU-SPS:** It covers the required systems modifications and upgrades to cope with a higher intensity and lower emittance beams.

The upgrades of the machines also concern upgrades on beam instrumentation, such as the case of beam wire scanners. The secondary particles acquisition system designed on this thesis should, not only cope with the current operational machine specifications detailed on the previous section, but also with narrower and more intense beams expected after the LIU. The Table 4.15 specifies the requirements for the HL-LHC [107] and the expected performance of the injectors after the baseline LIU implementations as detailed on [29].

Table 4.15 – Proton beams (25ns) after LIU and HL-LHC required characteristics at Injection energy [29] [107].

25ns Proton beams after LIU and HL-LHC required characteristics at injection energy									
		Injection Engergy [GeV]	**Bunch Intensity [$10^{11}p/b$]**	**Transverse Emittance [m]**	**Longitudinal Emittance [m]**	**Number of Bunches**	**Bunches Separation [ns]**	**Bunch Length [ns]**	**Energy Spread [Δp/p]**
PSB	LIU	0.16	29.6	1.55	1.4	1/ring		650	1.8e-3
	HL-LHC	0.16	34.21	1.72	1.4	1/ring		650	1.8e-3
PS	LIU	2	28.1	1.63	3	4+2	284	205	1.5e-3
	HL-LHC	2	32.5	1.8	3	4+2	284	205	1.5e-3
SPS	LIU	26	2.2	1.71	0.35	4x72	25	4.2	1.5e-3
	HL-LHC	26	2.57	1.89	0.42	4x72	25	3	1.5e-3
	LIU	450	2	1.88	0.65	10 x 288	25	1.65	
LHC	HL-LHC	450	2.32	2.08	0.65	10 x 288	25	1.65	

The previous calculations have been performed for the same monitors considering this time the 25ns beams after LIU. For ultimate parameters, the HL-LHC beams (with higher intensities) have been used for Table 4.16.

Table 4.16 – Bunch profiles and densities estimations for HL-LHC 25ns beams at the CERN BWS locations.

Beam profiles and bunch densities for HL-LHC 25ns beams on the BWS locations								
	σ_h **[mm]**		σ_h **[mm]**		**HD Bunch [10^{11}/mm]**		**VD Bunch [10^{11}/mm]**	
Proton Synchrotron Booster (PSB)	3.20	4.81	1.57	3.47	2.840	4.271	3.930	8.708
Proton Synchrotron (PS)	3.55	5.84	0.86	3.66	2.220	3.654	3.541	15.052
Super Proton Synchrotron (SPS)	0.82	4.56	0.29	2.61	0.225	1.254	0.393	3.572
Large Hadron Collider (LHC)	0.23	0.92	0.32	1.34	1.009	4.029	0.693	2.885

Roughly, factor 2 in bunch densities can be observed on these results when compared with the standard 25ns beams of the different machines on Table 4.4 (PSB), Table 4.7 (PS), Table 4.10 (SPS) and Table 4.13 (LHC). This factor 2 in signal intensity will be taken into account for the dynamic range calculations with respect to the nominal beams.

4.2. Secondary particles shower simulations

The solid angle in which the secondary particles are scattered when the proton beam interacts with the carbon wire is strongly dependent on the beam energy and the wire cross-section [108]. At CERN, each machine in the injector chain is characterised by a different beam pipe geometry and energy range. Under these circumstances, the point where the energy deposition is maximised in each machine varies with the beam energy. Table 4.17 collects a summary the CERN accelerators characteristics used later for simulations.

Table 4.17 – Energies and beam pipe sizes for the different circular accelerators at CERN.

Accelerator	**Injection Energy**	**Extraction Energy**	**Beam Internal**	**Beam External**	**Pipe Material**	**Wire Diam.**	**Wire Material**
PSB	50 MeV	1.4 GeV	120	123	Stainless Steel	30 µm	Carbon
PS	1.4 GeV	26 GeV	Elliptical 70 x 146 x 2				
SPS	26GeV	450 GeV	156	159			
			Elliptical 55 x 130.5 x 1.5				
LHC	450 GeV	7 TeV	80	84			

The analysis of the secondary particles created and scattered by elastic-inelastic interactions when a proton beam impacts a very thin carbon wire is a complex mechanism to describe

analytically. Monte Carlo simulations with FLUKA code [109] were done to analyse the dose deposition and the secondary particle composition in the vicinity of the beam pipe. The study was done for different energies and beam pipe geometries. The results on the dose deposition and particle spectra evolution over distance allows the identification of optimal locations for detectors placement. These simulations also provide valuable information to estimate the energy absorbed by a detector i.e. scintillator or pCVD diamond, at a given location. A report from the CERN FLUKA group was used as a baseline for these simulations [110].

The subsequent simulations define the system geometry as:

- A stainless steel beam pipe with vacuum in the internal volume and air outside.
- The vacuum volume includes a carbon wire (2 g/cm^3) with 30µm diameter placed horizontally (along the x axis).
- The proton beam is defined as a pencil beam with a Gaussian profile on the x axis (2.9 mm FWHM) and flat on the y axis (30µm). The beam is placed 1mm before the carbon wire and directed along z. This configuration assures that every primary proton crosses the wire.
- For the different simulations, the proton beam was specified the related energy with no energy spread, the beam pipe geometries were defined as shown on Table 4.17. Figure 4.6 shows the specific geometry used for LHC simulations.

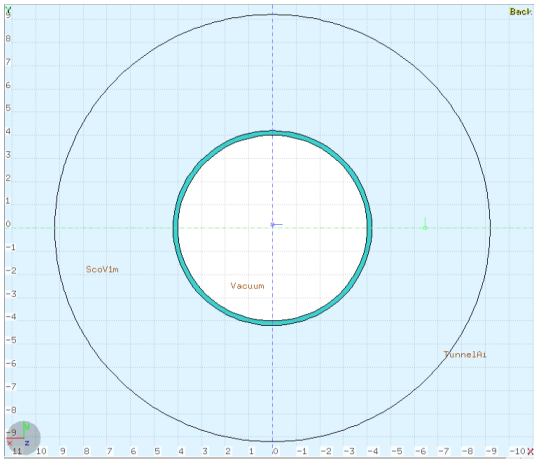

Figure 4.6 – Geometry definition for LHC FLUKA simulation.

The dose scoring around the beam pipe was estimated through the energy deposited on the air volume around the beam pipe in a mesh matrix of 100x100x1000 pixels, covering a different volume for each machine (USRBIN card). These volumes were 60x60x250 cm for PSB, 60x60x800 cm for PS, 60x60x1600 cm for SPS and 60x60x2600 cm for LHC. The energy distribution on these volumes was studied on the longitudinal and transverse plane to check the energy decay with distance. Some of the most important secondary particles produced by the interaction are analysed at two different volumes per machine, these volumes were located around the maximum energy deposition points found per machine at injection-extraction energies. The particles fluency scoring volumes were defined as air rings of 5cm around the beam pipe with 10 cm thickness. The energy spectrum of the secondary particles and the individual particle type fluence (per primary proton) allows to identify the main contributors to the secondary shower and their energy.

4.2.1. Proton Synchrotron Booster (PSB)

The energy boundaries of the protons travelling on this quad ring accelerator are 50 MeV at injection and 1.4 GeV at extraction, PSB features a stainless steel circular beam pipe geometry (external diameter 123 mm, 1.5 mm thickness). In low energy scans (50-10 MeV) almost no secondaries overcome the thin stainless steel layer of the beam pipe, thus a very weak signal is produced on the current scintillators, measurements in this case are dominated by noise. In practice, the scintillator and photomultiplier system starts showing acceptable profiles from 100-200 MeV. In order to properly measure injection beams (50 MeV) a second readout system, based on secondary emission current (SEM) on the wire, is employed [21].

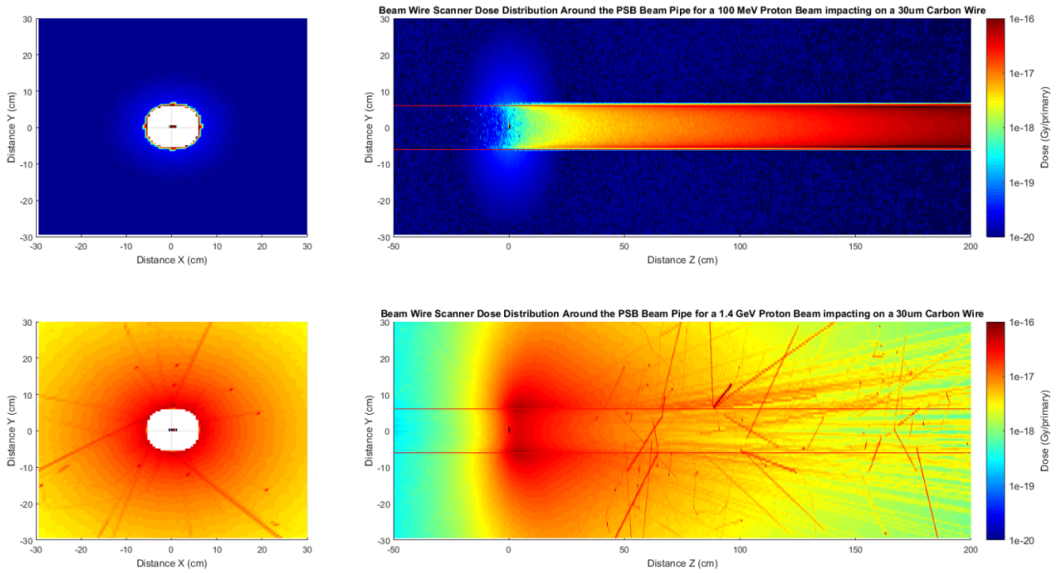

Figure 4.7 – Secondary shower dose deposition around the PSB beam pipe for 100 MeV and 1.4 GeV beams.

The simulations were run for 10 MeV and 1.4 GeV to observe the secondaries shower evolution with energy. As seen on Fig. 4.7 (top), for 100 MeV particles are mostly stopped by the beam pipe (high energy deposition on the stainless steel wall), almost no energy is deposited on the air volume, except for a small region near the interaction point. On the energy distribution at 1.4 GeV (bottom), a much higher number of secondaries escape from the beam pipe.

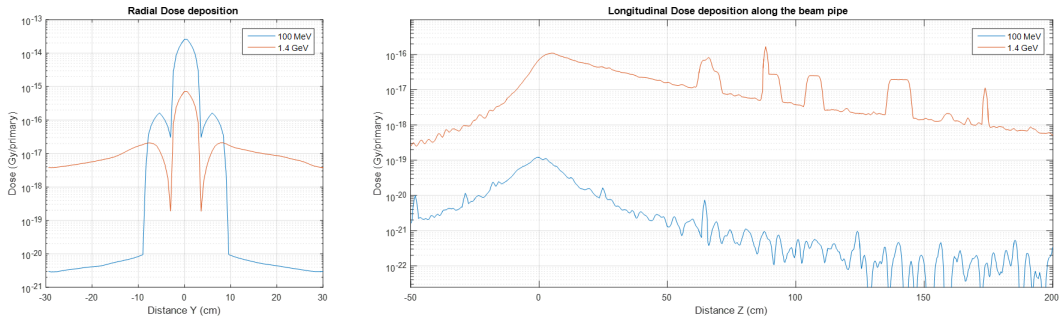

Figure 4.8 – Cross Section of dose deposition around the PSB beam pipe in Y and Z.

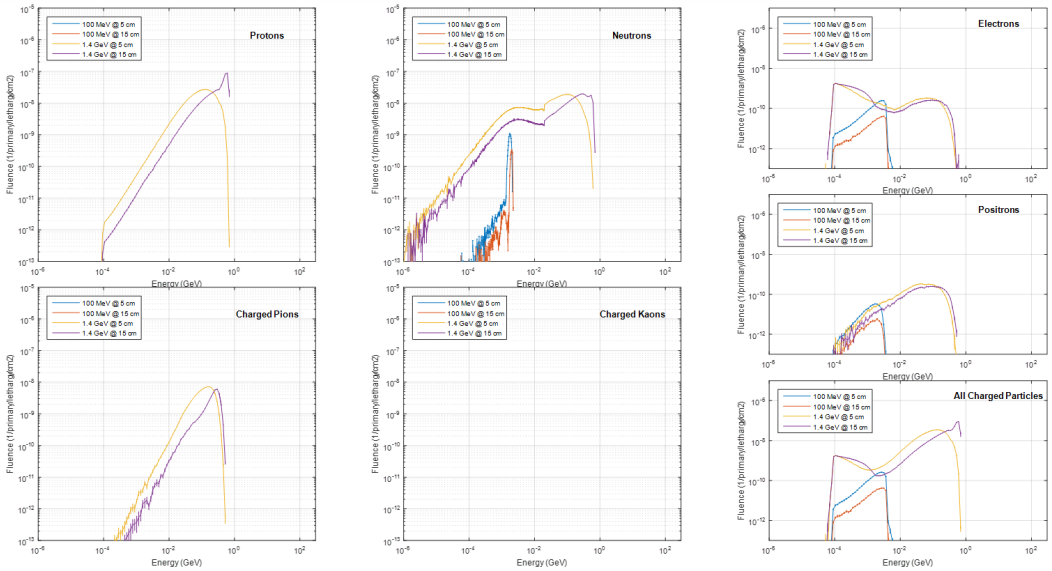

Figure 4.9 – Isolethargic energy spectrum of the most significant secondaries for the PSB at injection and extraction energies for 5 cm and 15 cm from the interaction point.

Table 4.18 – Secondary particles total fluence on the PSB scoring volumes.

PARTICLE FLUENCE FOR PSB AT INJECTION AND EXTRACTION ENERGIES				
Particle Type	**Fluence @ 5 cm (Particles/[cm^2*primary])**		**Fluence @ 15cm (Particles/[cm^2*primary])**	
	100MeV	**1.4GeV**	**100MeV**	**1.4GeV**
Protons (p)	7.86E-16	5.99E-08	1.99E-15	7.55E-08
Antiprotons (^{p})	0	0	0	0
Neutrons (n)	2.44E-10	6.41E-08	5.92E-11	4.80E-08
Antineutrons (^{n})	0	0	0	0
Charged Pions (π + / -)	0	1.14E-08	0	5.58E-09
Charged Kaons (k + / -)	0	0	0	0
KaonZero	0	0	0	0
Electrons (e^-)	2.89E-10	3.44E-09	4.87E-11	3.92E-09
Positrons (e^+)	4.04E-11	9.07E-10	6.68E-12	7.01E-10
Muons (μ)	0	1.07E-10	0	7.54E-11
All Charged Part	3.29E-10	7.66E-08	5.54E-11	8.58E-08

Table 4.19 – Secondary particles total dose deposited on the PSB scoring volumes.

DOSE DEPOSITION FOR PS AT INJECTION AND EXTRACTION ENERGIES			
Dose @ 5 cm (Gy/primary)		**Dose @ 15 cm (Gy/primary)**	
100MeV	**1.4GeV**	**100MeV**	**1.4GeV**
$8.46e{-}20$	$1.01e^{-16}$	$1.49e^{-20}$	$5.34e^{-17}$

Figure 4.8 shows the average radial dose deposition around the beam pipe for -50<Z<200 cm (left) and the longitudinal dose deposition at 3 cm from the beam pipe (right), both obtained from the volume studied on Fig. 4.7. This plot shows three orders of magnitude difference in dose deposition between the two energies and locates the maximal energy deposition points at 5 cm for 100 MeV and 15 cm for 1.4 GeV downstream respect to the wire. With regard to the dose extinction ratio, at 100 MeV only 20 cm displacement features a dose reduction of 1/10; this distance is increased up to 50 cm for 1.4 GeV.

Table 4.18, 4.19 and Fig. 4.9 show the results of the particle scoring volumes (placed at 5 and 15 cm).

4.2.2. Proton Synchrotron (PS)

The PS beam pipe is characterised for being mainly elliptical, 70x146 mm and 2 mm thickness, a rectangular section will be considered in simulation and for simplicity. For PS energies, the secondary particles produced by the beam-wire interaction can escape from the beam pipe and only scintillator systems are used for beam profile reconstruction with BWS. Figures 4.10 and 4.11 show the evolution with distance of the energy deposited by the secondaries shower outside of the beam pipe. For the boundary energies, there is around one order of magnitude difference in dose deposition, and as expected, for a higher primary beam energy the maximal dose deposition is located further and shows a smoother decay with distance. The maximal energy preposition point for 1.4 GeV was found to be 10 cm downstream the interaction point and about 1m for 26 Gev.

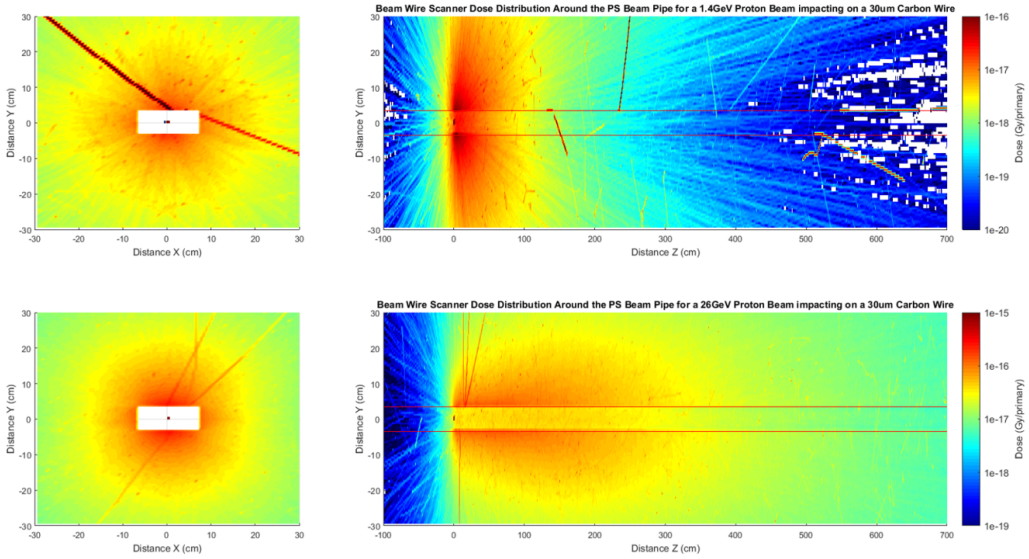

Figure 4.10 – Secondary shower dose deposition around the PS beam pipe for 1.4 GeV and 26 GeV beams.

As previously the scoring volumes have been placed on the points were the energy deposition was maximised for injection-extraction energies (10 cm - 1 m). The secondary particles energy spectres are shown on Fig. 4.12. Table 4.20 details the total fluence per primary proton impacting the wire. The main secondary particles contribution for injection energy beams are protons and neutrons (as on PSB for extraction), however for 26 GeV beams other particles such as pions, electrons and positrons appear to be the main contributors to the secondary particle rain.

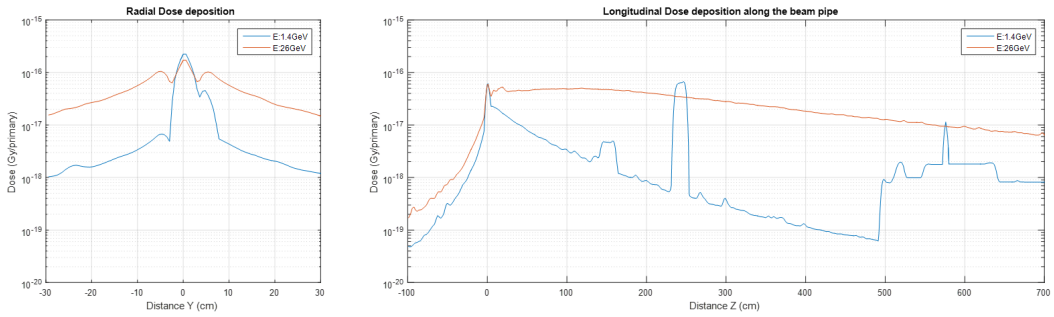

Figure 4.11 – Cross Section of dose deposition around the PS beam pipe in Y and Z.

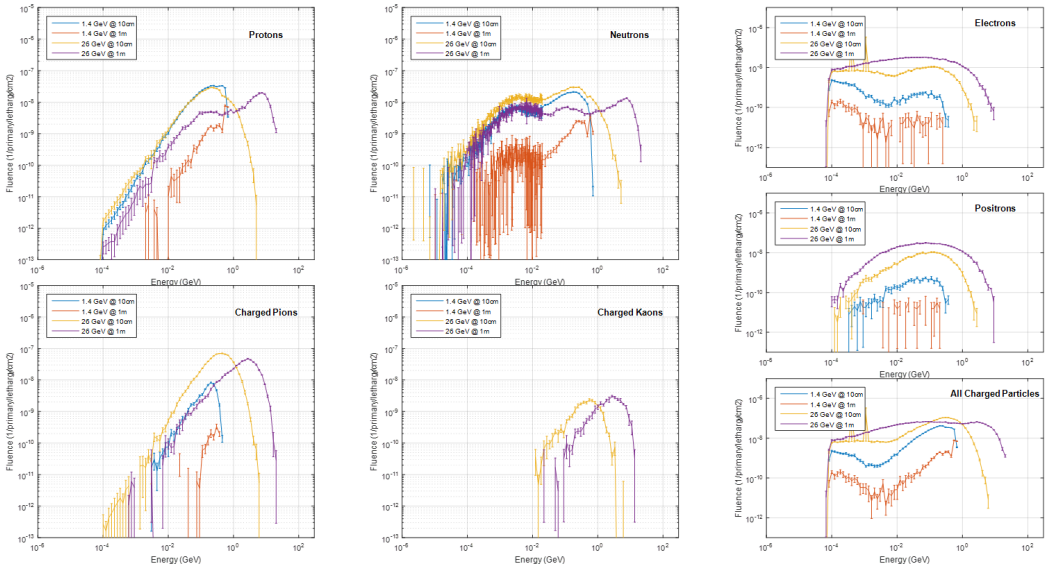

Figure 4.12 – Isolethargic particles energy spectrum of the most significant secondaries for the PS at injection and extraction energies for 10cm and 1m from the interaction point.

Table 4.20 – Secondary particles total fluence and deposited dose on the PS scoring volumes.

PARTICLE FLUENCE FOR PS AT INJECTION AND EXTRACTION ENERGIES				
Particle Type	**Fluence @ 10 cm (Particles/[cm^2*primary])**		**Fluence @ 1m (Particles/[cm^2*primary])**	
	1.4GeV	**26GeV**	**1.4GeV**	**26GeV**
Protons (p)	7.52E-08	7.12E-08	5.53E-09	4.69E-08
Antiprotons (^{p})	0	1.26E-10	0	3.76E-10
Neutrons (n)	6.80E-08	1.25E-07	5.06E-09	6.34E-08
Antineutrons (^{n})	0	9.97E-11	0	4.41E-10
Charged Pions (π +/-)	1.00E-08	1.49E-07	2.40E-10	9.69E-08
Charged Kaons (k +/-)	0	4.41E-09	0	5.72E-09
KaonZero	0	1.56E-09	0	1.72E-09
Electrons (e^-)	5.44E-09	1.30E-07	3.76E-10	2.09E-07
Positrons (e^+)	1.43E-09	3.45E-08	6.59E-11	1.45E-07
Muons (μ)	9.10E-11	1.08E-09	8.42E-12	1.20E-09
All Charged Part	9.26E-08	3.91E-07	6.25E-09	5.03E-07

Table 4.21 – Secondary particles total dose deposited on the PS scoring volumes.

DOSE DEPOSITION FOR PS AT INJECTION AND EXTRACTION ENERGIES			
Dose @ 10 cm (Gy/primary)		**Dose @ 1 m (Gy/primary)**	
1.4GeV	**26GeV**	**1.4GeV**	**26GeV**
$7.956e{-17}$	$1.7e^{-16}$	$3.44e^{-18}$	$1.60e^{-16}$

4.2.3. Super Proton Synchrotron (SPS)

The SPS takes the beam from the PS at 26 GeV and accelerates it to 480 GeV before injection in the LHC. The SPS features two types of stainless-steel beam pipes: circular with an external diameter of 159 mm and elliptical 55x130.5 mm both with 1.5 mm thickness. Only the elliptical pipe is considered for simulations. As previously, the longitudinal distance where the energy deposition is maximised strongly depends on the primary proton beam energy. For the SPS a longitudinal distance up to 15 m from the interaction point has been considered for the study. As shown on Fig. 4.13 and 4.14, the maximal energy deposition for 26 GeV with this geometry is located around 1 m from the interaction point, whereas for 450 GeV this distance is increased to 3 m.

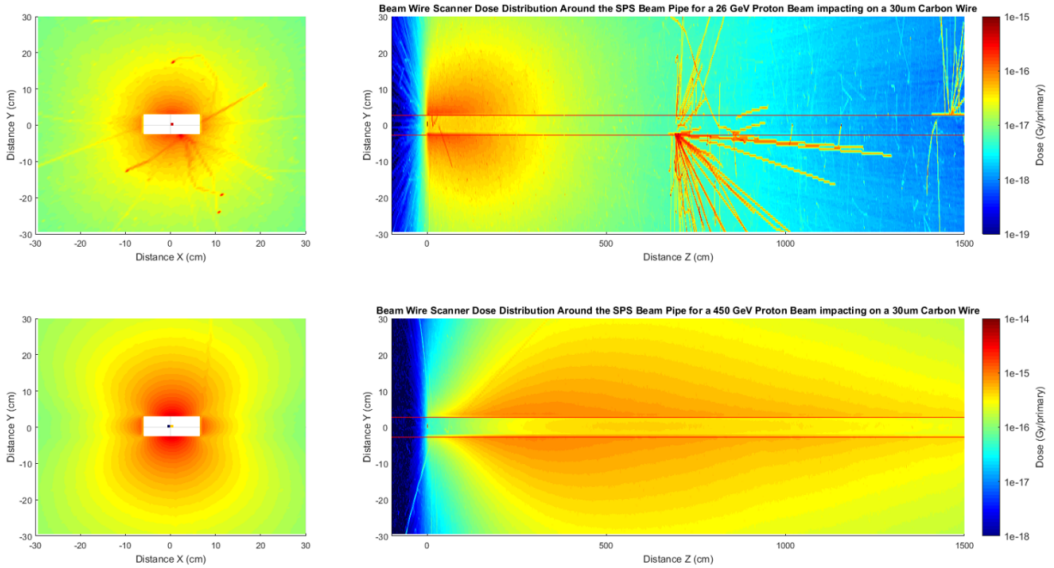

Figure 4.13 – Secondary shower dose deposition around the SPS beam pipe for 26GeV and 450GeV beams.

The energy spectra of the secondaries crossing the scoring volumes (placed at 1 m and 3 m) is shown in Fig. 4.15, whereas the total secondary fluence per square centimetre is summarised on Table 4.22. A higher proton beam energy produces more energetic secondaries and a higher quantity when interacting with the wire, this effect is especially visible on the spectra of kaons and pions. With regard to the secondary particle shower composition, for both energies it seems that electrons, positrons, and pions are the main contributors.

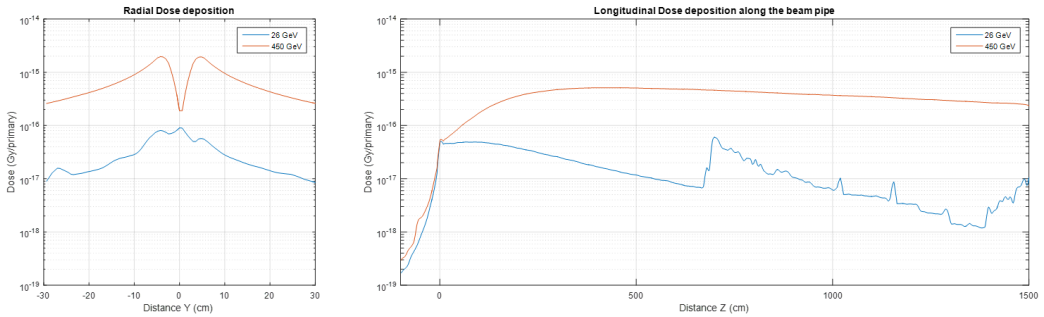

Figure 4.14 – Radial and longitudinal cross-section of the SPS dose deposition around the beam pipe.

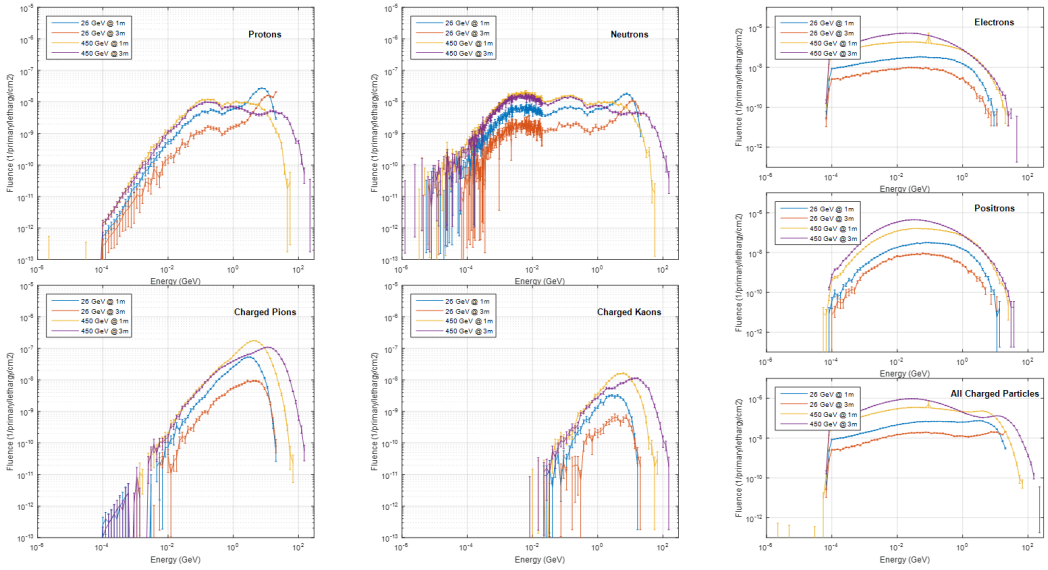

Figure 4.15 – Isolethargic particles energy spectrum of the most significant secondaries for the SPS at injection and extraction energies for 1m and 3m from the interaction point.

Table 4.22 – Secondary particles total fluence on the SPS scoring volumes.

PARTICLE FLUENCE FOR SPS AT INJECTION AND EXTRACTION ENERGIES				
Particle Type	**Fluence @ 1 m (Particles/[cm^2*primary])**		**Fluence@ 3 m (Particles/[cm^2*primary])**	
	26 GeV	**450 GeV**	**26 GeV**	**450 GeV**
Protons (p)	6.05E-08	5.76E-08	2.98E-08	4.87E-08
Antiprotons (^{p})	4.66E-10	6.98E-09	8.73E-11	6.64E-09
Neutrons (n)	7.02E-08	1.21E-07	2.71E-08	1.03E-07
Antineutrons (^{n})	5.18E-10	7.00E-09	9.82E-11	6.91E-09
Charged Pions (π +/-)	1.13E-07	3.93E-07	2.57E-08	3.26E-07
Charged Kaons (k +/-)	6.77E-09	3.40E-08	1.40E-09	3.07E-08
KaonZero	2.13E-09	9.82E-09	3.92E-10	8.72E-09
Electrons (e^-)	2.20E-07	1.30E-06	5.96E-08	2.82E-06
Positrons (e^+)	1.53E-07	8.29E-07	4.02E-08	1.91E-06
Muons (μ)	1.14E-09	3.12E-09	5.31E-10	3.05E-09
All Charged Part	5.55E-07	2.62E-06	1.57E-07	5.14E-06

Table 4.23 – Secondary particles total dose deposited on the SPS scoring volumes.

DOSE DEPOSITION FOR SPS AT INJECTION AND EXTRACTION ENERGIES			
Dose @ 1 m (Gy/primary)		**Dose @ 3 m (Gy/primary)**	
26GeV	**450GeV**	**26GeV**	**450GeV**
$1.816e{-}16$	$8.20e^{-16}$	$5.18e^{-17}$	$1.54e^{-15}$

4.2.4. Large Hadron Collider (LHC)

The simulation geometry used this time is a circular stainless steel beam pipe with 84 mm external diameter and 2 mm thickness. A longitudinal distance of 25 m has been considered for the energy deposition study.

Due to the high energy of the proton beam, the small beam size (≈ 100µm sigma) and the nominal bunch intensity (1e11 protons per bunch) on this machine, the LHC beam wire scanners produce losses that can be detected well downstream the interaction point. Secondaries produced by LHC wire scanners can be clearly measured by the LHC beam loss monitors placed >10 m downstreams. Other works have contributed to understand and quantify the losses produced by wire scanners on LHC, such as [31], where wire scanners performed controlled losses for testing and understanding the LHC super-conducting magnets quench levels. A baseline study on [110] shows previous simulations done by the CERN FLUKA team on the scope of this project, with results consistent to those on this section.

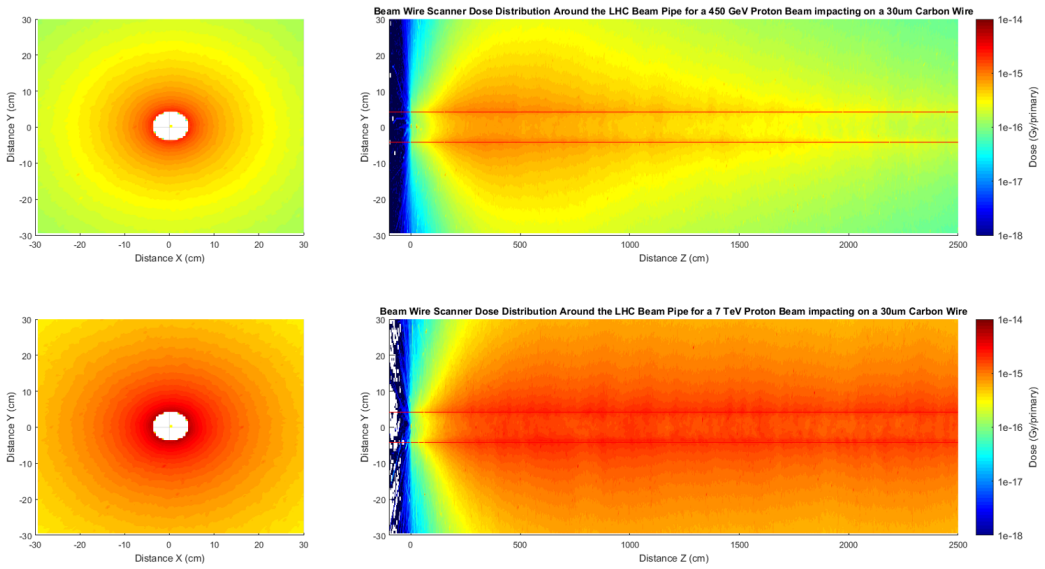

Figure 4.16 – Secondary shower dose deposition around the LCH beam pipe 450 GeV and 7 GeV beams.

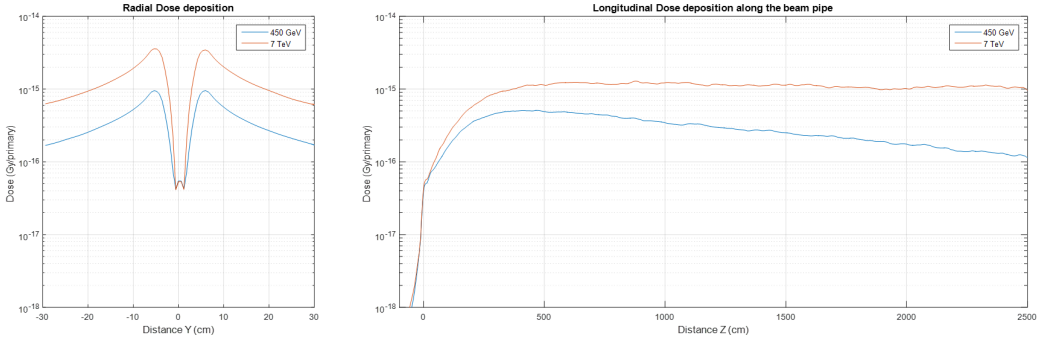

Figure 4.17 – Radial and longitudinal cross-section of the LHC dose deposition around the beam pipe.

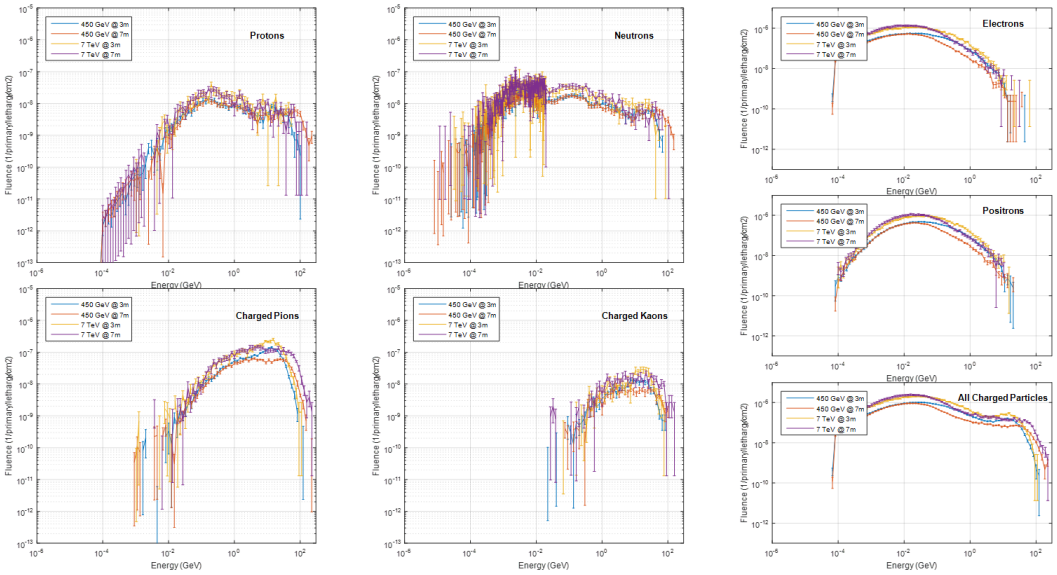

Figure 4.18 – Isolethargic particles energy spectrum of the most significant secondaries for the LHC at injection and collision energies for 3 m and 7 m from the interaction point.

Table 4.24 – Secondary particles total fluence on the LHC scoring volumes.

PARTICLE FLUENCE FOR LHC AT INJECTION AND EXTRACTION ENERGIES				
Particle Type	**Fluence @ 3 cm (Particles/[cm^2*primary])**		**Fluence @ 7 m (Particles/[cm^2*primary])**	
	450 GeV	**7 TeV**	**450 GeV**	**7 TeV**
Protons (p)	5.91E-08	1.03E-07	6.01E-08	1.02E-07
Antiprotons (^{p})	7.24E-09	1.45E-08	4.26E-09	1.35E-08
Neutrons (n)	1.39E-07	2.40E-07	1.30E-07	2.66E-07
Antineutrons (^{n})	8.86E-09	1.43E-08	5.15E-09	1.52E-08
Charged Pions (π +/-)	3.87E-07	6.75E-07	2.86E-07	6.35E-07
Charged Kaons (k +/-)	3.67E-08	6.22E-08	2.73E-08	6.79E-08
KaonZero	1.11E-08	1.85E-08	8.46E-09	1.79E-08
Electrons (e^-)	3.11E-06	6.17E-06	2.46E-06	6.61E-06
Positrons (e^+)	2.11E-06	4.14E-06	1.59E-06	4.28E-06
Muons (μ)	4.25E-09	7.24E-09	3.97E-09	7.56E-09
All Charged Part	5.71E-06	1.12E-05	4.43E-06	1.17E-05

Table 4.25 – Secondary particles total dose deposited on the LHC scoring volumes.

DOSE DEPOSITION FOR SPS AT INJECTION AND EXTRACTION ENERGIES			
Dose @ 3 m (Gy/primary)		**Dose @ 7 m (Gy/primary)**	
450GeV	**7TeV**	**450GeV**	**7TeV**
$1.71e{-}15$	$3.32e^{-15}$	$1.32e^{-15}$	$3.43e^{-15}$

4.3. Beam profile signal degradation on long transmission lines

Beam wire scanners placed on the tunnel are relatively far away from control and readout electronics, typically 100-250 m. High frequency signals coming from PMT detectors are typically 2-4 ns full with half maximum (FWHM) pulses spaced by 25 ns for nominal SPS/LHC beams. Fast analog signals may be degraded after transport with long coaxial lines. To evaluate such degradation, it is important to properly characterise the behaviour of the cable used (CK50 in this case). Cable modelling will allow to study the effect of bunch pile-up on bunch-by-bunch beam profiles, and determine the impact on the bunch profiles accuracy.

4.3.1. Transmission lines theory overview

Coaxial cables, microstript lines, twisted pairs and waveguides are a few examples of transmission lines used to transmit high frequency signals. The signal transmission over these media and its degradation (attenuation and dispersion) with distance and frequency can be studied from the circuit analysis point of view with lumped circuit model as shown on Fig. 4.19.

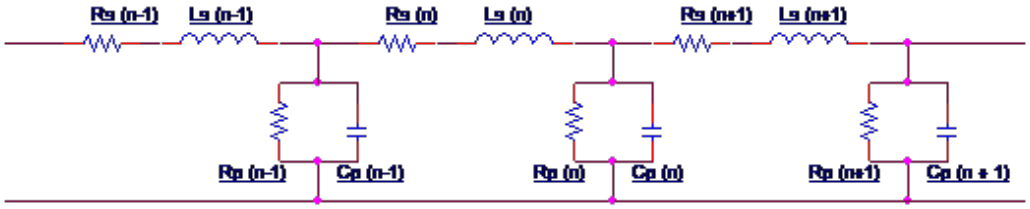

Figure 4.19 – Transmission line model as sequence of lumped circuit elements.

For a simplified analysis, a symmetric incremental length of line and wave propagation over the z direction can be considered. The different values of such model: R_s, L_s, R_p and C_p, are characterised with the transmission line physical properties per unit of length. This model contains the inductance, capacitance, shunt conductance and series resistance [111]. Since the selection of line looks the same from either end, the series elements will be divided in half of the resistance and inductance at each end (see Fig. 4.20).

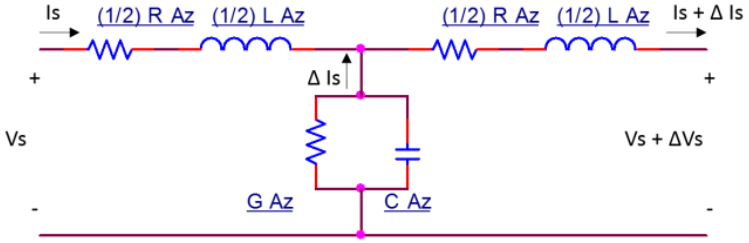

Figure 4.20 – An incremental length of a uniform transmission line. R, G, L, and C are functions of the transmission line configuration and materials given per unit of length.

Analysing the voltage equation around the perimeter of the circuit from Fig. 4.20 one can obtain:

$$V_z(z) = (\frac{1}{2}R\Delta z + j\frac{1}{2}\omega L\Delta z)I_s + (\frac{1}{2}R\Delta z + j\frac{1}{2}\omega L\Delta z)(I_s + \Delta I_s) + V_s + \Delta V_s \tag{4.6}$$

That can be simplified as:

$$\frac{\Delta V_s}{\Delta z} = -(R + j\omega L)I_s - (\frac{1}{2}R + j\frac{1}{2}\omega L)\Delta I_s \tag{4.7}$$

Taking into account that as Δz approach to zero ΔI_s also approaches to zero, the second term on the right vanishes. Then the voltage value in the limit would be:

$$\frac{dV_s}{dz} = -(R + j\omega L)I_s \tag{4.8}$$

For the current expression, second-order effects are neglected and the voltage across the central branch is approximated as V_s, obtaining the following equation.

$$\frac{dI_s}{dz} = -(G + j\omega C)V_s \tag{4.9}$$

For a uniform plane wave in a conducting medium, it is possible to extract the generalised solution for voltages and currents as:

$$\begin{aligned} V(z) &= V_f e^{-\gamma z} + V_r e^{\gamma z} \\ I(z) &= I_f e^{-\gamma z} + I_r e^{\gamma z} \end{aligned} \tag{4.10}$$

Where V_f and I_f are the forward waves for voltage and current, V_r and I_r are the reflected waves due to impedance mismatching on the load, z the position on the transmission line and γ is the complex propagation constant which is defined as follows:

$$\begin{aligned} \gamma &= \alpha + j\beta = \sqrt{(R + j\omega L)(G + j\omega C)} \\ \alpha &= \frac{\frac{R}{Z_0} + GZ_0}{2} \qquad and \qquad \beta = \omega\sqrt{LC} \end{aligned} \tag{4.11}$$

On these equations α is known as the attenuation constant and β as the phase shift per unit of length.

For the generalised equations, the characteristic impedance (Z_0) of the medium and the reflection coefficient (Γ) at the end of the line with a Z_L load are defined as:

$$Z_0 = \sqrt{\frac{R + j\omega L}{G + j\omega C}} \qquad and \qquad \Gamma = \frac{Z_L - Z_0}{Z_L + Z_0} \tag{4.12}$$

Therefore the generalised solution for a voltage wave with an arbitrary load on the transmission line would be:

$$V(z) = V_0 e^{-\gamma z}(1 + \Gamma e^{2\gamma z}) \tag{4.13}$$

For a loss-less transmission line (where R=0, G=0), and an adapted load, $Z_L = Z_0$ ($\Gamma = 0$), these analysis can be simplified:

$$V(z) = V_0 e^{-j\omega\sqrt{LC}z} = V_0 e^{-j\omega t_d} \tag{4.14}$$

This shows that at the end of the transmission line we will have the same signal that was introduced at the input but with a delay dependent on line length and its L and C parameters.

4.3.2. Loses on transmission lines

The previous simplification is acceptable for many analysis, however in real systems, as the signal frequency to be transmitted increases, the current density tends to concentrate on the conductors surface, meaning a reduction on the effective cross-section of the conductor and an frequency dependent Ohmic loss. This effect is known as "skin effect" and defines "skin depth" (δ) as the superficial layer of the conducting material where the current flows [112].

$$\delta_c = \frac{1}{\sqrt{\pi f \mu \sigma}} \tag{4.15}$$

Were μ and σ are the magnetic permeability and the conductivity of the material.

As an example to illustrate this effect, for copper lines ($\mu_{cu} = 1.2x10^{-6}h/m$, $\sigma = 5.8x10^{7}s/m$) and at frequencies near 10MHz, the skin depth is in the order of 20µm. Considering that the conducting region is equivalent to that of a thin shell with a depth of δ in a cylindrical conductor of diameter d, the frequency dependent resistance per unit of length can be calculated as:

$$R_{ac} = \frac{1}{\sigma(\pi d\delta_c)} = \frac{1}{\sigma(\frac{\pi d^2}{\sqrt{\pi\omega\mu\sigma}})} = \frac{1}{\pi d}\sqrt{\frac{\omega\mu}{2\sigma}} \tag{4.16}$$

Note that now the conductor's series resistance per unit of length has a square root dependency on the frequency ($R_{ac} \propto \sqrt{\omega} \propto \sqrt{f}$). For high frequencies the skin effect is the dominating source or losses since $R_{ac} \gg R_{dc}$, therefore R_{dc} can be neglected.

The dielectric used on the transmission line construction also influences on frequency-dependent losses. The "dielectric loss" appears due to the displacement current in the transmission line dielectric. If we describe the frequency dependent complex dielectric constant as:

$$\epsilon = \epsilon' + j\epsilon'' \tag{4.17}$$

The current through the equivalent capacitor formed by the transmission line in the dielectric with dielectric constant ϵ can be described as:

$$I = C\frac{dV}{dt} + G_d V \tag{4.18}$$

Where I is the current through the transmission line, V is the voltage applied, C is the capacitance per unit of length and G_d is the dielectric conductance per unit of length.

The dielectric conductance can be described using a factor known as dielectric loss tangent or $\tan\delta_d$:

$$G_d = \omega C \tan\delta_d \qquad where: \qquad \tan\delta_d = \frac{\epsilon'}{\epsilon''} \tag{4.19}$$

Typically $\tan\delta_d$ is considered constant within a specified frequency range of interest for common dielectrics used in transmission lines. However, it must be noted that in general $\tan\delta_d$ is frequency independent, thus, the line dielectric conductivity increases linearly with frequency ($G_d \propto \omega \propto f$).

Taking into consideration the "skin effect" and the "dielectric loss" for a given transmission line, the general solution for a voltage wave travelling on the z direction and with a perfect impedance matching ($Z_L = Z_o$) for a lossy transmission line can be expressed as:

$$V(z) = V_0 e^{(-\alpha+j\beta)z} \tag{4.20}$$

$$\alpha(\omega) = \alpha_c + \alpha_d = \frac{1}{2}\frac{R_{dc} + \frac{1}{\pi d}\sqrt{\frac{\omega\mu}{2\sigma}}}{Z_0} + \frac{1}{2}(\omega C \tan\delta_d Z_0) \tag{4.21}$$

Where α_c is the loss from the conductors due to the skin effect and α_d is the dielectric loss, expressed in Nepers per metre (Np/m). On transmission lines, the skin effect dominates the loss at frequencies bellow the Ghz region, whereas the dielectric loss is the dominant contributor above this region.

4.3.3. Coaxial cable CK50 parametrisation

For coaxial transmission lines, the characteristic parameters (R, G, C and L) per units of length can be extracted by its physical dimensions and material properties as follows on Fig. 4.21:

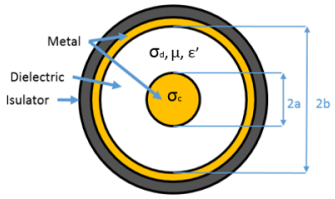

$$C = \frac{2\pi\varepsilon'}{ln(b/a)} \qquad G = \frac{2\pi\sigma_d}{ln(b/a)} \qquad L = \frac{\mu}{2\pi} ln(b/a)$$

$$R = \frac{1}{2\pi\delta_c\sigma_c}\left(\frac{1}{a} + \frac{1}{b}\right) \qquad Z_o = \frac{1}{2\pi}\sqrt{\frac{\mu}{\varepsilon'}} \ln\left(\frac{b}{a}\right)$$

Figure 4.21 – Left: Coaxial transmission line simplified construction schematic. Right: Coaxial transmission line parameters given per units of length based on physical properties.

Details about the physical properties of the CK50 cables under evaluation can be found, on [113].

4.3.4. Impact of long cables on bunch-by-bunch beam profiles

A cable model was developed on Matlab to evaluate the cable output signal resulting from arbitrary input signals, such as artificially generated beam profiles. Thus, bunch by bunch profiles degradation can be evaluated as a function of the cable length.

For the model extraction, the calculations from the previous section (that determine L, C, R_{ac} and G_{ac}) are used to build a transfer function (TF) as:

$$\begin{aligned} V_{out}(z,\omega) &= V_{in} e^{-(\alpha+j\beta)z} \\ V_{out}(z,\omega) &= V_{in} e^{-(\frac{1}{2}\frac{R_{ac}\sqrt{\omega}}{Z_0} + G_{ac}|\omega|Z_0)z} e^{-j\omega\sqrt{LC}z} \\ TF(\omega) &= e^{f(\omega)} e^{j\omega t_d} \end{aligned} \tag{4.22}$$

The model was obtained by using the IIRLPNORM Matlab function. This function is able to build an IIR filter with order "n" for the numerator and "d" for the denominator that approaches as much as possible to a given arbitrary frequency response. From our transfer function it is possible to get the Bode plot (magnitude and phase response) for the frequencies of interest by evaluating TF(ω) for a known cable length. An order 10 for numerator and denominator was found suitable for the model approximation. On Fig. 4.22 the magnitude response of two models obtained with Matlab and Pspice are plotted and against the attenuation data provided on the cable datasheet.

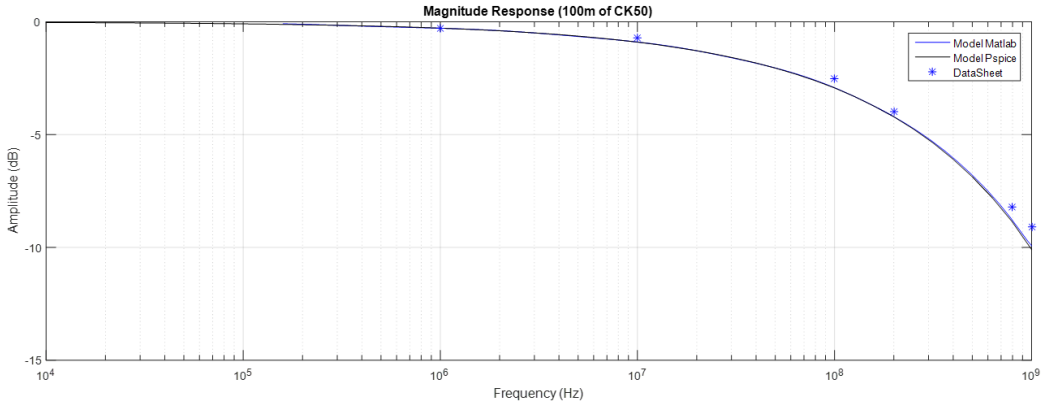

Figure 4.22 – Magnitude Response of the different models for comparison with datasheet information (cable length 100m).

A first model evaluation shows the bunch signal degradation over long cable distances in see Fig. 4.23. Here, the model response is evaluated for different cable length using a

continuous set of bunches (pulses) of different amplitudes spaced by 25 ns. Bunch overlap increases with the cable length.

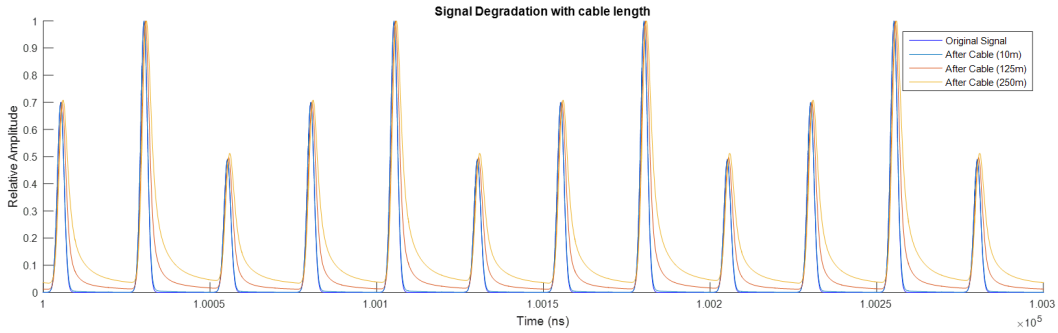

Figure 4.23 – Simulated cable output signals at different cable lengths for a typical train of 2 ns FWHM pulses spaced by 25 ns.

For the beam profile degradation study, a typical SPS bunch structure will be taken as a reference. The input signal contains a set of three consecutive short Gaussian pulses (2 ns FWHM) spaced by 25 ns, with 23µs repetition rate (corresponding to the SPS revolution period). To emulate the wire passage through such bunch structure, each "bunch" is modulated with a different Gaussian envelope. Figure 4.24 shows the input signal that emulates three consecutive bunches with different profiles on the SPS.

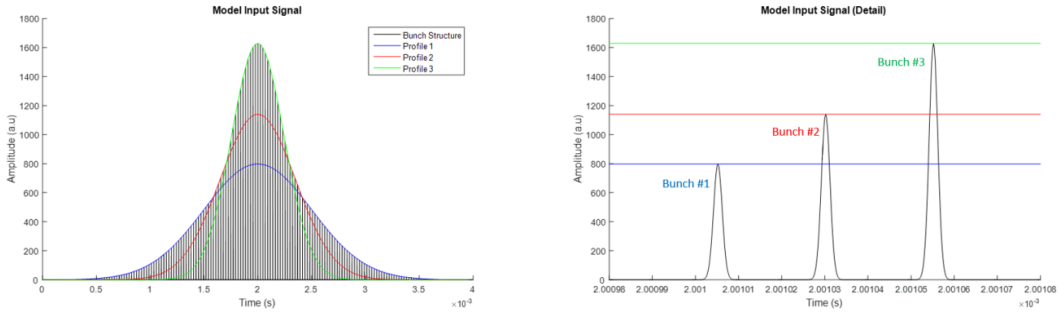

Figure 4.24 – Model input signal containing 3 bunches spaced 25 ns with 23µs repetition period.

The output signal is processed with 25 ns integrals around each bunch. The integrating window starts 2 ns before the maximum value of the peak, which avoids to integrate part of the tail of the previous bunch. To identify the worst case scenario, the three bunches are modulated with Gaussian profiles of sigma values: 500µm, 350µm and 245µm. The evaluation is done modulating the three bunches with two sequences: "Increasing" order (Bunch 1: 245µm, Bunch 2: 350µm, Bunch 3: 500µm) and "Decreasing" order (Bunch 1: 500µm, Bunch 2: 350µm, Bunch 3: 245µm)

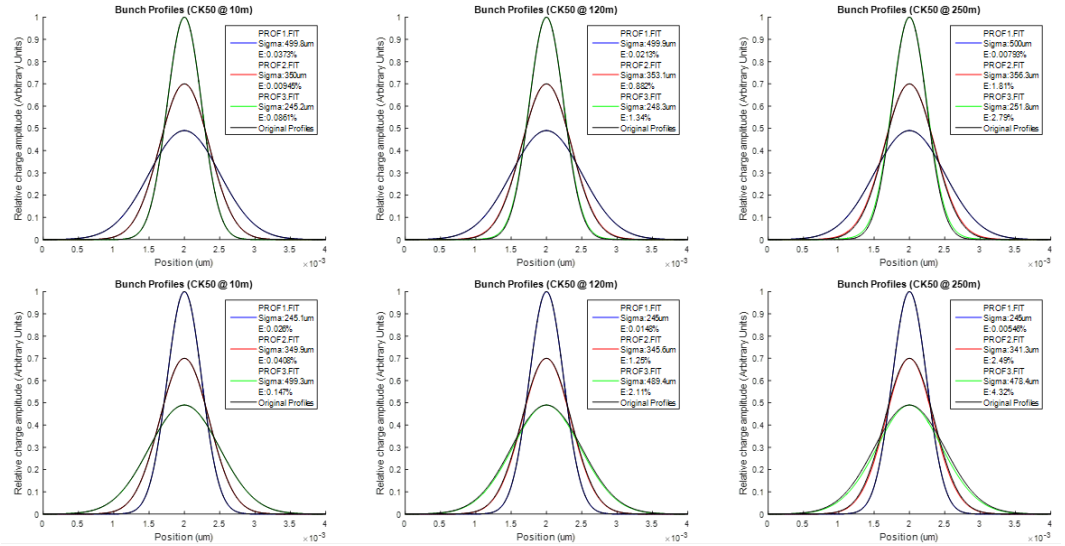

Figure 4.25 – Consecutive bunches profile determination in decreasing (top) and increasing (bottom) width over different CK50 cable length.

Figure 4.25 shows the processing results of the test signals after different cable lengths (10 m, 120 m and 250 m). The first bunch of the set is never going to be degraded on this configuration, the tail of the third bunch has more than enough time to recover the base line on the 23 µs SPS revolution period. With regard to the second and third bunches, they are degraded due to bunch pile-up, which ultimately leads to beam width determination errors.

On the specific case shown here as example, (with a ratio of 30% between profiles widths) the systematic error on beam width determination reaches up to 2.5% for the second bunch and 4.3% in for the third with 250 m of cable. The beam width determination error due to the cable does not only depend on the cable length, it also depends on the profiles like-hood. This is highlighted in Fig. 4.26 where the beam profiles are determined for different widths in increasing order for a constant cable length (120m).

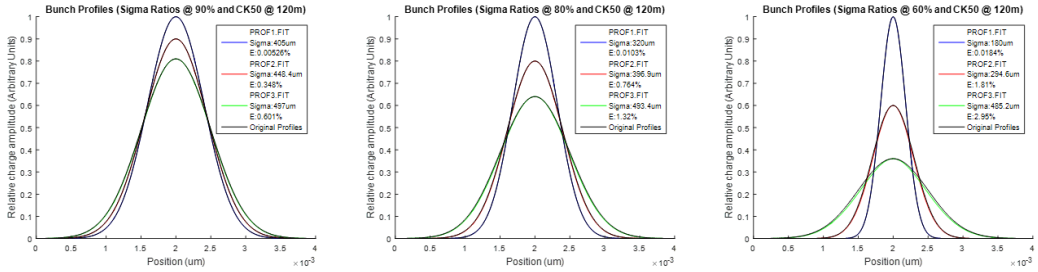

Figure 4.26 – Bunch profiles error variation with profiles like-hood for a fixed cable length (120 m).

A bi-dimensional sweep provides a complete picture of the influence of the pile-up on the beam profile error. The cable length and the sigma ratios are varied during consecutive simulations. The Gaussian SSE and beam sigma errors collected for bunches #2 and #3 in Fig. 4.27. The Gaussian goodness-of-fit is also shown for completeness, it states an artificial deformation of the measured bunch profiles due to pile-up.

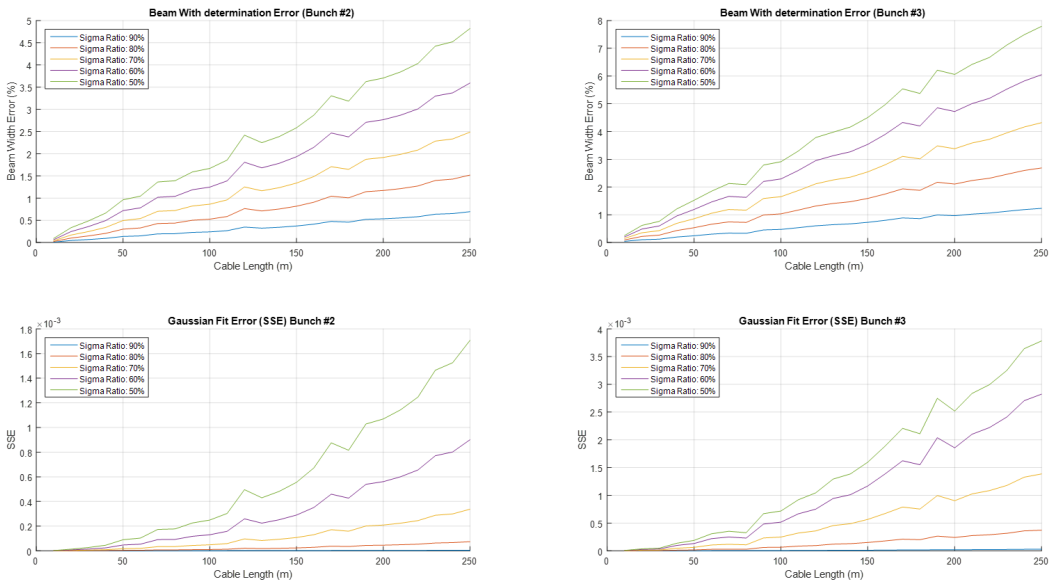

Figure 4.27 – Profiles degradation evolution over cable length and consecutive sigma ratios. (Left: Beam profile relative error. Right: Gaussian fit SSE).

4.3.5. Models validation and CK50 cable measurements

Direct measurements of long CK50 cables where done to assess the accuracy of the previous model. Two cables (around 88 m each) installed in the location of a SPS Beam Wire Scanner prototype (BA5) were used for tests here presented. The cables had one side on the tunnel and the other on the surface building. The cables were looped in the tunnel, allowing signal injection and measurements to be done on surface. The total cable length under study was about 176m.

Three different features of the cable were studied, **frequency response**, **the distortion of short pulses**, and **the induced noise**.

4.3.5.1. Frequency analysis

The cable attenuation versus frequency was determined by emulating the behaviour of a network analyser with a scope and a function generator (see Fig. 4.28). The characterisation consisted in injecting a pure sinusoidal signal at different frequencies on the cable link. The RMS amplitude ratio and the phase relationship of input/output waves were measured, obtaining the cable attenuation on dB and its phase shift on degrees (source and load were adapted to 50 Ω.

On Fig. 4.28, right, the amplitude of the output signal (in pink) decreases as the frequency increases, showing that the cutoff frequency of the cable was reached. The RMS values of the signals amplitude were calculated by the scope as well as its ratio and phase shift.

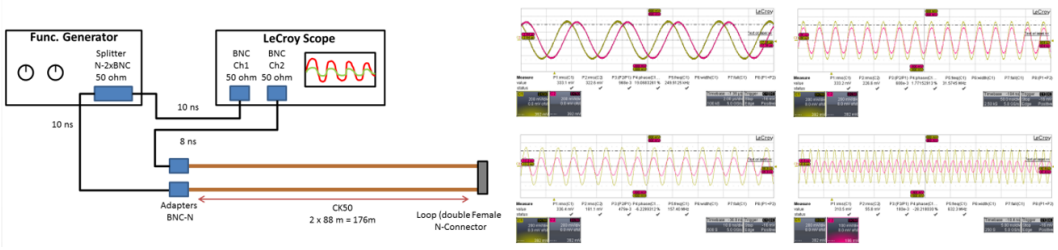

Figure 4.28 – Set-up for cable practical transfer function extraction (left) and scope measurements (right)

Figure 4.29 shows the attenuation and phase shift values practically obtained (blue dots) against the transfer function of cable models obtained from PSpice (black line) and Matlab (blue line) for the same cable distance, 176m. Measured and simulation model shown a good agreement, which demonstrates that the model was reliable from the frequency domain point of view.

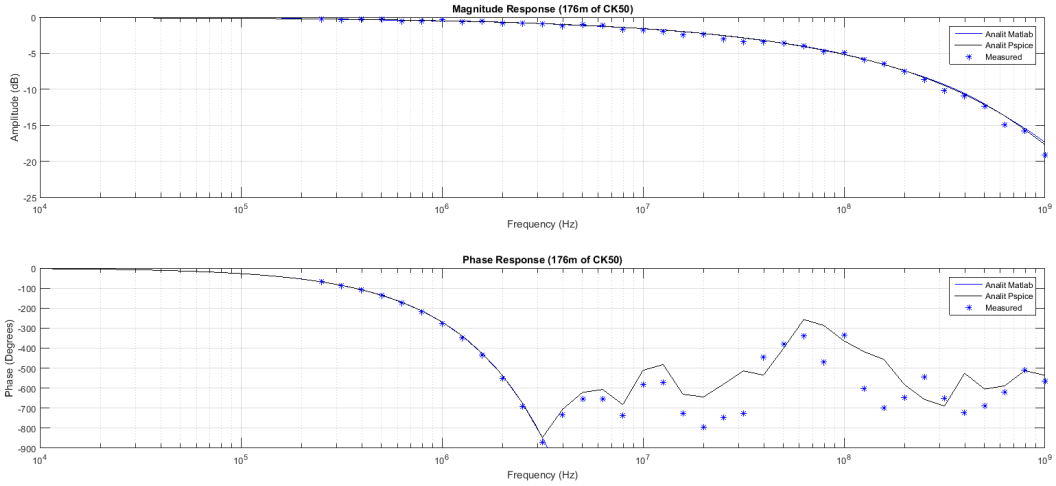

Figure 4.29 – Bode plot for 176m CK50 cable: Measurements (blue dots), PSpice (black) and Matlab (blue line).

4.3.5.2. Temporal analysis

The temporal validation of the model was checked practically verifying how parameters such as rise time, falling time and pulse width vary with cable distance. The setup used for the test is shown in the Fig. 4.30 (left), fast pulse generator a was used to provide short pulses lasting from 1 ns to 100 ns with a repetition rate between 1 KHz to 100 KHz. Source and load were impedance matched with the line (50 Ω).

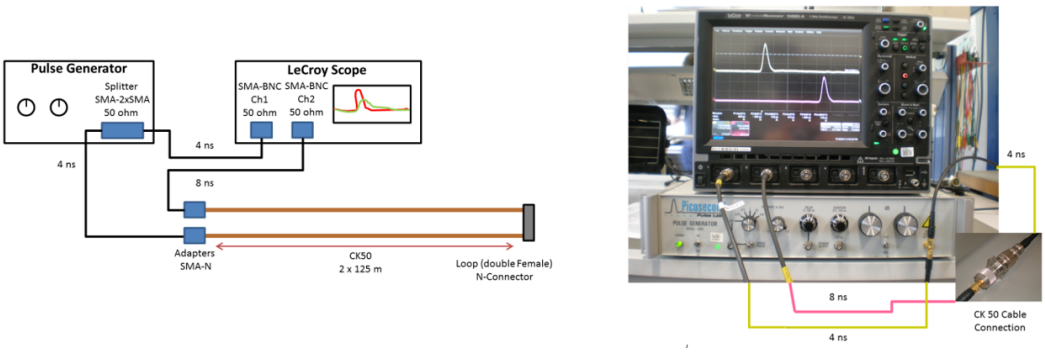

Figure 4.30 – Set-up for cable practical transfer function extraction (left) and scope measurements (right).

Evaluation on laboratory demonstrated that the setup and connections used had no impact on the system bandwidth or pulse distortion (Fig. 4.30 right).

To determine numerically the enlargement of a pulse on long CK50 cables, a couple of pulses (≈ 4 and 1.5 ns) were injected. Figure 4.31 shows the pulse distortion for both excitation signals with the same scope settings.

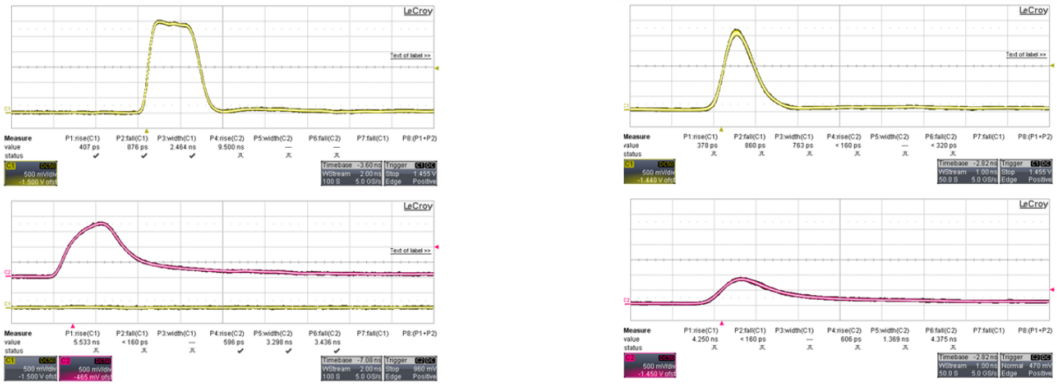

Figure 4.31 – Cable Input (yellow) and output (red) signals for 4 ns (left) and 1.5 ns (right) FWHM pulses.

Rise time, falling time (both defined for transitions from 10% - 90% of the signal maximum value), FWHM and attenuation were studied to evaluate the pulse degradation. Table 4.26 summarises these parameters for input/output pulses. Falling times were increased up to 5 times at the cable output, such long "bunch tails" are responsible of the bunch overlap.

Table 4.26 – Numeric summary of pulse parameters for input and output signals.

Pulsed signals degradation on long CK50							
	Rise Time (ps)		**Fall Time (ns)**		**Pulse FWHM (ns)**		**Att. (dB)**
Cable Length (m)	**0 m**	**176 m**	**0 m**	**176 m**	**0 m**	**176 m**	**176 m**
Long Pulse (4ns)	407	596	876	3436	2464	3298	4.68
Short Pulse (1.5 ns)	378	606	860	4375	763	1369	8.7

Several Input/Output measurement windows were recorded to evaluate the Matlab model. Each dataset contained excitation and response signals for different pulse lengths (1, 2, 3 and 5 ns FWHM). The recorded signals from the fast pulse generator were used as an input for the model. Later, the output of the model was compared with the cable measured response on the temporal domain. The normalised root mean squared errors (NRMSE), defined on Eq. 4.23, is used to assess the quality of the model fit (Fig. 4.32).

$$RMSE = \sqrt{\frac{\sum_{t=1}^{n}(y'_t - y)^2}{n}} \quad , \quad NRMSE = \frac{RMSE}{y_{max} - y_{min}}(\%) \tag{4.23}$$

where n is the number of samples in the acquired temporal window, y'_t is the value predicted by the model for the sample t and y the actual cable output for the same sample. NRMSE normalises the root mean squared errors by the amplitude of the signal, thus it is presented as a percentage.

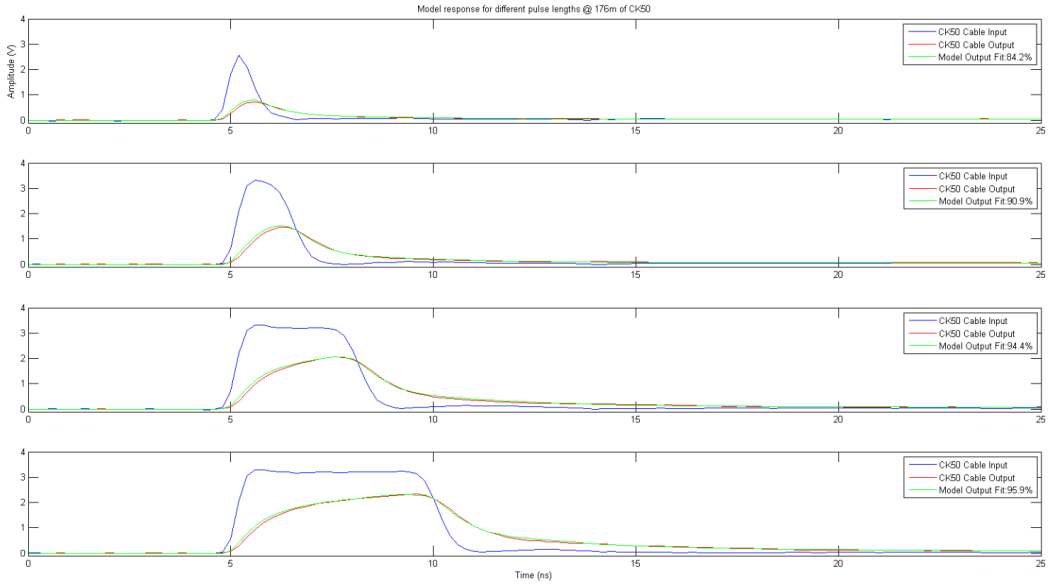

Figure 4.32 – Cable input (blue) and output (red) with model response overlapped (green) for short pulses 1-10ns.

The model NRMSE shown an agreement w.r.t the real cable response about 84 to 96%. Note that model output (green) and cable response (red) are practically overlapped.

A step response was simulated with a long pulse (100 ns), see Fig. 4.33. As previously, the model was accurately predicting the cable response with an agreement close to 96%. This successful model validation reinforces the conclusions on the cable impact for bunch profile measurements.

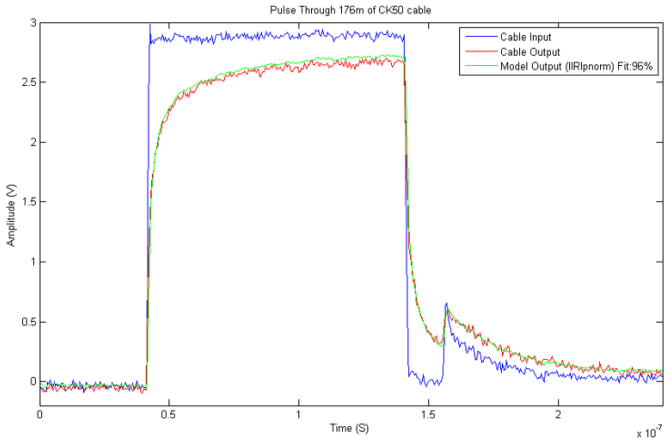

Figure 4.33 – Cable input (blue) and output (red) with model response overlapped (green) for a 100 ns pulse.

On operational systems, the bunch pile-up observed is not only linked to the cable length (which is location dependent), but to a combination of other factors including the detector signal length (FWHM) and the associated transmittance amplifier (TIA) bandwidth. Figure 4.34 shows the response of operational detector systems on SPS to particle bunch losses. On the figure belonging to a single bunch (left), the tail of the signal extends to the following bunch producing the pile-up observed on the right.

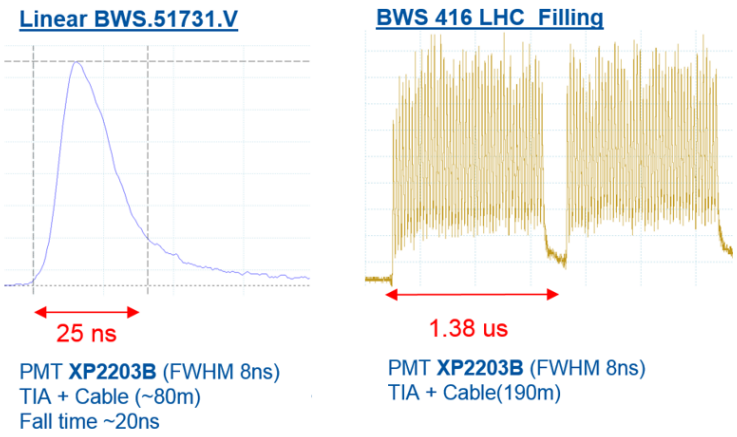

Figure 4.34 – Signals from two operational BWS acquisition systems corresponding to single bunch (left) and bunch train losses (right) produced by beam wire scanners.

Note the higher pile-up on the complete system (Fig. 4.34) compared to simulations when only considering the cable and short pulses (Fig. 4.23) or the empirical cable response (Fig. 4.32).

4.3.5.3. Pick-up noise

Studies carried out on operational systems in SPS demonstrated the presence of a significant noise coupled on the signal from the detectors. The Fig 4.35 shows scope traces from operational systems while the scanners were not being operated. The noise coupled on the lines featured two components. The first corresponded to the presence of particle bunches on the accelerator (bunch noise $\approx$ 80 Mhz) with an amplitude dependent on the beam intensity. The second contribution is independent of the bunch structure and is synchronous with the accelerator revolution frequency (turn noise $\approx$ 43 KHz).

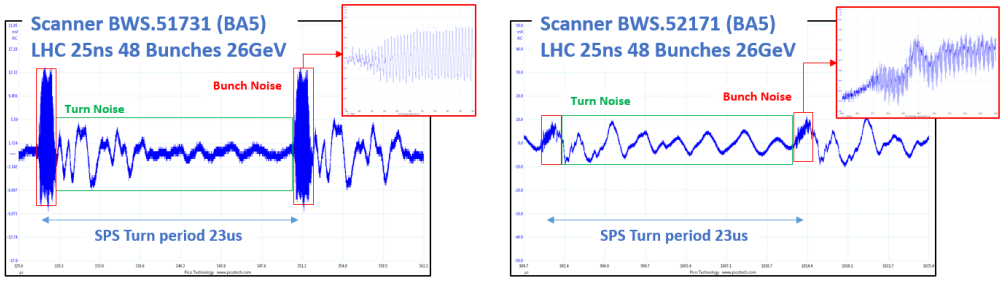

Figure 4.35 – Scope traces showing noise recorded for scanners 517(left) and 521(right) with a LHC25ns beam with 48 bunches at 26 GeV

Both noise types are present during the beam profile measurement and overlapped on the signal. The noise falls within the signal frequency of interest, which makes difficult to filter out without degrading the measurement. Such a noise is directly influencing on the profile measurement lowering the SNR and the bunch by bunch profiles quality. The noise amplitude is typically around 20 mVpp - 40 mVpp and depends on the location, which suggest some relationship with the cable routing or grounding strategy.

Figure 4.36 shows the analog signal from an operational BWS photo-multiplier tube recorded on surface being influenced by noise.

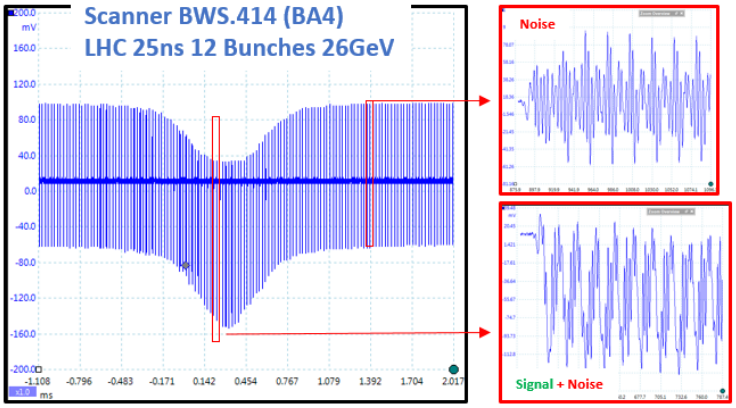

Figure 4.36 – Beam profile measurement (BWS.414) recorded with a scope on surface.

4.4. Error sources on beam profile determination

The beam size is strongly dependent on the monitor location, the accelerator and beam type. For instance, LHC beams with typical transverse emittances ranging 1-3.5µm, varies in terms of beam sigma, from injection (450GeV) to collision energies (7TeV), from about 1.19 mm to 0.16 mm (beam sigma). Beam profile monitors used at CERN are image-based (as ionization profile monitors or synchrotron light monitors), and interceptive (as beam wire scanners or SEM grids), for both methods, the accuracy of the measurement is limited by systematic and statistical errors contributions, typical of the instrument and measurement conditions.

The main sources that affect the beam profile accuracy are related with the spatial resolution of the monitor, the number of primary events detected (i.e. number of secondary particles crossing the detector, or photons detected) and the measurement noise in both axis, position and amplitude. Next sections analyse the contribution of the different error sources to the beam size uncertainty through simulations. These studies consider image based monitors and wire scanners.

For the simulations, we will refer to the relative beam size error (δ_{rel}), which is composed by a systematic (μ_σ) and statistical (σ_σ) contributions, defined as:

$$\delta_{rel} = \frac{\sigma_{measured} - \sigma_{beam}}{\sigma_{beam}} = \mu_\sigma \pm \sigma_{sigma} \tag{4.24}$$

The simulations contained on the following sections reproduce the procedure indicated in [4], and will provide valuable information for the specifications of the upgraded acquisition system.

4.4.1. Considerations

A different measurement simulation approach will be used for interceptive and imaging systems concerning the beam Gaussian distribution sampling. The beam distribution used for simulations is defined as:

$$\begin{gathered} G(x) = \frac{N_{part}}{\sigma\sqrt{2\pi}} e^{-\frac{1}{2}(\frac{x}{\sigma})^2} \\ \int G(x)dx = N_{part} \end{gathered} \tag{4.25}$$

where N_{part} is the total number of events that form the complete Gaussian profile, i.e. total number of photons illuminating the imaging detector area for imaging systems, or total number of particles crossing the detector surface for BWS.

- **Imaging systems:**

These systems are limited mainly by the measurement resolution (determined by the pixel size) and the magnification given by the optical path. Imaging systems capture a complete and continuous picture of the beam, however each pixel is integrating the photons distributed on their surface (see Fig 4.37 and Fig 4.38 left). For imaging systems with k pixels in one dimension, the measured Gaussian distribution would contain K points (pixels) with a value per pixel defined as:

$$\bar{y}_i = \int_{\bar{x}_{i-1}}^{\bar{x}_i} G(x)dx \tag{4.26}$$

On this case, if the sensor pixel size is comparable with the beam sigma value, these monitors will show a systematic error contribution on beam size determination.

Taking one coordinate for one pixel (x) and assuming that N photons are uniformly distributed along the pixel extension in that dimension (d), the normalized uniform distribution of the photons can be defined as:

$$f(x) = \left\{ \begin{array}{ll} \frac{1}{d}, & \text{for } -\frac{d}{2} < x < \frac{d}{2} \\ 0, & \text{for } x < -\frac{d}{2}, x > \frac{d}{2} \end{array} \right\} \tag{4.27}$$

The mean value and the variance of the photon locations can be obtained as for a uniform distribution:

$$\begin{aligned} \mu_{pixel} &= \int_{-\inf}^{\inf} f(x)dx = 0 \\ \sigma^2_{pixel} &= \int_{-\inf}^{\inf} x^2 f(x)dx = \frac{d^2}{12} \end{aligned} \tag{4.28}$$

The mean μ_{pixel} defines the pixel centre, the standard deviation σ^2_{pixel} represents the uncertainty on the location of a photon illuminating the pixel. When using imaging detectors for beam profile reconstruction, the uncertainty of each photon location propagates to the determination on the beam size. The measured beam width has a contribution from the particles distribution (σ_{beam}) and the pixel width determined by the detector resolution (σ_{pixel}). With the consideration of uniform photon distribution on each pixel, both terms are independent, and the resulting beam size from the measurement is:

$$\sigma_{measured} = \sqrt{\sigma^2_{beam} + \sigma^2_{pixel}} \tag{4.29}$$

Then, the systematic error introduced by these systems can be calculated as follows:

$$\mu_0 = \frac{\sigma_{measured} - \sigma_{beam}}{\sigma_{beam}} = \sqrt{1 + \frac{1}{12\eta^2}} - 1 \tag{4.30}$$

where η is the relationship between the beam size and the pixel size (bins/sigma).

- **Wire Scanner Systems:**

The previous conclusions can be extrapolated to beam wire scanners, the relationship between beam sigma and wire diameter introduces a small systematic error contribution to the measurement, especially if the wire is comparable with the beam size. The instantaneous rain of secondaries is produced by the integrated surface of the wire over the beam. The beam profiles measured with wire scanners and K number of points are defined as:

$$\bar{y}_i = \int_{\bar{x}_i - \frac{D_w}{2}}^{\bar{x}_i + \frac{D_w}{2}} G(x)dx, \text{where i=1}\ldots\text{k} \tag{4.31}$$

where D_w is the carbon wire diameter.

The profile measurement of a single bunch is reconstructed from several turns while the wire is crossing through the beam at constant speed. Thus, no profile information is available between two consecutive bunch-wire interceptions, this makes a bunch wire scanner profile a non-continuous measurement (see Fig. 4.37 and 4.38 right). The measurement resolution, in points per sigma (PpS), for a single bunch is determined by the scan speed (V_{scan}), the beam width (σ_{beam}) and the machine revolution frequency (f_{rev}) as:

$$PpS = \frac{\sigma_{beam}}{V_{scan}} f_{rev} \tag{4.32}$$

On wire scanners, the distance between consecutive measurement points varies, being smaller or bigger than the wire diameter itself (30µm) in function of the scan speed and the machine revolution frequency.

Table 4.27 collects a summary the reachable bunch profile resolutions for wire scanners at different speeds and accelerators.

Table 4.27 – Bunch profile resolutions for wire scanners working at 1 and 20 m/s for the CERN accelerators.

Wire Scanner Resolution as function of Speed and Accelerator				
	PSB	**PS**	**SPS**	**LHC**
Rev. Period	1.67 - 0.53 µs	2.2 µs	23 µs	89 µs
Res. @ 1m/s	1.67 - 0.53 µm	2.2 µm	23 µm	89 µm
Res. @ 20m/s	33.4 - 10.6 µm	66 µm	460 µm	1.78 mm

A common technique to increase the measurement resolution for a given bunch, is to perform several scans during the same cycle time with a programmable delay respect to the bunch phase. This way, the wire intercepts the bunch profile in different locations on each scan.

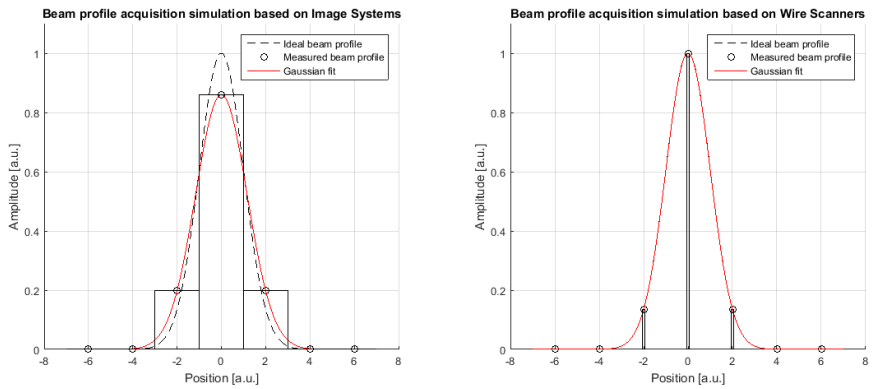

Figure 4.37 – Image-based (left) and Interceptive-based (right) acquisition considerations (this example shows 0.5 Bins/sigma and profile peak on bin centre).

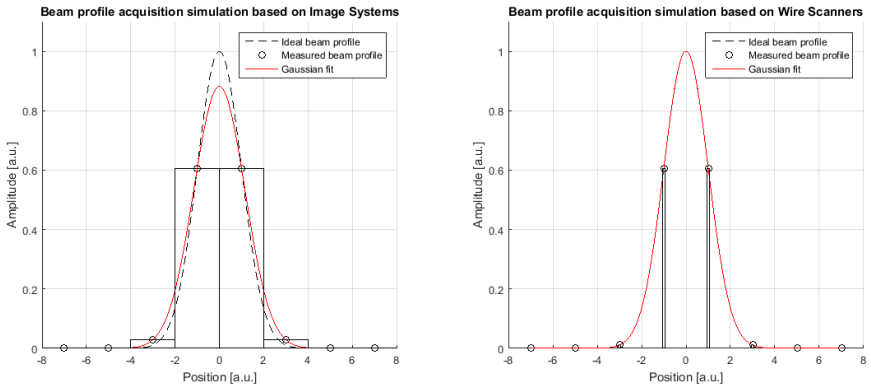

Figure 4.38 – Image-based (left) and Interceptive-based (right) acquisition considerations (this example shows 0.5 Bins/sigma and profile peak on bin side).

4.4.2. Simulation algorithm

To evaluate the different sources of error on the beam profile reconstruction and their random or systematic contribution to the measurement error, a set of numerical simulations were performed. The influence on the number of events and spatial resolution (bin width) will be evaluated for wire scanners and for imaging systems. For wire scanners also the influence of the wire diameter respect to the beam size will be studied.

The simulation script generates an ideal beam profile with a defined number of total events and size (sigma) as on Eq,4.25, this profile will be used as a reference. For each of the K measurement points (Eq. 4.26 or Eq. 4.31), the script generates a set of 500 random values following a normal distribution with $\mu_i = \overline{y_i}$ and $\sigma_i = \sqrt{\overline{y_i}}$. This sigma error estimation corresponds to the assumption of a Poisson distribution of the primary events along the integrated region (photons for imaging systems or secondaries crossing the detector and produced by the wire section).

The code generates, a set of 500 beam profiles (entries) with K points. The 500 profiles are fitted with a Gaussian distribution to obtain the measured beam sizes. Afterwards, the fit results (sigma values) are fed into a histogram, with a sufficiently large number of entries the histogram will result in a Gaussian distribution. The histogram collects the measured beam size of 500 repeated acquisitions with the profile monitor, and its distribution is fitted again to extract the mean value (μ_σ) and sigma (σ_σ) of the histogram. The difference between the original beam size (σ_{beam}), given as an input to the simulation, and the mean value of the measurements (μ_σ) represents the systematic error, whereas the standard deviation of the fitted histogram (σ_σ) provides the statistical or random error, see Eq. 4.33. Figure 4.39 shows an example of the processing algorithm for better understanding.

$$\begin{aligned} \epsilon_{systematic} &= \frac{\sigma_{beam} - \mu_\sigma}{\sigma_{beam}} \\ \epsilon_{statistic} &= \frac{\sigma_\sigma}{\sigma_{beam}} \end{aligned} \tag{4.33}$$

Other effects will be studied as well to check their contribution to the beam size error, such as the relative beam position respect the measurement points and the effect of random noise on X and Y axis.

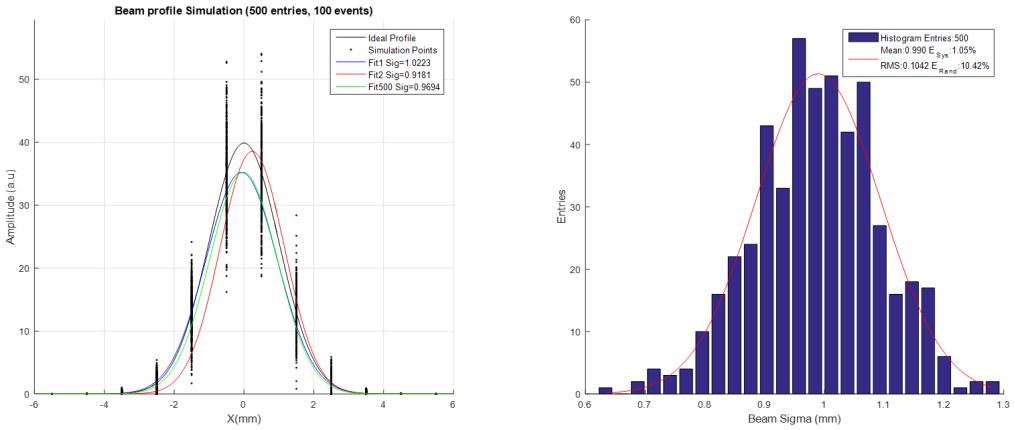

Figure 4.39 – The left plot is showing the ideal beam profile in black, and a set of 500 simulations (profiles) with 100 primary events (the original Gaussian integral), a Gaussian fit has been done in three random distributions. The plot on the left is a histogram of the sigma values obtained in each of the 500 fits on the left. A Fit on the histogram provides the monitor statistical (σ_σ) and systematic (μ_σ) errors on the beam size determination.

4.4.3. Simulation results

4.4.3.1. Imaging systems

The simulations performed have successfully reproduced the results obtained in [4] for imaging systems. The systematic error in due to the pixel size respect to the beam sigma (bins/sigma), in Fig 4.40, shows a good agreement with the analytic expression on Eq. 4.30 (black line).

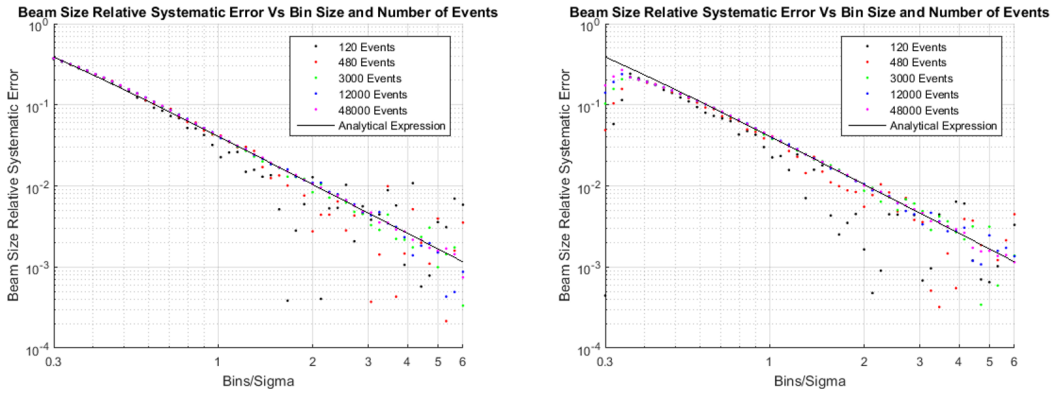

Figure 4.40 – Imaging monitors **systematic** error as function of pixels per sigma and number of primary events for beam peak at the bin centre (left) and at the bin edge (right).

On the other hand, the random error is showing to be only dependent on number of events. No significant improvement is observed as more bins per sigma are taken. In addition, for low resolutions (<1bin/sigma), the Gaussian fit is biased by the relative position of the Gaussian peak respect to the bin.

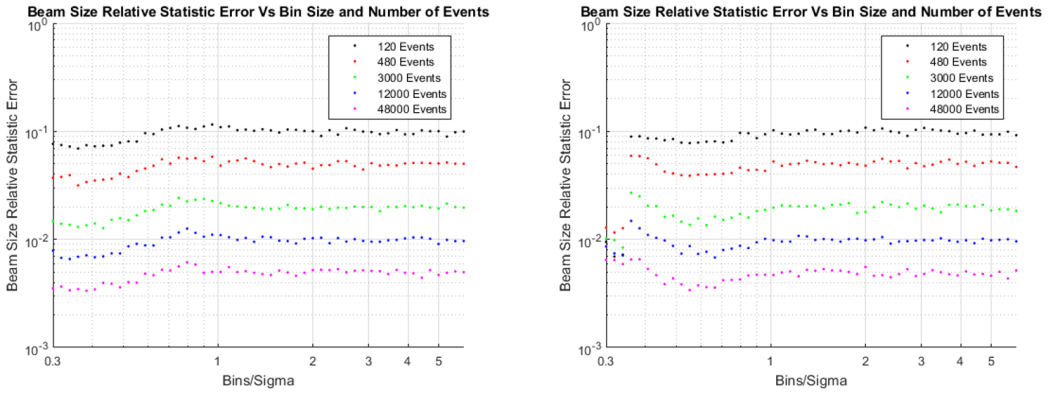

Figure 4.41 – Imaging monitors **random** error as function of pixels per sigma and number of primary events for beam peak at the bin centre (left) and at the bin edge (right).

4.4.3.2. Wire Scanners

Fig. 4.42 shows, that for wire scanners, systematic errors are practically uncorrelated to the number of events and number of points measured per sigma (wire diameter considered much smaller than the beam width). This is not the case when the wire diameter approaches the the beam width (see Fig. 4.44). As previously observed with the pixel size, the smaller the wire diameter is respect to the beam, the smaller is the systematic contribution according to Equation 4.30. The simulation results on Fig. 4.44 shows a match on the systematic error introduced by the wire diameter and the prediction from Eq. 4.30. Systematic errors on wire scanner are only dependent on the wire diameter and beam size relationship, and not on the number of points per sigma or number of number of events. A nominal beam on the LHC with 100µm sigma and being scanned with a 30µm carbon wire (Sigma/Wire diam = 3.3) will feature a systematic error in the order of 0.5% (0.5µm) independently of how many point per sigma are taken.

With regard to the random error contributions, there is a strong dependency on the number of events and to the number of points per sigma as shown on Figure 4.43. As a difference respect to the imaging sensors, on wire scanners there is an improvement on the random error when more points per sigma are used for beam profile reconstruction (assuming wire diameter « beam sigma). The results of these simulations suggest that for an accurate and precise beam profile measurement (<1% beam sigma total error), a high number of total events is required ($>$ 12000), the wire needs to be at least 3 times smaller than the beam sigma and the scan must record more than 1 point per sigma. For low resolutions ($<$ 1 bin/sigma) the profile width error is biased by the position of the sampling points w.r.t the Gaussian peak (see Fig. 4.42 and 4.42).

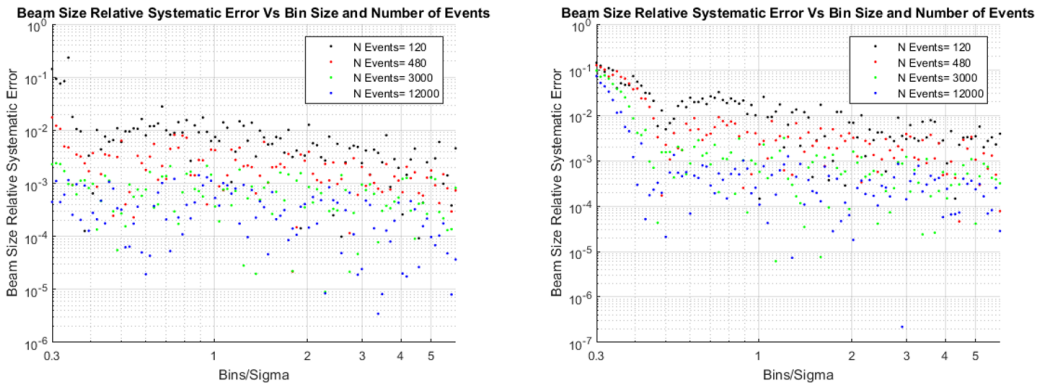

Figure 4.42 – Beam Wire Scanner **systematic error** as function of points per sigma and number of primary events for beam peak at the bin centre (left) and at the bin edge (right).Wire diameter is 10 times smaller than beam sigma.

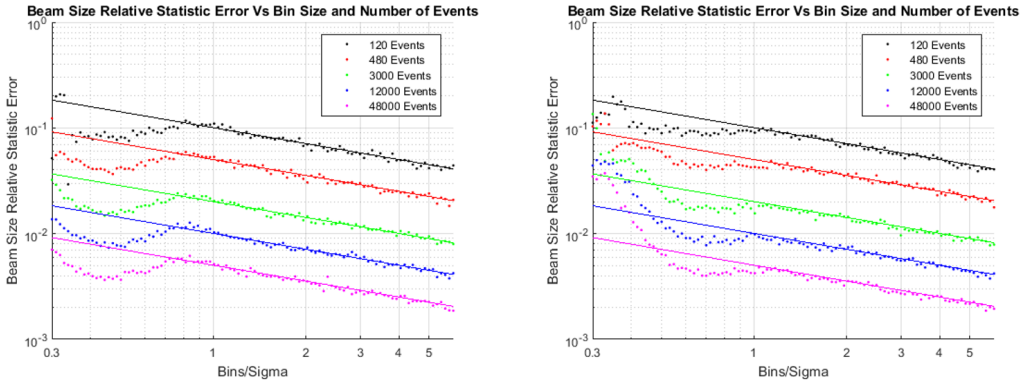

Figure 4.43 – Beam Wire Scanner **random error** as function of points per sigma and number of primary events for beam peak at the bin centre (left) and at the bin edge (right). Wire diameter is 10 times smaller than beam sigma.

From the previous measurements, an analytical expression can be extracted to evaluate the random error dependency with the measurement resolution (PpS) and the number of events (N_{TE}). This parametrization is adjusted for resolutions bigger than 1 bin/sigma and is shown in continuous lines in Fig. 4.43. The analytical approximation is as follow:

$$\epsilon_{statistic}(N_{TE}, PpS) = \frac{1.1}{\sqrt{N_{TE} PpS}} \tag{4.34}$$

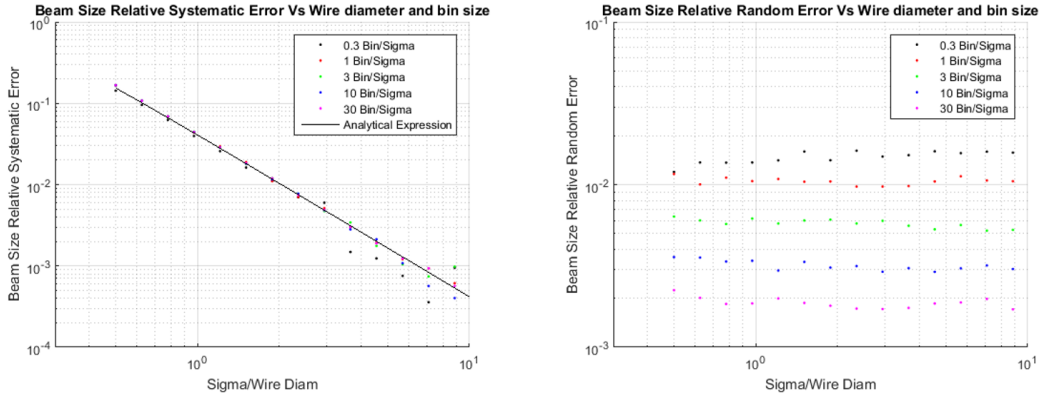

Figure 4.44 – Systematic (left) and random (right) errors associated to the number of points per sigma and Beam/Wire size relationship.

The effect noise on the amplitude axis is evaluated through the profile SNR_y, defined as the ratio between the Gaussian amplitude and the noise RMS value (σ_i).

$$\sigma_i = c = \frac{max(G(x))}{SNRy} \tag{4.35}$$

To isolate the contribution on the number of events a very high number was used ($1e^8$ events). Each of the K points of the 500 simulated Gaussians is defined as ($\bar{x}_i$, y_i), where $\bar{x}_i$ is the measurement position and y_i is a random value with mean $\bar{y}_i$ and standard deviation $\sigma_i = c$. The error assigned per point is set as on Eq. 4.35. The results on Fig. 4.45 explain how the noise on Y axis affects the measurement uncertainty.

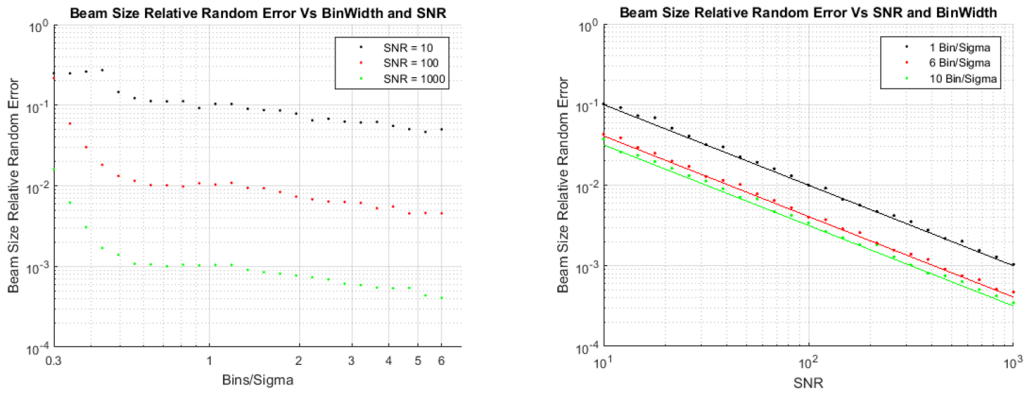

Figure 4.45 – Beam Wire scanner Random error versus amplitude SNR and points per sigma (PpS). Sweep on PpS (left) and SNR (right).

The influence SNR_y on the random beam width error was adjusted as previously with an analytical expression (Eq. 4.36), shown as continuous lines on Fig. 4.45 (right):

$$\epsilon_{statistic}(SNR_y, PpS) = \frac{1}{SNR_y\sqrt{PpS}} \tag{4.36}$$

The impact on the error due to the wire position incertitude is studied in a similar way as with the SNR in amplitude. This time the 500 Gaussians with K points have only incertitude on the x axis, defining each point as (x_i, $\bar{y}_i$), where $\bar{y}_i$ is the measurement amplitude and x_i is a position value with mean $\bar{x}_i$ and standard deviation $\sigma_i = c$. The incertitude in position is considered as a relationship with the beam sigma, defined as:

$$\sigma_i = c = \frac{\sigma_{beam}}{SNR_x} \tag{4.37}$$

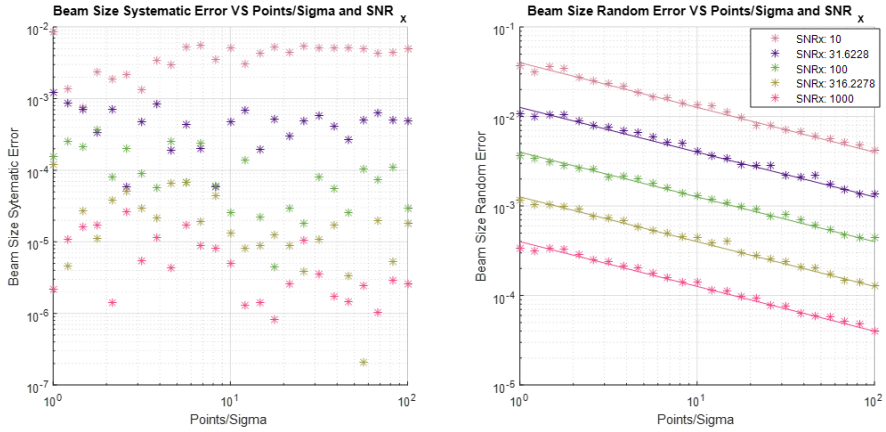

Figure 4.46 – Beam Wire scanner Random error versus amplitude SNR and points per sigma (Pps). Sweep on PpS (left) and SNR (right).

The results shown on Fig. 4.46 for SNR_x (or position uncertainty) are similar to those shown for SNR_y. The wire incertitude contribution to the statistical error has been adjusted the analytic approximation on Eq. 4.38:

$$\epsilon_{statistic}(SNR_x, PpS) = \frac{0.4}{SNR_x\sqrt{PpS}} \tag{4.38}$$

The simulations for the SNR in X and Y axis assumed a wire diameter 10 times smaller than the beam sigma, and give an approximated idea of the wire scanner and secondaries acquisitions system requirements for low beam width determination errors.

These simulations and analitic equations allow to obtain the beam size uncertainty as a combination of the three sources of error:

$$\epsilon_{\text{beamWidth}} = \sqrt{\epsilon^2_{\text{NTE}} + \epsilon^2_{\text{SNRx}} + \epsilon^2_{\text{SNRy}}} \tag{4.39}$$

As an example, to measure a 100µm sigma LHC beam with an incertitude below 1%, the precision in the wire position measurement must be better than 4µm and more than 3 points per sigma must be taken. Regarding uncertainty on Y axis, SNRy should remain avobe 100 and more than 10000 particles need to be detected at the Gaussian centre.

Chapter 5

Secondary shower acquisition system design

This chapter defines the proposed architecture for the BWS acquisition system and its main components, including details on the integrator ASICs selected for evaluation on this thesis. The development of a proof-of-concept prototype, including hardware and firmware, is also detailed here.

5.1. Acquisition system architecture

An upgraded electronics scheme for secondary particles readout is motivated by the findings detailed on Chapter 4. The scanner measurement can be degraded by the impact of long coaxial cable lines, which leads to bunch pile-up and therefore beam profile cross-talk on bunch by bunch measurements for cable lengths >100 m. The high frequency nature of BWS detector signals (>250 Mhz) and the low noise requirements (in the order of single particle detection) suggest the need of digitalization close to the detector to avoid capacitive effects of the cable. In addition, long copper links degrade the signal SNR by the presence of electromagnetic interference (EMI) produced by RF equipment or power lines nearby.

The architecture proposed on this thesis for the BWS secondary shower acquisition follows a modular design approach standardised by the CERN's beam instrumentation (BI) group for new developments, such as the Multi Orbit Position System (MOPOS) and Beam Loss Monitor (BLM) upgrades [114]. This architecture is based on the placement of a radiation hard front-end responsible of digitalization close to a detector and optical digital communication with a back-end system where the data is stored and processed.

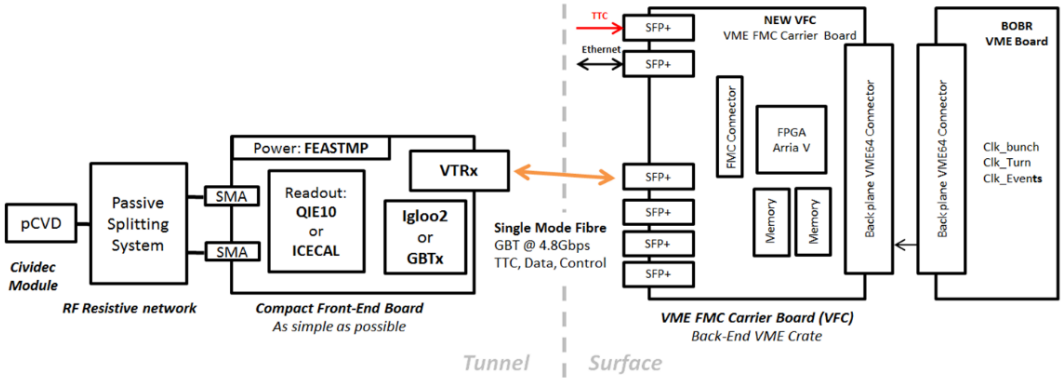

Figure 5.1 – Secondary shower acquisition system architecture for pCVD diamond detectors readout.

The system architecture employs a standard radiation-hard front-end board (GEFE [115]),

equipped with a custom mezzanine and an integrator ASIC capable of charge integration at 40MHz. Bunch synchronous acquisitions are needed to provide bunch by bunch profiles, and high dynamic range to cope with the accelerator dynamics. The GEFE Board is responsible to collect the digital data, from the detector readout mezzanine, and send it through a single mode optical fibre at 4.8Gbps using the GBT protocol to the back-end system. The front-end control and synchronisation are managed through the optical link by a VFC-HD board (back-end), which is responsible as well for the data reception and storage. With each front-end requiring a single GBT bridge, a single VFC-HD would be capable of driving up 4 acquisition systems.

5.1.1. Electronics exposure to radiation

Radiation affects electronics by cumulative and single event effects (SSE). Cumulative effects degrade the electronics performance as radiation dose is absorbed up to a final fatal failure, this effect is measurable and degradation parameters are provided when qualifying equipment up to certain radiation level in terms of total ionising dose (TID), expressed in Rad or Gy. The SSE are stochastic processes produced by nuclear interaction in the electronics from the direct ionisation of a single particle, these interactions may deposit enough energy in an electronic device to perturb its operation, i.e. flipping a bit on a memory. SSE are characterised only in terms of probability, and they are related to the particle type, fluence and electronics cross-section. SSE can be minimised with mitigation techniques such as Triple Modular Redundancy (TMR) or error detection and correction techniques on digital logic.

Tunnel electronics are specified for an operational life of 10 years, considering a radioactive environment it is expected a total ionising dose (TID) of 100 Gy per year (on SPS and LHC). General specifications for such type of electronics are about 1KGy during its operational life, same specifications as MOPOS project given the developments and environment similarities [116]. Such limit is constrained by the radioactive conditions of tunnel areas, deeply studied by the R2E group for the LHC injector chain [117] [118]. Radiation extinction ratio is very fast with distance, according to R2E surveys, readout electronics might be placed on the floor ≈70 cm from the beam pipe with moderate radiation levels. SPS measurements specify radiation levels in general <100 Gy/y on the cable trays (≈50 cm from beam pipe) except in some very specific locations (see Fig. 5.2).

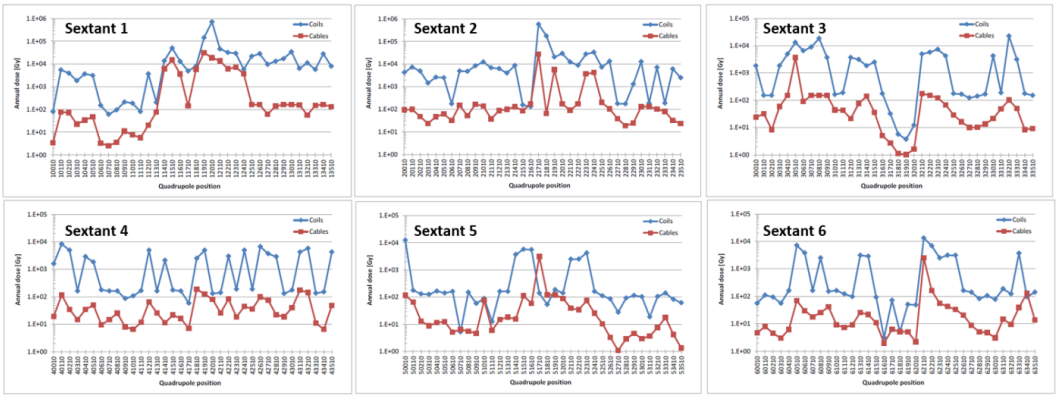

Figure 5.2 – Radiation levels for the six SPS sextants between 2009 and 2011, measurement from dosimeters placed on beam pipe (blue) and cable tray (red) are shown [118].

Radiation exposure in lower energy accelerators such as PS and PSB is more critical and electronics must be placed further away from the beam pipe or in shielded areas to survive the expected operational life. For these accelerators, surveys specify >1KGy/y in the close vicinity of the beam pipe (≈5 cm). Particular simulation campaigns for electronics placements study on PS the dose reduction with shielding and distance[119], a moderate exposure <10 Gy/y

can be reached if electronics are properly protected bellow floor level (see Fig. 5.3), these assumptions can be extrapolated to the PSB case.

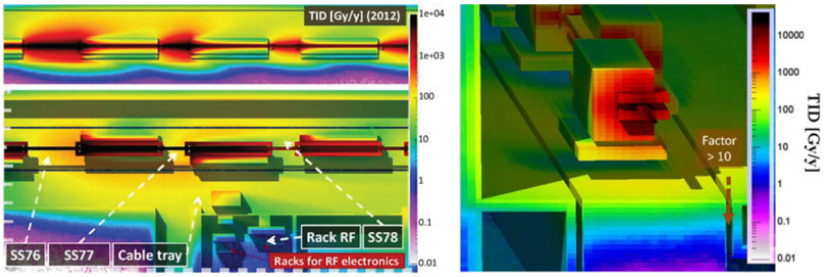

Figure 5.3 – Dose exposure FLUKA simulations for the PS and attenuation with distance and shielding [119].

5.1.2. The VME FMC Carrier Board (VFC) and GBT-Based Expandable Front-End (GEFE)

The architecture shown on Fig. 5.4 depicts the standard approach used on beam instrumentation developments and upgrades at CERN.

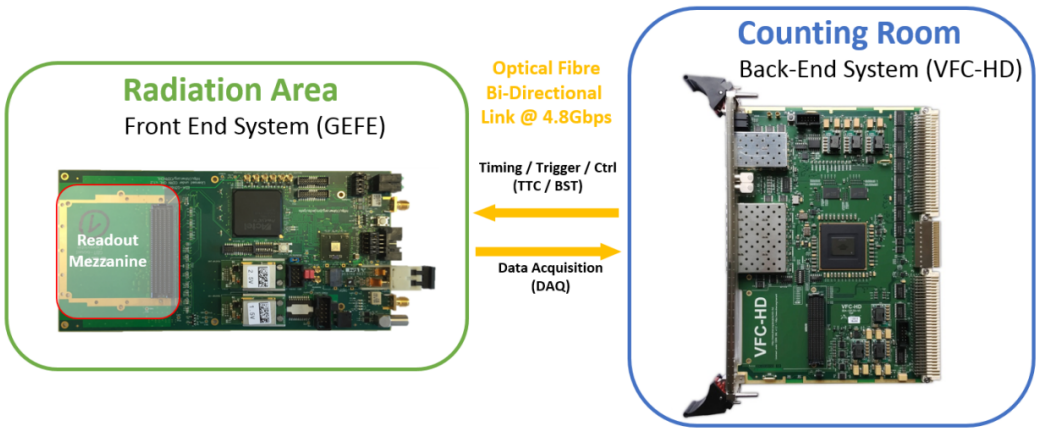

Figure 5.4 – GEFE board (left) and VFC-HD board communication as front-end and back-end systems respectively.

The VFC-HD board (Fig. 5.4 right) is conceived as a general purpose digital VME board for beam instrumentation, it is designed to replace the obsolete DABx64 boards detailed on Chapter 2. This is a FPGA-based (ARRIA V GX) 6U VME 64 module featuring a high pin count FMC slot that follows the FMC VITA57 standard for compatibility with commercial FMC modules. The FMC slot is foreseen for user specific applications. The board offers the possibility to connect to custom VME rear transition modules (RTM). It features 6 small form factor pluggable (SFP+) slots, from which 2 are dedicated to Ethernet and Beam Synchronous Timing (BST) interfaces, and 4 for user applications. Concerning memory, it is equipped with two 8Gb DDR3 memories, offering high storage capabilities (14Gb) intended for long datasets of raw data. The VFC is capable of receiving and decoding itself the BST signals distributed via optical link, avoiding the need of external equipment for such purpose. The board is fully compatible with the GBT standard for back-end systems and it is capable to offer high bandwidth and latency deterministic links with its front-ends (GEFE) through commercial optical transceivers on its user SFP+ sockets.

The GBT-based Expandable Front-End (GEFE) board is another general purpose digital board designed to be the standard FMC carrier board for beam instrumentation front-ends.

It is designed to operate close to beam lines in fast data acquisition systems (see Fig. 5.4 left). GEFE is conceived to work together with the VFC-HD board through a GBT link. This is a radiation-tolerant board that features the GBTx ASIC and VTRx transceiver following the Rad-hard optical link standard for GBT links. It is equipped with a ProAsic3 FPGA, mainly used as an interface between the FMC connector and the GBTx ASIC. The board contains the minimum active components possible and has been fully designed with radiation-tolerant components by design (as the GBT chipset or FEASTMP regulators) and radiation-characterised Commercial Off-The-Shelf (COTS) components. The radiation hardness of this board is limited by the FPGA, specified for TID up to 750Gy [115].

5.1.3. Readout ASICs

The acquisition system performance would be strongly linked to the readout ASIC responsible of detector digitisation and the dynamic range coverage technique on scope. Estimations for pCVD diamond detectors based on previous simulations specify a required dynamic range of 1-1e^6 MIPs, translated into charge results in 3fC to 3nC per bunch. The fast timing of diamond detector pulsed signals (2 ns FWHM) and the repetition frequency determined by nominal LHC beams (40Mhz) suggest analog signal integration with 25ns periods as the most optimal strategy in terms of data compression w.r.t direct ADC digitisation. This last approach would require very fast data conversion rates (>1GSPS) to properly reconstruct the pulses signal, or the use of pulse shaping techniques for reduced acquisition rates (≈650 MSPS), which may lead to undesired bunch overlap and therefore bunch profile cross-talk.

The large dynamic range coverage strategies under evaluation are focused on two different approaches: a single channel readout with logarithmic encoding, or a multi-channel readout splitting the detector signal dynamics on several linear channels with different gain/attenuation levels. The readout ASICS required must be radiation-hard (up to TID=1KGy) linear/logarithmic integrators, working at 40 MHz with no dead-time and able to resolve at least signals in the order of 1-7fC. QIE10 and ICECAL V3 detailed on this section were found as the most suitable readout ASICs candidates to evaluate for diamond detector readout matching the system requirements while at the same time kept compatibility with traditional PMTs.

5.1.3.1. QIE10

The QIE10 (Charge Integrator and Encoder) is an ASIC from the family of devices designed at Fermilab for measuring signals from photo-detectors. Its development is motivated by the phase 1 and 2 of the CMS hadronic calorimeter and Atlas TileCal detectors upgrade [120] [121]. The QIE10 integrates and digitalizes negative input current pulses with an effective rate of 25 ns periods. This is accomplished by using 4 integrator circuits operating in parallel with a different phase, each integrator circuit requires 100 ns to process its 25 ns integral.

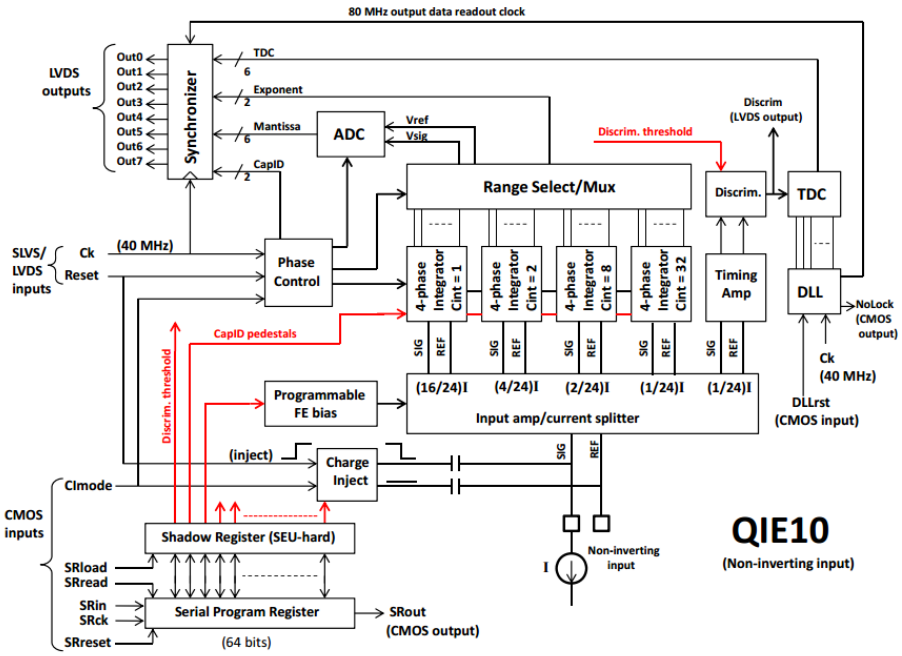

Figure 5.5 – QIE10 Schematic of main parts and pipelined operations [122].

Each QIE10 contains a single channel with 17 bits dynamic range, 3.2fC sensitivity and saturation at 340pC, logarithmically encoded into 8 bits (6 bits of mantissa and 2 range bits). This scheme provides a floating point dead-timeless integration and digitalization of the input charge at an effective rate of 40 MHz. Its logarithmic behaviour guarantees a constant quantification error 1%. The acquisition dynamics are covered by automatically switching between 16 linear resolution levels (spitted in a total of 4 ranges with 4 sub-ranges in each). This logarithmic response is accomplished by two parts. First, the input current is spitted into four logarithmically weighted ranges by means of a current splitter, each range integrates the resulting current fractions into separate capacitors by using gated integrators. The second part of the response is due to a nonlinear fast 6 bit ADC whose transfer function consists in 4 linear slopes. Different internal parameters can be set-up by means of a 64 bits programmable register. The ASIC ADC charge and TDC data is given digitally through 8 DDR LVDS lines at 40Mhz (80Mhz effective rate) and a LVDS clock line. Figure 5.5 shows a schematic of the QIE10 structure.

The QIE10 is fabricated in a 350 nm SiGe process, providing intrinsic hardness against ionising radiation. First irradiations showed no degradation on the ASIC performance up to a total ionisation dose (TID) of 520 Gy with only 2 single events upsets (SEU) observed when the board was exposed to 6e12 p/cm2 [123]. Further studies detected radiation-induced pedestal drift at a TID $\approx$ 2.50 KGy and critical failure about 2.70 kGy [124].

The nominal 8 bits response the QIE10 for its input dynamics is shown in Fig. 5.6, together with a simulated digitalization of a Gaussian profile (digitalization slope changes with signal amplitude). Both cases show the associated quantization error δ, defined as:

$$\delta = \frac{1}{\sqrt{12}}\left(\frac{S_i}{q_i}\right) \tag{5.1}$$

where S_i is the bin sensitivity and q_i is the central value of the bin, expressed in charge.

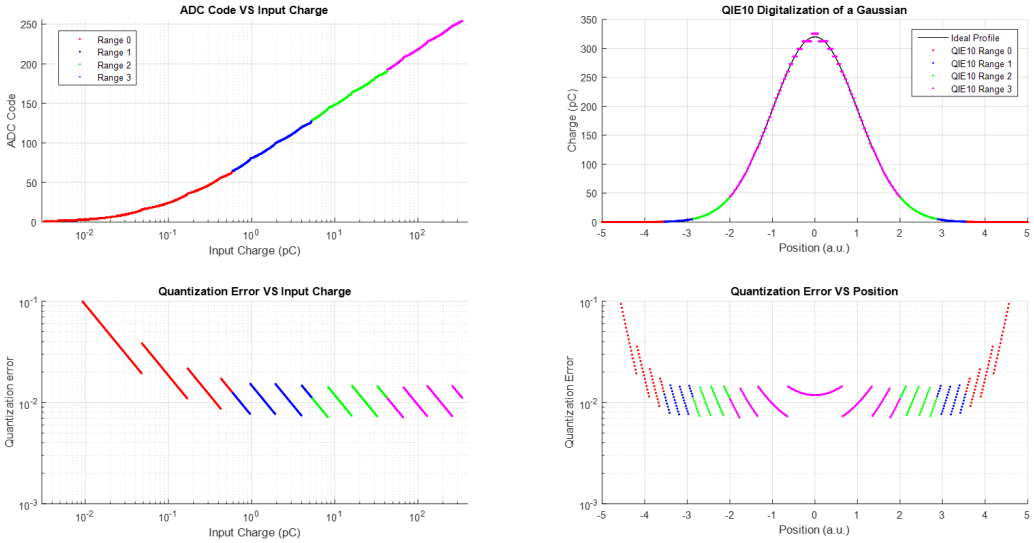

Figure 5.6 – Theoretical QIE10 Digitisation scheme and quantization error (left top and bottom) and a QIE10 digitised Gaussian profile with its quantization error (right top and bottom) with the different ranges highlighted in colours.

The impact of the QIE10 logarithmic encoding was evaluated to check for systematic or random error contributions on the beam width determination. The simulations shown in section 4.4.2 were reproduced by considering the theoretical QIE10 digitisation scheme. As depicted on Fig. 5.7, the results under same circumstances shows different results when including the QIE10 behaviour (note an increase of both, systematic and random errors).

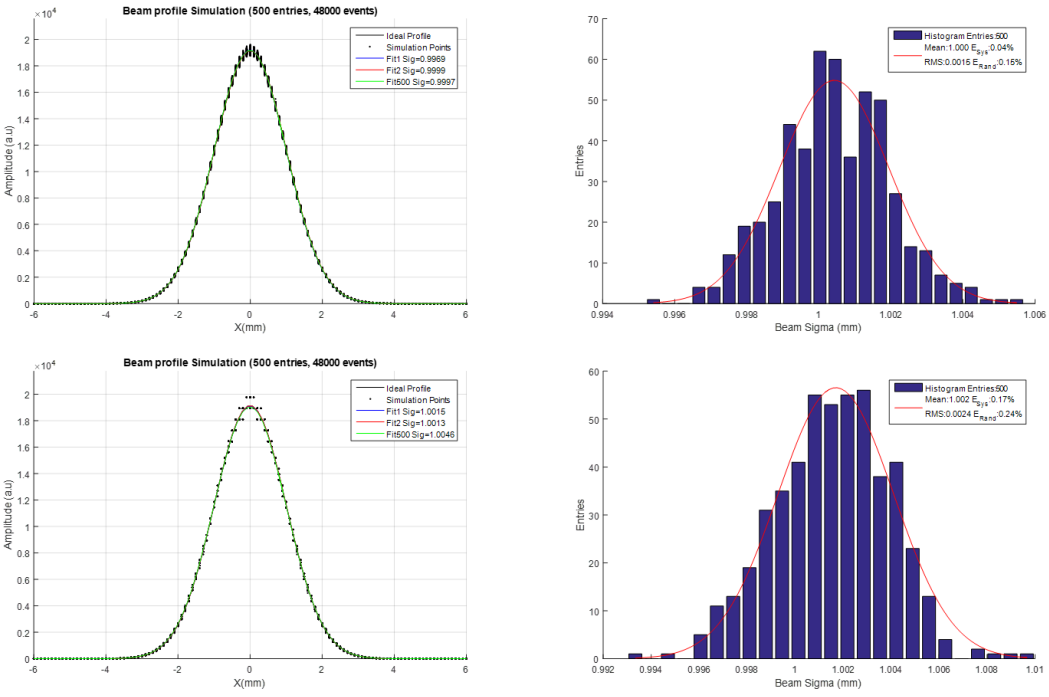

Figure 5.7 – Comparison of statistical and systematic errors obtained for 500 simulation profiles at 10 bins/sigma and 48000 events, nominal results on top and results with QIE10 digitisation scheme on bottom.

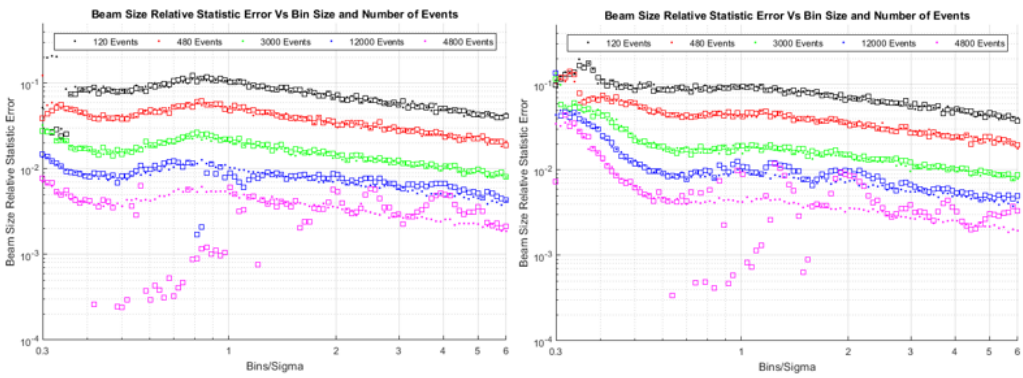

Figure 5.8 – QIE10 digitalization algorithm impact on Beam Wire Scanner **random error** as function of number of points per sigma and primary events for beam at the bin centre (left) and bin edge (right). Nominal results (points) versus results with QIE10 (squares).

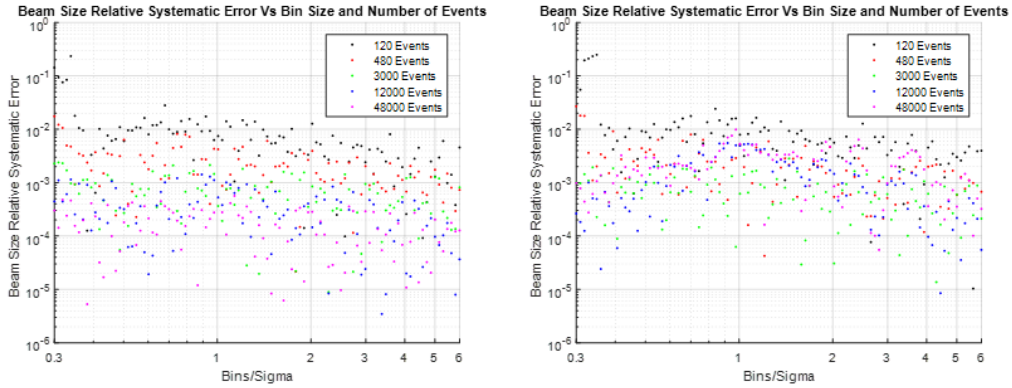

Figure 5.9 – QIE10 digitalization algorithm impact on Beam Wire Scanner **systematic error** as function of number of points per sigma and primary events for beam at the bin centre. Nominal results (left) versus QIE10 (right).

An analysis of the simulation results is provided in Fig. 5.8 and 5.9. The results suggest that, as expected, when the amplitude uncertainty due to the number of events is small enough the quantization effect of the QIE10 dominates on the amplitude incertitude (12000 or 48000 events on Fig. 5.8). On smaller number of events the quantization impact remains negligible (120, 480 and 3000 events). Independently of the number of events, the systematic beam width error induced by the QIE10 is in the order of 0.5% within the range 1-6 bins per sigma. The encoding algorithm is also degrading the expected random error, increasing it in some cases up to another 0.5% for the range under study. With such random/systematic errors this ASIC is on the limit of the specifications given for the LIU-BWS highlighted on chapter 4. With a beam sigma incertitude in the order of 0.5%, emittance determination incertitude would be translated into 1%. However, due to the high dynamic range coverage this ASIC remains as a very attractive candidate for evaluation with pCVD diamond detectors.

5.1.3.2. ICECAL V3

The ICECAL V3 is a radiation hard dead-timeless integrator ASIC developed by the university of Barcelona intended to be used for PMT readout in the framework of the LHCb calorimeters upgrade [125]. Each ICECAL V3 features 4 analog channels with 12 bits dynamic range each, 4fc sensitivity and saturation around 16pC. Its output signal is a differential voltage proportional to the integrated current over 25 ns windows that must be digitalized

with an external ADC. This ASIC is designed with the same technology as the QIE10 (AMS 0.35µm SiGe BiCMOS) for enhanced radiation hardness.

For dead-timeless operation, each of the channels consists of two fully differential interleaved sub-channels with switched integrators. A 50 ns refresh cycle is required for each sub-channel while working in opposite phases (as one integrates the other discharges). After multiplexing the sub-channels output, the ASIC provides an effective 25 ns output rate. This technique was successfully applied in the current BWS generation, with an integrator ASIC from the LHCb pre-shower [126]. ICECAL V3 also includes dedicated delay locked loops (DLLs) capable of phase shifting in steps of 1 ns for channels synchronization and triple modular redundancy configuration registers, accessible through a SPI interface to adjust key parameters of its operation. The detailed ASIC schematic is shown on Fig. 5.10.

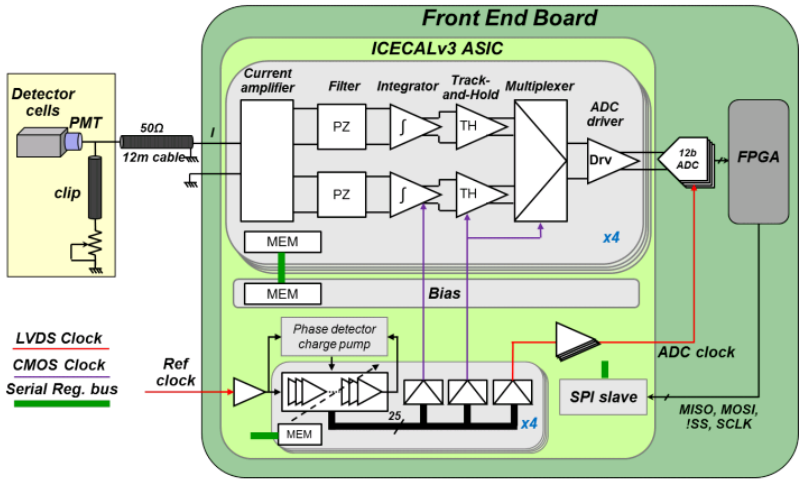

Figure 5.10 – ICECAL V3 architecture schematic and connectivity interfaces [127].

An active cooled input termination with 50 Ω impedance and a differential internal architecture are used for low noise operation. The input stage includes pole zero filters to shape the input current pulses. Its analog outputs are differential, with a maximum voltage swing $V_{diff} = 2V_{pp}$ and a common mode voltage $V_{cm} = 1.5V$.

Table 5.1 collects a summary of the main parameters of the ASICs under study:

Table 5.1 – QIE10 and ICECAL V3 main specifications

ASICs SPECIFICATIONS		
	QIE10	**ICECAL V3**
Dynamic Range	3.2fC - 340pC (10^5)	4fC - 16pC (10^3)
Integration Window	25ns (40Mhz)	
Channels per ASIC	1	4
Input Impedance	50Ω	
Dead-timeless	Yes	
Number of bits	8	12 (ADC Dependent)
Quantification Error	≈ 1%	«1% (ADC Dependent)
Linearity Error	≈ 1% (Logarithmic)	<1%
TDC Capability	Yes	No
Radiation Resistance (TID)	≈ 0.5kGy	*
ASIC Technology	AMS SiGeBiCMOS 0.35μm	
Designer Entity	Fermilab for CMS/ATLAS	U.Barcelona for LHCb

5.1.4. Radiation Hard Optical Link

The CERN's "Radiation Hard Optical Link project" aims the standardisation of a bi-directional optical link with a deterministic latency for use on the LHC and injectors upgrade programs. The link is capable of providing data transmission, timing distribution, trigger and control between on-detector and off-detector electronics. The project is divided in several different parts (the GBT, Versatile Link and GBT-FPGA projects) that provide the required infrastructure for the development of the optical link. Radiation hardness the link is specified to be ≈1 MGy.

Custom rad-hard chipset developed in the GBT project drive optical receivers/ transmitters, protocol encoding and communication with the LHC experiments readout ASICS. Opto-electronic transceiver modules and radiation hard optical fibres are procured by the Versatile Link project. On counting room (radiation free environment) the link implementation is based on with COTS components and FPGAs for protocol encoding/decoding. The GBT-FPGA project procures the FPGA firmware to implement the GBT core. Figure 5.11 shows the link architecture.

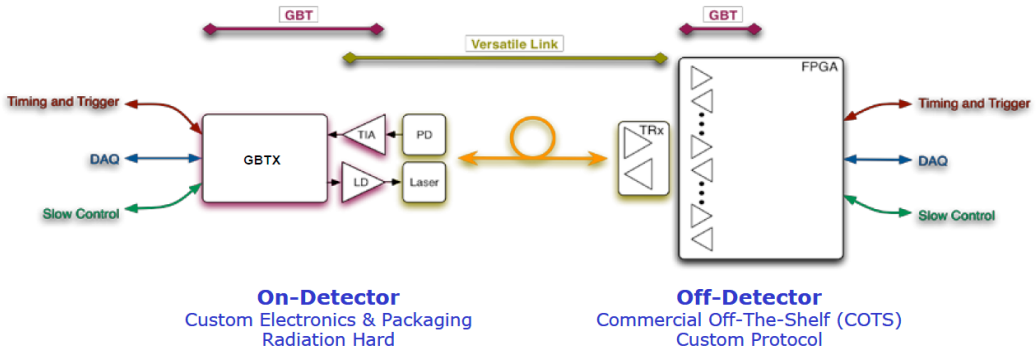

Figure 5.11 – Radiation-Hard optical link architecture.

The radiation-hard chipset developed by GBT project includes GBTIA (a transimpedace amplifier for optical receiver), GBTLD (a laser driver), GBT-SCA (a slow control adapter ASIC), and the core component of the whole radiation-hard optical link, the GBTx ASIC.

GBTx is a radiation-hard 4.8 Gbps serializer/deserializer able to encode/decode data into the GBT protocol. This ASIC uses TMR techniques to palliate SSE and converts the input data received from front-end electronics (experiments readout ASICS) into a serial data stream with a selectable format (GBT, 8b/10b or Wide frame), allowing 3.2-4.48 Gb/s of user bandwidth. It also de-serializes the incoming data transmitted form the counting room to perform control actions on the front-end electronics. The ASIC Clock and Data Recovery (CDR) system recovers the main link clock frequency with deterministic phase and latency. It is capable of providing different clocks to the front-end (40, 80, 160 Mhz), in synchronization with the main LHC/SPS 40 Mhz. GBTx interfacing with front-end readout logic is performed through bi-directional ports called "e-links". The e-links transmit/receive data in DDR fashion at three possible data rates 80,160 and 320Mbps. The GBTx ASIC would be the only piece of digital logic actually needed to operate a front-end (apart of readout electronics), minimising the need of FPGAs under radiation.

5.1.4.1. The GBT frame

The GBT format is the preferred standard on the Radiation hard optical link, it consists on frames of 120 bits transmitted every 25 ns (40 MHz), meaning 4.8 Gbps effective link speed. This frame consist of a header, control bits (IC and EC), user data and forward error correction (FEC) fields distributed as shown in Fig. 5.12. GBT mode allows 3.2 Gbps for user bandwidth, that can be extended to 3.36 Gbps using EC and IC fields for data transmission.

SSE happening on the GBTx itself are palliated by its TMR logic design, however, SEE produced on the transceiver modules might still introduce errors on the GBT frames. Among the different transmission modes, the GBT mode is the most attractive in terms of security and SEE immunity since FEC field allows error correction. Wide frame sacrifices the FEC field to provide a higher effective user data bandwidth (4.48Gbps), allowing 112 bits for user data per frame.

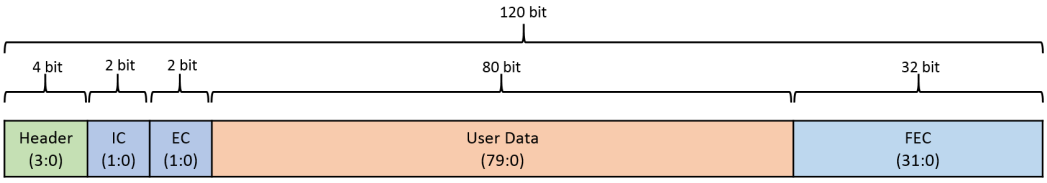

Figure 5.12 – GBT frame structure.

Data is transmitted over the optical fibre DC-balanced, this is ensured by scrambling the data contained on the "slow control" and "user data" fields. To obtain forward error correction codes, the scrambled data and the header are Red-Solomon encoded before serialisation. The process of line encoding-decoding is shown on Fig. 5.13

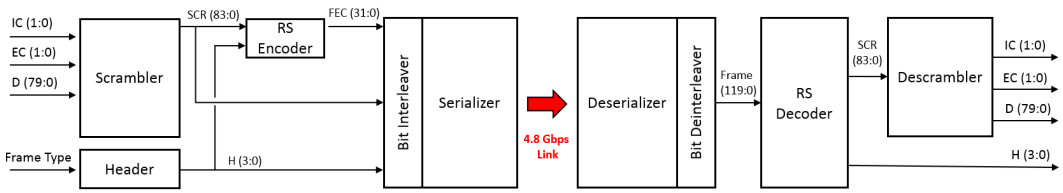

Figure 5.13 – GBT mode encoding-decoding schematic

5.2. Proof-of-concept prototypes

A couple of prototypes were developed to proof the concept with the main purpose to validate the improvements on signal integrity, noise reduction and dynamic range coverage with upgraded electronics. Unfortunately, many of the main components, that define the system architecture, were in a very early stage of development or unavailable for users at the moment of this thesis developments. The only parts available were the VTRx transceiver, GBT-FPGA firmware for some supported SRAM-based FPGAs and pre-series ASIC samples of QIE10 and ICECAL V3, kindly provided by Fermilab and University of Barcelona respectively.

To bypass the lack of components, and procure a functional front-end prototype, it was decided to emulate the GBTx. The base-line solution consisted on using an FPGA, with embedded gigabit transceivers, and the firmware implementation of the GBT core.

Tunnel environmental conditions require a radiation-tolerant design and careful FPGA technology choice. The prototype architecture is shown in Fig. 5.14, where a custom front-end is placed on radiation areas and a FPGA development kit acts as back-end system.

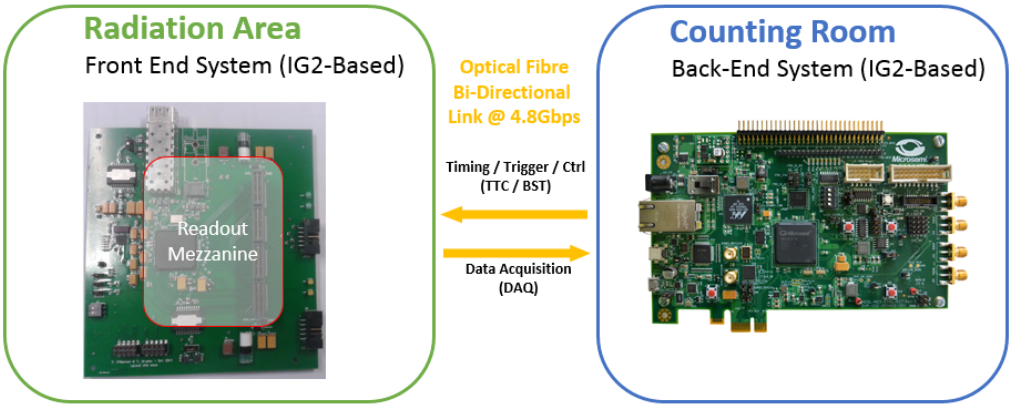

Figure 5.14 – Proof-of-concept system architecture schematic

5.2.1. Front-End implementation

The trends in high energy physics (HEP) concerning FPGA usage (SRAM and Flash-Based) consist on the characterisation of commercial devices under radiation, and the implementation of scrubbing and TMR logic design for SEE mitigation [128]. The power and capabilities that newer technologies offer on such re-programmable devices (high speed links for increased data readout, PLLs for clock management, DSP blocks for data compression... etc.) is increasing the interest of using FPGAs for front-end systems in particle physics. CERN experiments already feature FPGAs in radiation areas and their number is foreseen to increase with upgrade plans [129].

FPGA technology choice for operation under radiation is strongly dependent on the application, radiation levels and mitigation techniques implemented. The characteristics of flash-based cells on FPGAs offers a much higher radiation-induced SEE immunity in the configuration memory when compared with SRAM based FPGAs [130] [131]. The implementation of mitigation techniques on Flash-based FPGAs is not as critical as on SRAM-based. Irradiation campaigns with Flash-based FPGAS, such as ProAsic3 and Igloo families from Microsemi (formerly ACTEL), asses the usage of this technology when exposed to moderate radiation levels around 200-900Gy [132] [133].

The Microsemi Igloo2 was the chosen FPGA for front-end developments, this is the first Flash-based FPGA with embedded gigabit transceivers available on the market. CMS also chose this specific FPGA family for the CMS Hadron Calorimeter (HCAL) electronics upgrade, including HF and HB/HE detector acquisition systems [134].

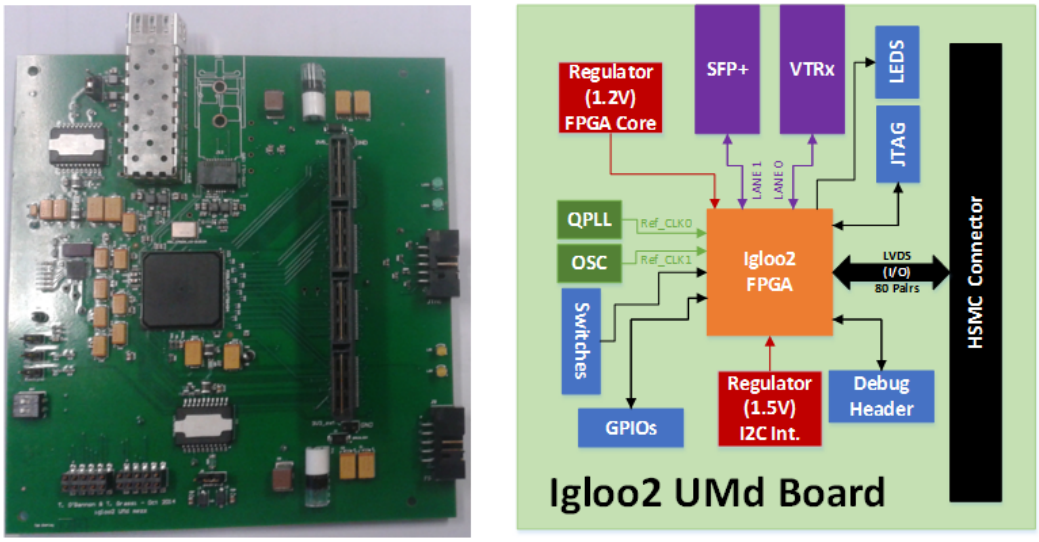

Figure 5.15 – Igloo2 Umd Mezzanine (left) and schematic (right).

The Igloo2 UMd mezzanine board, intended for the CMS HCAL upgrade, was the board used in our project as substitute of GEFE (see Fig.,5.15). This is a radiation tolerant board intended to work joint with the CMS HCAL ngCCM and it is designed to provide a bi-directional GBT link for slow control and LHC 40MHz timing distribution [135]. A collaboration started this way between CMS and BE-BI concerning design reviews, board procurement and a common firmware development.

Irradiation tests performed on Igloo2 shown critical FPGA logic failure at 1 KGy [136], no effects were observed for a TID $\approx$ 100 Gy on the high speed serializer/deserializer (SERDES), however at this level the programming circuitry was seriously damaged [137]. Critical SERDES failure was found to be around 200 Gy [138]. Being still far from the final system specifications (1 kGy), and with the total TID constrained by the FPGA SERDES ($<$200 Gy), this value was considered acceptable for a proof-of-concept prototype envisaging a next iteration with final components (GEFE + VFC).

The front-end electronic developments covered in this work were developed around the Igloo2 UMD board. Two mezzanine boards were designed and fabricated for testing the ICECAL and QIE10 readout ASICS and the GBT-FPGA code was migrated from Xilinx FPGA to this specific Microsemi model. This work allowed, for the first time, to drive the GBT link with a flash-based FPGA. The new GBT core was later distributed to CMS and adapted for use in their application.

5.2.1.1. The GBT core on an Igloo2 Flash-Based FPGA

The GBT-FPGA core provides a custom physical coding sub-layer (PCS) to drive the GBT protocol in FPGAs. The code is available and officially supported by CERN for different FPGAs from Xilinx and Altera families in two different flavours, "Standard" (STD) and "Latency-Optimized" (LATOP). The STD implementation is targeted for non-time critical applications. The LATOP version ensures a fixed and deterministic latency on the link [139], its use is intended for Timing Trigger and Control (TTC) on HEP experiments. The determinism of clock phase and data delay is provided through a careful design of clock domain crossings and by using clock alignment techniques. Figure 5.16 shows a schematic of the GBT core.

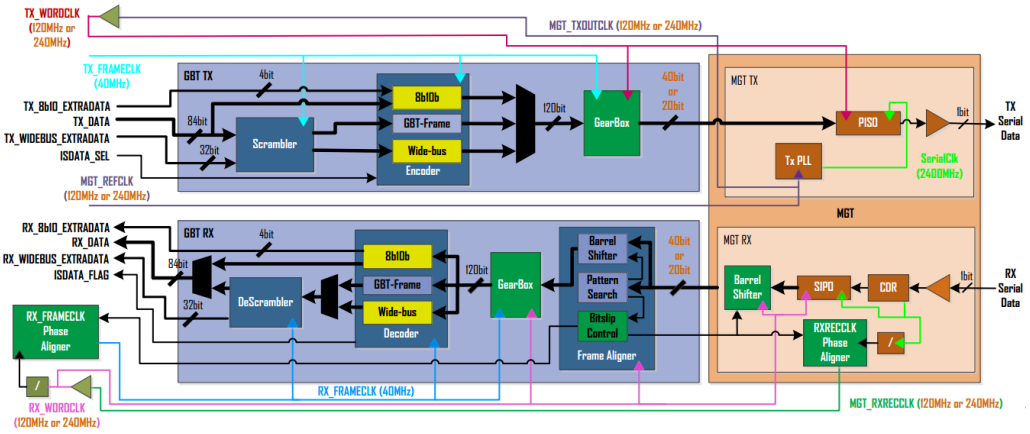

Figure 5.16 – Schematic of a GBT core implementation with critical components for latency deterministic highlighted in green [140].

The GBT core consists of three main blocks: Transmitter (GBT_TX that scrambles and encodes the transmitted parallel data), Multi-gigabit transceiver (MGT that serializes, transmits, receives and de-serializes the data) and Receiver (GBT_RX that aligns, decodes and de-scrambles the incoming data stream). The GBT core is distributed as generic VHDL modules with some vendor and device specific modules (specific IP cores for transceivers, PLLs, memories... etc).

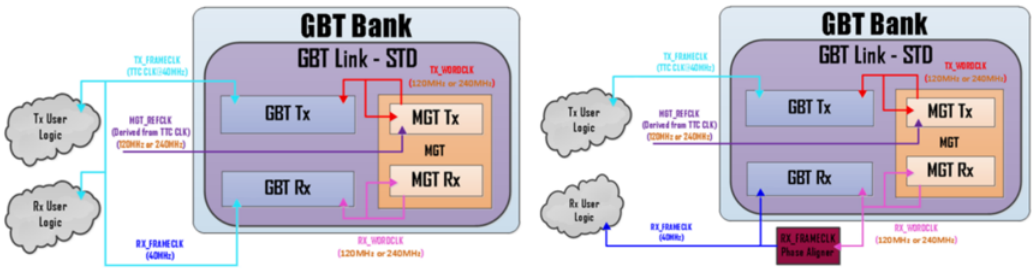

Figure 5.17 – Simplified clocking schemes of the GBT core for STD (left) and LATOP (right) versions [139].

The LATOP version features four different clock domains (see Fig. 5.17 right), two are TX/RX frame clocks (40 MHz) and other two are TX/Rx word clocks (240 or 120 MHz). For the STD version there are three clock domains, TX and RX frame clocks can be shared since clock domain crossing are implemented with elastic FIFOs. On the transmitter part, scrambled GBT frames (120 bits) are generated at 40 Mhz with the TX_FRAMECLK domain (40Mhz bunch clock in LHC experiments). The GBT frame need to be split in smaller words to match the size of the FPGA gigabit transceivers parallel bus, and transmitted at a higher rate (TX_WORDCLK) to keep the effective 4.8Gbps.

Clock domain crossing between frame/word clocks (and vice-versa) are managed by the "Gearbox" modules. On GBT STD version the TX and RX Gearboxes are implemented with a dual port RAM memories (vendor specific). On the LATOP version this component is register-based, this way the latency is minimised, and the number of clock cycles for the data to go through is constant. On the other hand, metastability problems may be faced, so the phase of frame and word clocks needs to be properly constrained and extra logic added to implement a phase alignment mechanism for calibration purposes.

In our design, the front-end will be continuously performing acquisitions and sending data to the back-end system (Back-End ← Front-End, upstreams) at 40 Mhz. Control actions are received through the link (Back-End → Front-End, downstreams) to set-up some ASIC

parameters and for Front-End (FE) synchronisation. The 40 Mhz LHC/SPS clock is feed on the Back-end (BE) system, propagated "downstreams" through the GBT link and finally recovered on the FE system. The recovered clock (RX_FRAME_CLK) will be used as a digitalization clock for the FE ASIC, in synchronisation with the bunch crossing frequency. On this scenario, every time the link is established, the recovered clock on the front-end must always be on the phase respect the bunch crossing to place the ASICs integrating windows at the same location respect to the bunch. From the back-end point of view it is also required that the data arrives with a deterministic latency to properly tag the incoming data frames with their corresponding bunch identifier. Thus, the LATOP version is targeted for both sides of the link.

- **Implementation on Igloo2**

Igloo2 evaluation kits, as shown in Fig. 5.18, were used for the migration of the GBT core. The FPGA included on this board contains a couple of clock conditioning circuits (CCC or PLLs) for user applications and a single SERDES with its 4 lanes configured as shown in Fig. 5.18 right. Loopback tests and connection with optical transceivers is possible on Lane 2 through SMA connectors. The GBT-FPGA code distributed for Xilinx Virtex6 FPGA was taken for migration given the similarities with the Igloo2 serializers.

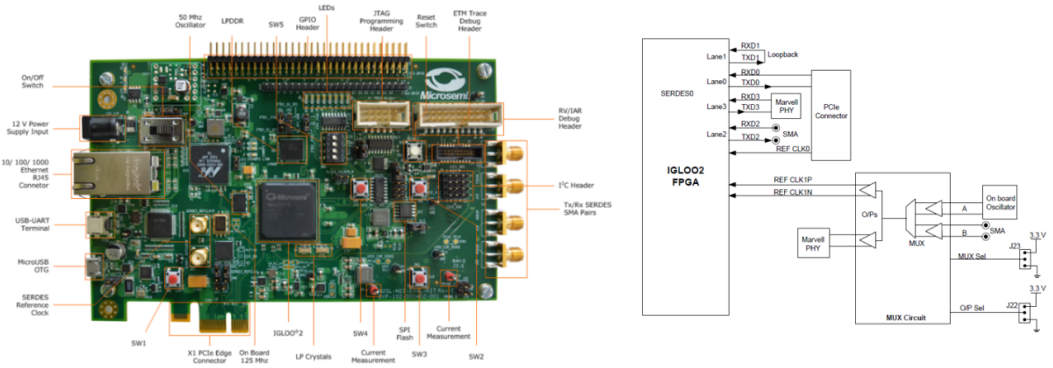

Figure 5.18 – Microsemi Igloo2 Evaluation Kit (left) and SERDES clocking and lanes connections (right) [141].

The migration process started with the STD version and incrementally adapted to reach the LATOP version.

- **GBT STD version**

Minor modifications were required on the GBT_TX and GBT_RX "Gearbox" modules for compatibility with Igloo2. These clock domain crossings are based on dual SRAM memories. Figure 5.19 shows the schematic structure of the TX_Gearbox along with the Igloo2 dual port RAM memory configuration used for the GBT_TX.

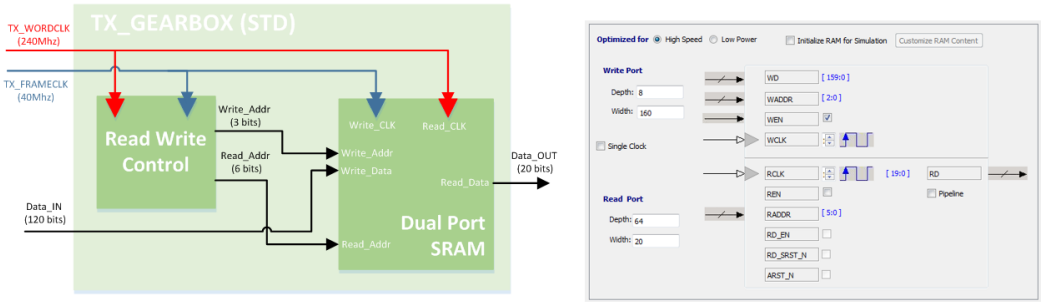

Figure 5.19 – Schematic of TX_Gearbox in GBT STD version (left) and Igloo2 Dual Port SRAM used.

The modifications where tested in simulation and hardware. The GBT_TX and GBT_RX modules where tied together, emulating a loopback test where the MGT was bypassed. Test data was provided through a pattern generator, which can generate dynamic or static data frames (84 bits). On this design an error checker looks for data corruption. In "dynamic data mode" the error checker predicts the expected data frame to be received based on previous frames. A couple of modules monitor the data bus and sets a flag (TX_Match_Flag and RX_Match_Flag) to 1 during a clock cycle when a specific data frame is detected. The delay between these flags provides an estimation of the system latency. The first tests used shared "Frame" and "Word" clocks on TX and RX domains. A schematic view of the test implementation is shown in Fig. 5.20.

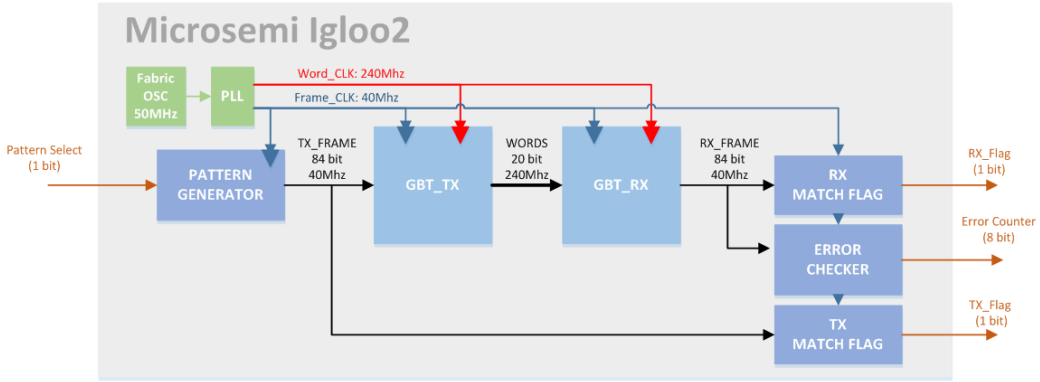

Figure 5.20 – Evaluation of the GBT_TX and GBT_RX modifications for Igloo2 compatibility (STD version).

The simulations shown successfully recovered frames with no errors and with an estimated latency around 314 ns, see Fig. 5.21.

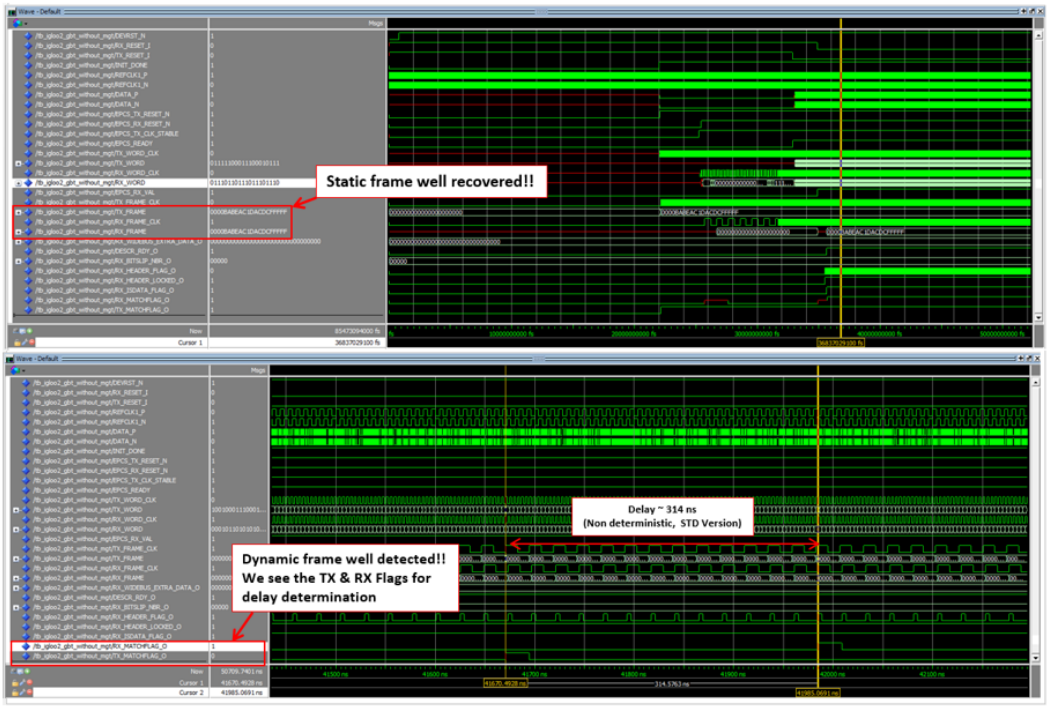

Figure 5.21 – Simulations on Mentor Graphics ModelSim for the test design shown on Figure 5.20.

In the hardware evaluation, TX_Match_Flag and RX_Match_Flag were routed to general purpose Input/Output pins (GPIO) and connected to a scope. Measurements agreed simulations, showing a data latency about 320 ns. The error counter was also checked through the JTAG programmer with Microsemi "Idenfity Debug Design", no errors were detected during data transmission.

The MGT inclusion required a deep understanding of the Igloo2 SERDES module to provide a proper configuration and integration with the GBT core. This module has integrated functions to support multiple protocols within the Igloo2 FPGA. The possible protocols include peripheral component interconnect express (PCIe) and ten gigabits attachment unit interface (XAUI). The user can implement custom high speed serial protocols bypassing these modules and directly accessing to the physical media attachment layer (PMA), this is done configuring the SERDES in external physical coding sublayer (EPCS) mode (see Fig. 5.22).

The Igloo2 SERDES is configured by a large number of internal registers. These registers can be dynamically accessed and configured while in operation through an advanced peripheral bus (APB) interface. Igloo2 FPGAs employ a dedicated module to initialise peripherals through APB and access the system controller. This module is known as High Performance Memory Subsystem (HPMS) and it is used for the SERDES initialisation after start-up.

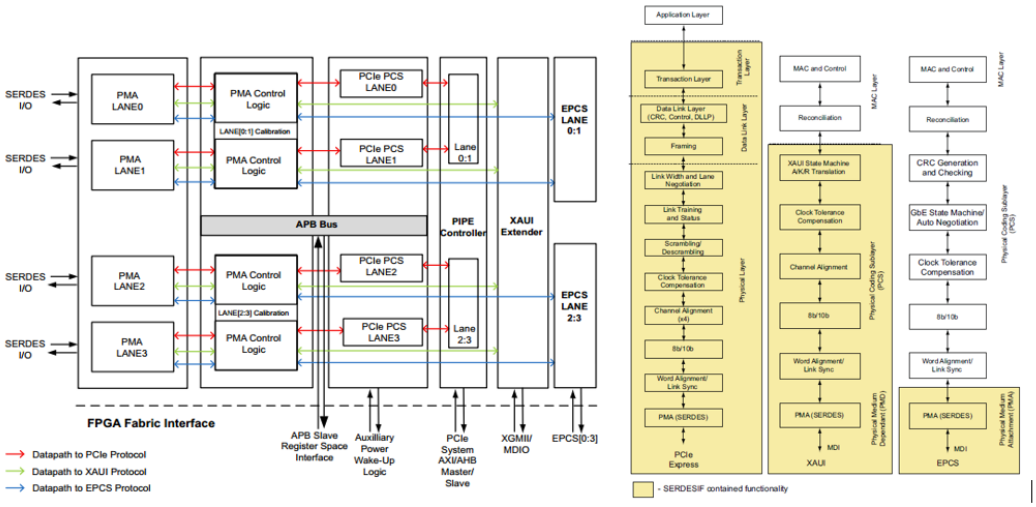

Figure 5.22 – Igloo2 SERDES data-path schematic (left) and contained functions in each configuration (right) [142].

The SERDES offers a total of 4 EPCS input-output interfaces, 4 differential pairs for high speed data transmission and another 4 for data reception corresponding to the 4 EPCS available lanes. APB interface is exposed to the fabric for connection with the HPMS. Figure 5.23 shows the input-output ports as well as high speed lines for Lane0.

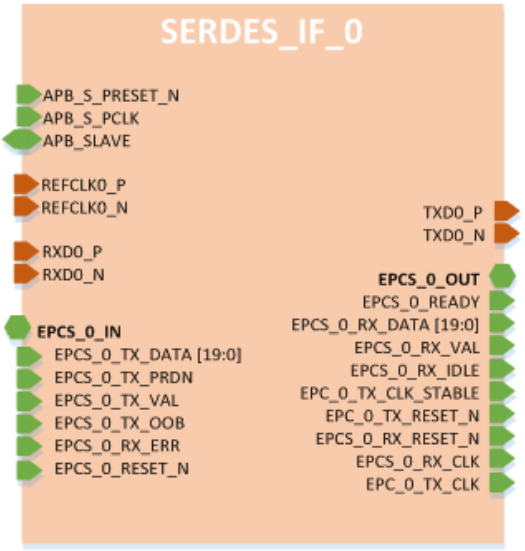

Figure 5.23 – SERDES interface ports when configured in EPCS mode.

At start-up, the SERDES module needs to be initialised with suitable register values, afterwards a specific initialization sequence is required. Initialization comprises a reset sequence, TX and RX PLLs clock locking and PMA impedance calibration on high speed lines.

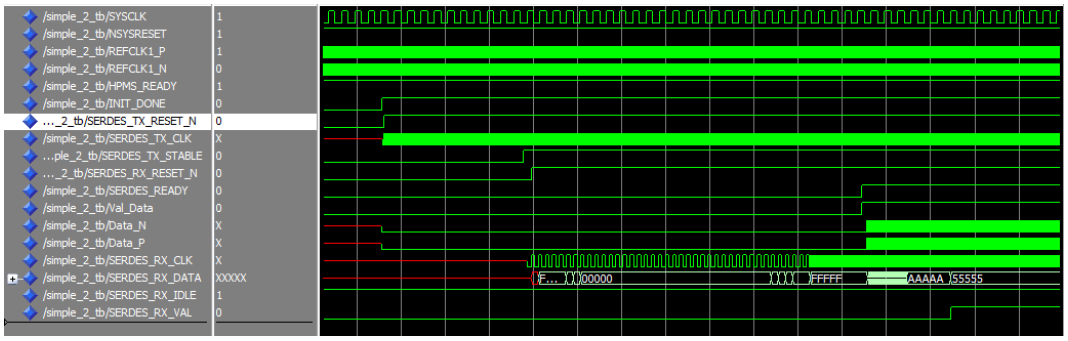

Figure 5.24 – SERDES Start-up sequence, TX PLL lock and RX CDR lock.

During data transmission, the data from the TX_DATA bus (20 bits) must be generated on the rising edge of TX_CLK, validity is notified with TX_DATA_VAL. Concerning data reception, RX_IDLE notifies if there is not data streaming on the bus (idle status). When the PMA macro detects incoming data on the bus, and the CDR PLL locks on the bit stream and RX_VAL is asserted, this condition is matched at the end of the simulation on Fig 5.24 and confirms a correct initialisation. On reading operations, RX_DATA must be sampled on the rising edge of RX_CLK while RX_VAL flag is asserted. Timing diagrams for TX/RX parallel bus shown in Fig. 5.25.

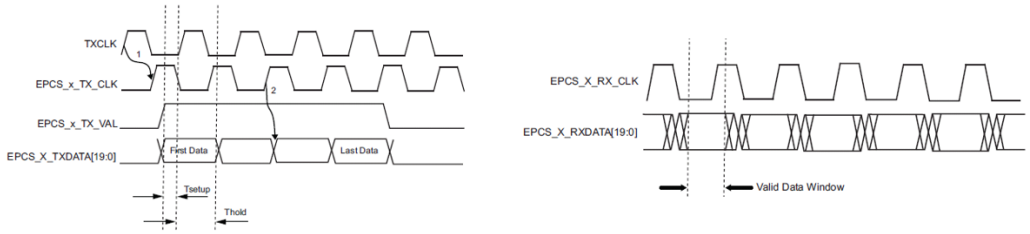

Figure 5.25 – EPCS Transmitter (left) and receiver (right) interfaces timing diagrams.

Timing closure is critical to interface the Igloo2 SERDES with the rest of the user logic (GBT_TX and GBT_RX), specially when running the transceiver at high speeds (>3Gbps). A careful floor planning, interface design and clock constraints are needed to achieve good performance. On the RX interface, the RX_CLK incurs in a significant delay when routed to the FPGA main clock tree and back to the fabric flip flops. The same happens on the TX interface. On this large clock delays, setup and hold times might be violated. For a proper interface, clock and data delay must be correctly matched as in Fig. 5.25.

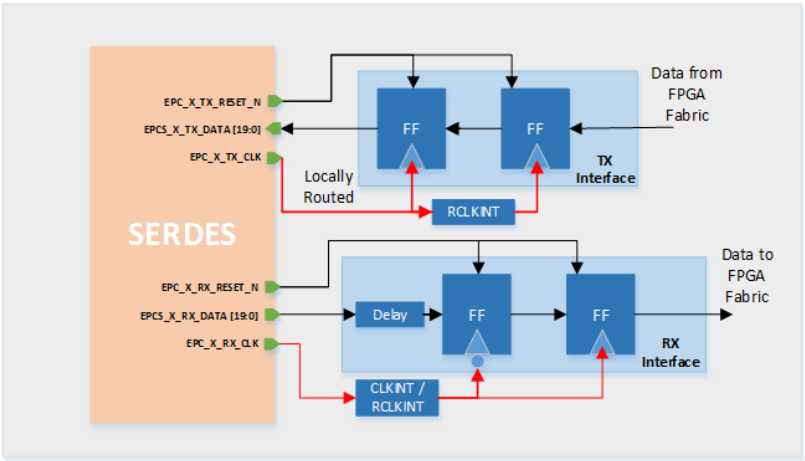

Figure 5.26 – Igloo2 SERDES interface with user logic for high speed designs.

To run the transceiver at 4.8Gbps, SERDES data lines, TX_Data and RX_Data, must be interfaced by means of a couple of flip-flops (FF) to pipeline the design. This allows placement flexibility to match timing constraints. High fan-out clock nets are automatically routed by the synthesis tool to the FPGA clock trees (clock buffers) in order to avoid data skew. However on this specific FPGA SERDES interface, clocks routing must be controlled given the internal FPGA structure and delays introduced by the clock tree. The synchronisation interface with data and clock routing is shown in Fig. 5.26.

The Igloo2 FPGA on the Dev.Kit (and on the Igloo2 UMd board) featured only two PLL. The GBT latency optimised version needs both PLL (one for transmitter another for receiver parts) in order to derive the frame clocks from the word clocks and perform clock alignment. If the HPMS is included, for SERDES initialisation, one of the user PLLs is assigned to the HPMS logic. To leave both PLL available for the GBT core, a custom APB interface was implemented to manage the SERDES initialisation. For debugging purposes, a universal Asynchronous Receiver-Transmitter (UART) interface was included and an expert application was developed. This way the status of critical GBT flags could be easily checked and control actions on the link were possible.

The SERDES initialiser module was simulated including the SERDES itself with a loop-back on its high speed TX and RX lines. Transmission-reception operations were successfully simulated at 4.8 Gbps. Simulations (Fig. 5.27), and hardware tests confirmed the desired SERDES behaviour.

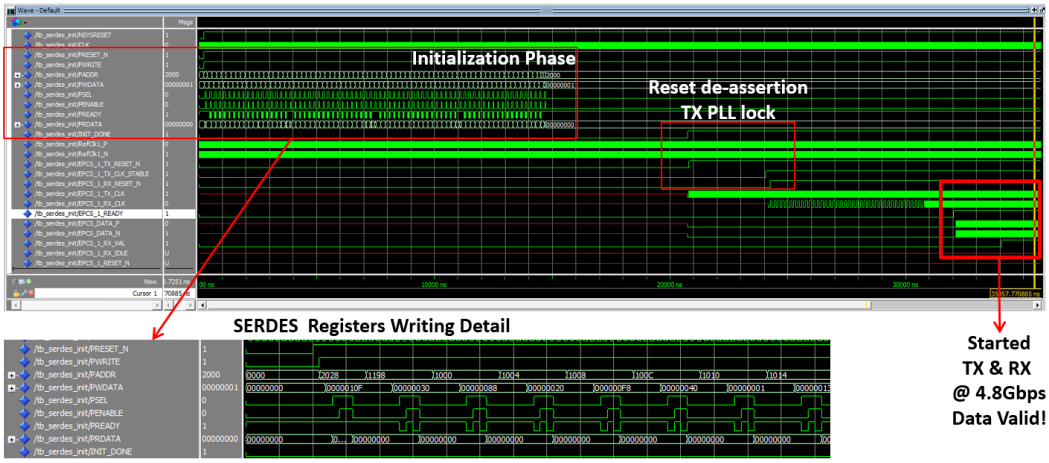

Figure 5.27 – Post-Synthesis simulations for SERDES initialization through custom APB interface.

The final implementation of the STD GBT core is shown in Fig. 5.28. All clocks interacting with the GBT core are derived from the SERDES REF_CLK (nominally 120 MHz). Frame and word clocks for transmitter and receiver remain independent, having 4 clock domains in prevision for the LATOP version. When a transmission is active between two boards, each of the TX_Word_CLK will continue synchronous with their local REF_CLK, however the receiver parts will lock on the bitstream present on the link, coming from the transmitter of the other board, thus RX_WORD_CLK will not be synchronous anymore with its local REF_CLK but with the REF_CLK from the other board.

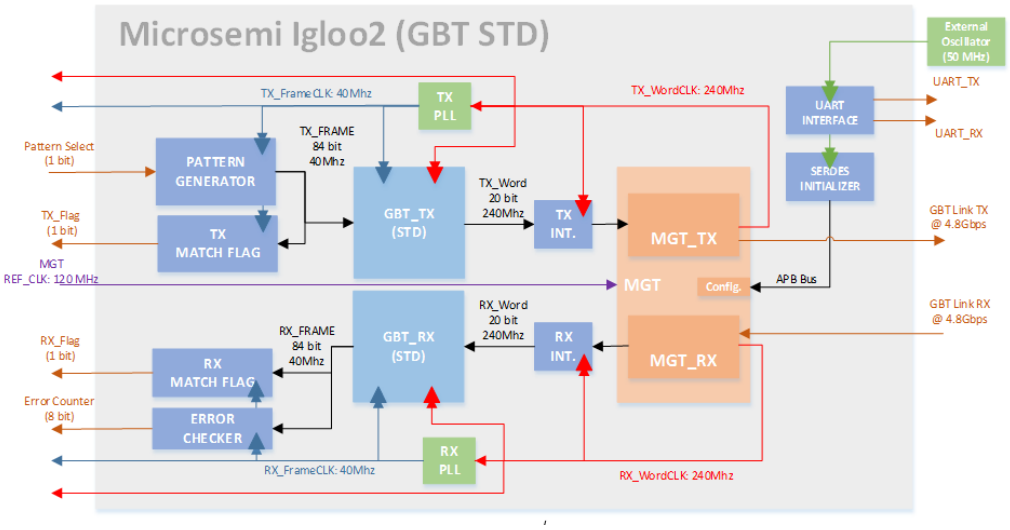

Figure 5.28 – GBT STD Core Implementation on Igloo2.

Hardware tests are shown in Fig. 5.29. Two Dev.Kits were tied together through the differential TX and RX high speed lines of the SERDES lane2 (side SMA connectors). They were physically connected to a PC with a USB to allow monitoring and control actions with the expert application. The link ran smoothly and the GBT STD core migration finished successfully.

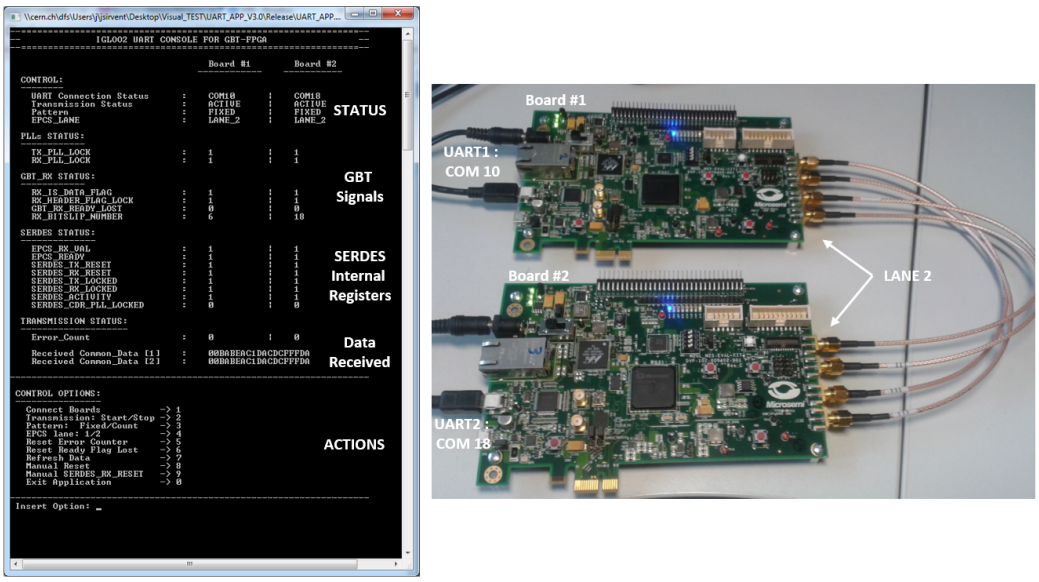

Figure 5.29 – Two Igloo2 Development Kits running the GBT STD core (right) and connected to a PC through UART_to_USB interface. Expert application (left) shows communication status, GBT and SERDES status registers.

The expert application monitors on the two boards the PLLs status, key flags and on the GBT_RX parts (such as bitslip_nbr, header_flag_lock or rx_isdata_flag) and the status of internal SERDES registers. Received data frames and error counter values are monitored to check data integrity. Control actions performed by the user include: start/stop the transmission, select the transmission pattern (fixed or counter), lane selection, reset the error counter and manual reset operations on the GBT core or the SERDES.

Several tests were performed with a scope and the expert application to study the phase of the different clock domains (all clocks were routed to GPIOs for debugging). Link latency

variations (using TX and RX match flags) were also measured every time the link was re-stablished. All measurements were taken after a GBT link reset.

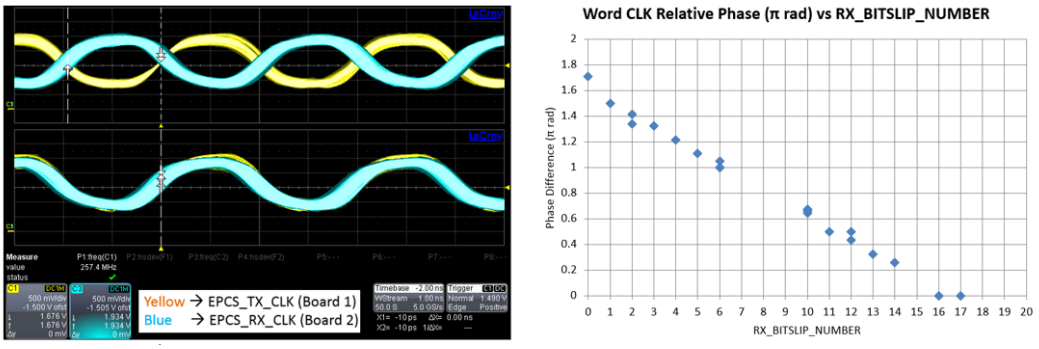

Figure 5.30 – Word_CLK phase relationship studies using scope cursors for TX (board 1) and RX (board 2) word clocks (left). Phase measurement results compared with the board 2 bitslip_nbr (right).

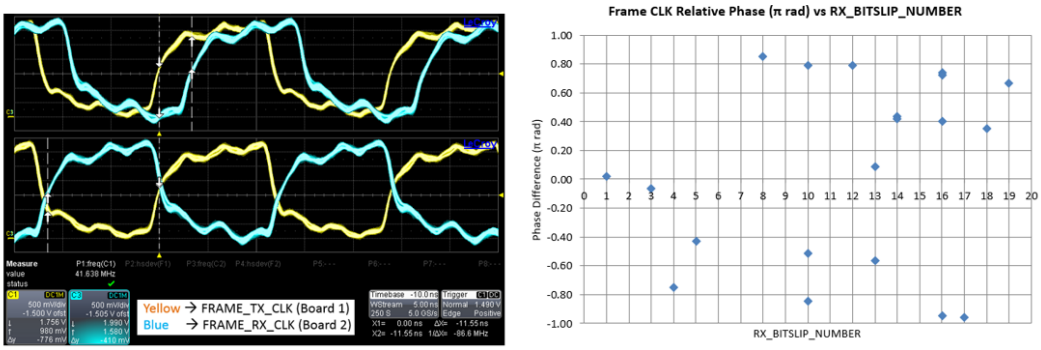

Figure 5.31 – Frame_CLK phase relationship studies using scope cursors for TX (board 1) and RX (board 2) frame clocks (left). Phase measurement results compared with the board 2 bitslip_nbr (right).

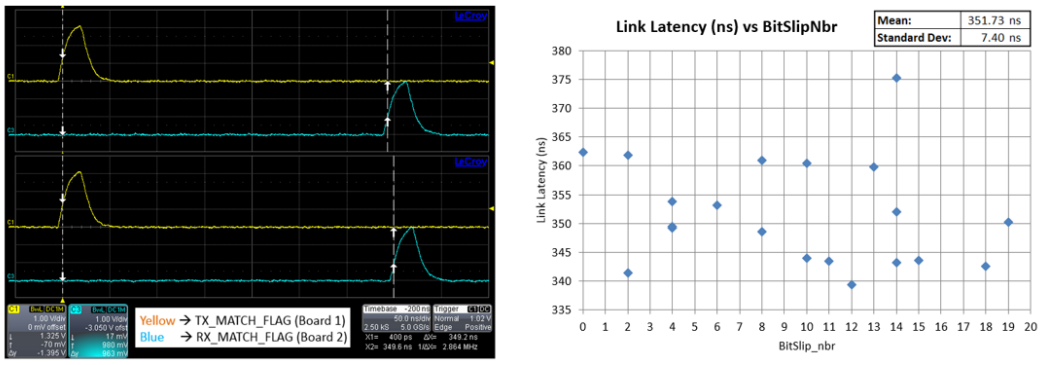

Figure 5.32 – Link latency studies for GBT STD version using scope cursors on TX (board 1) and RX (board 2) match flag (left), latency measurement results (right) compared with the board 2 bitslip_nbr.

The phase alignment between TX_WORD_CLK from board 1 and RX_WORD_CLK from board 2 shows a correlation with bitslip number (number of bit displacements for data header alignment), see Fig. 5.30. This shows that the data aligner provides a reliable indicator of the clocks phase difference for later clock alignment. When the RX CDR PLL is locked

of any possible bit of a word on the bitstream, the received data might be shifted, the data aligner shifts the data words on the positions specified by bitslip_nbr for a correct alignment.

No correlation with bitslip number is shown on the FRAME_CLK domains (see Fig. 5.31), the phase relationship is fully random, as expected since no clock alignment techniques were implemented. The RX_FRAME_CLK corresponds to the LHC clock recovered on the front-end, with the GBT STD version, its phase with respect to the clock on surface varies randomly every time the link is stablished.

Regarding data latency, the elasticity of the "Gearbox" SRAM memories, and the lack of clock alignment techniques leads to a random variation of data latency after each link start-up. Measurements nicely fit with the simulations previously presented, with a mean latency of 351 ns (simulations without MGT showed 320 ns). The data latency varied from 340 ns to 375 ns (35 ns incertitude) on the 20 measurements taken after a link restart (see Fig. 5.32).

- **GBT LATOP Version**

The register-based "Gearboxes" of the GBT LATOP version were included on the design as well as modifications on the clocking structure to provide a proper and deterministic LHC clock recovery.

The LHC/SPS clock propagation and the deterministic phase recovery on the FE system is FPGA dependent, given the specific clocking resources and MGT architecture. On the supported FPGAs of the GBT-FPGA project, the phase tuning of word_clks was possible, however this is not possible on the Igloo2 SERDES. The strategy followed for a deterministic clock recovery, based on rx_frame_clk alignment, is detailed on Figure 5.33.

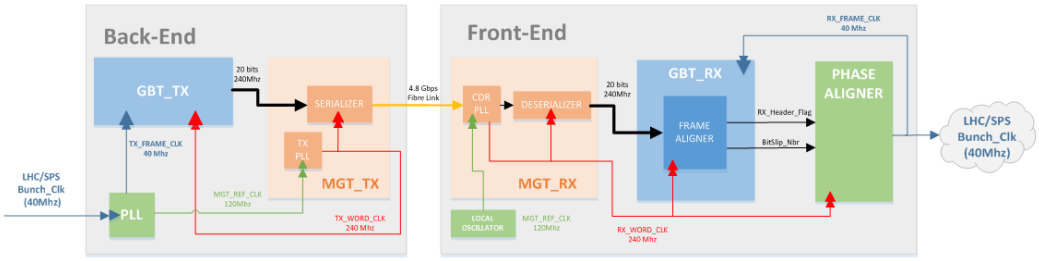

Figure 5.33 – LHC/SPS Clock propagation through GBT link and phase deterministic recovery on Front-End.

For the LATOP implementation, every clock is derived from a single source, in this case the LHC or SPS bunch 40 Mhz clocks. On the transmitter part of the back-end, the LHC clock is used for the 40 MHz TX_FRAME_CLK, and multiplied to provide a 120 MHz reference clock to the MGT. The MGT itself multiplies its reference clock by two to obtain the 240 MHz TX_WORD_CLK, used by the MGT serializer and part of the GBT_TX register-based "Gearbox" logic. The phase alignment of the transmitter clocks is automatically managed by the different PLLs of the design. The data deterministic latency on the GBT_TX is guaranteed by the LATOP "Gearbox".

The critical part is located on the FE system clock recovery. The MGT clock and data recovery (CDR) system recovers the 240 MHz (RX_WORD_CLOCK) from the 4.8Gbps bit stream, this clock is used for the de-serializer and the 240 MHz logic of the GBT_RX. The RX_WORDCLOCK can be randomly locked in any of the 20 possible bits of a word (as seen previously on the STD implementation). If a single PLL were used to derive the RX_FRAMECLK (40 MHz) from the RX_WORDCLK (240 MHz), its phase would be linked with the 20 possible phases of the RX_WORDCLK. In addition, the RX_FRAMECLK rising edge might fall in any of the 6 possible rising edges of the RX_WORDCLK per frame. On this situation, the recovered clock is synchronous with the original LHC clock but with 120 possible random phases every time the link is re-started. This situation was previously observed on

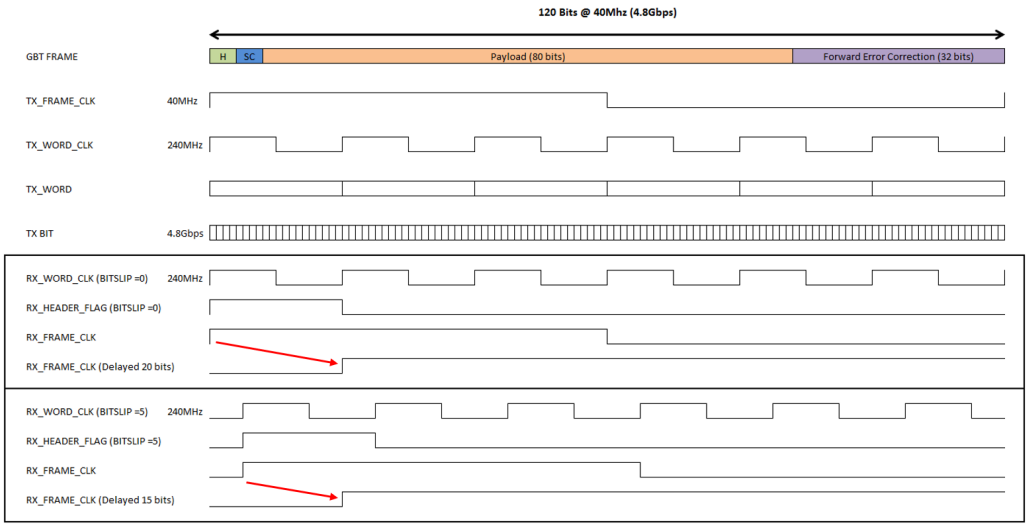

Figure 5.34 – GBT TX and RX Data and clocks schemes. RX_WORD_CLK and RX_HEADER_FLAG are shown for different BITSLIP_NBRs.

Fig. 5.31 and is not acceptable for our acquisition system. For a proper RX_FRAME_CLK phase alignment, the frame aligner module of the GBT_RX provides a couple of signals needed for a custom "Phase Aligner" module, these are RX_HEADER_FLAG and BITSLIP_NBR.

The RX_HEADER_FLAG signal is only active during a RX_WORDCLK clock cycle once the header word is detected. This signal can be used for PLL as a reference to set the 40MHz RX_FRAMECLK rising edge in the correct RX_WORDCLK rising edge (out of the 6 possible words). The BITSLIP_NBR is a 5 bits signal that notifies the performed bit displacement when aligning the word to match properly the header (0 to 19), this number is directly related with the phase of the RX_WORD_CLK w.r.t the first bit of the header. BitSlip_nbr can be used for a fine phase tuning of the RX_FRAME_CLK (delaying the clock) in order place its rising edge always on the same "GBT frame" bit. Figure 5.34 provides a clock and data schematic for a better understanding of the RX_WORD_CLK phase relationship with BITSLIP_NBR and RX_HEADER_FLAG behaviour, and the required delay on RX_FRAME_CLK to correctly place its rising edge.

The RX_FRAME_CLK phase aligner is implemented with a PLL, where RX_HEADER_FLAG is used as a 40 MHZ reference. The fine tuning of the output RX_FRAME_CLK clock is performed through programmable delay lines available on the clock conditioning circuit (CCC). The delay lines can be programmed through an APB interface, and allow a clock delay or advance up to 6.3 ns (total adjustment range 12.6 ns) in steps of 100 ps. The required adjustment range was 0-4 ns corresponding to one word_clk period.

Considering the usage of a register-based "Gearbox" for the RX clock domain crossing (CDC) on the receiver part, the code might face metastability issues, for certain bitslip_nbr, given the variable phase of RX_FRAME_CLK w.r.t RX_WORD_CLK. A workaround solution to avoid metastability and keep a deterministic clock phase and link latency was based on forcing the GBT_RX to always work on the same bitslip_nbr by resetting the GBT_RX and MGT until the desired value is matched. For this schema the rx_header_flag is still used as PLL reference and fine phase tuning avoided.

The front-end ASIC acquisitions follows the recovered LHC/SPS clock (RX_FRAME_CLK) in synchronization with the machine. Data entering the FPGA will follow the RX_FRAME_CLK clock domain, thus, to maintain uplink synchronization without elastic buffers, TX_FRAME_CLK must be derived from RX_FRAME_CLK. On the current design, TX_FRAME_CLK and RX_FRAME_CLK are the same physical clock (which simplifies front-end clocking schema). Provided that the GBT_TX LATOP "Gearbox" is register based, TX_WORD_CLK must

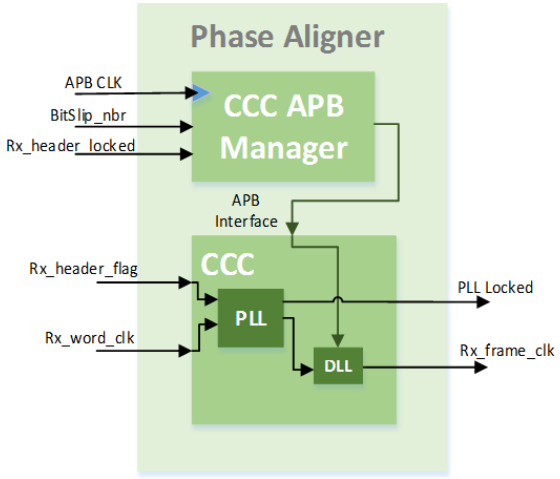

Figure 5.35 – Phase aligner for the RX_FRAME_CLK on Igloo2 for GBT LATOP version.

also be in synchronization with RX_WORD_CLK to keep data integrity. By default the MGT transmitter part uses the REF_CLK as reference for the TX_PLL, being asynchronous to the RX CDR PLL when locked on the bitstream. The SEREDES initializer module was configured to use the CDR PLL as reference for the TX PLL once the CDR is locked on the bitstream, which forces synchronization on the different clock domains.

For our GBT LATOP implementation schema, different clocking schemes are needed for FE and BE systems. Link synchronization is managed by the BE system downstreams by using the LHC/SPS clock as TX_FRAME_CLK and deriving the MGT REF_CLK from it to properly propagate the LHC/SPS through the link. On the FE system, clock is recovered and properly aligned to a deterministic phase, the transmitter part is forced to be synchronized with FE receiver when the MGT RX is locked on the bitstream. Finally, acquisitions are send upstreams in a latency deterministic fashion. The implementations for BE and FE systems are shown in Fig;5.36 and 5.37 respectively.

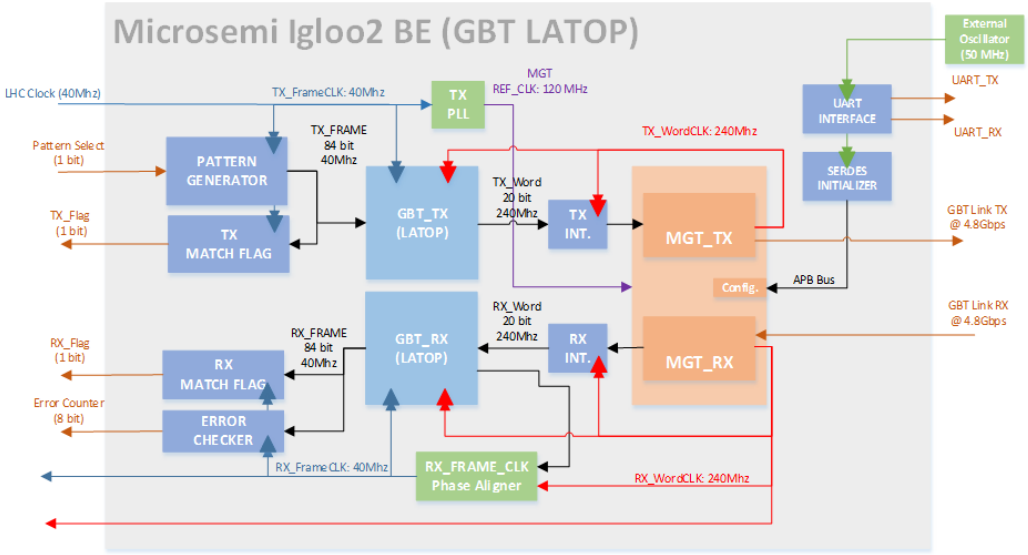

Figure 5.36 – GBT LATOP core implementation for an Igloo2-based Back-End System.

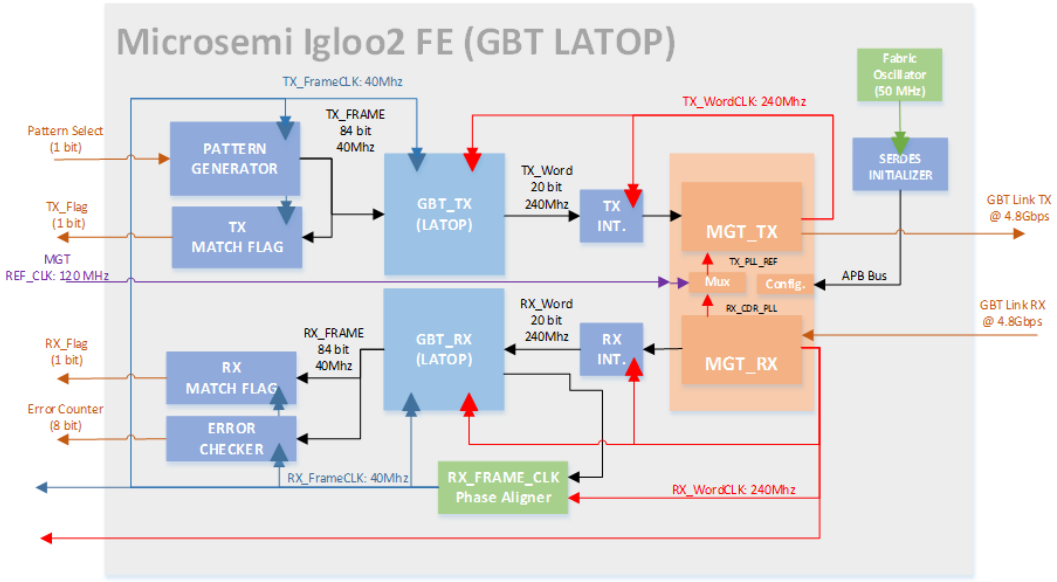

Figure 5.37 – GBT LATOP core implementation for an Igloo2-based Front-End System.

The final effects on a back-end / front-end system with the GBT LATOP version implemented on both systems are the following:

- No dedicated turn and bunch clocking cables are needed on the tunnel for the FE system (LHC clock is propagated through the GBT link).
- Data received on surface keeps a constant delay w.r.t the turn SPS/LHC reference and is in synchronization with the LHC/SPS 40MHz clock.
- After a single calibration, the received data can be identified and tagged on surface with its corresponding bunch number based on the constant delay w.r.t. the SPS/LHC turn clock.

Both schemes were successfully implemented on development kits. While one board operated as BE system (Board 1) the other was configured as a FE system (Board 2). LHC Clock recovery was practically evaluated by studying the phase difference between TX_FRAME_CLK from board 1 (injected as LHC clock on BE) and RX_FRAME_CLK from board 2 (recovered LHC clock on FE) in correlation with bistlip_nbr.

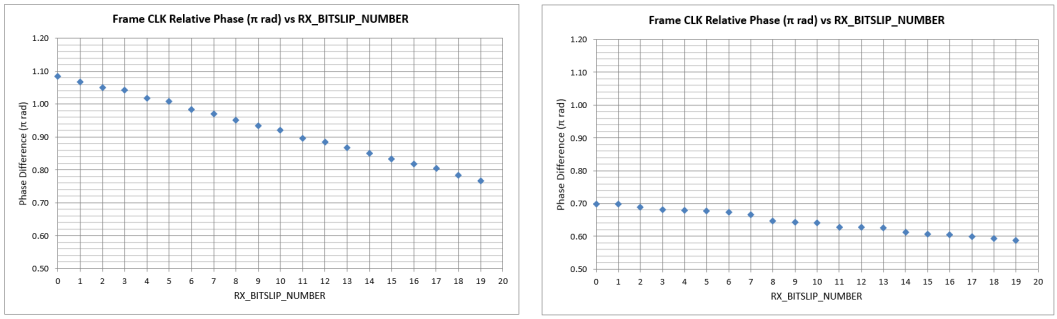

Figure 5.38 – Phase alignment between TX_FRAME_CLK (Board 1) and RX_FRAME_CLK (Board 2) compared with bitslip_nbr from board 2. RX_FRAME_CLK aligned only with RX_HEADER_FLAG (left), and with fine phase tuning (right)

The first implementation (see Fig;5.38 left) only aligned the RX_FRAME_CLK using RX_HEADER_FLAG, with no fine phase tuning. On this case, the phase of the

RX_FRAME_CLK varied linearly with bitslip_nbr in 20 possible phases (0-20), with a total phase incertitude of 4 ns (a complete WORD_CLK period), 16% incertitude for a 25 ns clock. The fine phase alignment mechanism was implemented for the second measurement (Fig. 5.38 right), the fine clock alignment reduces the phase variation from 4 ns to 1.3 ns, 5.6% phase incertitude.

As expected, link latency was drastically reduced with the LATOP "Gearbox" up to around 100ns (STD was ≈ 300 ns), the incertitude on latency was measured to be near 1.4ns, matching with the recovered clock incertitude (see Fig. 5.39).

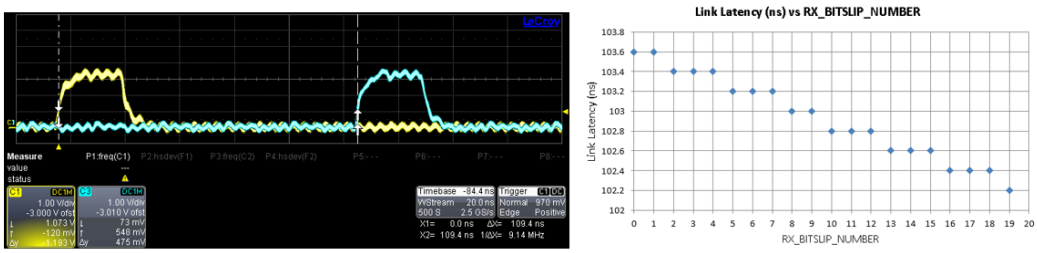

Figure 5.39 – Link latency studies for GBT LATOP version using scope cursors on TX (board 1 in yellow) and RX (board 2 in blue) match flag (left), latency measurement results (right) compared with the board 2 bitslip_nbr.

During the LHC and SPS acceleration cycle the bunch clock changes its frequency as the beam is accelerated. Bunch clock frequency variation on LHC cycle varies 2.5ppm, however in SPS this variation is about 800ppm. The optical link between BE-FE must remain stable during the acceleration cycle and follow the frequency variations of the reference clock to maintain synchronism with the machine.

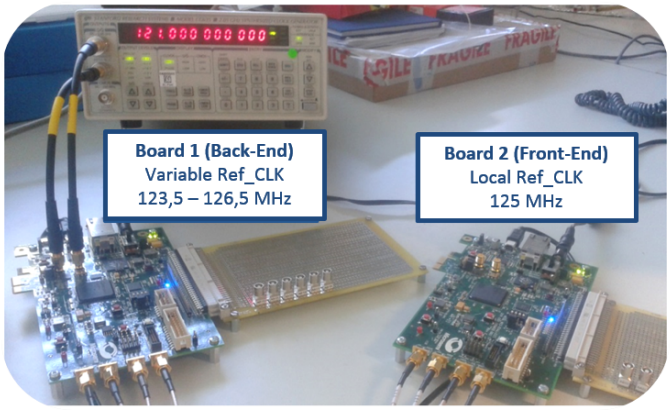

Figure 5.40 – Set-up to check link stability versus MGT reference clocks difference

From the clocking scheme point of view, the BE MGT reference clock (derived from Bunch Clock) will vary, whereas the MGT reference clock of the FE (provided by a local oscillator) will remain static. To ensure link stability during the acceleration cycle, the link was tested with different MGT clock frequencies on BE and FE systems. The reference clock of the BE was varied from 123.5 MHz up to 126.5 MHz in steps of 250 Khz while keeping the FE reference clock static at 125 MHz. After every change the link was manually reset. On this configuration the nominal link speed was 5 GBPS. The link status for the receiver part of both boards is collected on the Table 5.2. The test showed the link runs successfully with a maximum difference of ±0.5MHz on FE and BE reference clocks. The 1 MHz window in which the link can operate properly represents 8000 ppm on reference clocks difference, much bigger than LHC and SPS variations so the link is expected to remain stable during the accelerators ramp.

Table 5.2 – Optical link stability versus MGT reference clocks frequency difference on BE and FE systems

Ref Frequency Tolerance Test on Igloo2 with GBT firmware implemented @ 5Gbps											
Diff Freq	Board 1					Board 2					
(Mhz)	Freq (Mhz)	RX_Locked	RX_Val	GBT_Error_Counter	Comments	Freq(Mhz)	RX_Locked	RX_Val	GBT_Error_Counter	Comments	
1.5	123.5	No	No	Increments	RX_Freq remains constant and stable respect B1 TX_Freq	125	No	No	Increments	RX_Freq remains constant and stable respect B2 TX_Freq	
1.25	123.75	No	Sometimes	Increments	Received frames look like spected but with errors	125	No	Sometimes	Increments	Received frames look like spected but with errors	
1	124	Sometimes	Yes	No errors	GBT Frames well received and no error observed	125	Sometimes	Yes	No errors	GBT Frames well received and no error observed	
0.75	124.25	Sometimes	Yes	No errors	GBT Frames well received and no error observed	125	Sometimes	Yes	No errors	GBT Frames well received and no error observed	
0.5	124.5	Yes	Yes	No errors	GBT Frames well received and no error observed	125	Yes	Yes	No errors	GBT Frames well received and no error observed	
0.25	124.75	Yes	Yes	No errors	GBT Frames well received and no error observed	125	Yes	Yes	No errors	GBT Frames well received and no error observed	
0	125	Yes	Yes	No errors	GBT Frames well received and no error observed	125	Yes	Yes	No errors	GBT Frames well received and no error observed	
-0.25	125.25	Yes	Yes	No errors	GBT Frames well received and no error observed	125	Yes	Yes	No errors	GBT Frames well received and no error observed	
-0.5	125.5	Yes	Yes	No errors	GBT Frames well received and no error observed	125	Yes	Yes	No errors	GBT Frames well received and no error observed	
-0.75	125.75	Sometimes	Yes	No errors	GBT Frames well received and no error observed	125	Sometimes	Yes	No errors	GBT Frames well received and no error observed	
-1	126	Sometimes	Yes	No errors	GBT Frames well received and no error observed	125	Sometimes	Yes	No errors	GBT Frames well received and no error observed	
-1.25	126.25	Sometimes	Yes	Increments	Received frames look like spected but with errors	125	Sometimes	Yes	No errors	GBT Frames well received and no error observed	
-1.5	126.5	No	No	Increments	RX_Freq remains constant and stable respect B1 TX_Freq	125	No	No	Increments	RX_Freq remains constant and stable respect B2 TX_Freq	

Impossible
Caution!
OK

CDR (Mhz): (125.5 - 124.5) = 1Mhz --> 8000 ppm
LHC Frequency Variation(Mhz): (400.789 - 400.790) = 1Khz --> 2.5ppm
SPS Bunch Spacing Variation(ns): (24.97 - 24.95) = 0.02ns --> 800 ppm

5.2.1.2. QIE10 mezzanine board

A radiation-tolerant mezzanine board was designed to host a couple of QIE10 ASICs and for interfacing with the Igloo2 UMd board. The board designed features a 6 layer stack-up. The QIE10 provides its digital output through 8 LVDS pairs in DDR fashion at 40 MHz (80 Mbps per line), meaning an effective rate of 640 Mbps per ASIC, a total data throughput of 1.28 Gbps for both QIE10. The data stream provides 16 bits of data containing TDC and ADC information every 40 MHz clock cycle per ASIC. Clock input/output lines as well as reset digital input are driven by LVDS pairs. The inputs/outputs interfacing the 64 bits "serial shift register" configuration are single ended lines working at CMOS levels.

The front-end continuously sends the raw QIE10 data packed on GBT frames, no services are build on top of the GBT protocol. Concerning ASIC control and re-configuration, serial shift register lines, as well as control lines, are directly mapped to bits of the received GBT frames. With this configuration, the back-end system uses the GBT link as a transparent bridge from the data acquisition and front-end control point of view.

On the Igloo2 UMd mezzanine board all Inputs/Outputs on the HSMC connector are configured as LVDS pairs for consistency with the GBTx ASIC interfaces. LVDS drivers and receivers were included for the QIE10 CMOS interfaces. Drivers and receivers were DS90LV047A and DS90LV048A respectively, characterised under radiation up to a TID=0.7 KGy [143]. The Igloo2 UMd board and QIE10 supplies (3.3 V, 2.5 V and 5 V) are distributed with TL1963A low-dropout (LDO) regulators, characterised under radiation up to a TID=1 KGy [144].

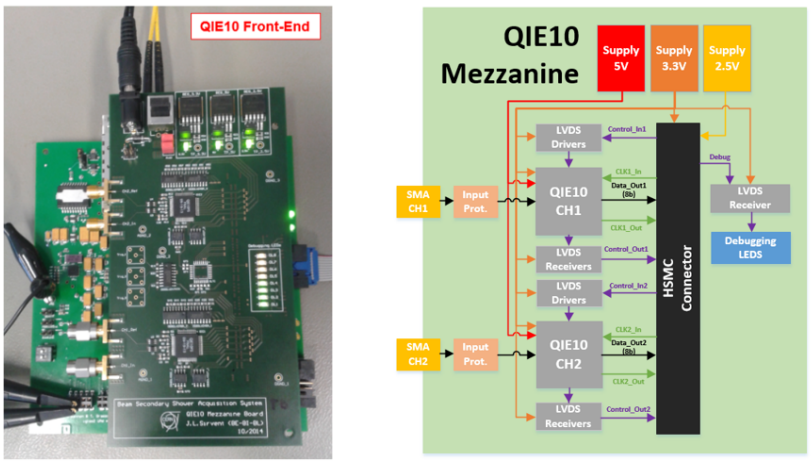

Figure 5.41 – QIE10 complete front-end (left) and QIE10 mezzanine simplified schematic (right).

The QIE10 analog input stage is configured as differential, one pad is the signal input and the other acts as a reference. Ideally for operation, an open cable can be included on

the reference input parallel to the signal cable for common mode noise rejection. The board features identical layout for signal and reference pins including SMA connectors. The analog input stage is protected against overcurrents by means of clipping diodes BAV99W to the supply and ground rails.

To estimate the power dissipation in each regulator, the current drawn by all the LDO was measured once connected to the Igloo2 UMd board. The board was powered at 6V to guarantee at least a minimum voltage drop of 1V on the 5V regulator. The TL1963A junction temperature, related to power dissipation, must remain <125°C to meet part specifications. The junction temperature can be calculated as follows:

$$P_{disip} = I_{out(max)}(V_{in\_max} - V_{out\_max}) + I_{gnd}(V_{in\_max}) \tag{5.2}$$

$$T_j = P_{disip}\theta_j \tag{5.3}$$

$$T_{j\_max} = T_j + T_a \tag{5.4}$$

Where P_{disip} is the power dissipation on the regulator, I_{gnd} is the GND pin current, T_a is the ambient temperature, θ_j is the junction-to-ambient thermal resistance and T_j is the junction temperature.

The current drawn by each power supply and the maximum junction temperature per regulator is detailed in Table 5.3, considering a worst case scenario with an ambient temperature of 50°C.

Table 5.3 – Current drawn per supply rail and calculated junction temperature per regulator

QIE10 LDO regulators current drawn and Junction Temperature		
Source	**Current (mA)**	**Tj_max (°C) ***
2.5V	535	105.8
3.3V	735	107.2
5.0V	55	53.24
Total Current: 1.344 A		
Board power consumption: 8.064W (powered at 6V)		
* Tj_max calculated with θ_j=28 deg/W, $T_a = 50°$ C and $I_{gnd} = 10mA$		

Under the circumstances detailed previously the max junction temperature is not reached. The metal pad on the back of the regulator is soldered to a big ground plane that acts as heatsink helping on the heat dissipation. For further safety, forced ventilation was added when installed on tunnel.

5.2.1.3. ICECAL V3 mezzanine board

Another mezzanine was developed to host an ICECAL V3 and associated digitalization circuitry. As with QIE10, radiation-characterised components were used on its design. ICECAL V3 required a single 3.3V power supply and some complementary reference and bias voltages (Vcm, Vcontrol and Vref). The 2.5V and 3.3V supplies are distributed by a couple of FEASTMP modules, a CERN radiation hard development designed for operation up to TID > 2MGy [145]. FEASTMP are buck or step-down switched DC-DC converters, they are suited to work with a wide voltage supply range (from 5V to 12V), its switched topology minimises power/heat dissipation.

The reference and bias voltages for ICECAL are generated from the 3.3V source by a MCP1826 (Vref), and a couple of LM4121 (for Vcm and Vcontrol), characterised under radiation up to TID≈ 1kGy [146] and TID≈ 300Gy [147] respectively.

ICECAL V3 provides four differential analog voltages every 40 MHz clock cycle proportional to the integrated current seen in each channel input. The ICECAL differential outputs feature 1.5 Vcm with a maximum amplitude of 2 Vpp. Two different quad channel ADCs

were evaluated on this board for digitalization (AD41240 and ADS6445). The AD41240 is a radiation hard 4 channels 12 bits ADC developed at CERN, tested up to 100 kGy [148]. The ADS6445 is a commercial radiation-characterised 14 bits ADC with 4 channels tested up to 2.1 KGy [149]. The digitalization circuitry to use with ICECAL is settable by soldering/de-soldering a set of 0 Ω resistors. The LVDS digital data interfaces of both ADCs is compatible with GBTx E-ports in terms of data rates.

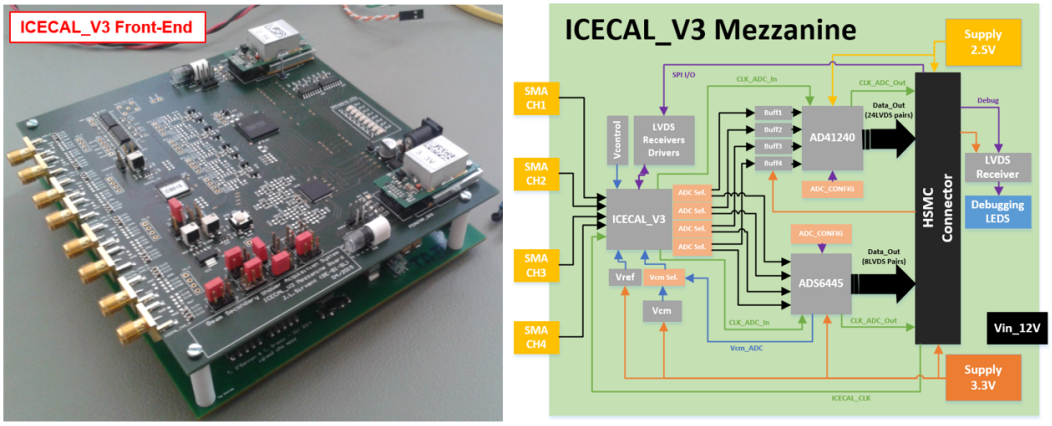

Figure 5.42 – ICECALV V3 complete front-end (right) and ICECAL V3 mezzanine simplified schematic (right).

The analog interface between the ICECAL and the AD6445 is straightforward, only using low value resistors (10 Ω) in series with each input pin to damp out ringing caused switching currents, common mode and differential swing voltages are compatible. The digital output of this ADC is provided through serial DDR LVDS interfaces, two LVDS pairs are used per channel with an effective data rate of 320 Mbps per pair. This ADC also provides LVDS bit and frame clocks for correct data sampling.

A buffer stage is required to interface in DC the ICECAL outputs with the AD41240. The input common mode voltage for AD41240 is 1.25V, differential buffers are used to simply shift the ICECAL 1.5V common mode voltage to 1.25V. These level shifters are based on fully differential amplifiers THS4521, qualified under radiation up to a max TID=1kGy. AD41240 provides the digital data for its four channels in parallel through a total of 24 DDR LVDS pairs with an effective rate of 80 Mbps each.

Concerning the board clock scheme, a 40 MHz clock is provided to the ICECAL through the HSMC connector, ICECAL generates independent 40 MHz clocks per channel intended for digitalization circuitry, configuration through SPI allows to tune the phase of these clocks w.r.t. the ICECAL input clock in order to match data lines delay. Each ADC on this board is using the clock of different ICECAL channels, AD41240 uses ADC clock from CH2 whereas ADS6445 uses the ADC clock from CH3. Finally each ADC is responsible of providing bit/frame clocks for sampling digital data lines.

To keep LVDS standard in all I/O interface with the HSMC connector, LVDS drivers and receivers are to interface the ICECAL SPI lines.

5.2.2. Back-End implementation

The back-end was implemented by means of commercial boards. An Igloo2 Development kit with the GBT firmware is the core of the system. An external PLL evaluation board is used to generate the required SERDES 120MHz from the 40Mhz LHC/SPS bunch clock. A SMA-to-SFP+ module allows optical transmission with gigabit optical transceivers. External connectivity includes: “turn clock” and trigger signals, fed into the FPGA GPIOS through 50 Ω single ended to differential buffers, a couple of USB ports (one for the PLL board and

another one for the FPGA) and E2000 SMF connectors (for the GBT link). The back-end system also provides +12V,-12V and the 10V power supplies used by the front-end. A relay connected to the FPGA allows to remotely perform power cycles on FE from the expert application.

All electronics and associated power supplies were integrated into a 6U Eurocard Subrack chassis to ease transport and installation on existing infrastructure. Figures 5.43 and 5.44 shows a schematic of the back-end and the chassis front-panel respectively.

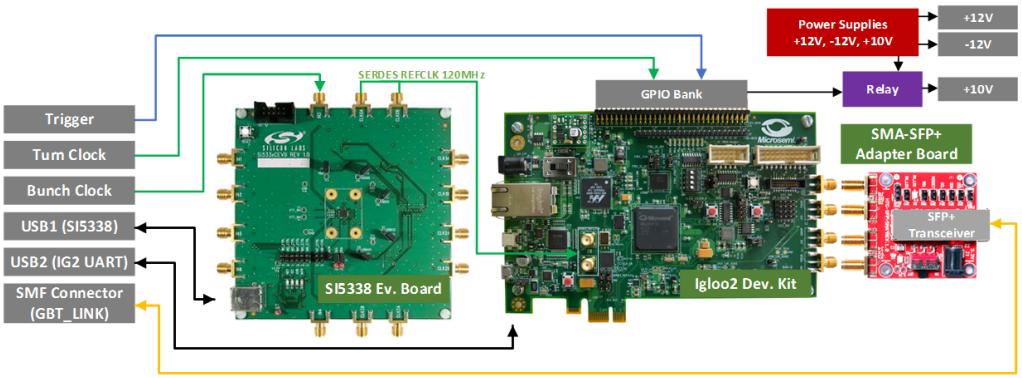

Figure 5.43 – Back-End prototype system schematic.

Figure 5.44 – Back-End prototype integration into a 6U EuroCard subrack chassis.

As previously detailed, the back-end (BE) propagates the LHC clock to the front-end and performs control actions through GBT link (i.e. reset and acquisition ASICs registers programming). The BE system is also responsible to store the data contained on the GBT link while a scan is being performed. A trigger signal is used to inform when a scan starts so data can be stored. The latency deterministic implementation in both directions of the link, allows to set an identifier to each 25ns acquisition window, this way bunches can be identified and profiles from single bunches re-constructed. Communication with a PC is performed through a UART interface and an expert application provides feedback to the user about the GBT link status and control over the complete system. Through the expert application the system can be configured and the acquisition data, contained on the back-end memory, downloaded to a PC for analysis.

5.2.2.1. Firmware organisation

The firmware on the BE system is developed around the GBT LATOP implementation. The data acquisition system has been completed with data storage capabilities and data

transmission through the UART interface. The full implementation is organised in six parts as shown in Fig. 5.45:

- **GBT Core:** Manages the GBT link protocol physical layer and the clocking delivery.
- **Memory Write management:** Received GBT data frames are identified with their respective bunch identifier by the "Bunch Tagger". When the system initiates an acquisition (trigger received from "Trigger manager"), the "Data acquisition status machine" starts data transactions to the "Memory Access Module" through an elastic FIFO. The FIFO is used for data buffering prior to memory storage, this eases the memory access and ensures no frames lost.
- **Memory Access module:** The physical access to the memory is done through the Igloo2 "High performance memory subsystem" (HPMS). This IP core deals with the memory initialisation and the required MDDR bus protocol for memory read/write operations. HPMS is interfaced with the FPGA fabric through an AXI bus and requires of an "AXI master" to interact with the rest of the logic. Memory access works in 80 Mhz clock domain, data transmission is performed with 16 word bursts of 64 bits each.
- **Memory read management:** This module is designed to interface the "memory access module" with the "PC Communication Module", this way data contained on the memory can be transmitted through UART. The read data bursts from the memory are temporally stored in a "two port dual ram", the data of this memory is read afterwards by the "PC communication module" for transmission to the PC. When all data contained on the dual Ram memory has been transmitted a new read burst is requested to the "Memory access module".
- **PC Communication module:** The Igloo2 UART IP core is the physical link with the UART to USB converter on the Igloo2 Development kit, communication is set-up at 921.6KBaud. The "UART interface" module is used to interact with the rest of the logic and manages the transmission of system supervision data and memory acquisition data, it also checks for incoming data or commands from the PC in order to set system configuration registers.
- **Back-End control and supervision:** This is a set of registers used for configuration and supervision of the modules in the design. Supervision registers monitors the GBT link status and the data acquisition status. Control registers set the different configurations of the GBT link (Test/DAQ mode, Manual resets...etc), manages the acquisition procedure (system arming, software trigger, acquisition delays...etc) and also sets the configuration for memory data transmission (starting address, number of words...etc).

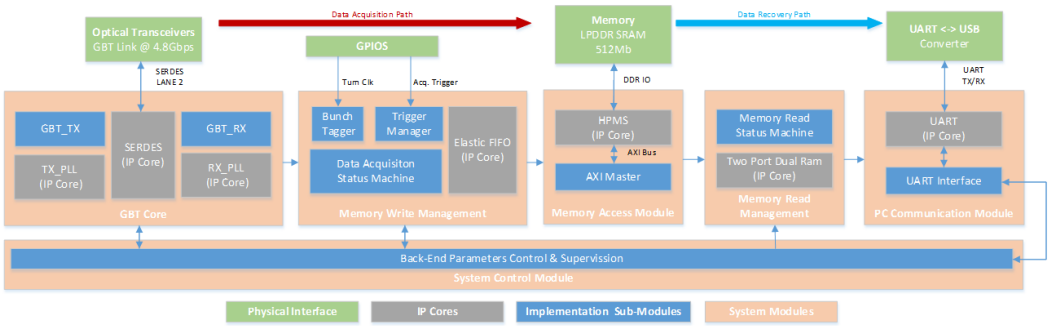

Figure 5.45 – Simplified schematic of the BE firmware implementation.

5.2.2.2. Memory mapping and storage capabilities

The back end memory management is supported by the on-board 512 Mb LPDDR SDRAM included on the Igloo2 Dev. Kit. On the FPGA firmware implementation, half of the memory addresses are reserved for IN scan data whereas other half is reserved for OUT scan. The storage limit is set to 256Mb per scan. Data frames are 64 bits width and consist on 1 bit as "turn marker", 12 bits for "bunch identifier", to cover a complete LHC fill with 2808 bunches, and 51 bits for "DAC payload". This data format limits memory storage to $4e^6$ acquisitions per scan. In order to optimize data storage, several acquisition modes were implemented:

- **Continuous Recording:** After trigger reception the system records data in a continuous fashion, with $4e^6$ acquisitions per IN or OUT scan at 40MHz, maximum storage time is 100ms for each.

- **Selected Bunches:** Single, or a window of consecutive bunches can be selected for storage. Bunches are recognized by their identifier and only the identifiers selected are stored. Boundary values goes from a single bunch up to 2808 consecutive bunches, meaning a maximum storage from $4e^6$ or 1424 turns respectively.

- **Selected Turns:** It is also possible to store data in alternating turns, meaning that acquisitions of selected bunches are only stored each x number of turns, x ranges from 0 to 255.

The data frames format on memory and detailed payload for each of the mezzanine boards is shown in Fig. 5.46. The data payload corresponds to the 50:0 bits of the 80 bits data payload from the received GBT frames, the data acquisition manager remains this way "generic" to receive ICECAL or QIE10 data frames.

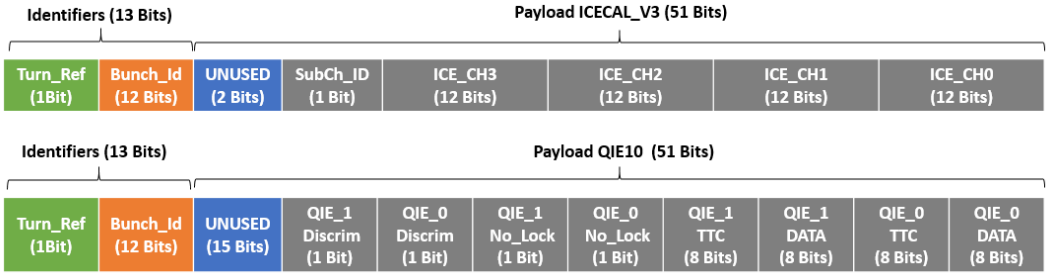

Figure 5.46 – Data frames format on memory with detailed payload for ICECAL (top) and QIE10 (bottom) mezzanines

5.2.2.3. Expert application

A Matlab-based expert application is executed on the computer attached to the BE system. Instrument control toolbox was used for communication at 921.6 KBaud, the maximal speed reachable by the Igloo2 UART IP core. Through the application the user has full control over the system and real-time information of the optical link status. Application GUI is shown in Fig. 5.47.

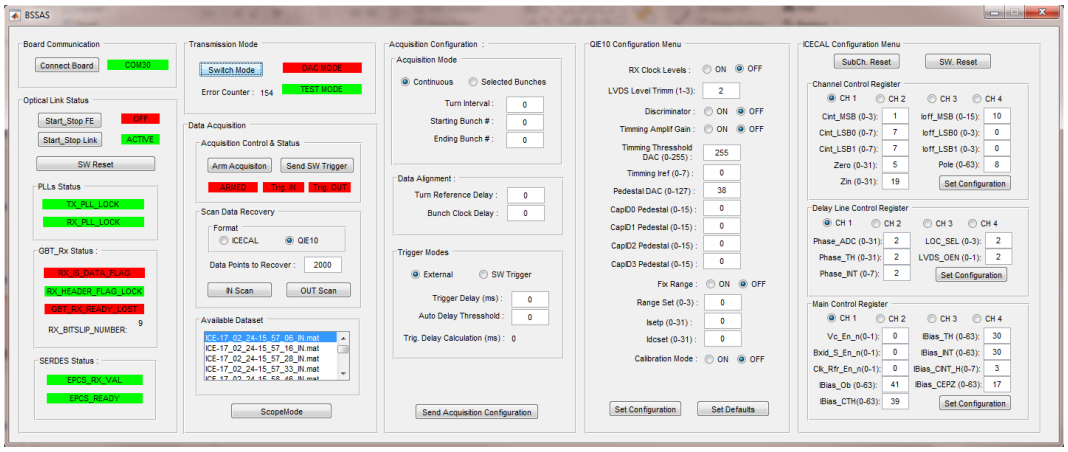

Figure 5.47 – Matlab based expert application for acquisition system control.

The BE is continuously sending status information that updates the different status "indicators". BE also checks for any input command to react in consequence.

Status indicators and actions present on the **"Optical Link Status"** and **"Transmission mode"** blocks are mainly used to check the GBT link health status.

- **Button Start_Stop FE:** Power cycles (hardware reset) on the front-end (FE) system are possible by changing the status of the 10V relay.
- **Button Start_Stop Link:** The BE GBT TX and RX can be started-stopped with this button. When the link is stopped, the SERDES TX and RX parts are hold in reset status, no data is sent on the link which obliges the FE to enter in bit lock status until the link is re-started and data is present.
- **Button SW Reset:** Completely resets the BE SERDES, this forces a complete BE initialization.
- **PLL Status Block:** Information on the BE GBT_TX and GBT_RX PLLs lock status.
- **GBT_RX Status Block:** Information on the BE GBT core RX status. It shows frame type received (RX_IS_DATA_FLAG), if the RX is locked on the header flag (RX_HEADER_FLAG_LOCK) and the link was lost at some point "GBT_RX_READY_LOST". This block also shows the BE RX Bit_Slip number.
- **SERDES Status Block:** Shows key SERDES native status signals, they asses that the BE SERDES RX is locked on the incoming FE data stream (ECPS_RX_VAL), and the correct SERDES Initialization and configuration (EPCS_READY).
- **Transmission Mode Block:** The GBT link can be operated bi-directionally in two different modes. One of the bit of GBT frame is assigned to inform of the transmission mode.
  - **DAC Mode:** This is the data acquisition mode, BE sends GBT frames (dummy, idle or control) to keep the FE synchronisation. On this mode, the FE is sending data frames containing ASICs acquisitions.
  - **Test Mode:** BE and FE system are set in test mode, both are sending test pattern frames. The BE can check the received frames and determine if errors have been received on the data frame (not corrected by the FEC mechanism), an error counter is shown in this block.

"Acquisition Configuration" and **"Data Acquisition"** blocks manage the acquisition settings and data taking process.

- **Acquisition Mode Block:** Sets the data storage configuration as detailed on section 5.2.2.2
- **Data Alignment Block:** It is possible to specify an offset on the bunch identifier reset, based on the LHC/SPS turn clock received on the BE. This way the system can be tuned to properly tag bunches with their corresponding ID number.
- **Trigger modes Block:** Acquisitions can be triggered manually from firmware (SW_Trigger) or externally from the "Trigger" hardware input. In both cases it is possible to specify a delay after trigger detection to start data storage, this delay helps to optimise the acquisition window placement. An automatic delay calculation feature was added to assist on the trigger delay setting. By applying a threshold on the acquisition data received, the BE system provides the delay from the trigger detection up to the data threshold crossing detection.
- **Acquisition Control and Status block:** Prior to an acquisition, the system must be manually armed. "Arm" and "SW Trigger" buttons are available here, the acquisition status is also show on the coloured indicators to provide user feedback and check that IN & OUT triggers are correctly detected.
- **Data Scan Recovery Block:** Data on the BE memory can be recovered and stored on the computer with this block. The data format (QIE10 or ICECAL), as well as the total number of measurement points (up to $4e^6$) have to be specified. When pushing IN/OUT scan the transmission of data from the memory starts on the address associated to IN or OUT scans. Received data is locally stored on "*.mat" files and displayed on the available dataset list box.
- **Available dataset Block:** : Local files stored on the application directory are shown on the list box with their associated timestamp as filename. Double click on an item on the list displays a plot showing the data.
- **Scope mode Button:** Pushing this button the "Scope Mode" is set to active. On this mode the BE arming, triggering, data recovery and plotting is automatically managed by the application in a continuous way. This mode shows a plot with "online" data coming from the FE, this is especially useful to check changes on the incoming data stream while tuning ASICS parameters (offset, gain changes...etc.).

"QIE10 Configuration" and **"ICECAL Configuration"** blocks are used to set values on the configuration registers of the two possible front-end ASICs. The application shows the default register values at start-up, new values are assigned on the FE ASICS once "Send configuration" is pushed. At this point the BE receives the specific ASIC configuration, and propagates it through the GBT link.

Chapter 6

Laboratory evaluation and beam test results

This chapter details the evaluation of the proof-of concept prototype in laboratory as well as with beam in SPS and PSB accelerators. In addition, the beam-test presented on this chapter shows the LIU-BWS evaluation and performance comparison with operational systems.

6.1. Front-End prototypes laboratory evaluation

6.1.1. QIE10 Front-End

A full prototype set-up was used for the first laboratory measurements with the QIE10 front-end. The front-end evaluation consisted in the injection of known DC currents (and therefore a known charge in 25ns timeslots) in the inputs of both QIE10 in the front-end mezzanine. Applying DC current sweeps, the ASICs linearity can be studied. The expert application was adapted to perform automatised test by controlling a sub-femtoamp current source (Keithley 6430) through a general purpose instrumentation bus (GPIB).

As in nominal operation, the FE is continuously sampling and sending data at 40 MHz to the BE system in synchronised with an external clock (SPS/LHC bunch clock). When the BE receives a software trigger from expert application, the data from the optical link is temporally stored on the BE, afterwards the memory content is downloaded in the PC through an UART. The data taking process consisted on setting the current source to a known value and increase it by a known step for subsequent triggers. For each current value, a temporal window of 25 µs was recorded. The laboratory set-up is shown in Fig. 6.1.

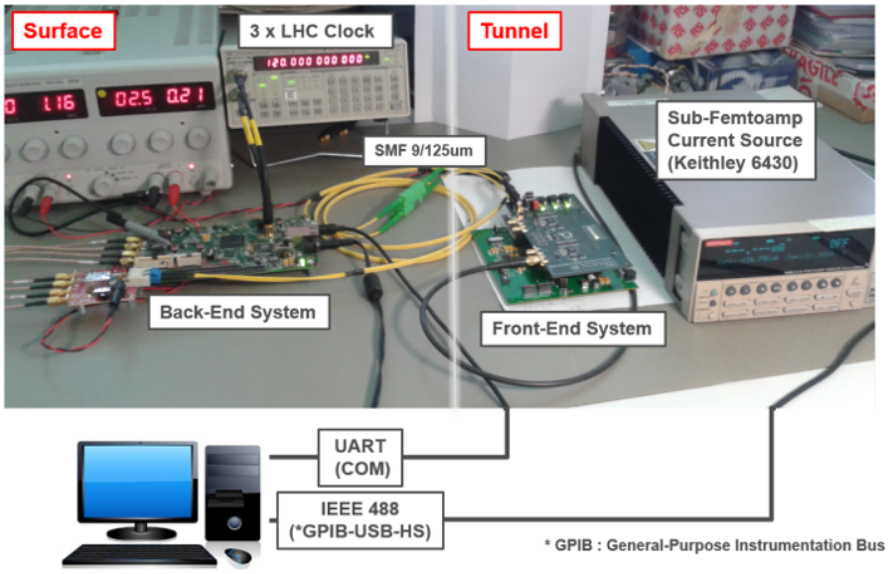

Figure 6.1 – Laboratory Set-up for QIE10 front-end evaluation.

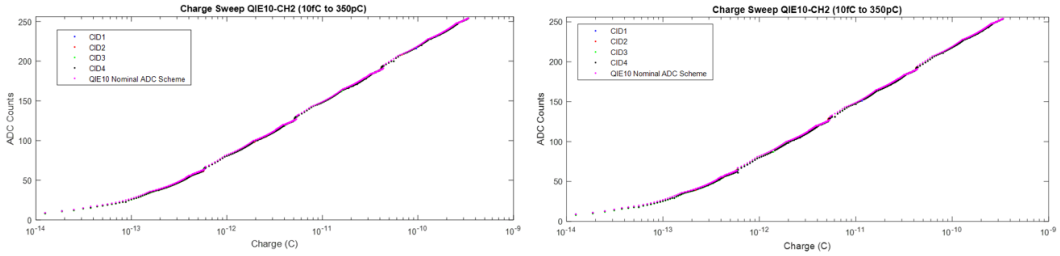

Figure 6.2 – QIE10 mezzanine logarithmic response check for both QIE10 and comparison with nominal response. QIE10_A (left) and QIE10_B (right).

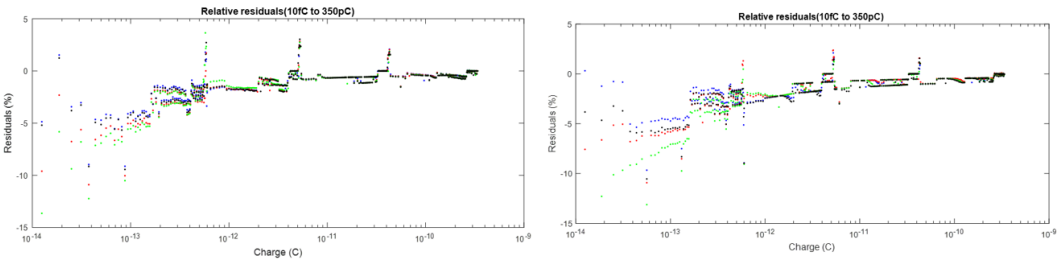

Figure 6.3 – QIE10 linearity residuals w.r.t nominal response. QIE10_A (left) and QIE10_B (right).

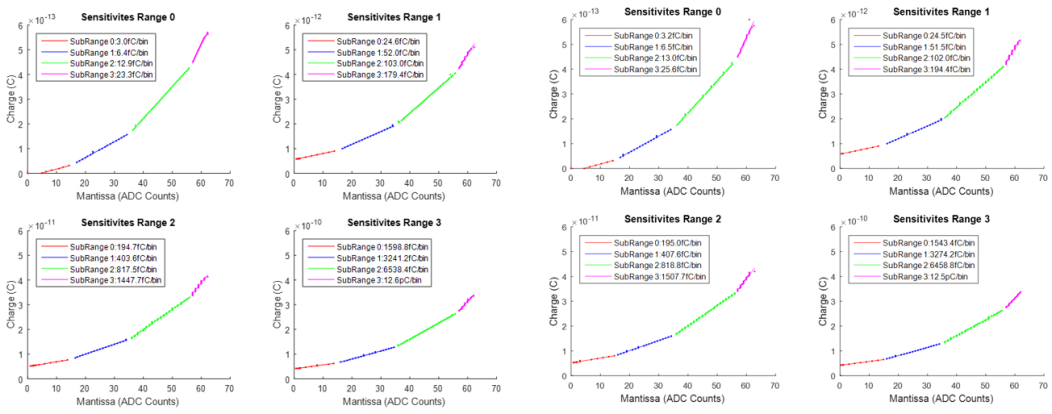

Figure 6.4 – QIE10 Mezzanine sub-Ranges sensitivities tests for QIE10_A (left) and QIE10_B (right).

To be able to provide a measurement every 25 ns, QIE10 works in a pipelined fashion by using 4 parallel integrator circuits. Consecutive 25 ns integrations are performed with a different integrator capacitor (0, 1, 2, 3, 0, 1...). In order to compensate possible differences between integrator circuit, and allow calibration for each of the 4 sub channels independently, QIE10 provides an integrator identifier along with the data.

Figure 6.2 shows the digital QIE10 output values (0-256) corresponding to an input charge sweep ranging from 10 fC to 340 pC (DC currents from 400 nA up to 13.6 mA), for both ASICS on the front-end. A uniform logarithmic behaviour is measured for all integrator capacitors. The response properly follows the expected QIE10 ASIC digitalization schema shown as purple points, over its 5 orders of magnitude dynamic range.

The relative residuals w.r.t the nominal response is shown in Fig. 6.3. There is a clear division between the 4 ranges in which the ASIC splits its dynamics (see the little spikes in the residual error). The measured values in the prototype shown a good agreement w.r.t the ASIC nominal response and non-linearities lied below 5 %, except for a small portion of the first range.

The 16 QIE10 sensitivity levels (4 per range) are shown in Fig. 6.4, where the input charge versus mantissa bits are displayed in a linear scale. The sensitivity levels are seen as the slope of the linear fits performed in each sub-range.

Both of the QIE10 ASICs contained on the front-end board shown a identical behaviour, the data collected during these studies was used later for calibration. The tests shown that the complete front-end performed according to specification, which qualified the electronics in terms of functionality and accuracy for installation in the SPS tunnel for further testing.

6.1.2. ICECAL V3 Front-End

This board features two possible digitalization circuits for the ICECAL V3 signals. Selection between the 12 Bits ADC AD41240 or 14 Bits ADC AD6445 is possible by means of 0 Ω resistors. The laboratory tests qualified both acquisition branches separately, the best one was selected for a final configuration.

6.1.2.1. ICECAL V3 Preliminary testing

Functional tests on the ICECAL V3 mezzanine checked that the conditioning circuitry and the ASIC itself were fully operational. A function generator AFG3252 generated test signals and the 40 MHz system clock. The system clock was provided to the back-end and recovered on the front-end through the optical link, the input test pulses were attenuated and AC coupled to the readout ASIC. Finally, the analog output was monitored with an AC

coupled differential probe connected to a scope. The set-up and readout ASIC response is shown in Fig. 6.5.

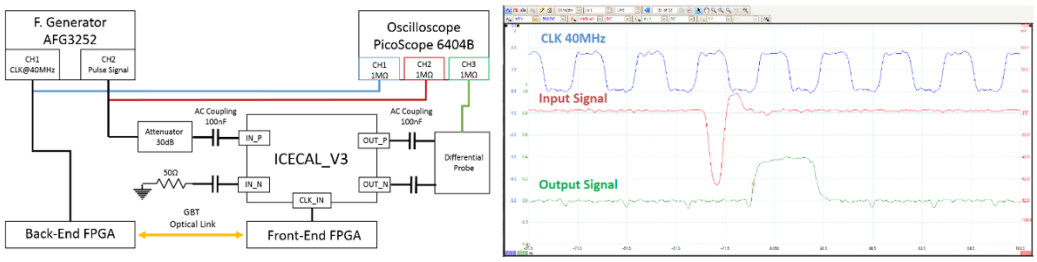

Figure 6.5 – ICECAL V3 mezzanine functional tests setup (left) and corresponding scope signals (right).

On the scope signal, Fig. 6.5 right, the system clock (blue), the input tests pulse (red) and the ICECAL response (green) are shown. The ASIC shown a correct operation, its output signals (square pulses) shown an amplitude proportional to the input charge.

6.1.3. Performance Test ICECAL V3 and AD41240 Readout

The ICECAL linearity was studied with short current pulses and AC coupling in the ICECAL inputs. The input pulse signals were synchronised with respect to the ICECAL integrators and ADC acquisition clocks. Synchronisation was provided with a single Tektronix AFG3252 function generator, where one channel provided test signals and another the system clock (40 MHz). The system clock was propagated through the optical link, allowing the front-end to be in synchronisation with the generator. The 50 ns test pulses were generated every 25μs, in synchronisation with the main 40 MHz clock. This configuration ensured that the input signal and the ICECAL acquisition and digitisation clocks had no phase drift. Figure 6.6 shows the test set-up and the related parts of the board under test on this section. The data taking process was similar as previously, controlling this time the function generator through GPIB.

The ICECAL outputs (with a differential swing of 2 Vpp) were AC coupled to the ADC buffers while the buffers outputs are DC coupled to the ADC. With this configuration, and when no signal is present, the ADC buffers set Vcm on both differential pins (Vdiff = 0 V), thus making the ADC work at half of its scale (2048 ADC counts).

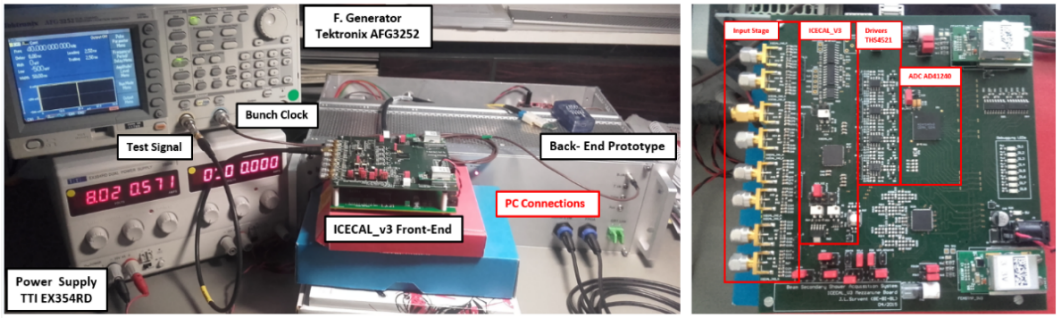

Figure 6.6 – Test set-up and components under evaluation for ICECAL V3 board characterisation with AD41240 readout.

- **Linearity**

The linearity measurements were done with an amplitude sweep of short negative pulses. The test pulses were 50 ns long with a repetition frequency of 40 KHz. Such configuration

allowed two consecutive acquisitions (25 ns each) performed every 1000 samples (25 μs), thus the characterisation of both ICECAL sub-channels was possible with a single sweep.

The generator pulses amplitude varied between 50 mV-800 mV, a 30dB attenuator was placed just after the function generator. With the inputs AC coupled (100 nf), the charge sweep seen by the ICECAL (in 25 ns slots) was 790 fC-12.6 pC. The amplitude of the tests pulses remained constant during each measurement window. Prior to data acquisition, the ICECAL configuration registers were tuned to correct for any gain or offset offset deviation in all the ASIC channels and subchannels.

Figure 6.7 shows the outcome of the linearity measurements for the four ICECAL channels, subchannels are identified with different colours. The typical slope for all the ICECAL channels (in default configuration) together with the ADC and drivers is translated into approximately 6.25 fC/LSB. The acquisitions shown an estimated saturation around 24 pC. The ASIC linearity was studied by applying a linear fit on the measured data and studying the fit residuals, sub-channels were fitted independently. Systematic linearity deviations are observed in the data for every subchannel, leading to non-linearities >1%. Further studies identified the THS4521 ADC buffers as the source of the non-linearities due to an asymmetric powering supply 0-3.3V, the low output Vcm (1.25V) and the required differential swing (2Vpp).

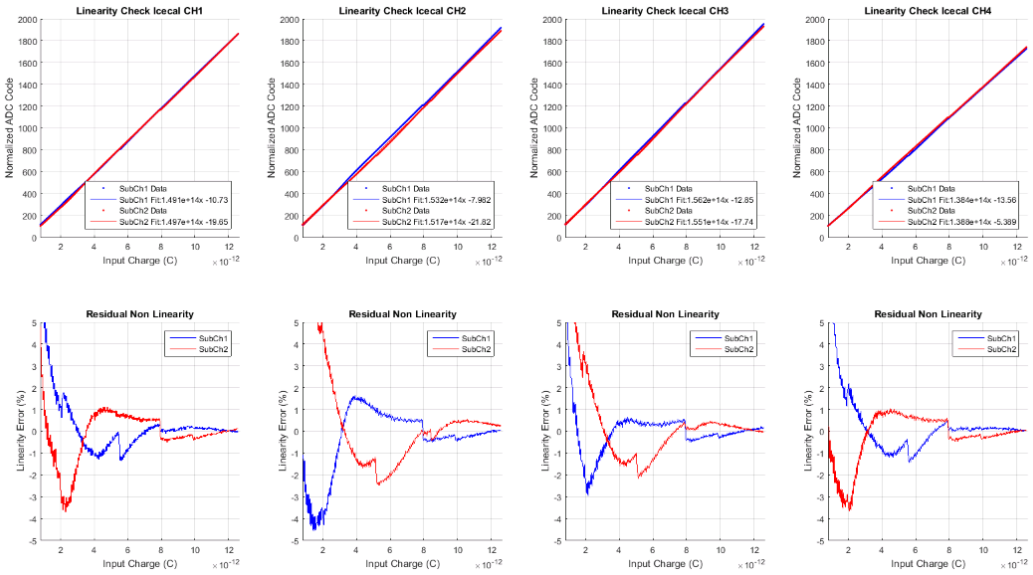

Figure 6.7 – Linearity test results for the four ICECAL Channels (top) and residual non linearity (bottom) with AD41240 readout. Subchannels studied independently.

- **Noise**

The noise distribution of the whole readout assembly was measured by loading the ICECAL mezzanine inputs with 50 Ω (while keeping the AC input coupling). Temporal windows of 2.5 ms were taken with no signal injection (1.000.000 Samples at 40 MSPS), finally a histogram was applied on the raw ADC data. To obtain the noise level, a Gaussian fit was applied on the histogram and the noise sigma value extracted in ADC counts.

As seen in Fig. 6.8, each subchannel has a different offset, which can be minimised by internal registers configuration. However, even under the best possible configuration, a small offset difference between subchannels is practically unavoidable.

The noise (histogram sigma) for all channels and subchannels remained below 1.7 ADC Counts, this value varied when the function generator was connected to the ASIC inputs up to 2-3 ADC counts.

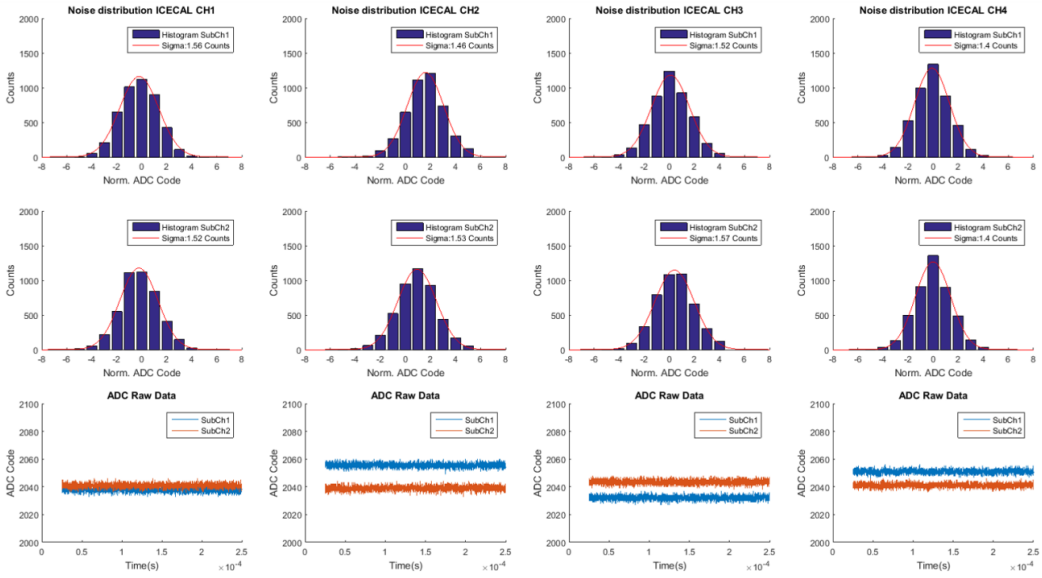

Figure 6.8 – Noise distributions for the four ICECAL channels with AD41240 readout, each subchannel is studied independently (first two rows), and raw ADC data (bottom row).

- **Characterisation outcome**

The ICECAL readout with the AD41240 branch resulted in a noise sigma ≈ 2 ADC counts with 6.25 fC/ADC_count slope. This sets the detection threshold around 25 fC pulses (2 x noise sigma) with ADC saturation about 24 pC (1e^3 dynamics per channel). The linearity study showed serious deviations >1% linked to the buffers working point. A numeric summary is collected in Table 6.1.

Table 6.1 – Performance summary for ICECAL with AD41240 digitalization

ICECAL & AD41240 PERFORMANCE SUMMARY				
Sensitivity	**Slope**	**Saturation**	**Dynamics**	**Linearity deviation**
25fC	6.25fC/LSB	24pC	1e3	>1%

6.1.4. Performance Test ICECAL V3 and AD6645 Readout

The AD6645 is a 14 bits quad ADC, its input specifications match the ICECAL output characteristics in terms of Vcm (1.5 V) and differential swing (2 Vpp). The interface between the ICECAL and the ADC was DC coupled passively through a set of resistors. In addition, both ICECAL and the AD6645 were powered by the same 3.3V supply. Readout with this ADC highly optimised the board design by reducing the complexity and the number of components.

Measurements on this branch were done as detailed on the previous section, test set-up and board parts under tests are shown on Fig. 6.9. The Igloo2 FPGA firmware was adapted to sample and de-serialize the digital data from the AD6645 (two LVDS DDR lines pairs at 320 Mbps per ADC channel).

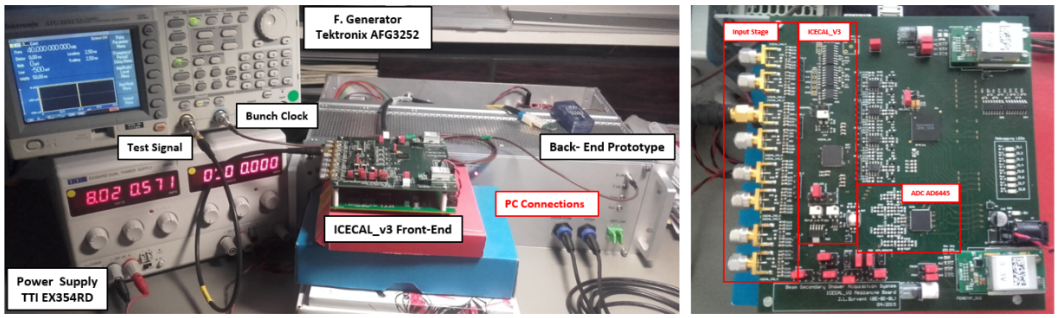

Figure 6.9 – Test set-up and components under evaluation for ICECAL V3 board characterisation with AD6645 readout.

- **System Linearity**

The ICECAL analog inputs were AC coupled (100 nF) with the function generator, where a 30 dB attenuator was attached. The DC coupling between the ICECAL outputs and the ADC allows to use the full ADC dynammics. This time, the pulses amplitude sweep was performed between 50 mV-1.4 V, considering the attenuator influence and 25 ns integrating windows, the charge seen by ICECAL was 790 fC-22 pC. As previously, delay lines and subchannel integrators were set to properly match the signal and acquisition window phase into two consecutive subchannels, a minimum offset and gain difference was set between subchannels.

As shown in Fig. 6.10, default ASIC configuration, the readout chain shows a slope of 1.3 fC/LSB with saturation around 22 pC, linearity remained $< 1\,\%$ for the complete readout dynamics. The study was repeated for the maximum and minimum programmable integrator capacitor values in order to check the slope range or sensitivity levels of the ASIC, see Fig. 6.11. All configurations showed a similar linearity performance, $< 1\,\%$ deviations except for a small portion of the low end. The programmable slope boundaries ranged from 0.8 fC/LSB to 1.9 fC/LSB, leading to saturation ranging from 14 pC to 30.3 pC respectively. The discontinuity jumps observed on the residual plots correspond to changes of scale of the function generator, thus linearity results seems to be biased by the generator performance.

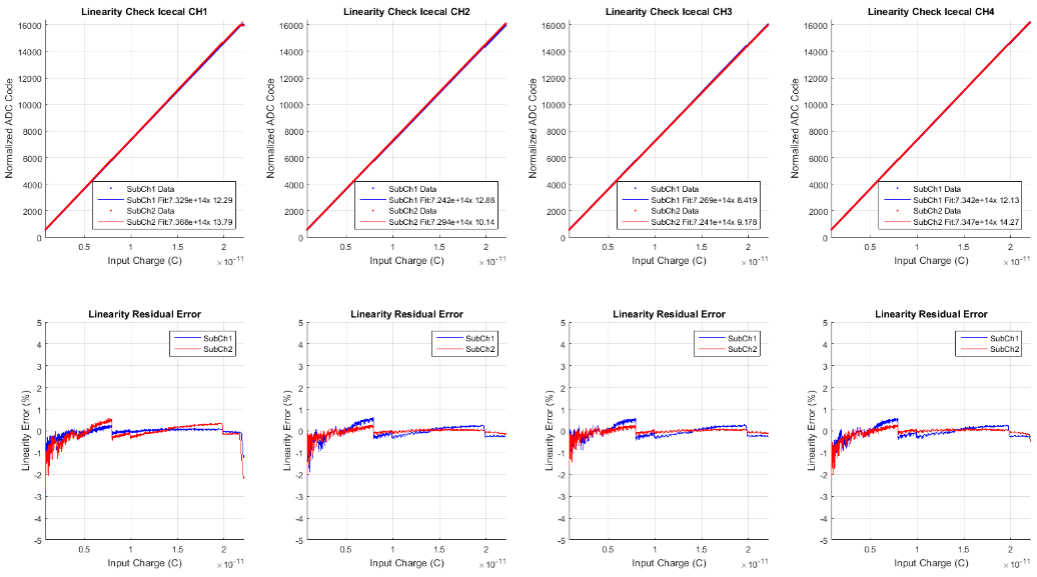

Figure 6.10 – Linearity test results for the four ICECAL channels (top) and residual non linearity (bottom) with AD6645 readout branch (ICECAL in default configuration).

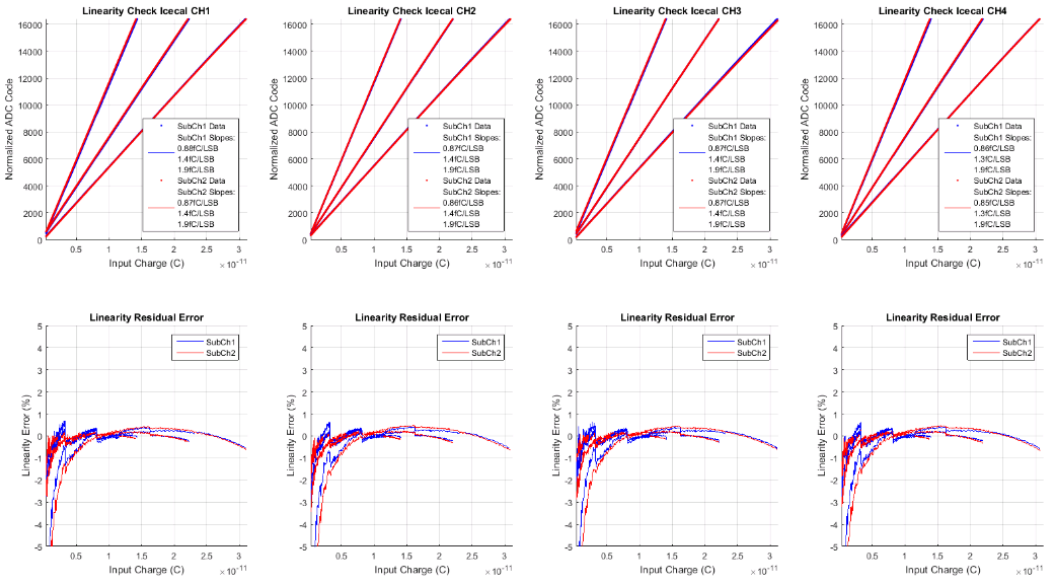

Figure 6.11 – Linearity results for three programmable integrator capacitors (Cint), minimum, nominal and maximum values are displayed.

- **System Noise**

By studying every subchannel independently, see Fig. 6.12, the RMS noise level was determined to be below 6 ADC Counts.

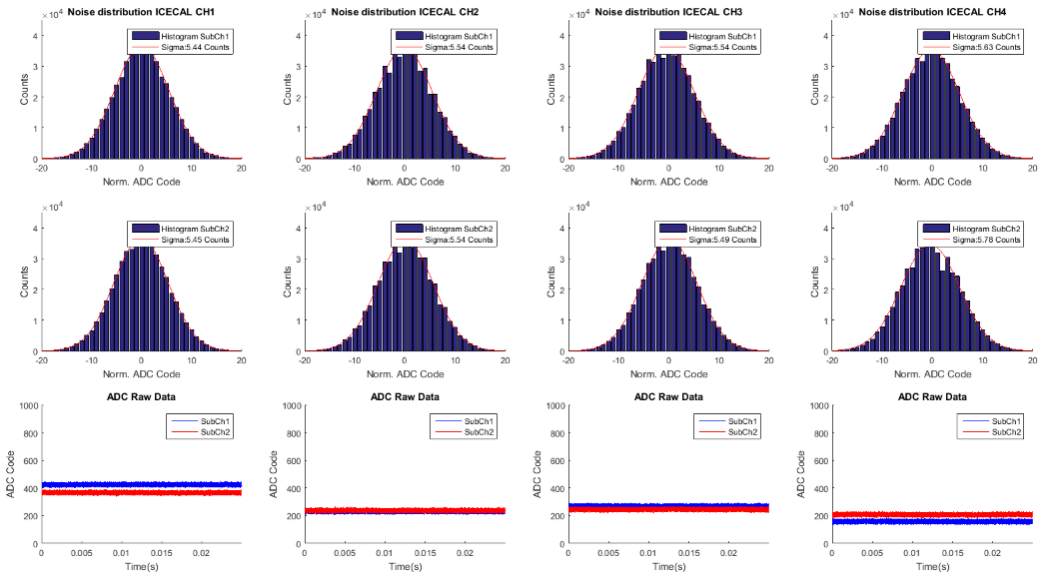

Figure 6.12 – Noise distributions for the four ICECAL channels with ADS6645 readout (first two rows), and raw ADC data (bottom row).

- **Outcome**

This readout branch featured a total dynamics of 1.3e^3 given the 14 bits ADC scale (16384 counts) and a noise level 6 LSB RMS. The system linearity shown a more consistent behaviour (in comparison with the AD41240), with non-linearities below 1 % on all its acquisition dynamics. This was the readout branch selected for evaluation in the PSB tunnel. The characteristics of the different working points of the ASIC are summarised in Table 6.2.

Table 6.2 – Performance summary of different ICECAL integrator capacitor values with ADS6645 digitalization.

ICECAL & ADS6645 PERFORMANCE SUMMARY					
Configuration	**Sensitivity**	**Slope**	**Saturation**	**Dynamics**	**Linearity deviation**
Max Sensitivity	10.4 fC	0.8fC/LSB	14pC	$1.3e^3$	<1%
Default	16.8 fC	1.3fC/LSB	22pC	$1.3e^3$	<1%
Max Input Charge	22.8 fC	1.9fC/LSB	30pC	$1.3e^3$	<1%

6.2. Diamond detector and acquisition system tests with beam

This section shows the results obtained with diamond detectors as beam profile monitors for BWS application in SPS. Beam profiles with different operating scenarios could be recorded and the performance commercial pCVD diamond detector modules from CIVIDEC (area $1cm^2$) evaluated. The QIE10 FE version was also tested in operational conditions with such detectors.

6.2.1. Diamond detector set-up and tests on laboratory

An analog front-end was prepared and tested with an alpha source (241Am) prior installation on the SPS tunnel. To properly drive the detector signal into adapted 50 Ω lines and enhance the signal-to-noise ratio (SNR), the current signal from the detector was transformed into a voltage by a fast transimpedance amplifier (TIA). The amplifier module matches input/output impedance to the transmission line while providing a transfer function as shown on Eq. 6.1. Figure 6.13 shows the electrical model of the set-up.

$$V_{out(Rl\ 50\Omega)} = I_{in} * R_f/2 \tag{6.1}$$

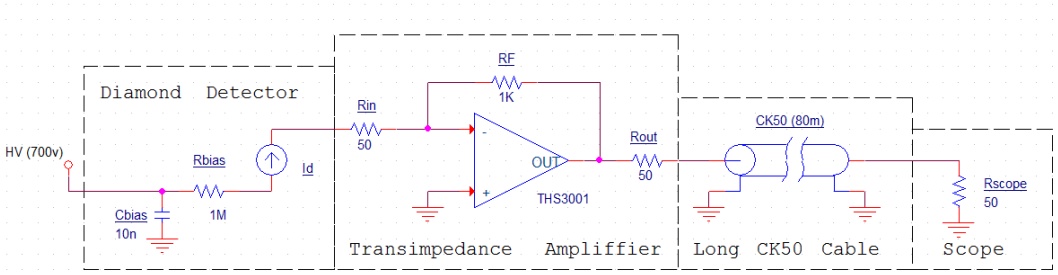

Figure 6.13 – Set-up for diamond detector testing including a THS3001 TIA.

The pCVD diamond detectors were biased with positive and negative high voltages to assess the bi-polar nature of these detectors. The signal out the custom TIA was compared with the response of a commercial AC-coupled module from CIVIDEC, widely used by the CERN's diamond beam loss monitors (DBLMs). The signal from the amplifiers were sampled with a fast oscilloscope at 5 GSPS. The typical detector response for such radiation source, with the THS3001 TIA, resulted on pulses of 4.5 mV amplitude with an approximate duration of 8 ns (FWHM) and a little undershoot (due to the amplifier response). This amplifier was set-up in inverting configuration, thus, negative HV on the detector provided a positive response out of the amplifier. The signal baseline was recovered in around 13 ns, adequate to reach the 25 ns resolution with no pile-up. Concerning the commercial CIVIDEC 40 dB module, it featured a non-inverting configuration with a much faster signal (3.5 ns FWHM) and a higher amplification (40 mV pulses), however the AC-coupling made it not suitable for our BWS applications. The high pass time constant may degrade the beam profile.

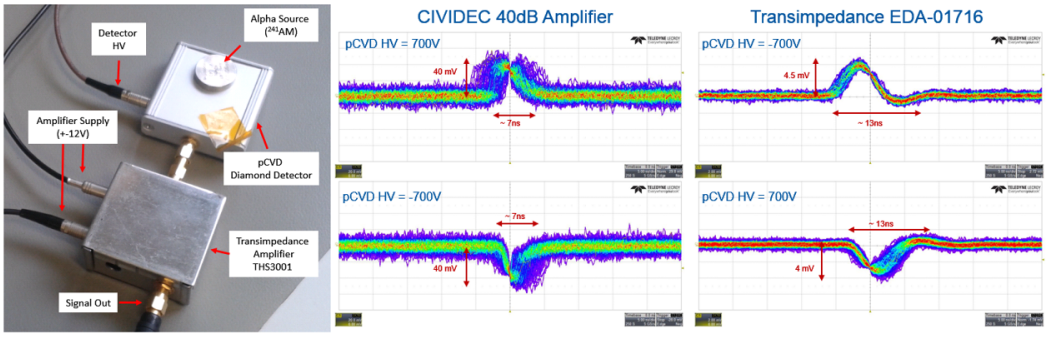

Figure 6.14 – pCVD Diamond detector signal resulting from single Alpha particles (using a 241Am source) at different high voltages (up/down) and front-end amplifiers (left/right).

The charge created in the detector by a single Alpha particle was determined to be around 90 fC. In contrast with other charged particles typical on secondaries shower, such as pions, electrons (>400kEv) or protons (>10MeV) that fully cross the detector and deposit a MIP equivalent charge (1.6fC), Alpha particles are stopped after travelling through a few tens of um in the material and are fully stopped on the diamond bulk. Alphas deposit all their charge on the detector and the signal observed is much higher than a MIP equivalent.

6.2.2. Test with an operational linear beam wire scanner in SPS

6.2.2.1. Installation in SPS tunnel and test set-up

A test system was installed in the SPS cavern, close to a linear BWS (BWS.51731). The system consisted on a set of four diamond detectors placed in pairs above and below the beam pipe at about 1.6m from the BWS. The test acquisition system was placed close to the operational system, based on a scintillator and a photomultiplier. A set of two diamond detectors (above and below) were connected to TIAs with analog signal transmission through long C50 coaxial cables (≈80m), on surface where a scope performed digitalization. The other pair of diamond detectors were attached to the QIE10 Front-End for tunnel digitalizaton. The full front-end was powered and controlled from the surface by the back-end system included on a 6U Europa sub-rack.

The test system allowed to acquire the secondary shower produced by a single scan with three different systems:

1. Two diamond detectors digitalized on surface with a high speed (2.5 GSPS) and bandwidth (500MHz) LeCroy scope.

2. Two diamonds digitalized on tunnel with the QIE10 Front-End prototype.

3. Operational system acquired with existing infrastructure (IBMS card) or with a scope.

Subsequent figures show the system installed on tunnel and surface infrastructure (see Fig. 6.15, 6.16 and 6.17).

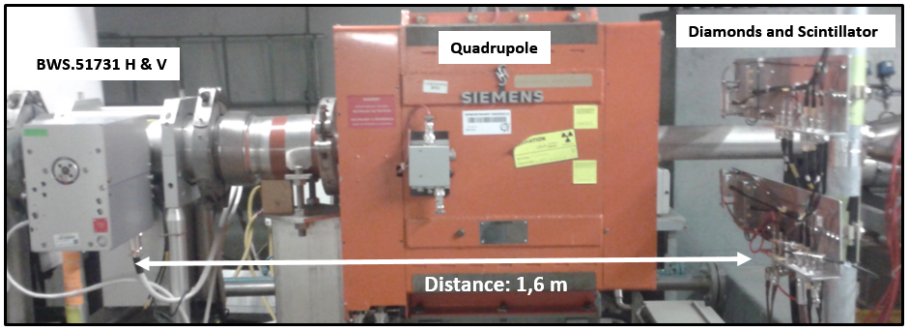

Figure 6.15 – Diamond and operational detector systems placement with respect to BWS51731.

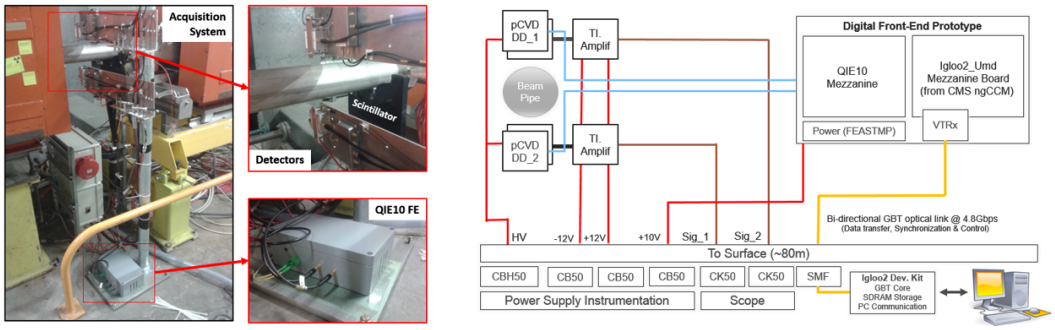

Figure 6.16 – Test set-up installed in the SPS tunnel close to BWS.51731 (left) and connectivity schematic (right).

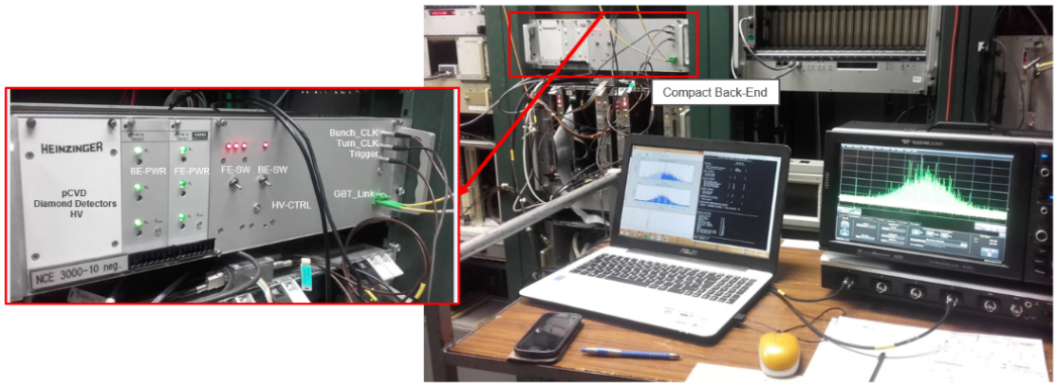

Figure 6.17 – Set-up installed on surface for diamond detector and acquisition system tests.

6.2.2.2. Loses detection

The diamond detectors were tested with the natural loses produced on the accelerator. The loses shown in Fig. 6.18 correspond to a LHC filling with consecutive bunches spaced by 25ns.

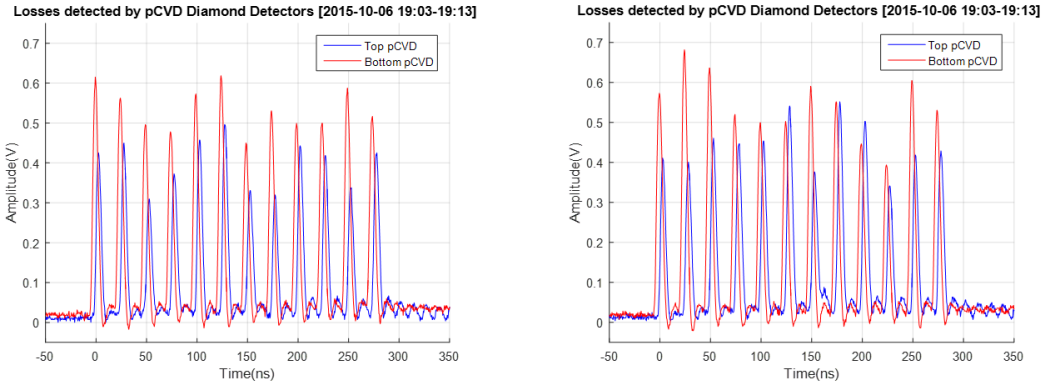

Figure 6.18 – Losses measured by diamond detectors, placed on top and bottom of the beam pipe, during a SPS fill with a nominal 25ns structure (06/10/2015).

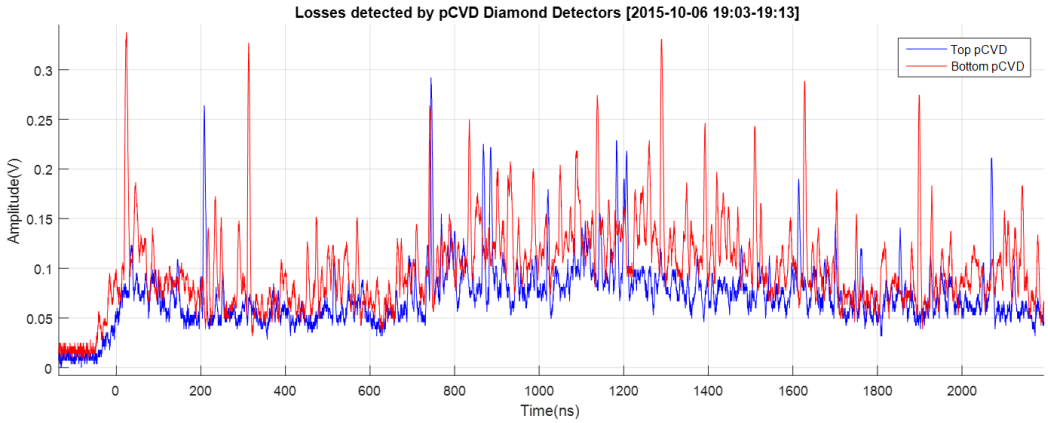

Figure 6.19 – Long injection loses measured with diamond detectors, placed on above and below the beam pipe, in SPS (06/10/2015).

The first signals from the front-end could be recorded with a scope and some highlights were extracted from these measurements:

- The bottom diamond detector systematically shown a higher signal. This could be explained by the directivity of the losses or by the presence of any shielding in the particles trajectory up to the top diamond. It could be also related to differences on the detectors response or amplifiers gain.

- Whereas the general behaviour of both detectors seems to be consistent, there are significant differences between them. The amplitude relationship of both detectors for the same bunch is not constant over subsequent bunches, which suggest a difference in the number of particles crossing each detector.

- On the long losses in Fig. 6.19, both previous effects are present, the spikes on both detectors and their non-coincidence in time can be also explained by different number of particles crossing each detector or by the presence of less energetic particles among the cocktail of secondary particles forming the loss, that are stopped by the diamond bulk and deposit higher energy, producing therefore a much higher amplitude than more energetic particles.

- It worth mention that in some cases loses were only detected by one detector.

6.2.2.3. Diamond detectors tests with nominal intensity beams at 26 GeV

A first measurement campaign was initiated in 2015 after the long shutdown 1 (LS1) and allowed to study the performance of diamond detectors as beam profile monitors with SPS beams at injection energy. The measurements were taken on surface with the set-up previously shown, a fast scope performed digitalization at 1 GSPS on the signal from two diamond detectors and from the operational scintillator-PMT system for comparison.

The beam test were done in 09/10/2015 with a single bunch at nominal intensity, 1e^{11} protons per bunch (PpB). The linear scanner BWS.51731_H was used to perform scans at 1 ms^{-1} at the beginning of the acceleration cycle (26 GeV). The signals recorded by the scope were later processed in Matlab by performing digital signal integrals of 25 ns around the signal generated by the only bunch on the machine, thus, extracting single bunch profiles. Processing results for the three detectors and the combination of both diamond detectors are shown in Fig. 6.20, every point on the profiles correspond to a single beam/bunch interaction, and their separation correspond to the SPS revolution period, ≈23μs.

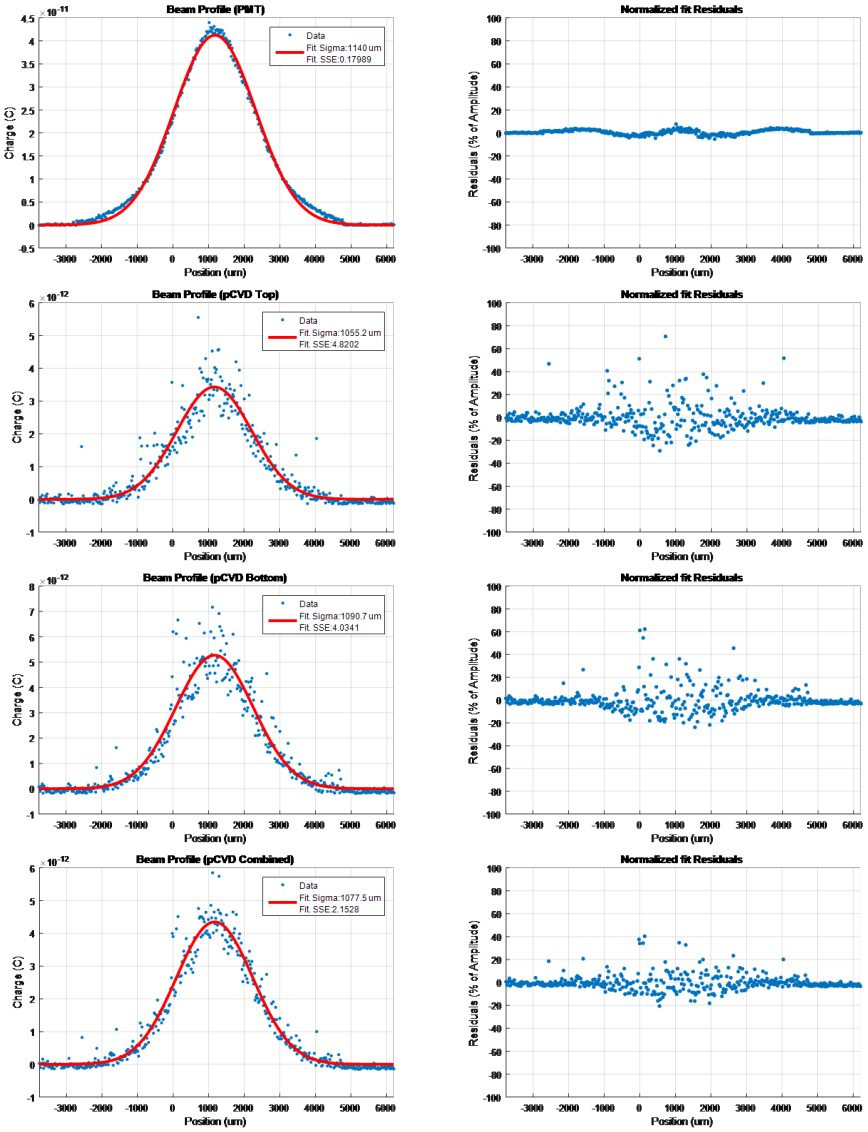

Figure 6.20 – Beam profiles from top to bottom: PMT, diamond detector top, diamond detector bottom and diamonds combination. Beam conditions: Single bunch 1e^{11} PpB at 26 GeV.

There is a clear difference on the detectors signal concerning amplitude spread. While the

operational system shows a smooth Gaussian-like shape, the diamonds feature a big spread around profile. This signal spread is not linked to noise on the scope trace. As shown in Fig. 6.21, the amplitude of the pulsed signal is varying randomly with an amplitude one order of magnitude bigger than the noise present on the diamond signal (≈10 mV). These results suggest that whether there is a significant difference on the number of particles crossing the detectors surface turn after turn, or certain particles of the shower are fully being stopped by the diamond bulk.

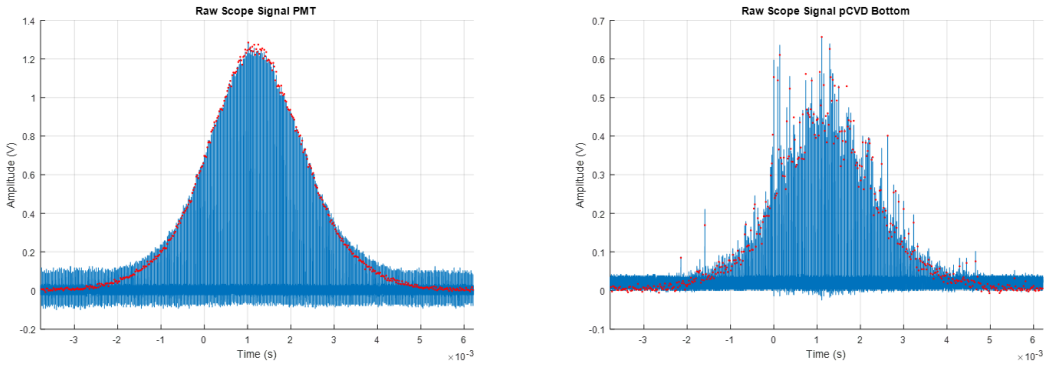

Figure 6.21 – Raw scope traces (blue) with processing results showing bunch integrals overlapped (red dots). PMT signal (left) and pCVD diamond detector (right).

The limited beam time only allowed to capture a set of 5 scans under with this specific beam configuration. The processing results were analysed with the parameters extracted from the Gaussian fit: sigma, centre, sum of square errors (SSE) and standard variation of residuals (normalised to the Gaussian amplitude). The results are summarised in Fig. .6.22.

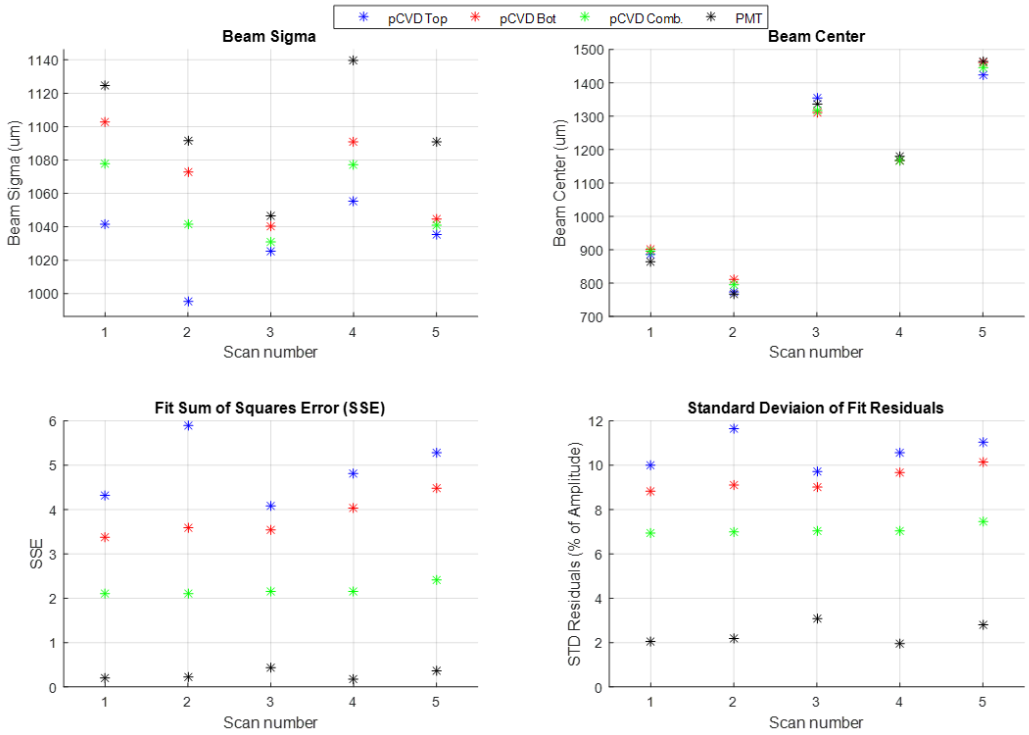

Figure 6.22 – Graphical summary of beam profiles fitting parameters acquired by diamond detectors and PMT.

Given the beam size ($\sigma \approx 1$ mm), the scan speed (1 m/s) and the SPS revolution period

(23 μs) the measures featured approximately 43 points per sigma. Under these circumstances, the beam size measured by diamond detectors seems to be systematically smaller (2-6%) than those measured by the PMT, which could be an effect of the Gausian fit routine given the spread of the diamond measurement. Concerning the goodness of fit (SSE and STD of residuals) the PMT system is showing a much better fitting quality than diamonds. The diamond detectors spread can be slightly reduced by averaging profiles of both diamonds, this emulates an increase on detector area.

Table 6.3 – Numeric summary of beam profile measurements with diamonds detectors and PMT system on SPS for a single proton bunch scanned at 1ms^{-1} with 1.1e^{11}PpB and 26GeV.

	Mean Beam Sigma	**Beam Sigma Error w.r.t PMT**		**Fit SSE**	**STD Fit Residuals (% Amplitude)**
		Systematic	**Random**		
pCVD Top	1030 μm	6.2 %	2.6 %	4.9	10.6 %
pCVD Bot	1070 μm	2.5 %	1.6 %	3.8	9.4 %
pCVD Comb	1054 μm	4.1 %	1.5 %	2.2	7.1 %
PMT	1098 μm	-	-	0.3	2.4 %

These measurements were confirmed in a second iteration with the same beam conditions, the performance of diamonds compared with the PMT system shown similar results.

6.2.2.4. QIE10 FE and diamonds performance for different beam intensities (450GeV)

The detector assembly and the QIE10 Front-End were tested on 23/10/2015 at higher energy. Scans were performed at extraction energy (450 GeV) with a single bunch in the accelerator at two different beam intensities (nominal at 1.1e^{11} PpB and low intensity at 5.2e^{9} PpB). As previously, two diamond detectors and the PMT signal were digitalized on surface with a fast scope. In addition, the signals of another two diamond detectors were digitalized with the QIE10 FE in the tunnel. This configuration allowed to correlate the data of all acquisition systems for the same scan. Position data from the scanner was not recorded and a constant speed of 1 m/s was considered. Figures 6.23 and 6.24 show measurements with all acquisition systems for the same scan at a two different intensities.

Table 6.4 – Beam Tests conditions for measurements at different intensities.

Testing Conditions						
Scan Speed	HV for pCVD D.D.	C. Wire Diam	# of Bunches	Bunch Lengh FWHM	PpB	Energy
1 m/s	-500 V	30 μm	1	4ns	5.2e^{9}-1.1e^{11}	450 GeV

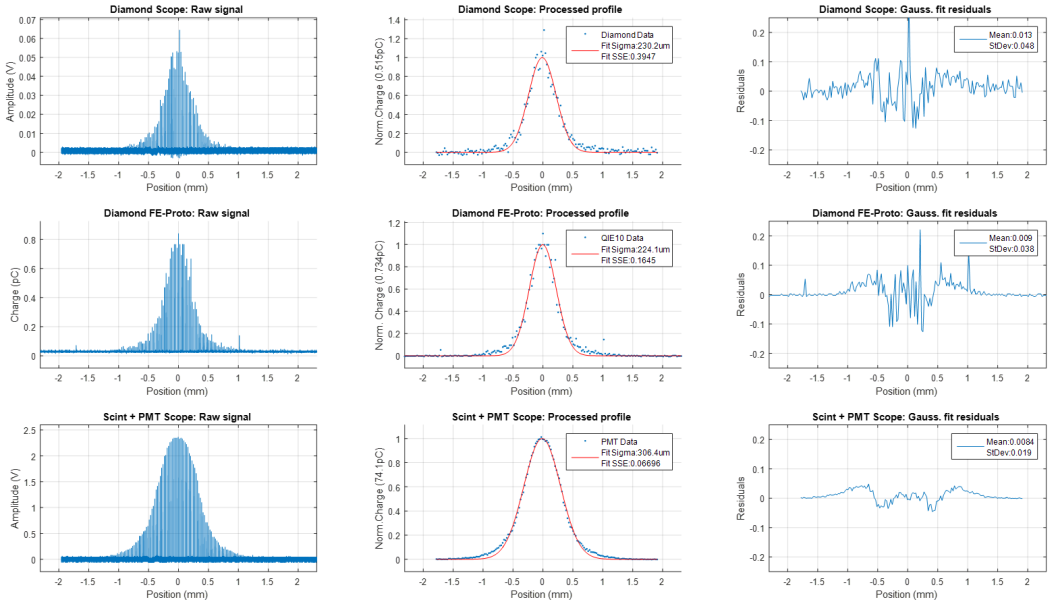

Figure 6.23 – Beam profile measurements from diamond detector (top) and PMT(bottom) digitalized on surface, and from a diamond detector acquired in the tunnel with the QIE10 FE prototype (centre). Beam conditions: Single bunch 5.2e^9 PpB at 450GeV.

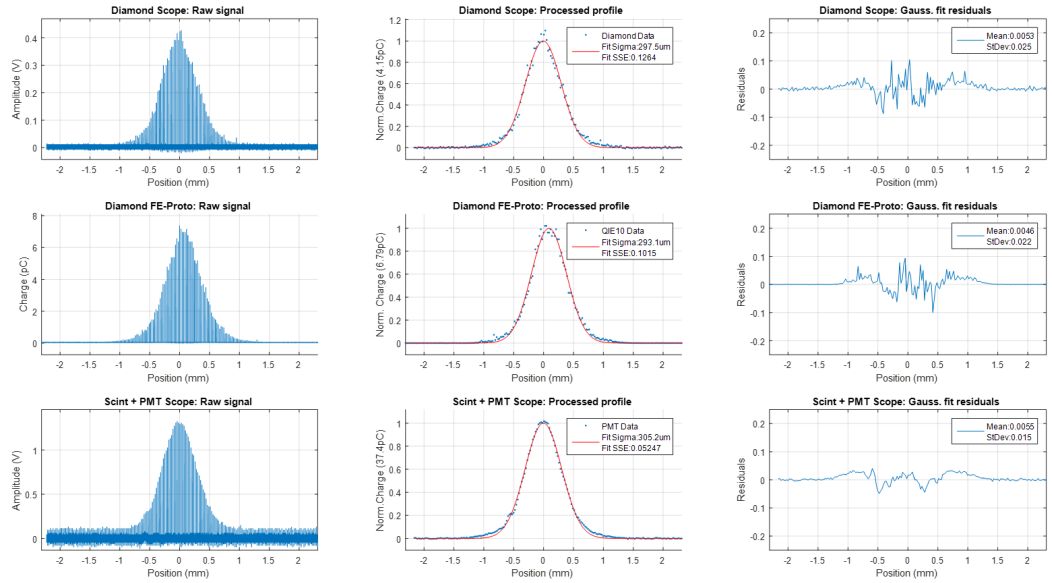

Figure 6.24 – Beam profile measurements from diamond detector (top) and PMT(bottom) digitalized on surface, and from a diamond detector acquired in the tunnel with the QIE10 FE prototype (centre). Beam conditions: Single bunch 1.1e^{11} PpB at 450GeV.

Whereas the scope was freely performing acquisitions at a 2.5 GSPS, the front-end was operated synchronously with the SPS bunch clock to avoid phase drift on the QIE10 integrating windows w.r.t the bunch crossing. A total of 5 scans were possible with all acquisition systems working in parallel (three at 5.2e^9 and two at 1.1e^{11}PpB). Unfortunately, the PMT working point was not correctly set during the whole campaign, the signal from the PMT pre-amplifier was being clipped by a protection diode (see PMT signal shape in Fig. 6.23).

A graphical summary of the processing results is shown in Fig. 6.25.

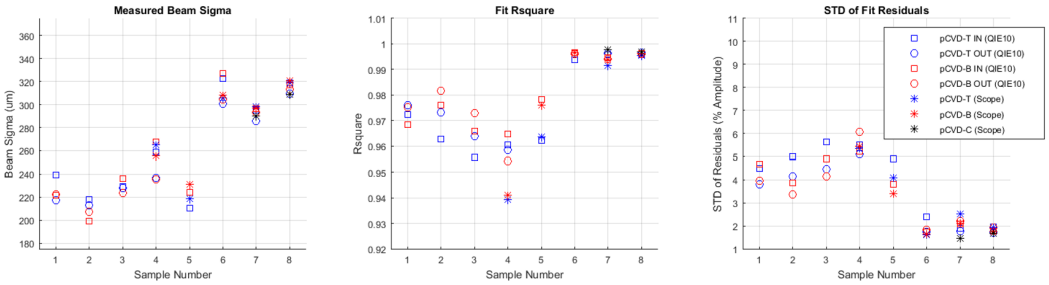

Figure 6.25 – Graphical summary of beam test at different beam intensities for all acquisition systems. Low intensity measurements correspond to sample number 1-5 and high intensity to 6-8.

The large scan-to-scan beam size variations are explained by the fact of doing the measurements during acceleration cycles (injection, acceleration and extraction), each measurement shown in Fig. 6.25 corresponds to a physically different beam. In addition, the lack of a triggering system did not allow to correlate the scanner position with the secondaries acquisition, the beam size calculated might be biased by scan-to-scan speed variations and by the systematic speed difference that the scanner features for IN/OUT scans.

The beam profiles were analysed as previously and the fit quality of the three acquisition systems was studied through the determination coefficient of the fit (R^2) and the standard deviation of the fit residuals (expressed in percentage of the Gaussian amplitude). See Fig. 6.25, note the PMT system was only set in a proper working point for measurements #7 and #8.

With a factor 20 in beam intensity increase ($5.2e^9 \rightarrow 1.1e^{11}$), the profiles amplitude measured by diamond detectors shown a factor 10 increase (0.7pC $\rightarrow$ 7pC) and a significant improvement on the measured spread around the general Gaussian shape. Concerning fit quality, the plots for fit "Rsquare" and "STD of Residuals" show that the performance of diamond detectors is comparable with the PMT system only with high intensity beams (R^2>0.99 and STD $<$ 2%), where the diamond statistical amplitude fluctuations were smaller in comparison with the Gaussian amplitude.

The signals recorded with the QIE10 FE featured a higher SNR than the signals acquired by the scope. Surface acquisitions were influenced by pick-up noise and the limited resolution of the scope (see the tails of the residuals in Fig. 6.23 and 6.24).

The beam size error for diamond detectors was determined based on the beam size difference between top and bottom detectors, calculated as:

$$E_\sigma = \frac{100}{N} \sum_{i=1}^{N} \frac{\sigma_{\sigma_i}}{\mu_{\sigma_i}} \tag{6.2}$$

where σ_{σ_i} is the standard deviation of the beam width measured by top /bottom detector on the scan i, μ_{σ_i} is the mean value measured by the detectors and N is the number of scans at each intensity.

The Table 6.5 shows a numeric summary of the measurements analysis.

Table 6.5 – Numeric summary of the beam profile measurement performance of diamond detectors by using QIE10 FE and Scope readout.

Beam profile measurements summary for the different detectors and readout for Low and High Intensity beams								
	Low intensity				**High Intensity**			
	Mean Sigma	**R2**	**Res. Std.**	**Width. Err.**	**Mean Sigma**	**R2**	**Res.Std**	**Width. Err.**
QIE10_FE IN	230 μm	0.967	4.8 %	4.0 %	313 μm	0.995	2.0 %	0.5 %
QIE10_FE OUT	223 μm	0.969	4.4 %	1.3 %	301 μm	0.996	1.9 %	1.1 %
SCOPE Diamonds	242 μm	0.955	4.5 %	3.1%	308 μm	0.995	1.9 %	0.4 %
SCOPE PMT	-	-	-	-	300 μm	0.997	1.6 %	-

The measurements shown that diamond detectors featured a beam size error within 1-4% for low intensity beams and 0.4-1.1% for high intensity beams at 450GeV. Digitalization with QIE10 FE featured enhanced SNR, see Fig.6.26, and its logarithmic behaviour seem not to impact on the beam profile measurements. The diamond profiles were, in all cases, dominated by statistical amplitude fluctuations.

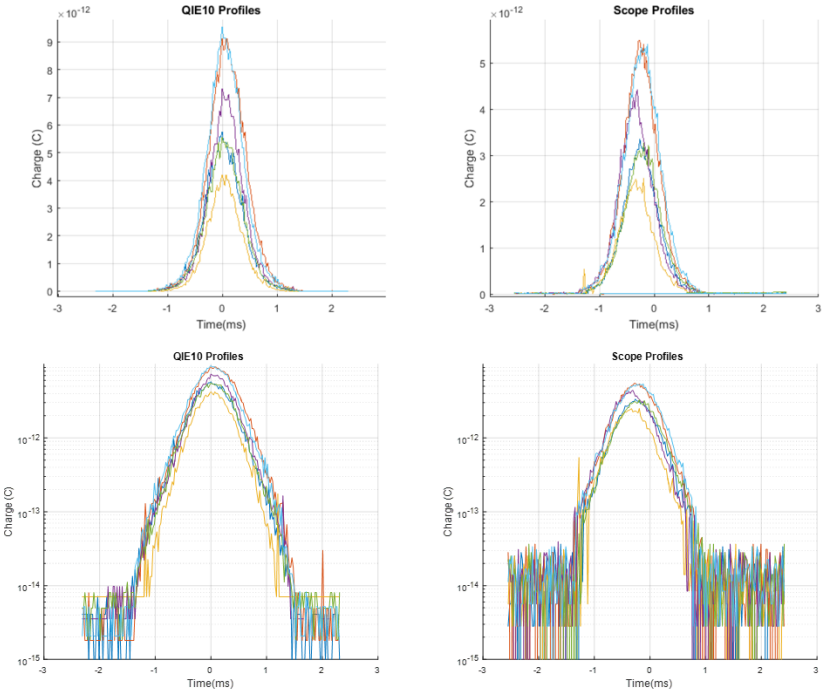

Figure 6.26 – One-to-One comparison of single bunch profiles acquired by QIE10 (left) and by a scope on surface (right) for 1m/s scans performed with BWS.51731.H at 1.1e11PpB and 450GeV. Lineal (top) and lotarithmic (bottom) representation.

6.2.2.5. QIE10 FE and diamonds performance for different beam energies (1e11 PpB)

The test detailed on this section kept the beam intensity constant (1e^{11}PpB) and aimed to study the performance variation over the SPS beam energy boundaries. The SPS performed acceleration cycles with a single bunch (bunch # 45 21:00-21:36) and with two bunches (bunch #45 and #85 21:36-23:30). The beam intensity during the campaign is shown in Fig. 6.27, increase at 21:36 indicates the injection of a second bunch. Acquisitions were performed only with the QIE10 FE digitalizing diamond detectors (one above and other below the beam pipe). Table 6.6 details the testing conditions.

Table 6.6 – Beam Tests conditions for measurements at different energies.

Testing Conditions						
Scan Speed	**HV for pCVD D.D.**	**C. Wire Diam**	**# of Bunches**	**Bunch Lengh FWHM**	**PpB**	**Energy**
1 m/s	-500 V	30 μm	1 - 2	4ns	1.1e^{11}	26 $\rightarrow$ 450 GeV

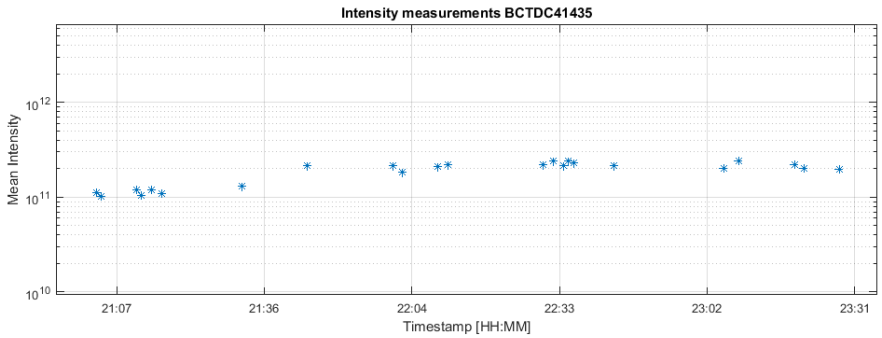

Figure 6.27 – Measured beam intensity by beam current transformer SPS.BCTDC41435 during tests

As previously fitting parameters were extracted from the measurements to study the performance of the diamond profiles. The beam size difference measured between top and bottom detectors was used to estimate the beam with error in each configuration as detailed on Eq. 6.2. In and Out scans, as well as each of the two bunches in the machine, were treated independently on the analysis.

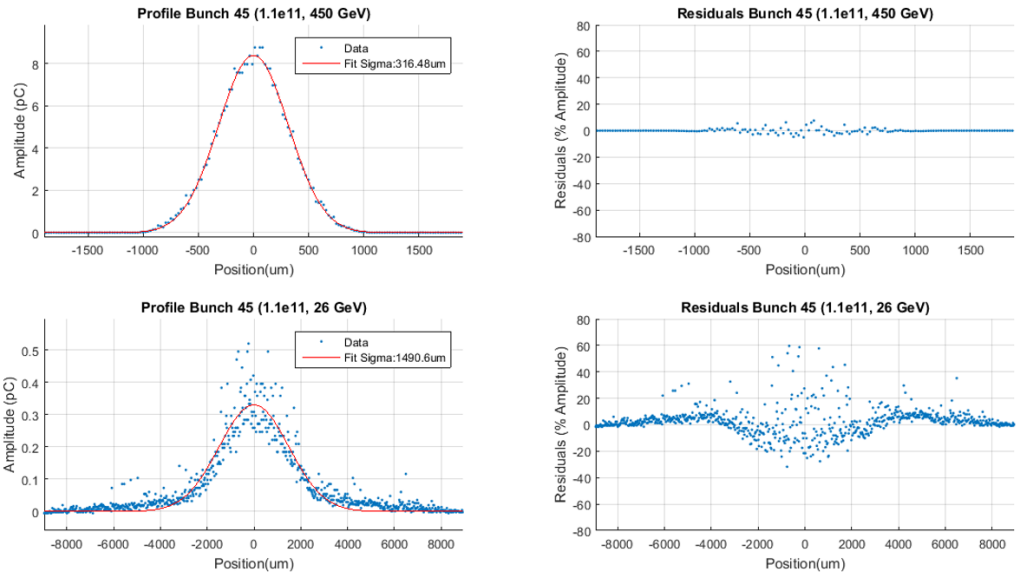

Figure 6.28 – Beam profiles measured with diamond detectors and acquired by the QIE10 FE at SPS extraction energy (top) and injection energy (bottom).

Three important observations can be extracted from Fig. 6.28. The Gaussian amplitude is 20 times bigger, 4.7 times narrower and the profiles looks much better at extraction energy. The amplitude increase on the detector signal is explained as a combined effect of the increase in beam energy and bunch density. A factor 4.5 energy deposition on the diamond was expected between 26 GeV and 450 GeV based on the FLUKA simulations presented on Chapter 2, combined with a 4.7 bunch density increase derived by the narrowing of the beam leads to this factor 20 in amplitude.

A total of 10 scans were measured, 9 of them at low energy and the last one at high energy, limited beam time did not allow to record more data for analysis. Fig. 6.29 (left) shows the beam size measurements analysis of both diamond detectors (top and bottom). The measurements of both detectors were averaged to extract the mean value and the standard deviation of the beam size per scan and bunch. The fit Rsquare was used to evaluate the goodness of the Gaussian fit.

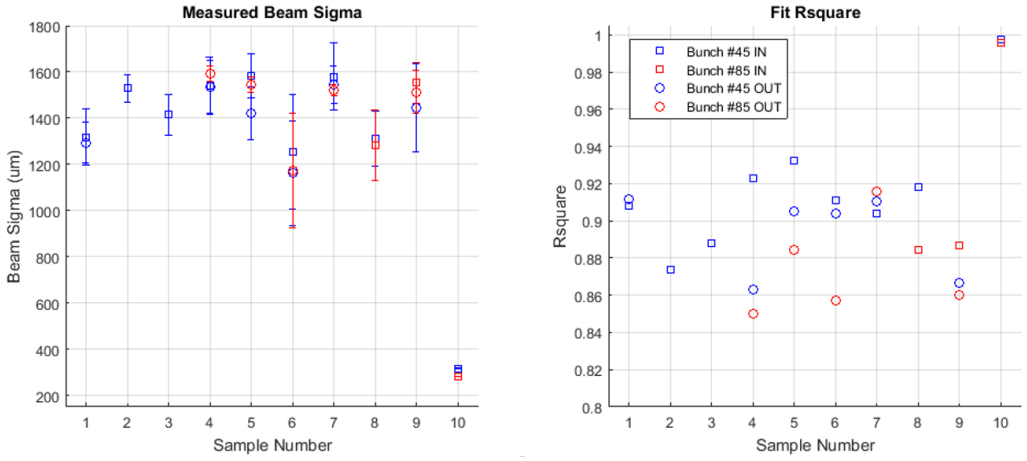

Figure 6.29 – Graphical summary of beam test at different beam energies for diamond detectors acquired with QIE10 FE. Injection energy measurements (1-9) and extraction energy (10) results are shown.

On the measurements performed at injection energy the diamonds showed a beam profile measurement error of 6-10% and a very poor Gaussian fit quality (R2 $<$ 0.89). The measurement at extraction energy for both bunches in the machines shown a beam width determination error $<$1% and a good fitting quality (R$>$0.995). The Table 6.7 collects a numeric summary of the analysis of the results at the two beam energies.

Table 6.7 – Numeric summary of the beam profile measurement performance for QIE10 readout of diamond detectors for different beam energies.

Beam profile measurements summary for the different detectors and readout for Low and High Intensity beams						
	Injection Energy (26 GeV)			**Extraction Energy (450 GeV)**		
	Mean Sigma	**R2**	**Width. Err.**	**Mean Sigma**	**R2**	**Width. Err.**
QIE10_FE IN (45)	1453 μm	0.905	8.0 %	316 μm	0.998	0.14 %
QIE10_FE IN (85)	1417 μm	0.886	8.5 %	281 μm	0.996	0.81 %
QIE10_FE OUT(45)	1400 μm	0.893	9.7 %	-	-	-
QIE10_FE OUT(85)	1469 μm	0.873	5.9 %	-	-	-

The results on previous table and the comparison w.r.t the previous tests suggest that diamond detectors perform better with pilot beams (1-5e^9 PpB) at SPS extraction energy (450GeV) than nominal beams (1e^{11}PpB) at injection energy (26GeV). It can be concluded therefore that, on the SPS context, the performance of diamonds as beam profile monitors is highly affected by both factors, intensity and energy.

6.2.3. Tests with a pre-series LIU beam wire scanner prototype

The full detector assembly was displaced at to a new location in SPS to operate with a LIU-BWS prototype. The Scanner was installed in the SPS location 51740 and the set-up was used for the initial evaluations of the LIU-BWS with particle beam under operational conditions. The presence of other equipment constrained the detector placement to be approximately at 3 metres from the interaction point. The connectivity schematic and configuration with diamonds was maintained as previously. Figure 6.30 shows the location of the BWS prototype system and the placement of the diamond detectors.

According to the FLUKA simulations presented earlier, at this distance the dose deposited by the rain secondaries with a primary beam of 450 GeV is in its maximum. Concerning beams at 26 GeV, it is two meter away from its maximum; the energy deposition on the detector at this distance is one third of that deposited in the optimal point. The shielding effect of the magnets in-between was not considered on simulations and may influence on the measurements.

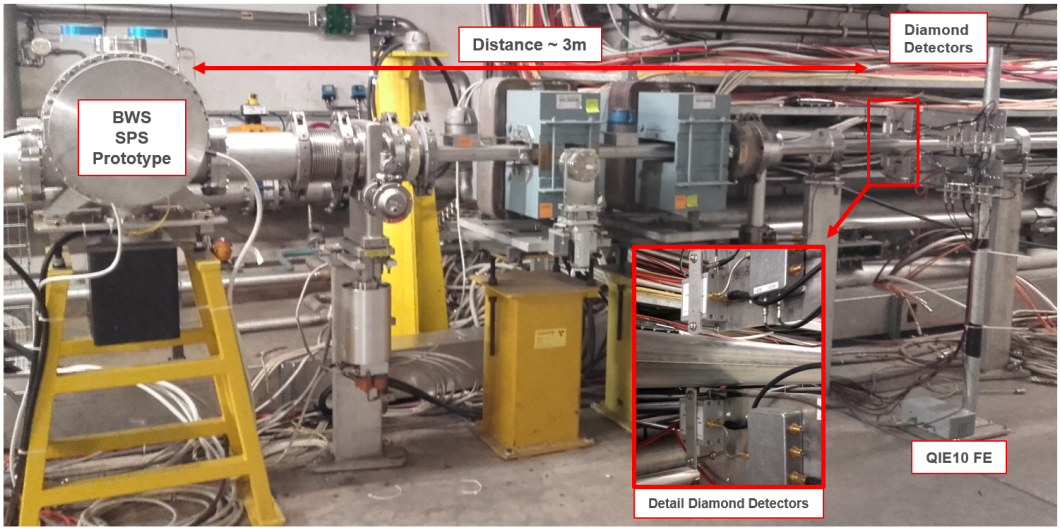

Figure 6.30 – Location secondary particles readout system w.r.t SPS BWS Prototype.

6.2.3.1. Detector system assembly

After some tests, the system was complemented with a PMT and Scintillator system. This system was equipped with a wheel of neutral density filters controlled by a stepper motor. The aim was firstly to have a reference acquisition system for comparison with diamonds and secondly to assess the LIU-BWS precision. The scintillator chosen was a 100x100x10 mm block of scintillator BC-408 (or EJ-200) type, coupled with a fishtail ligthguide and a cylindrical section (Φ=40 mm) that matches the PMT photo-cathode diameter. The PMT is the model Philips XP-2243 whose photo-cathode spectral characteristics matches the scintillator light spectra. The PMT is operated with negative voltage and it was shielded against magnetic fields with a layer of Mu-metal, and electrostatically with a HV shield connected to the photo-cathode potential through 1 Mohm resistor.

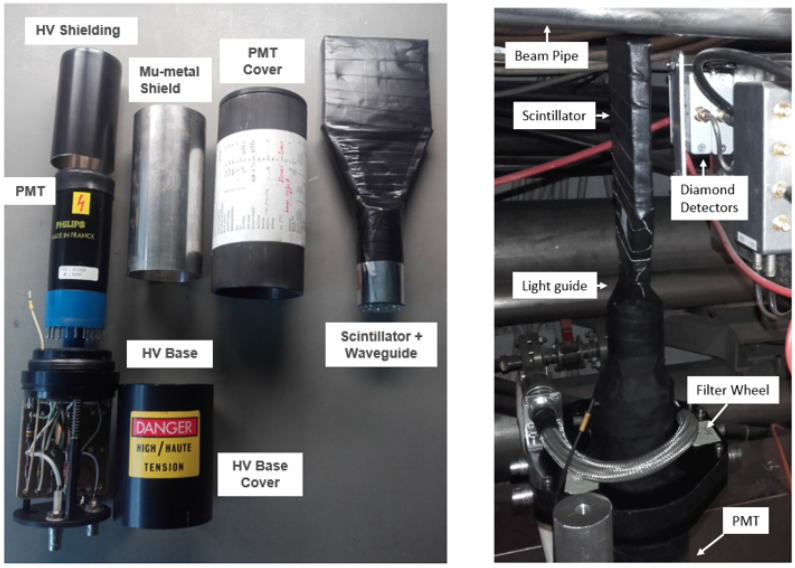

Figure 6.31 – Main parts of the detector in detail (right) and assembled detector installed in front of diamond detectors in SPS tunnel.

- **Modifications and tests prior to installation**

Prior to installation, several modifications on the default HV resistive network were re-

quired to palliate the effect known as "PMT Saturation". This effect is linked to the demand of a high amount of charge during a scan.

It is known that DC current linearity of a PMT is limited to a small portion of the HV divider current, this is also applied to pulsed operation. The performance limitation of PMTs is mainly linked to voltage re-distribution on the dynode chain while the signal is being formed. To enhance pulsed linearity, decoupling capacitors are normally added between dynodes to restrain the resistors voltage drop during the measurement. Pulsed anode current is limited by space-charge effects present on the PMT dynodes only if the base is equipped with suitable decoupling capacitors, the light pulses are short enough and they feature a very small duty cycle. Under these conditions, the max amplitude of a current pulse can be up to thousand times higher than the HV divider current (XP2243 specifies an anode linearity due to space-charge up to 200 mA with 2ns FWHM pulses). Standard bases are intended for very low duty cycle signals and require to be adapted for operation on BWS applications.

The correct operation of a PMT during a measurement when operating bellow the space-charge limit is a matter of total charge per measurement and the value of the capacitors included on the HV resistive chain. Bibliography suggest that to keep linearity $< 3\%$ the capacitors of the last stages are the most critical (those that should deliver more charge), and their values should be calculated as:

$$C_{D4-D5} = 25\frac{Q_o}{V_{D4-D5}},\ C_{D5-D6} = 50\frac{Q_o}{V_{D5-D6}},\ C_{D6-A} = 100\frac{Q_o}{V_{D6-A}} \tag{6.3}$$

Where Q_o is the total desired output charge, $V_{Dx-Dx+1}$ is the voltage drop between two dynodes and C_{Dx-Dy} is the value of the capacitor value.

The specifications for SPS/LHC BWS state that the PMT should respond to light pulses of 4ns FWHM with a repetition period of 25ns (according the bunch structure), this is a 16% duty cycle. The biggest nominal LHC beams on these accelerators oscillate around σ=2mm, translated in measurement time (4σ), this is about 8 ms when the scan is operated at 1,m/s or 0.4 ms at 20 m/s. The maximal desired voltage on 50Ω out of the PMT is 1V, corresponding to a maximal current amplitude 20mA. By approximating the Gaussian shape to a square signal lasting 4σ, the max Q_o required is $\approx 26\mu$C (8ms * 16% * 20mA). The provider recommends a maximum HV supply voltage of 1600V for operation (even if maximum ratings are 2200V), with this supply, the voltage drop on the last stage is about 250V. Under this circumstances, according Eq. 6.3 the last capacitor should be bigger than 10.4μF (C=100* 26μF/250).

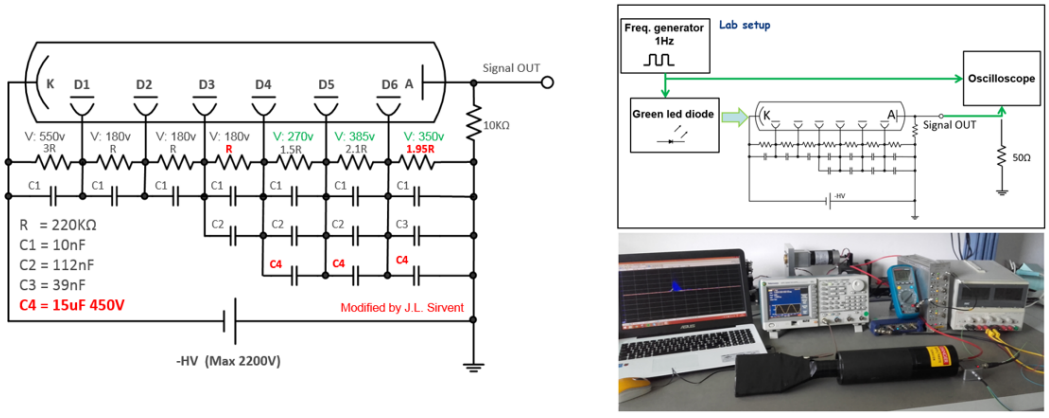

Figure 6.32 – LHC HV base for PMT XP-2243 with modifications in red (left) and saturation effect test set-up (right).

Figure 6.32 (left) shows a standard HV base used on LHC BWS with original components on black and modifications performed on red. For simplicity and according the previous

calculations, 15μF capacitors were included on the last three stages. A couple of resistors were changed to match the provider recommendation on the HV network and reach the best compromise on timing, linearity and gain.

The detector response was tested for different output charges before and after modifications with the set-up shown in Fig. 6.32 (right). A function generator was used to drive a couple of UV LEDs in contact with the scintillator surface (inside the black wrapping), the PMT output signal was supervised with a scope. The detector HV was set to 1600V and its photo-cathode excited with square light pulses of different lengths and amplitudes with 1Hz repetition frequency.

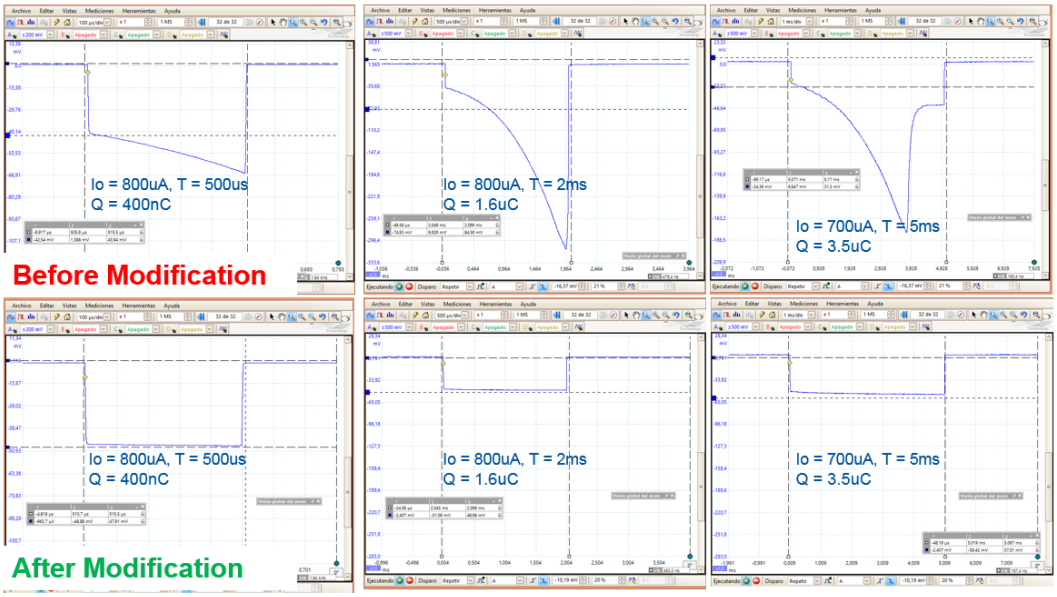

Figure 6.33 – PMT responses to different light input pulses before and after HV base modifications.

As Fig. 6.33 shows, the PMT response is not able to keep the square shape of the pulse for any of the input stimulus (400nC, 1.6μC or 3.5μC) without the last capacitors. This indicates a voltages re-distribution on the HV base that is dynamically changing the gain characteristics of the PMT as the signal is being formed. When the capacitors are included, the PMT can deliver a much higher charge with no apparent saturation. This configuration guarantees that under the SPS beam conditions, the PMT linearity is only limited by space charge effects.

The technique here described was successfully applied on LHC BWS PMTs to virtually eliminate the saturation effect observed in some measurement campaigns.

6.2.3.2. Lead Ions beam profile measurements with diamonds

A lead ion beam containing a single batch of 24 bunches, spaced by 100 ns, was used to test the BWS mechanics and control system (08/12/2015). The scanner was operated at a speed of 10ms^{-1} (half of the nominal speed). These tests also served to study the behaviour of diamond detectors profiles with ion beam. At the moment of the tests, the detectors were placed at 1m from the interaction point, just before the blue magnets, see Fig. 6.30. A set of 11 scans were recorded, 4 at injection and 7 at extraction energy. Only scopes were used to record both the optical position signals and diamond detector signals. The QIE10 FE and the PMT system were not operated.

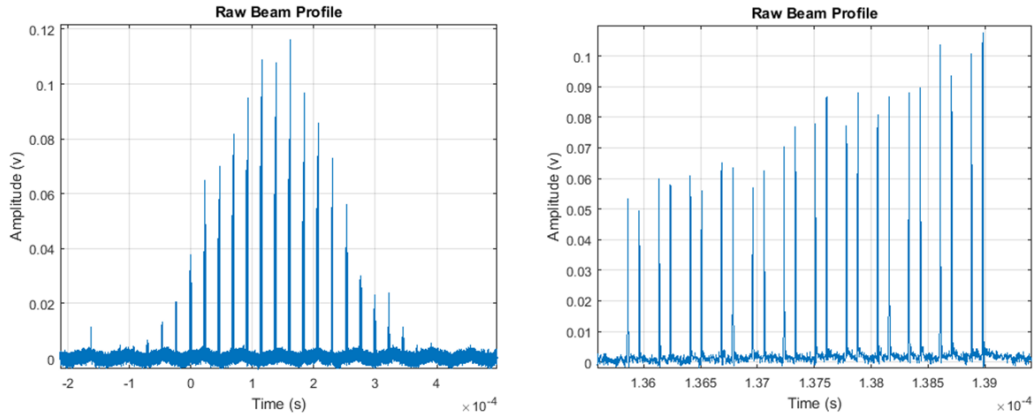

Figure 6.34 – Raw scan signal of a diamond detector seen on scope (left) and zoom in one batch containing the 24 bunches spaced by 100ns (right).

The profiles of the 24 bunches were extracted for each scan, correlated with the scanner position an fitted with a Gaussian. A diamond detector scan signal and bunch structure are shown on Fig. 6.35. The fitting parameters were used to determine the beam sigma incertitude for the different energies, and the determination coefficient (R^2) to assess the goodness of the fit. The fitting parameters per bunch were averaged over all the scans at the same energy, the mean values and standard deviations calculated for the Gaussian amplitude, beam sigma and R^2 .

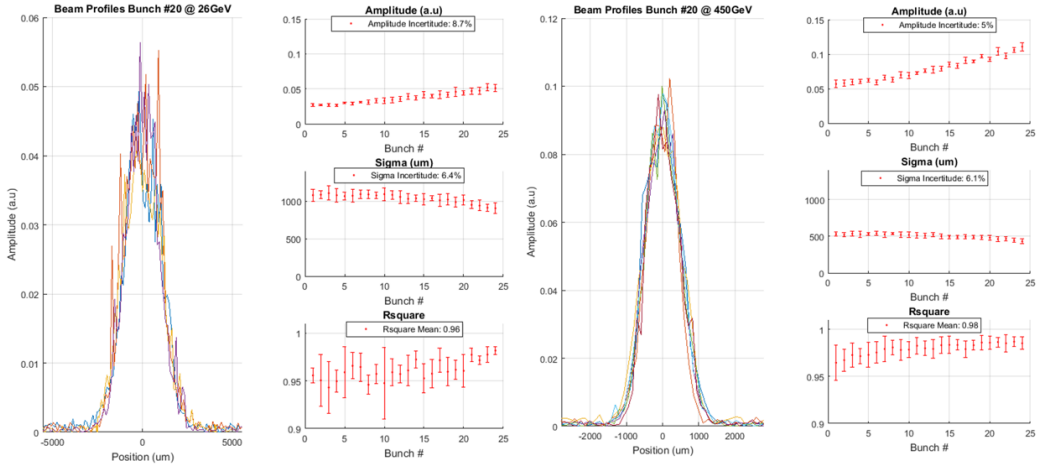

Figure 6.35 – Lead Ion beam profiles measured with BWS SPS prototype and pCVD Diamond detector at SPS injection energy (left) and SPS extraction energy (right).

The Fig. 6.35 shows the processing results for all measurements at each energy, the profiles of a single bunch are also displayed. As seen on the Fig. 6.34 (left) the analysis shows that, for both energies, subsequent bunches feature an increasing amplitude. Concerning beam width, the last bunches show a slightly narrower profile.

As expected, the increase on energy leads to an increase on signal amplitude and a reduction on beam size characteristic of the acceleration cycle. At both energies the beam sigma incertitude is dominated by the statistical fluctuations on the profile amplitude. In relative terms, the sigma incertitude remains ≈6.4% for 26GeV and ≈6.1% for 450GeV of the sigma mean value, in absolute terms this corresponds to ≈60μm and ≈30μm respectively. The incertitude on amplitude of the Gaussian fits per bunch varies from 8.7% to 5% between the two energies. Higher energies feature R^2 values closer to 1, showing that the data has a lower spread around the fit.

In contrast with the diamond detector signal difference for proton beams during the acceleration cycle (20 times higher amplitude and 4 times narrower beams), lead ions featured only a factor 2 increase on the signal amplitude between 26 GeV and 450 Gev, and a factor 2 reduction on beam size. The clear improvement observed on the proton beam profiles with the energy increase cannot be extrapolated to lead ions.

6.2.3.3. SPS LIU-BWS prototype performance and comparison with operational systems

6.2.3.3.1. COAST Beam #1: The precision validation of a pre-series BWS prototype on SPS was done by using a COAST beam with a single bunch at 270 GeV and $0.17e^{11}$ to $0.41e^{11}$ protons per bunch (07/12/2016). This beam consist on keeping a circulating bunch at a fixed energy during long periods of time, consecutive measurements can be done physically with the same beam. This type of beam remains stable in terms of intensity and energy, and only features a little emittance growth with time during the measurements.

For this measurement campaign a total of three scanners were used, a linear scanner at 1 m/s (BWS.517.V), a rotational scanner at 6 m/s (BWS.416.V) and the LIU pre-series prototype (BWS.PROT.V) at its nominal 20 m/s, all of them on the vertical plane. The data from operational scanners was taken from the CERN's logging database. For the prototype system, the signals from the optical position sensors, the PMT system and a diamond detector were acquired with scopes on surface, the QIE10 FE was operated also for diamond detectors digitalization in the tunnel. The data of all systems was processed and fitted with Matlab to calculate the beam width measured by each monitor. Figure 6.36 shows beam profiles from operational systems (BWS.517.V and BWS.416.V) as well as profiles from the LIU-BWS scanner acquired with a diamond detector and the PMT system.

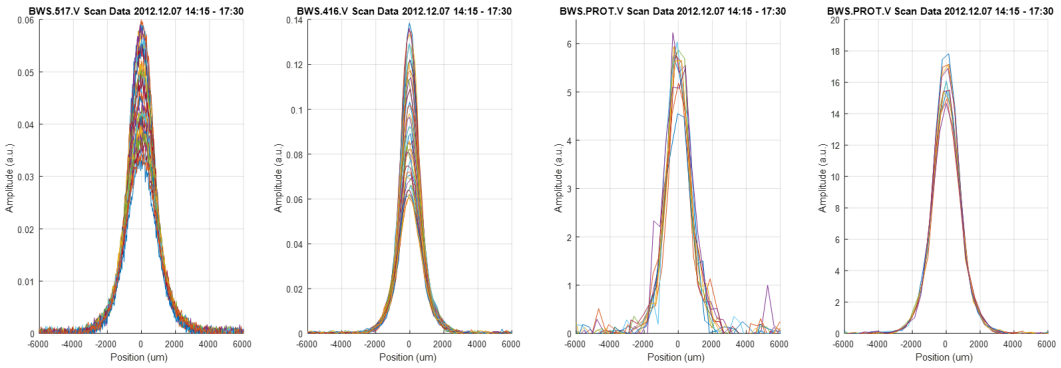

Figure 6.36 – Beam profiles overview from the different scanners, from left to right: BWS.517.V, BWS.416.V, BWS.PROTO.V with Diamond readout and BWS.PROTO.V with Scintillator and PMT readout.

As seen on the previous figure, by increasing the speed of the scan, the number of points per sigma for the Gaussian fitting routine is reduced, potentially increasing the fitting incertitude. In this beam configuration (intensity/energy) the diamond detectors were showing degraded profiles.

The data taking was divided in three periods where beam was dumped and re-injected. The scanners were triggered periodically during each period and the data recorded for post-processing. The beam sigmas, emittances and centroids were calculated for each BWS.

The precision of a wire scanner can be determined with a COAST beam through repetitive measurements over time. By studying the residuals of the beam width measurements w.r.t a linear fit performed on the data (to compensate for emittance/sigma increase) the measurement spread can be estimated. This process was done on the data acquired by the three systems as shown in Fig. 6.37 and 6.38. The Gaussian sigma of the residuals histogram

is defined as the measurement incertitude.

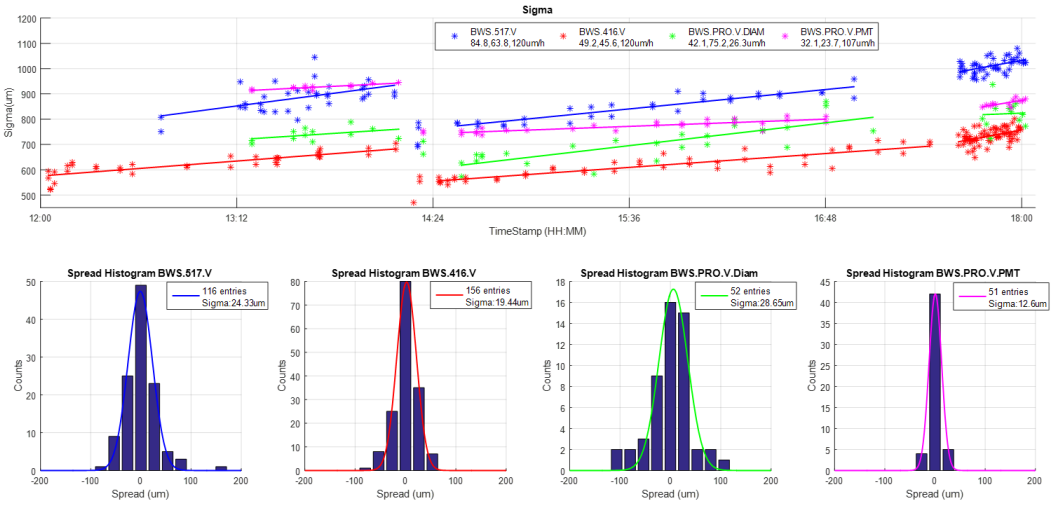

Figure 6.37 – Sigma measurements and evolution for the scanners under test during COAST 2016.12.07, linear fits for emittance growth correction (top), and measurement spread after correction for the different scanners (bottom).

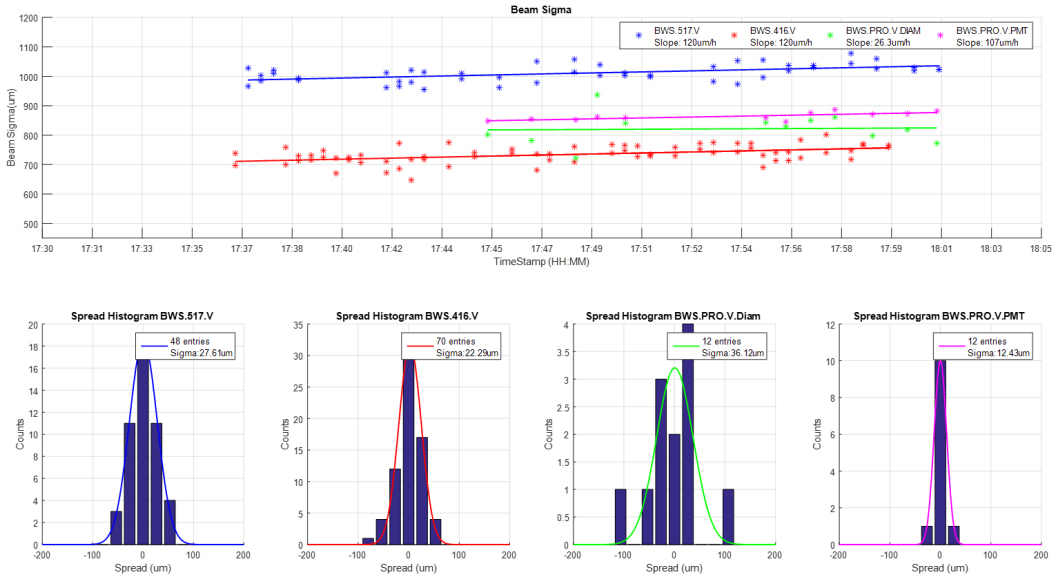

Figure 6.38 – Zoom on beam sigma measurements (17:30-18:00) and evolution for the scanners under test during COAST 2016.12.07, linear fit for emittance growth correction (top), and measurement spread after correction for the different scanners (bottom).

The previous plots are showing the beam sigma measured by each scan as a function of time. The optics of the accelerator (beta parameter) are different at the location of each scanner, so the beam width measured by each scanner is also different. Note that there is an important difference on the measurements provided by the diamond and PMT for the prototype scanner, especially during the first two periods (12:00-14:20 and 14:24-17:00). At this point the PMT system was not equipped with a filter wheel, the photon yield provided by the scintillator was too strong, and the PMT had to be operated with very low HV. Under this conditions, beam profiles linearity was compromised by the presence of space-charge effects on the PMT, leading as a result an apparent wider beam. On the second period this effect is slowly being palliated, the emittance growth leads to a lower beam density and therefore

a smaller amplitude on the PMT signal, so progressively the PMT was exiting from its non-linear region and measurements were getting closer to the values determined by diamond detectors. This was not applicable to the first period where the intensity was four times higher (0.4e^{11}PpB). On the third period the PMT was fully out of the non-linear region and the measurement slope was closer to operational systems (see Fig. 6.38).

The data analysis (see Fig. 6.37) resulted in a beam sigma measurement incertitude of 24 μm for the linear BWS.517 and 19 μm for the rotational BWS.416. Concerning the LIU-BWS, the measurement incertitude was 36 μm when using diamond detectors and 12 μm with the PMT system. These numbers were consistent when the analysis only covered the last measurement period (see Fig. 6.38), where the PMT was operating correctly.

Figures 6.39 and 6.40 show the beam emittance calculated for all scanners, dispersion on the vertical plane was neglected. A systematic difference is clearly shown between BWS517 and BWS416 were emittance is overestimated and underestimated w.r.t to the LIU-BWS prototype. Emittance incertitude resulted on ≈123 nm (6.1 %) for BWS517, ≈107 nm (5.4 %) for BWS416, ≈44 nm (2.2 %) for the LIU-BWS prototype using the PMT system and ≈140 nm (7 %) with a diamond detector.

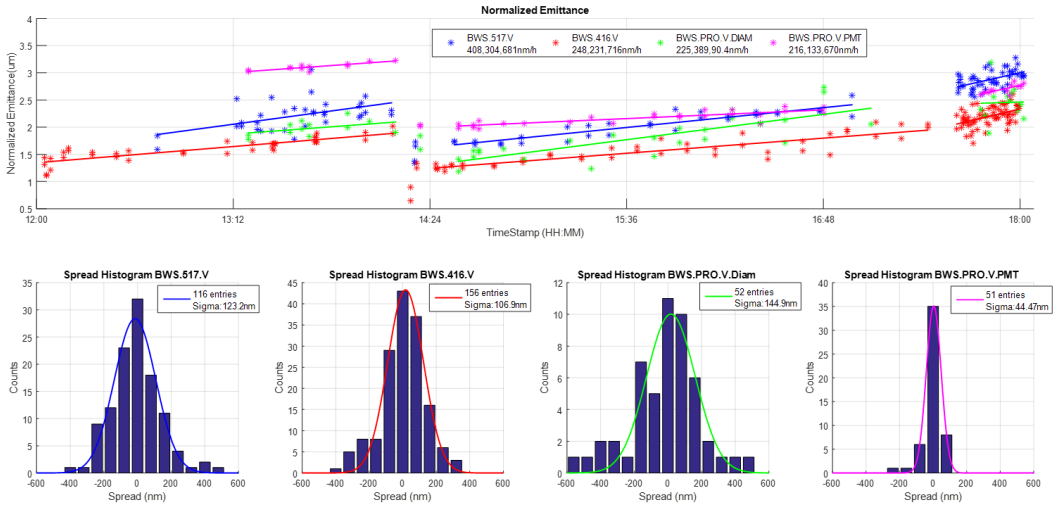

Figure 6.39 – Normalized emittance measurements and evolution for the scanners under test during COAST 2016.12.07, linear fit for emittance growth correction (top), and sigma measurement spread after correction for the different scanners (bottom).

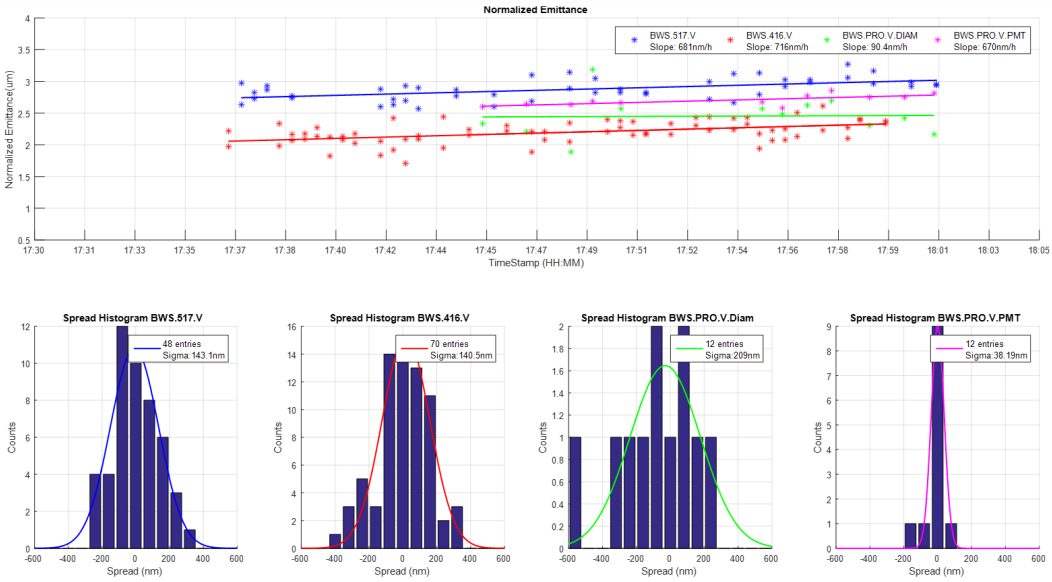

Figure 6.40 – Zoom on normalized emittance (17:30-18:00) measurements and evolution for the scanners under test during COAST 2016.12.07, linear fit for emittance growth correction (top), and sigma measurement spread after correction for the different scanners (bottom).

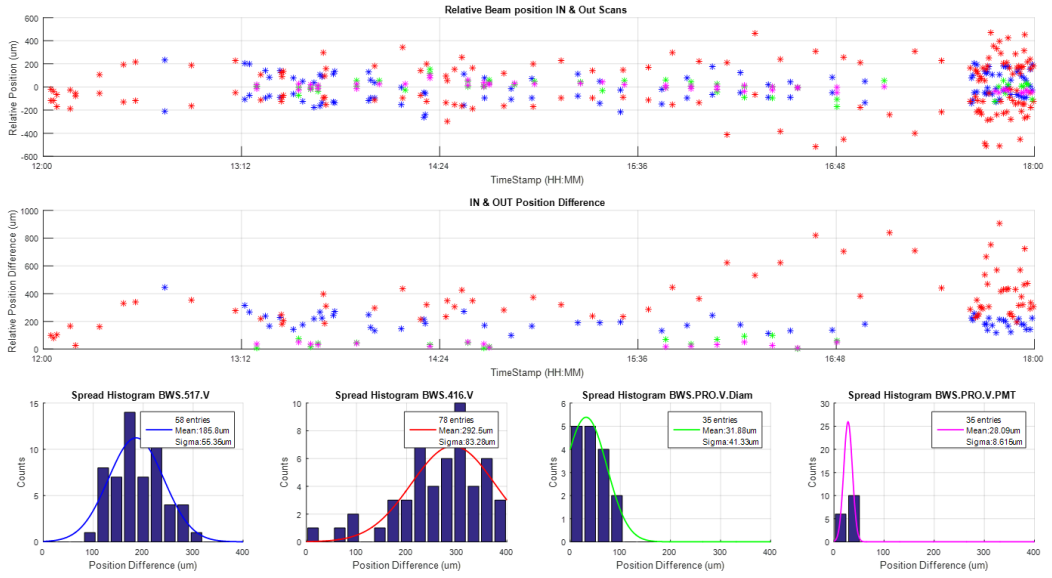

Figure 6.41 – Systematic IN/OUT beam positions measurement error. Measured beam position for IN/OUT scans (Top), IN/OUT position difference (Middle) and histogram of the position difference for the scans under test.

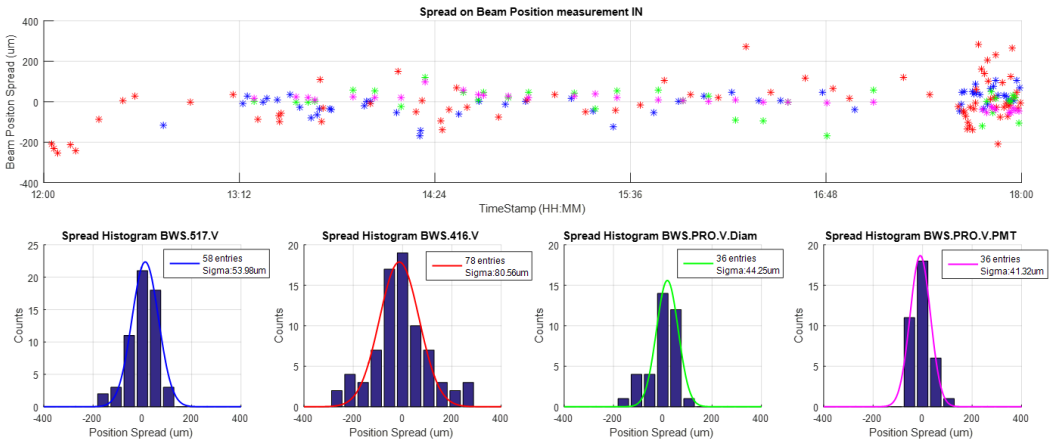

Figure 6.42 – Beam position measurement spread (top) and histograms for IN scans.

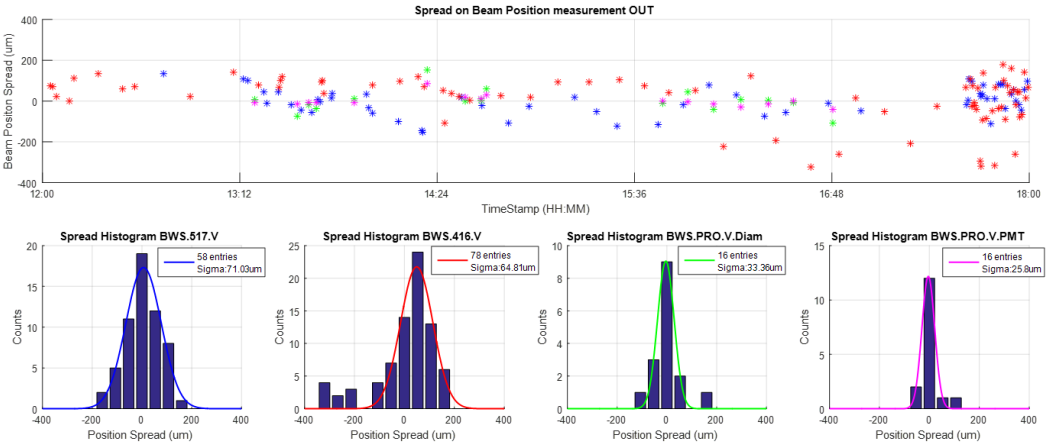

Figure 6.43 – Beam position measurement spread (top) and histograms for OUT scans

The Figs. 6.41, 6.42 and 6.43 show a detailed analysis of the beam centroid determination. Operational scanners feature a systematic beam position difference for IN and OUT scans in the order of 100-200 μm, this is reduced to $\approx$20 μm on the prototype scanner with the use of the optical position sensor. In addition, the prototype scanner featured around 2 times smaller spread on the beam position measurement independently of the detector used. A global summary the campaing resutls is collected in Table 6.8.

Table 6.8 – Numeric summary of BWS performance test with a COAST beam 07/12/2016.

Numeric summary COAST 2016.12.07 (Operational scanners performance VS Prototype)								
Scanner Name		Scan Speed (m/s)	Points per Sigma	Sigma Incertitude (μm)	Emittance Incertitude (nm)	Beam Position Syst. Diff IN - OUT (μm)	Incertitude IN (μm)	Incertitude OUT (μm)
BWS.517.V LIN		1	37	24.3	123 (6.1%)	186±55	54	71
BWS.416.V ROT		6	4	19.4	107 (5.4%)	292± 83	81	65
BWS.PROT.V	DIAM	20	1.5	28.6	140 (7%)	32±41	44	33
	PMT			12.6	44 (2.2%)	29±9	41	26

During the second measurement period (14:20 - 16:50) the QIE10 FE was operated in parallel to digitalize the signal of one diamond detector in the tunnel at the same time that another was being acquired on surface. With both systems it was possible to acquire not only

secondaries produced by the LIU-BWS prototype but also the ones coming from BWS517, located approximately 5 meters upstreams. Figure 6.44 shows a one-to-one comparison of the profiles acquired in each case, an improvement in terms of noise can be noted for the QIE10 FE profiles.

The normalised emittance was calculated for both scanners and acquisition systems (see Fig. 6.45). Both acquisition system shown a very good agreement, especially on the profiles from BWS517 that featured a higher number of points per sigma due to the scan speed, however, despite the QIE10 noise improvements, profiles were still strongly influenced by the typical amplitude statistics from diamond detectors.

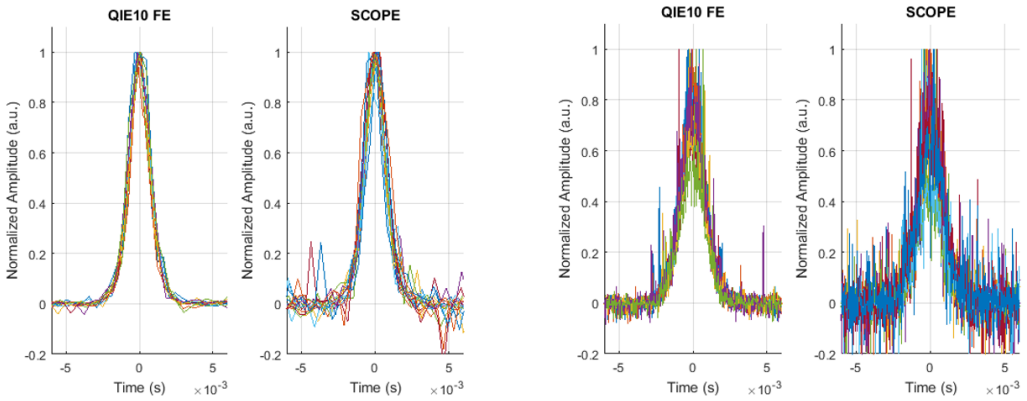

Figure 6.44 – Diamond detectors beam profiles acquired with QIE10 and by a scope on surface for scans from BWS Prototype (left) and BWS517 (right).

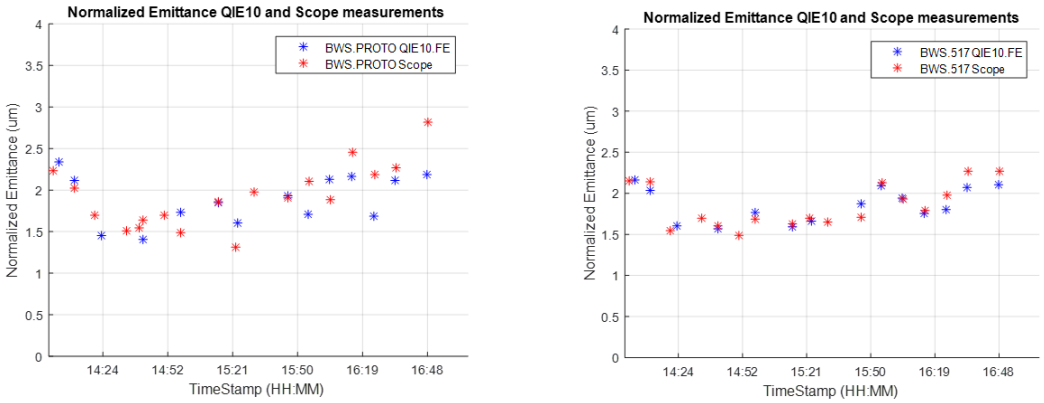

Figure 6.45 – Normalised emittance measured with pCVD diamond detectors with QIE10 front-end prototype and scope.

6.2.3.3.2. AWAKE Beam: The AWAKE beam was used to further test the LIU-BWS accuracy and diamond detectors performance (09/12/2016). The beam consisted of a single bunch in the accelerator with 1.1e^{11} PpB at 400 GeV. As previously, prototype scanner measurements were compared with the linear BWS517 in terms of beam size and centroid spread. Only a single pCVD diamond detector acquired on surface was used to measure the beam profiles of the LIU-BWS. The PMT system could not operate within its linear region since the filter wheel was not yet mounted and the scintillator photon yield was too strong, thus PMT profiles were strongly influenced by space-charge effects.

As shown in Fig. 6.46, and on previous tests with similar beam conditions, the diamond detectors profiles shown clean profiles. The maximal charge generated on the diamond detector by the secondaries at the centre of the Gaussian reached 8pC, at this point amplitude statistics were negligible (≈5000 MIPS).

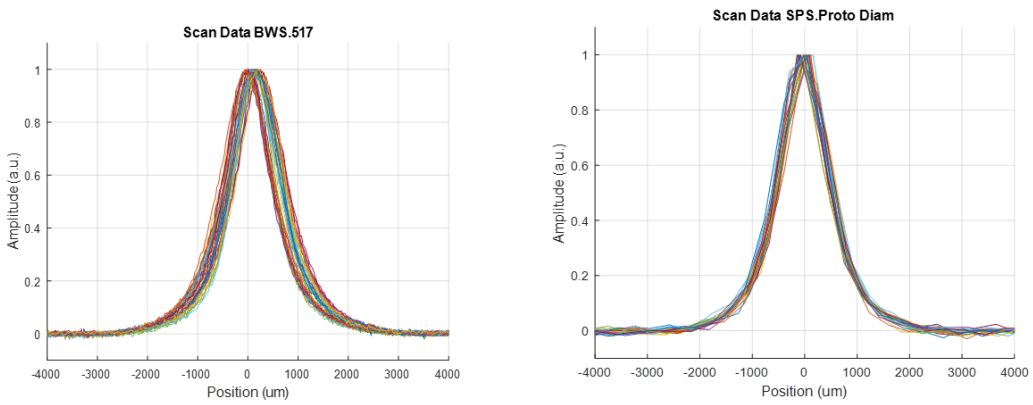

Figure 6.46 – Beam profiles obtained with linear BWS.517 at 1ms-1 with potentiometer position reading and scintillator-PMT for secondaries acquisition (left) and rotational BWS.SPS.Prototype at 20ms^{-1} (right) with optical encoder position reading and pCVD diamond detector secondaries acquisition.

These beam conditions enhance the performance of diamond detectors for profile monitoring, in Fig. 6.47 the beam sigma measured with the LIU-BWS system and BWS517 is shown, as well as the spread around a linear fit. The smaller spread of the LIU-BWS profiles with diamond detectors, allows the identification of potential shot-by-shot emittance growth, hidden behind the measurement incertitude on the case of BWS517. The reproducibility of the new scanner and the clean profiles acquired with diamond detectors leaded to a factor 2 improvement on beam sigma measurement precision w.r.t linear scanners (20 μm incertitude for the LIU-BWS prototype and 40 μm incertitude for BWS517). Emittance calculation and beam centroid analysis are shown in Fig. 6.48 and 6.49 respectively.

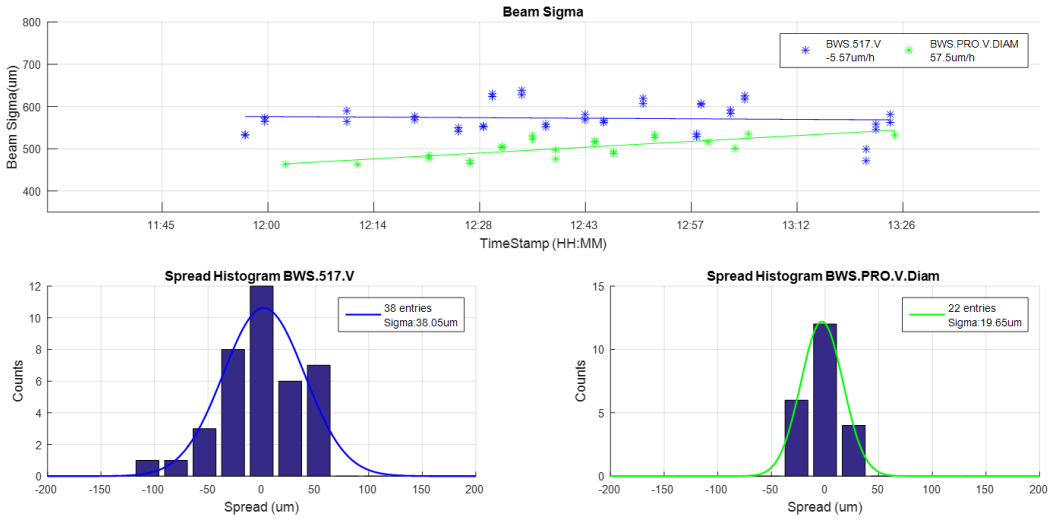

Figure 6.47 – Beam Sigma measured with BWS517 and BWS.SPS.Prototype with pCVD Diamond Detectors

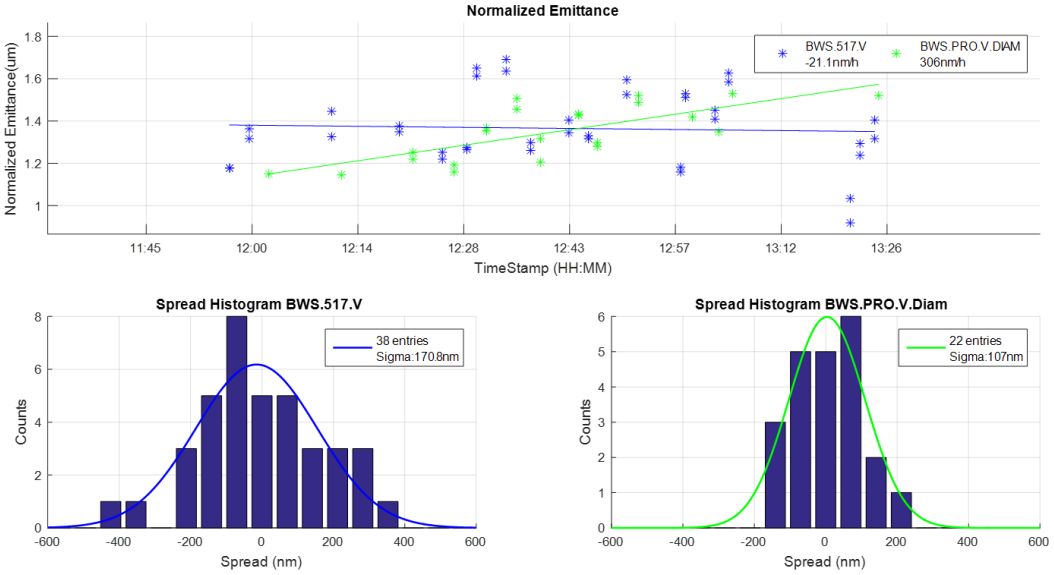

Figure 6.48 – Normalized Beam emittance measured with BWS517 and BWS.SPS.Prototype with pCVD Diamond Detectors

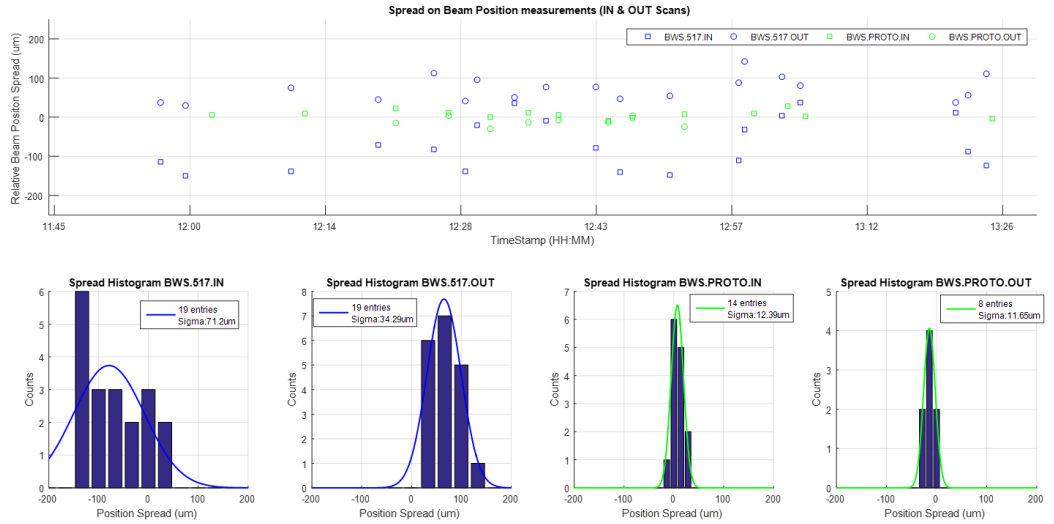

Figure 6.49 – Relative beam centre position measurements for BWS.517.LIN and BWS.PROTOTYPE.ROT and histograms for IN and OUT spread on each scanner

Table 6.9 – BWS measurements summary with AWAKE beam

BWS test beam,summary (AWAKE Beam Single bunch 1.1e11p @ 400GeV)							
Scanner	**Scan Speed (m/s)**	**Points per Sigma**	**Beam Sigma**		**Beam Centroid**		
			Mean Sigma (um)	**Sigma Spread (um, %)**	**In Spread (um)**	**Out Spread (um)**	**I/O Difference (um)**
BWS.517	1	25	572.2	38.7, 6.8%	71.2	34.3	143.0
BWS.PRO	20	1.1	501.0	20.9, 4.2%	12.4	11.7	18.9

The LIU-BWS prototype featured an improvement not only on absolute sigma precision, but also on the systematic IN/OUT beam centroid position difference and on the beam centroid position precision. Considering the scanners speed, the linear BWS.517 scanner provides a total of 25 point per sigma (PpS) for beam profile fitting (1 m/s), this number is drastically reduced on the prototype scanner (20 m/s) to about 1 PpS. Which is translated in fewer points

on the prototype measurements to perform profile Gaussian fitting, and therefore a higher incertitude on the fitting results. Even under these circumstances the prototype scanner is shown to perform better.

The result of this test confirmed the usability of diamond detectors for BWS with nominal intensity beams at high energies (> 400 GeV). Whereas their performance seems not suitable for SPS energy boundaries (specially on the low end), they could be good candidates for the LHC BWS.

6.2.3.3.3. COAST Beam #2: Another beam tests with a COAST (0.23e^{11} PpB at 270GeV) was done to assess the scanner and diamond detector performance with the PMT detector system working properly (10/05/2017) for comparison, a filter wheel was included on the PMT assembly. On this campaign only data from BWS517 (scan speed = 1 m/s) and BWSProto (scan speed = 20 m/s) were considered. The detectors signals from the BWSProto (PMT and diamond detector) were digitalized on surface with a scope as well as those from the optical position sensors. For these measurements, BWS517 was set up in bunch-by-bunch mode to avoid known issues on the turn-by-turn acquisition mode, such as the over estimation of beam width.

The beam sigma determined by both detectors form the LIU-BWS prototype shown consistent results, which indicates that PMT was operating properly (see Fig. 6.50). Diamond detector profile measurements featured a lower precision given the impact of amplitude statistics.

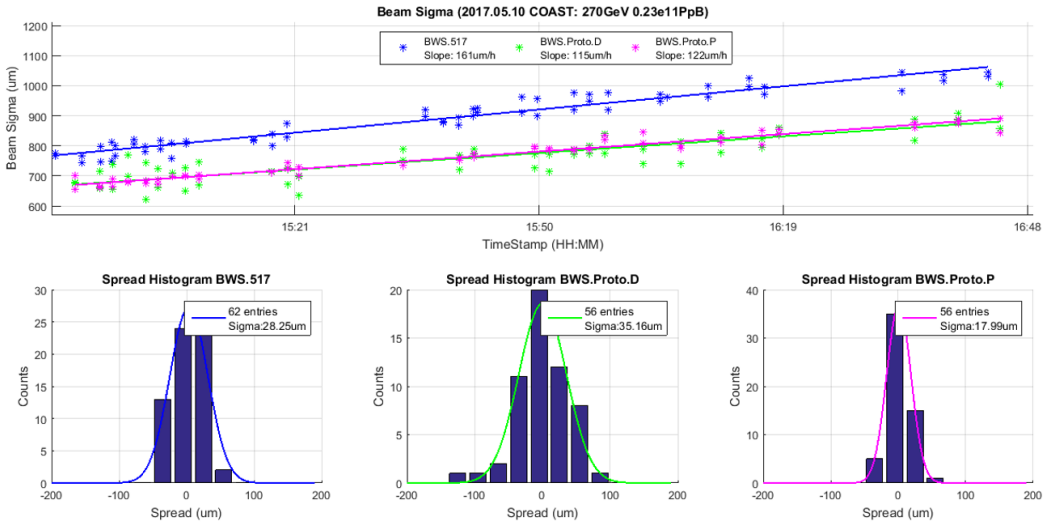

Figure 6.50 – Beam width determination and fit residuals for BWS517 (blue) and BWS prototype with a pCVD diamond detector (green) and a PMT system (magenta).

The beam size incertitude based on the fit residuals was determined to be 28.2 μm (3 % of sigma) for BWS517, 35.2 μm (4.3 % of sigma) for BWS proto with pCVD diamond detector readout, and 18 μm (2.3 % of sigma) with PMT readout. These numbers are consistent to those calculated on the previous COAST and confirms the measurement precision improvement (around a factor 2) with the new scanner mechanics, despite measuring a lower number of points per sigma.

Figure 6.51 shows the normalized emittance calculated by both scanners. The previous COAST determined that the scanner BWS517 was over-estimating the beam emittance w.r.t the BWS prototype. This effect might be linked to the strong low pass filtering effect of the turn-by-turn mode, which distorts the measured beam profile. In bunch-by-bunch mode, and after applying a 5% downscaling on the potentiometer position reading of BWS517, the linear fits and data points of both scanners are practically overlapped. The beta parameters were taken from the optics database for the LHC beams (ByBWS517=101.5 and

ByBWSProto=73.5) and no dispersion was considered for the scanning plane (vertical). The incertitude on beam sigma was translated into the following precisions on emittance: 119 nm (4.7 % of emittance) for BWS517, 219 nm (8.7 % of emittance) for LIU-BWS prototype with diamond detectors and 76 nm (3 % of emittance) for LIU-BWS prototype with PMT readout.

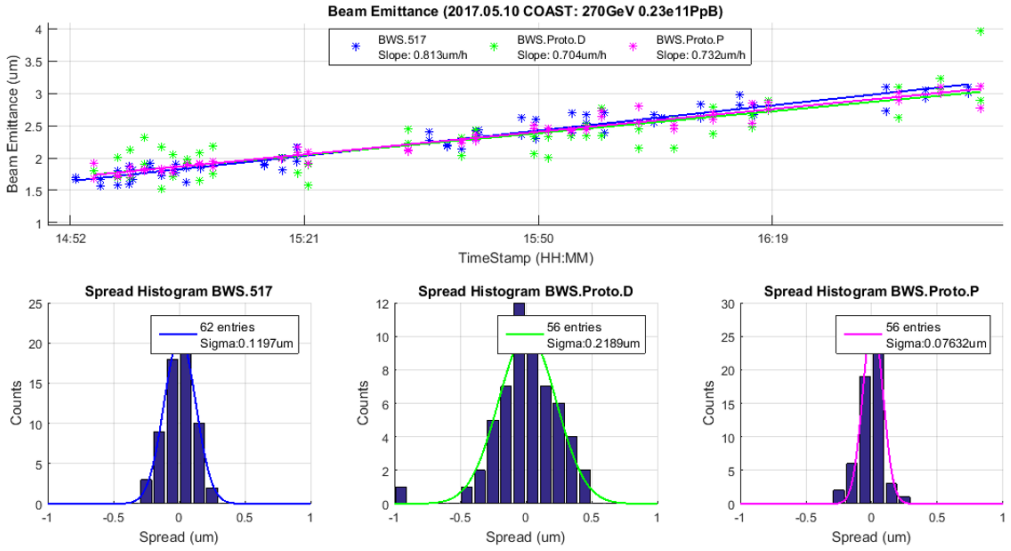

Figure 6.51 – Normalized emittance determination and fit residuals for BWS517 (blue) and BWS prototype with a pCVD diamond detector (green) and a PMT system (magenta).

Concerning the beam centroid detection, the linear BWS517 features, on this specific configuration, a systematic difference on the beam centroid position measurement ≈1mm, much higher as the one shown on the previous tests. Figure 6.52 shows the relative beam centroids measured by both scanners, the prototype scanner featured negligible systematics on beam position for in/out scans, the spread histograms on the bottom of the figure also show that the beam centroid was measured with a higher precision with the prototype scanner (30% better with a diamond detector and 46% with a PMT readout).

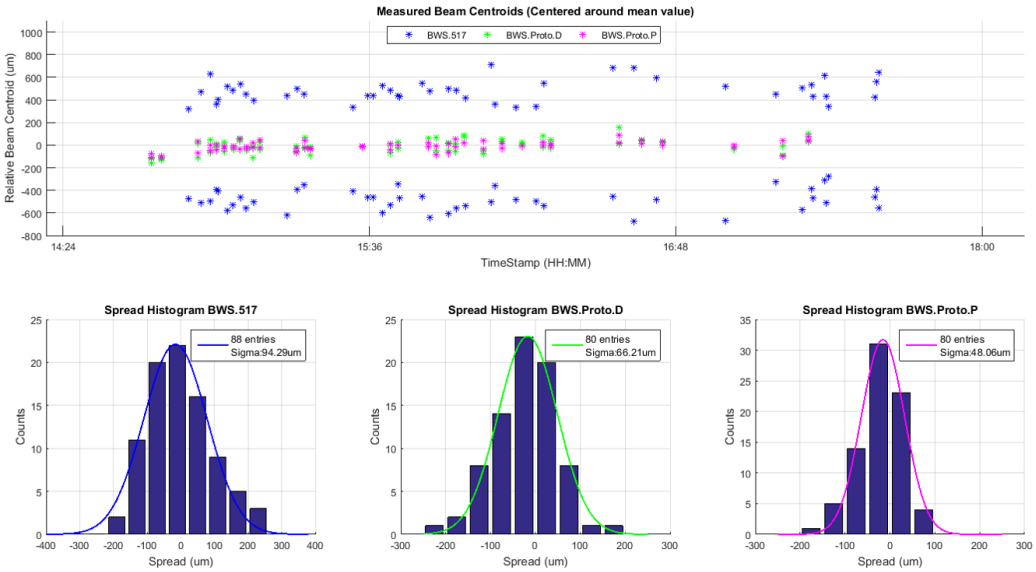

Figure 6.52 – Relative beam centroid measured for BWS517 (blue) and BWS prototype with a pCVD diamond detector (green) and a PMT system (magenta).

The outcome of the measurements is summarized in Table 6.10. In agreement with previous campaigns, the LIU-BWS featured a higher measurement reproducibility (2.3% incertitude compared to 3% for BWS517), when the secondaries are acquired with the PMT system. This is a remarkable improvement considering that the prototype scanner works with a lower (22 times) number of points per sigma at its nominal speed. In addition, the upgraded scanner featured a factor two improvement on precision for the beam centroid determination.

Table 6.10 – BWS measurements summary with COAST beam #2.

BWS test beam,summary (COAST Beam Single bunch 0.23e^{11}p @ 270GeV)							
Scanner	**Scan Speed (m/s)**	**Points per Sigma**	**Beam Sigma Mean (μm)**	**Beam Sigma Spread (μm, %)**	**Beam Emittance Mean (μm)**	**Beam Emittance Spread (nm, %)**	**Beam Centroid Spread (μm)**
BWS.517	1	39	900	28, 3.0%	2.5	119, 4.7%	94
BWS.PRO (D)	20	1.7	800	35, 4.3%	2.5	219, 8.7%	66
BWS.PRO (P)				18, 2.3%	2.5	76, 3.0%	48

6.2.4. Conclusions on diamond detectors for secondary shower detection

The performance of diamond detectors for beam profile monitoring in wire scanner applications is strongly linked to the geometry and fluence of the secondary shower produced by the wire/beam interaction.

The observations collected in this work determined that, the intensity and energy of the secondary shower defines the random amplitude variations on the detector signal around the general Gaussian shape. The performance of diamond detectors were only comparable with PMT systems with high energy ($>400\,\text{GeV}$) and intensity beams ($>1\text{e}^{11}\,\text{PpB}$). This fact suggest that such small detectors (with an area of $1\,\text{cm}^2$) suffer from the stochastic nature of the secondary shower, linked to the number of particles crossing the detector surface per bunch. This effect is practically negligible on the operational scintillator-PMT systems, since scintillators feature about 2 orders of magnitude bigger area ($>100\,\text{cm}^2$).

To understand the diamond detector profiles, we can reconstruct an estimated beam profile with different number of particles crossing the detector on the top of the Gaussian. The secondary shower can be considered as a stochastic process, where in each bunch crossing there is an average number of particles crossing the diamond (μ) normally distributed and with standard deviation defined as the square root of the mean ($\sigma = \sqrt{\mu}$). Figure 6.53 shows beam profile simulations with different number of particles.

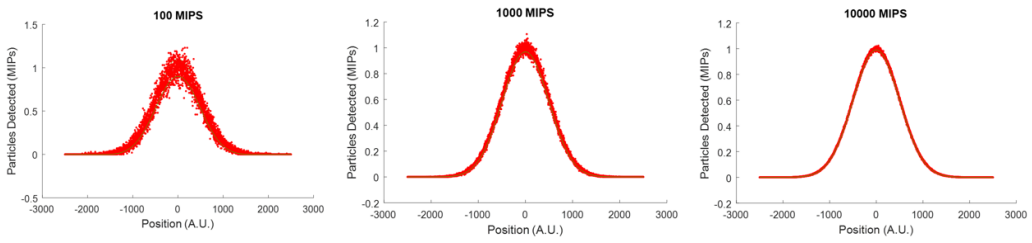

Figure 6.53 – Beam profile simulations considering a different amplitude in terms of number of particles crossing the detector (MIPS).

As Fig. 6.53 shows, the measurement incertitude decreases as the number of crossing particles (or events increase). In relative terms, the standard deviation of the amplitude w.r.t its mean value varies as as $\sigma_{\%} = 100/\sqrt{\mu}$. Taking a mobile window on a simulated profile, we can determine local mean values and standard deviations to check if the spread varies as expected in function of the mean value (or amplitude in MIPS). The figure 6.54 shows the result of the analysis for a simulated beam profile.

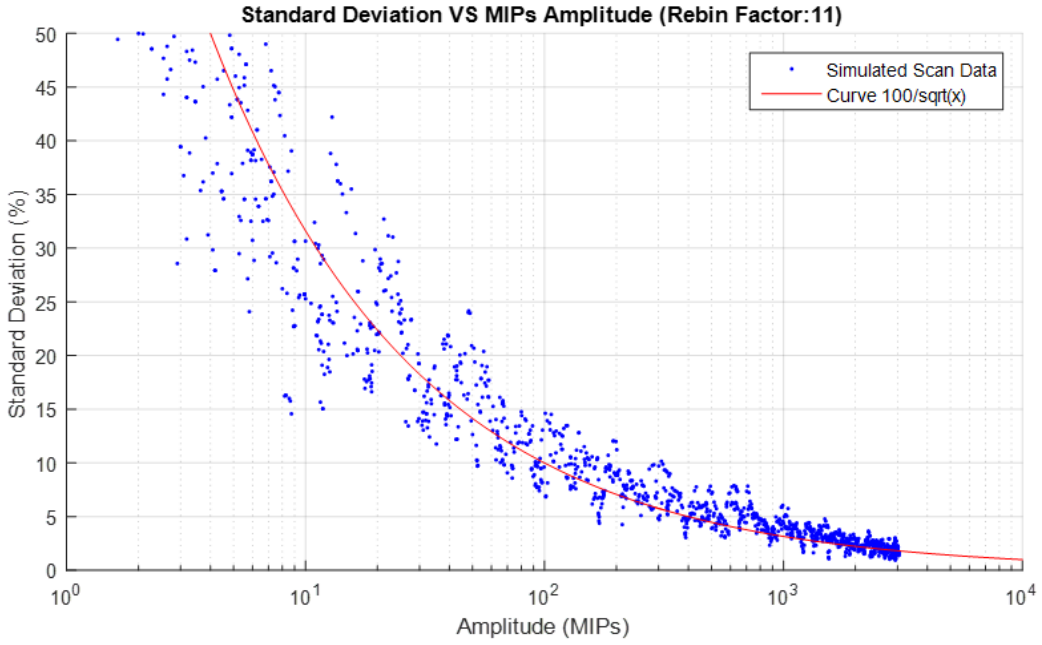

Figure 6.54 – Amplitude spread analysis on a simulated beam profile (blue points) in function of the number of events (MIPs) and expected evolution (red line)

This analysis was extrapolated measured beam profiles with diamonds. The charge per bunch was normalised to number of MIPs. For a 500 μm diamond detector biased at -700 V the charge per MIP was estimated to be 1.6fC. Figure 6.55 shows this analysis considering measurements at two different energies.

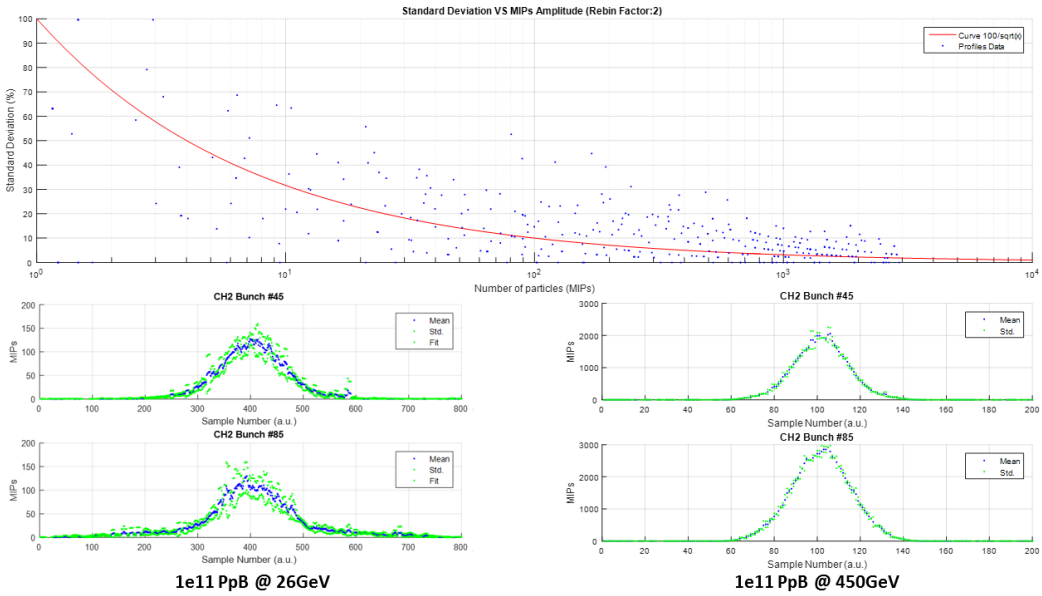

Figure 6.55 – Amplitude spread analysis on diamond detector beam profiles.

In general, beam profiles measured at injection energy (26 GeV), or with low intensity, featured an amplitude of a few hundred MIPs per bunch crossing, meaning about 10% amplitude incertitude at the Gaussian peak. For profiles measured at extraction energy (450 GeV), the number of MIPs crossing the detector at the center of the Gaussian reached several thousand MIPS, which reduced the amplitude incertitude to about 1%. The analysis in Fig. 6.55 shows how the spread of the profiles follow the expected behaviour.

The analysis of the measurement campaigns here reported shows that, in spite of the

high efficiency of diamond detectors, linearity and radiation hardness, their performance for this application is highly limited by their reduced area. A slightly improvement was reached when combining the measurements of two diamonds (doubling the detector area), however their performance was still far from traditional scintillators and PMTs. The high amplitude incertitude linked to the schocastic nature of the secondary shower and the detector small cross-section ultimately leads to statistical errors on the beam width determination, which compromises the accuracy of the whole beam wire scanner instrument.

Wire scanner systems must provide a beam width measurement within 1-2% precision when measuring more than 2-3 points per sigma. According to the analytic equation previously from chapter 4, to estimate the beam width random error:

$$\epsilon_{Statistic}(N_{TE}, PpS) = \frac{1.1}{\sqrt{N_{TE} PpS}} \tag{6.4}$$

Where PpS is number of points per sigma and N_{TE} is defined as the total number of events that forms the Gaussian.

The specified incertitude (1%) with 2 PpS is only reached with $N_{TE} > 6000$ events. The Gaussian amplitude must be higher than 2000 events (MIPs) considering the following relationship:

$$Amplit_{MIPs} = \frac{N_{TE}}{\sqrt{2\pi}} \tag{6.5}$$

This condition was only accomplished at extraction energy (450 GeV) and with a nominal beam intensity (1.1e^{11} PpB). We can conclude that these detectors are not suitable to accurately measure bunch-by-bunch beam profiles over all the SPS dynamics, but show a good potential for LHC BWS applications.

6.2.5. Conclusions QIE10 Front End operation

During operation with diamond detectors, the signal amplitude incertitude was dominated by the detector statistics. The impact of the QIE10 quantization effect, induced by its logarithmic digitalization scheme, could not be appreciated in the beam profile measurements. The tunnel readout featured higher SNR than scope acquisitions on surface reaching an equivalent noise of 2.6 fC (in the order of the QIE10 sensitivity), no noise degradation was observed in the different testing campaigns carried out along 1.5 years (see Fig. 6.56).

The noise improvement with the QIE10 FE might be linked to two facts, firstly the limited resolution of the scopes used for tests, and secondly the small amplitude of the signal arriving to surface and the pick up noise on cables. The diamond detector signal amplitude after the TIA was around 60-400 mV for the different machine configurations. The front-end demonstrated to properly synchronise with the accelerator, showing no drift on single bunch measurements turn after turn.

The ASIC has successfully demonstrated to exploit the pCVD diamond detector properties given its high dynamic range and resolution, being able to resolve from 6 to 0.2e^{6} MIPs.

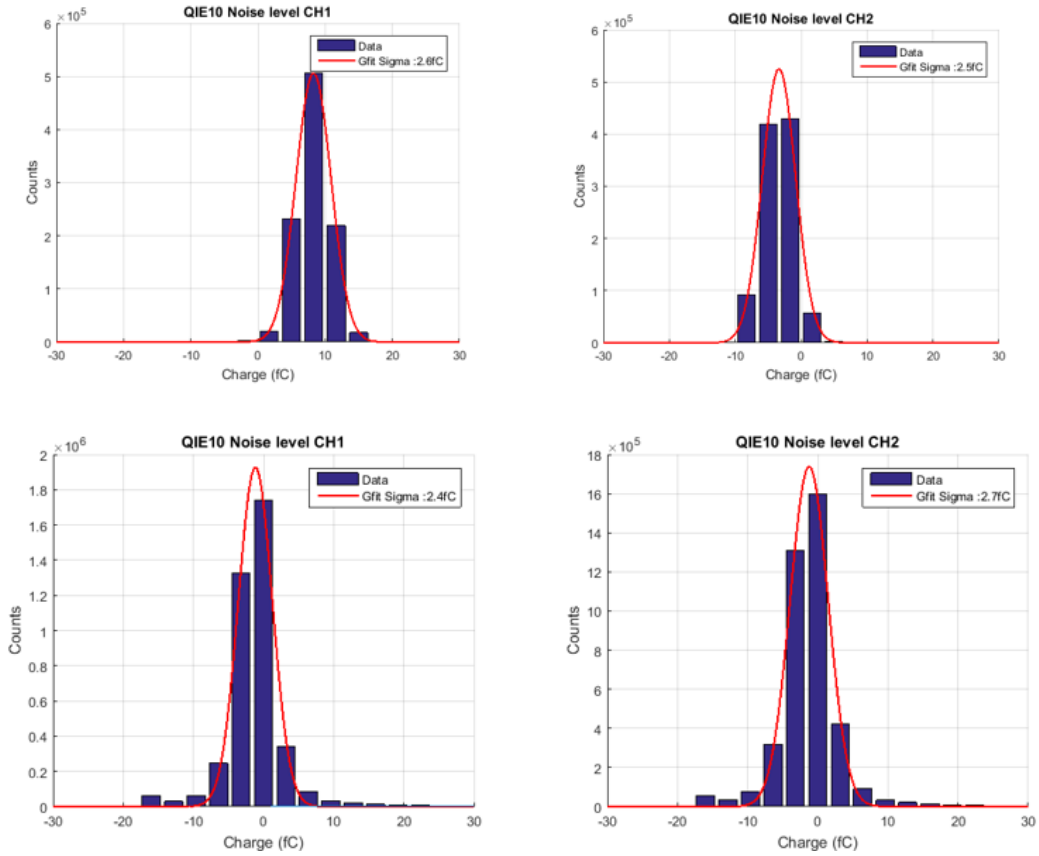

Figure 6.56 – QIE10 Front-End noise distribution in the SPS tunnel, 10/2015 (top) and 05/2017 (bottom).

6.3. Multi-PMT detector and ICECAL FE tests in the PSB

The installation of a new LIU-BWS prototype in one of the PSB rings (BR3.BWSH.4L1) provided the infrastructure to evaluate the ICECAL front-end system joint with a second detector alternative. The baseline of this detector consists on the combination of traditional scintillators, to overcome the area limitations of pCVD diamond detectors, with a multi PMT readout system, where the system dynamics is split in several linear ranges by using different fix neutral density (ND) filters on the photocathode of each PMT.

As the schematic on Fig. 6.57 shows, the PSB LIU-BWS was equipped with two acquisition systems:

- A **standard detector** similar to those installed on operational PSB scanners, featuring a single PMT (R9880U Series from Hamamatsu) with its output signal routed to surface. It is intended for scanner accuracy validation and as reference monitor.

- A **prototype system** built with same mechanics and housing as the previous system but equipped with four PMTs (1 x R7600U and 3 x R9880). The four outputs are connected to a relay bank so they can be acquired on tunnel with the ICECAL V3 FE or on surface. This assembly is intended to be used for testing purposes.

Both detector systems are based on little cylindrical BC-408 scintillator blocks (30 x 30 mm), wrapped with aluminium foil, and followed by a 240x30mm air lightguide with reflective material on its internal walls. The lightguide is connected to an eight positions filter wheel with different ND filters. The PMTs selected were small metal package type with a 10 stage metal channel dynode structure. To avoid radiation damage on the PMTs, they are placed

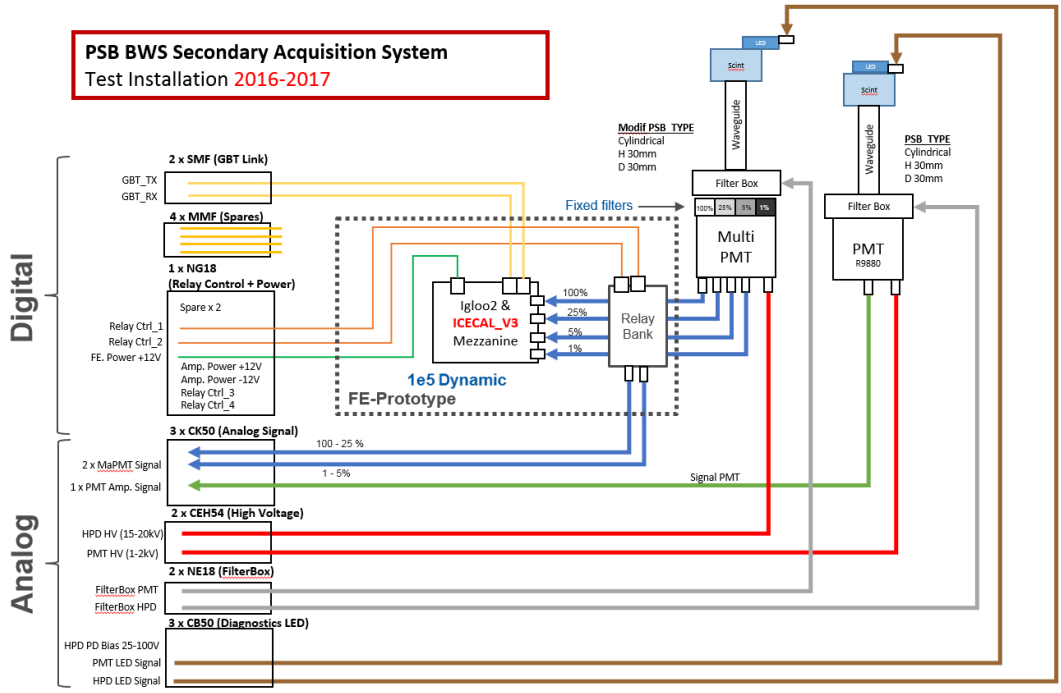

Figure 6.57 – Secondary shower acquisition systems installed on PSB for the BR3.BWSH.4L1 wire scanner prototype.

at 30cm from the beam pipe and shielded with a thick lead layer (5cm). Ultra-Violet (UV) LEDs were included on the scintillator housing for diagnostics.

6.3.1. Scintilator light yield estimations and Multi-PMT system construction

The light yield generated from the scintillator was analytically estimated to properly scale the photomultiplier set-up. The number of photons excited on the scintillator per bunch crossing is dependent on the material properties and the energy deposited by the rain of secondaries. The energy deposition can be calculated from the number of particles impacting the wire (or primaries), the detector properties and the dose deposition per proton impacting on the wire (estimated by FLUKA simulations).

The maximum number of protons impacting on the wire for an arbitrary beam is dependent on the bunch intensity, its transversal width and the wire diameter. It is calculated as the transversal bunch integral over the wire diameter, locating the wire on the centre of the Gaussian as:

$$\overline{\gamma} = \int_{-\frac{D_W}{2}}^{+\frac{D_W}{2}} g(x)dx \tag{6.6}$$

where $\overline{\gamma}$ is the amount of impacting particles, D_W is the carbon wire diameter and $g(x)$ is the transversal distribution of the protons on one dimension.

Considering the D_W much smaller than the beam sigma, this expression can be simplified to:

$$\overline{\gamma} = D_W \frac{N_p}{\sigma\sqrt{2\pi}} \tag{6.7}$$

Where N_p is the number of particles per bunch and σ is the beam transversal sigma.

The energy, in MeV, deposited on the scintillator is calculated as:

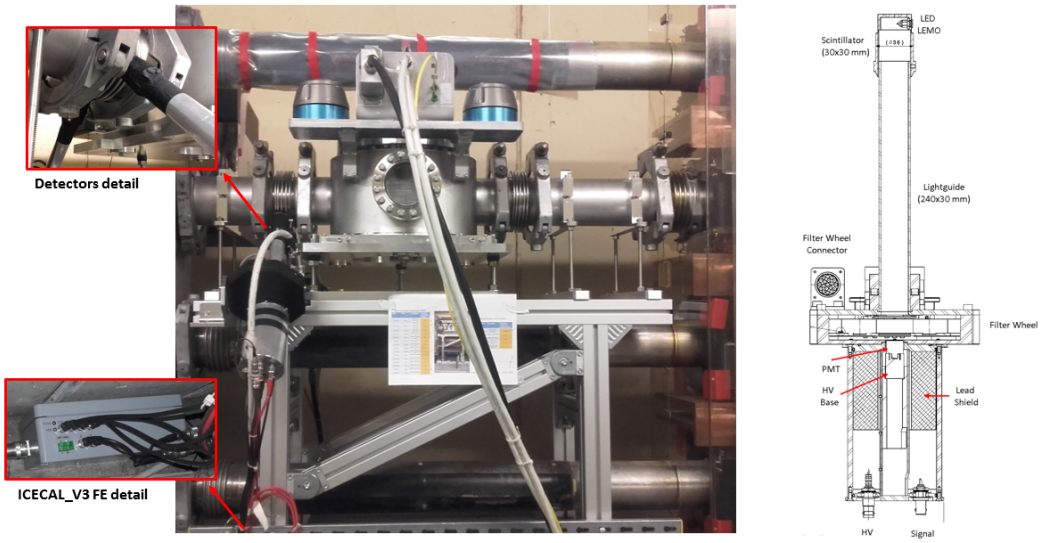

Figure 6.58 – Beam wire scanner prototype on PSB (left) and standard detector mechanics (right).

$$E(MeV) = D_{prim} * \overline{\gamma} * m \tag{6.8}$$

Where Dprim is the energy deposited per primary particle (from FLUKA simulations) in Gy and m is the detector mass in Kg (for our geometry m = 0.02 Kg).

The photon yield can be calculated from the deposited energy on the scintillator. For the BC-408 type, light yield is 11136 ph/MeV.

To estimate the number of MIPS crossing the detector from the total energy deposited, it is needed firstly to calculate the energy deposited by a single MIP on this particular detector. The BC-408 its mainly composed by PMMA whose stopping power (dE/dx) is 1.96 MeV cm^2/g, the energy deposited by a MIP is calculated from the product dE/dx and the material density (1.032 g/cm^3), resulting on 2.02 MeV per cm. Considering a cylindrical detector geometry of θ = 30 mm and h= 30 mm, the mean path of a particle impacting perpendicular to the cylinder volume is 1.5 cm, which leads to 3.03 MeV per MIP crossing the detector. Photon yield per MIP results in 3.37e^4 photons. Table 6.11 shows a summary of the detector properties and geometry, along with the calculations for energy deposition, photon yield and crossing MIPs for a typical LHC pilot beam at 1.4 GeV on PSB.

Table 6.11 – Detector properties and estimations for energy deposition, number of crossing MIPs and photon yield for a typical scan of a LHC Probe beam on PSB at 1.4GeV.

Scintillator Material Characteristics		
Material	BC-408	
Density	1.032	g/cm3
Refractive index	1.58	
Rise Time	0.7	ns
Decay Time	2.1	ns
FWHM	2.5	ns
Att. Length	210	cm
Wavelength	425	nm
Photon Yield Anthr	17400	ph/MeV
Photon Yield	64	% Antrh
Photon Yield	11136	ph/MeV
MIP Stopping Power	1.96	MeV cm2/g
Energy MIP	2.02	MeV/cm

Scintillator Geometry #1		
Shape	Cylindrical	
L	30	mm
D	30	mm
Volume	21.21	cm3
Mass	0.02	Kg
Ef.Area	9	cm2
MIP Energy	3.03	MeV
Photons MIP	3.37E+04	Photons

Beam Parameters		
Bunch Intensity	5.00E+09	Protons
Bunch Length	100	ns
Beam Sigma	1.2	mm
Rep. Period	1	us
Scan Speed	20	m/s
Wire Diam	30	um
Max Interacting P.	4.99E+07	Prim
Total Interacting P.	7.50E+09	Prim
Time 4 Sigma	0.24	ms
PpS	240	Points

FLUKA Simulations (15cm)		
100MeV fluence	5.40E+11	part/cm2*prim
100MeV dose	1.50E-20	Gy/prim
1.4GeV fluence	8.58E-08	part/cm2*prim
1.4Gev dose	5.34E-17	Gy/prim

Extraction E = 1.4 GeV		
E. Deposited	3.64E+02	MeV
Max MIPS	1.2E+02	MIPS
Max Photons	4.05E+06	Photons

Considering the different PSB beams, the crossing MIPs estimations results in an ex-

pected dynamics on secondary particles fluence and photon yield of 4 orders of magnitude, see Fig. 6.59. On this estimations, the lowest intensity beam (LHCProbe) would be detected with a Gaussian amplitude of 100 MIPs. A bigger detector surface would be required to resolve low intensity beams with higher resolution in terms of crossing particles, the results approximately scale down for injection energy with the dose simulated in FLUKA.

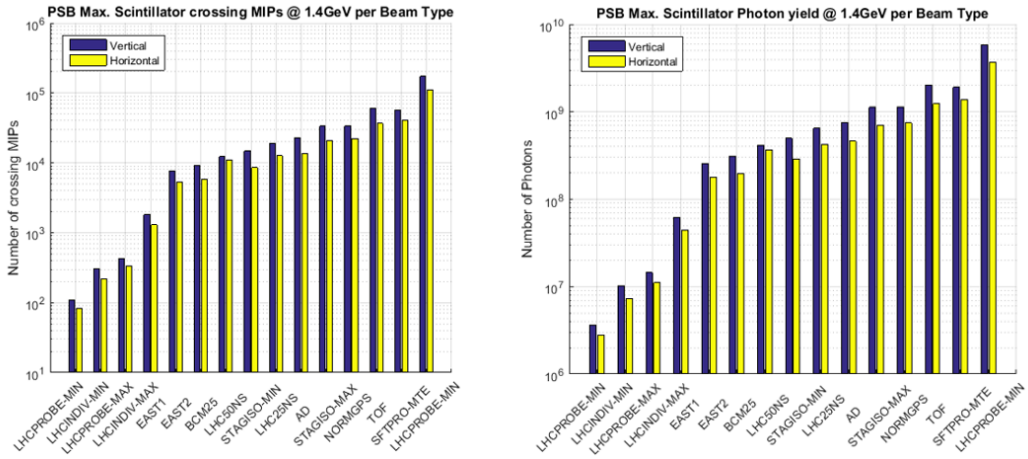

Figure 6.59 – Estimation of number of crossing MIPs (left) and photon yield (right) per bunch in a cylindrical 30x30mm scintillator for the different PSB beams

From the photon yield generated on the scintillator, only a small portion will be captured by the PMTs. Zemax simulations on our detector geometry allowed to estimate that about 20% of the optical power generated on the scintillator is propagated up to the detector plane with a Gaussian image. The simulations considered the scintillator as PMMA cylindrical block wrapped with aluminium foil, the waveguide was modelled as an empty tube made of reflective aluminium. To emulate the scintillator excitation, an isotropic light source was randomly located in the scintillator volume with a total power of 1 Watt.

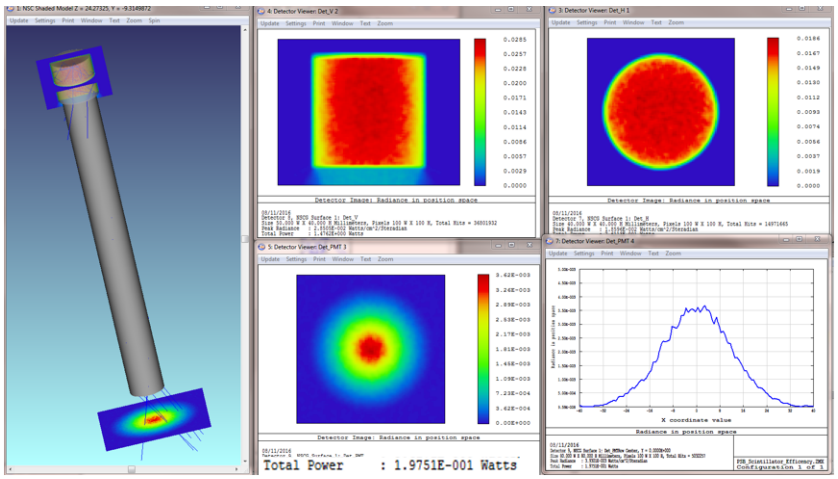

Figure 6.60 – Light transport efficiency optical simulations on Zemax.

On PSB operational systems, a little R7400 metal package PMT is located at about 25 mm from the end of the light-guide, this distance is imposed by the filter wheel located in-between. These PMTs have an active area of 0.5 cm^2 with a round photocathode of 8 mm diameter. On this configuration the detectors only capture about a 10% light exiting the lightguide exiting, thus, 2% of the photons generated in the scintillator.

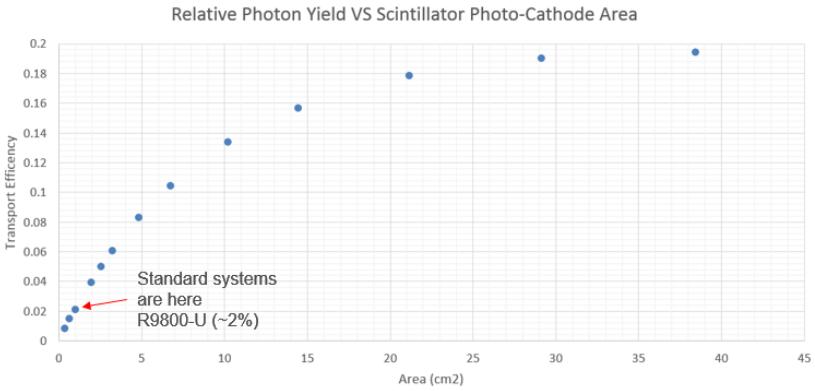

Figure 6.61 – Transport efficiency VS PMT photo-cathode area at 25mm from light guide

The multi-detector system (M-PMT) is built with two PMT types, a square type (R7600U-M4) located at the centre with 0.81 cm^2 active area (9x9 mm) surrounded with three round types (R9880) with 0.5 cm^2 active area. On this new configuration the detector plane must be pushed backwards to properly illuminate all detectors after the housing aperture. Each detector works in a different range given their photocathode size, location and the use of neutral density (ND) filters. On the configuration shown in Fig. 6.62, the central PMT (A) captures about 2% of the scintillator photons (equivalent to operational systems), detector B receives about 0.15% due to the Gaussian decay of the optical power, its off-centre location and smaller photocathode. The illumination level is similar for detectors C and D, where neutral density filters are added to still attenuate the photon yield up to 0.028 and 0.0028%.

The detector assembly sensitivity level is set to single MIP level. With a 2% transport efficiency to the central PMT this is translated into 700 photons ($35e^3$ ph/MIP * 2%). The typical photocathode quantum efficiency is 25%, meaning 175 photo-electrons on the tube per MIP. The PMT will operate with a $1e^4$ gain, the expected output charge is per MIP is therefore $280e^{-15}$ C, with 4ns FWHM pulse response, the estimated output peak current per MIP is 70μA. On this design, each PMT aims to reach $1e^3$ dynamics ranging from 1 μA to 1 mA peak currents (matching this way the ICECAL V3 dynamics). According this estimations, to properly profit the ASIC input dynamics, a 10% transmission ND filter would be required. The detectors working point would lead to: Detector A 1-$1e^3$ MIPS, Detector B $1e^1$-$1e^4$ MIPS, Detector C $1e^2$-$1e^5$ MIPS, Detector D $1e^3$-$1e^6$ MIPS. In any case, a filter wheel was included on this detector for configuration flexibility.

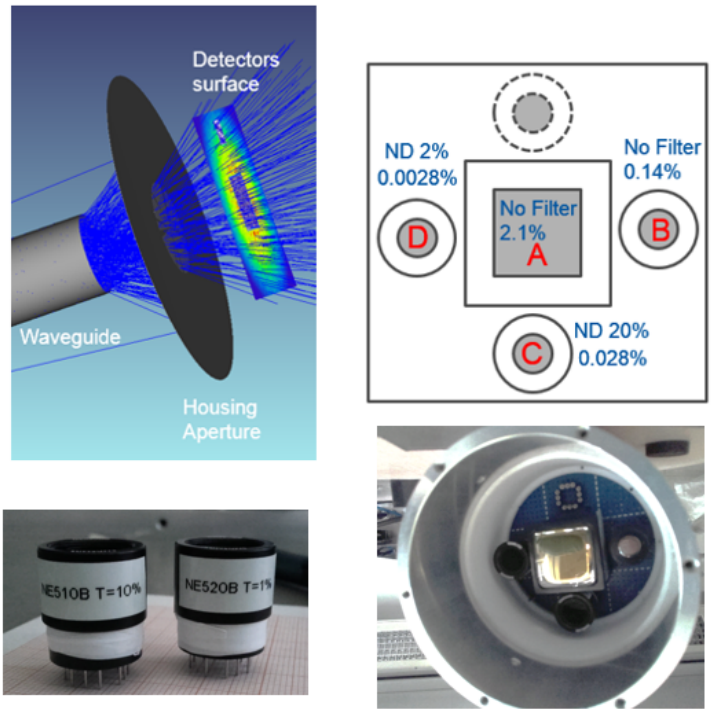

Figure 6.62 – Zemax simulations to estimate the photon yield received by each PMT and detector assembly.

6.3.2. Photo-Multipliers characterisation

The photomultipliers where characterised to study their linearity and HV saturation limits. The M-PMT system was assmbled in a custom HV base, build with the nominal resistor values specified on their respective datasheet and with extra capacitors to provide the required charge during a scan. The standard detector was equipped with a commercial HV base. This characterisation is essential to properly determine the working point of the photomultipliers.

- **Anode Linearity in pulse mode (Space - Charge limit):**

The pulsed linearity determines the maximum output current peak due to the PMT space charge effects. This characterisation was done with a LED operated in double-pulsed mode, providing a high and low pulse amplitudes alternately. The pulse amplitude ratio is fixed (1:4) and the PMT is set at a distance from the light source so the amplitude of the current pulses is very small ($\approx 10\mu$A) and their ratio is as specified. As the light source is approached to the PMT the received light intensity, and pulses amplitude, increase. By studying the pulses amplitude ratio, at different distances, the PMT linearity can be determined for a given output peak current. The Eq. 6.9 is used to evaluate the PMT pulsed linearity.

$$L = \frac{(\frac{I_{p2}}{I_{p1}} - \frac{I_{p02}}{I_{p01}})}{(\frac{I_{p02}}{I_{p01}})} x100\% \tag{6.9}$$

Where $\frac{I_{p2}}{I_{p1}}$ is the pulses ratio at an arbitrary distance and $\frac{I_{p02}}{I_{p01}}$ is the initial pulses ratio.

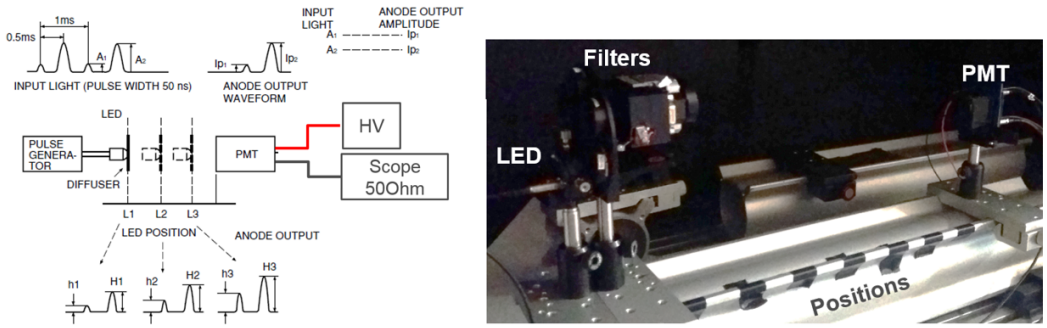

Figure 6.63 – Measurement method schematic (left) and set-up (right) for PMTs linearity characterization.

A schematic of the measurement process as well as the set-up used is shown in Fig. 6.63. Both PMT types were characterized with different high voltages to check for any dependency. The pulsed linearity of the PMTs under test is displayed on Fig. 6.64, the data from the MaPMT R7600U-M4 shows only a single channel.

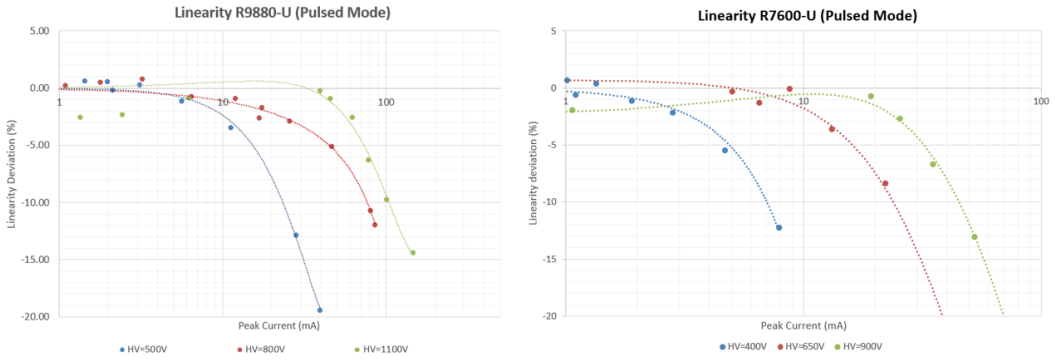

Figure 6.64 – Pulsed linearity characterization for R9880-U (left) and one channel of R7600U-M4 (right).

As expected, the PMTs anode is capable of delivering more charges per pulse with no linearity deviation when applying higher voltages. By setting the linearity deviation limit at 5%, the R9880-U can deliver current pulses (100 ns FWHM) of 15, 50 and 70 mA when applying 500, 800 and 1100V respectively. Concerning one channel of R7600U-M4 the linearity limit is set to 5, 17 and 30 mA when applying 400, 650 and 900V respectively, however, since its four channels will be shortcut in our application these limits are extended to 20, 68 and 120 mA pulses.

- **Total charge per scan (base discharge):**

The saturation effect due to the re-distribution of the voltage on the dynodes is linked to the discharge of the capacitors on the last stages. This effect is present on the beam profile, distorting the measurement, before it becomes evident. The aparison of this effect and the maximum allowable charge per scan was empirically determined for the R9880U. The characterization used the previous set-up, the LED was in a fixed position and modulated with a burst of 100ns FWHM pulses spaced by 1 μs. Each burst consisted on a train of 1000 pulses with a repetition period of 1 second. The radio between the charge of the first pulse and the charge of the complete train was measured for a fixed amplitude, when no saturation is present this ratio must be 1:1000. Subsequent measurements increased the power of the laser and determined the deviation w.r.t the ideal ratio as:

$$S = \frac{(\frac{Q_{Train}}{Q_{p1}}) - (\frac{Q_{0Train}}{Q_{0p1}})}{(\frac{Q_{0Train}}{Q_{0p1}})} x100\% \tag{6.10}$$

As with the anode linearity, the PMT R9880U saturation was determined for different HV. Both versions of the HV base were tested, standard (as shown in Fig. 6.65, left) and custom (with 100 nF capacitors on the last stages instead of the standard 10 nF).

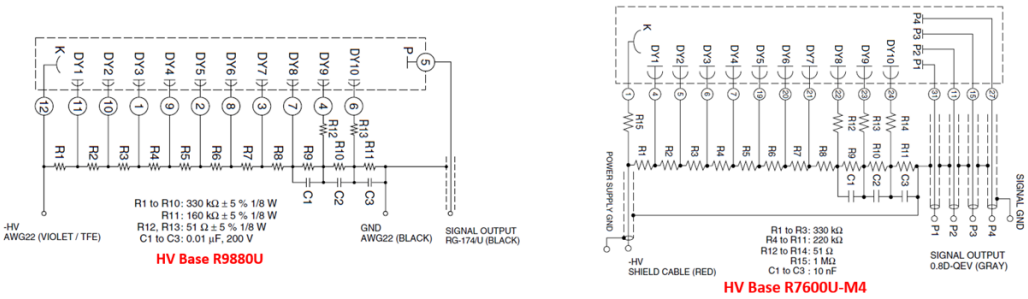

Figure 6.65 – Standard HV bases for the two PMTs under study, R9880U (left) and R7600U-M4 (right).

The results for R9880U are summarized on the plots from Fig. 6.66. The maximum allowable charge per scan was set to 0.1-0.4 μC for the standard base and 1 μC for the custom version when applying a HV>800V. However, this limit seems to vary when very low voltages are applied. Similar results were obtained for the R7600 model.

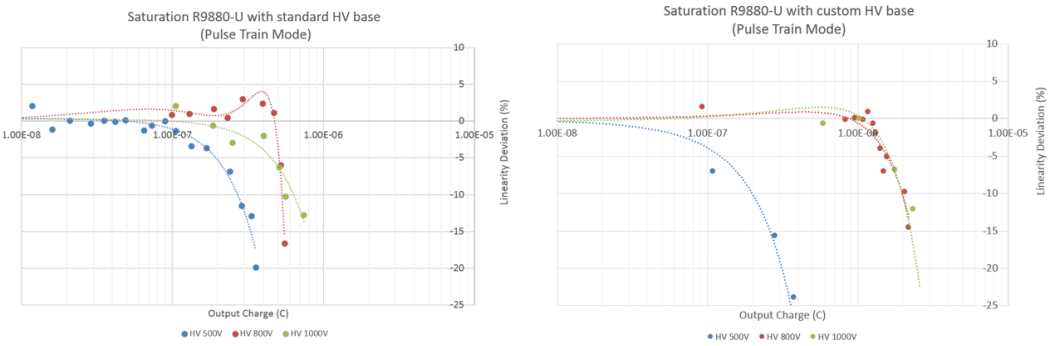

Figure 6.66 – Maximum charge per scan allowable with standard (left) and custom (right) HV bases.

For both PMTs under study, the following limits are to be respected for proper operation on beam profile monitoring:

- Maximum current pulse amplitude per bunch < 10mA.
- Maximum allowable charge per scan: 1μC for the custom base operating at HV>700 and 0.1-0.4μC for the standard base.

As an example, such configuration allows each PMT to provide reliable measurements for: a beam profile lasting 1ms (2 x sigma) with a maximum bunch amplitude of 3mA when measuring a typical PSB bunch structure of 200ns pulses width and 600ns repetition period. On this case neither total charge nor maximum amplitude limitations are violated. Bigger capacitors can be included to still push the saturation limit to a higher charge.

6.3.3. Beam Tests with LHC 25ns and ISOLDE beams

A beam test was carried out on 28/06/2017 to evaluate the scanner mechanics, its precision compared to a operational system, and the performance of the M-PMT detector with the ICECAL V3 front-end. The beams used were LHC 25 ($180e^{10}$ PpB) with scans performed at 1.4GeV and ISOLDE beams ($820e^{10}$ PpB) with scans done at different beam energies. An operational scanner on the same PSB ring (BR3.BWS.2L1.H) was operated in parallel to serve as a basis for comparison.

PSB beams consisted on a single circulating bunch with 100-180 ns FWHM and 0.6-1 μs revolution period. Typical beam sigma was 2-5mm; with scans performed at 15-20m/s the total number of beam/wire interactions per sigma oscillates from 200 to 700 (points per sigma). To recover the beam profile, operational scanners in PSB operate in turn-by-turn (TbT) mode, a low bandwidth acquisition mode that low-pass filters the PMT signal and performs direct digitisation on the filtered data. The effect is an averaging on the beam profile over several turns that prevents from big turn-to-turn amplitude variations on the profile.

6.3.3.1. Scanners beam width measurement precision comparison

Only the "standard" PMT assembly was used for the mechanical validation of the LIU-BWS PSB prototype. The detector signal was acquired on surface (at 65 m distance) with a scope at 650 MSPS, the optical position sensors were acquired with another scope at 20 MSPS. A common trigger was used for the BWS control and acquisition electronics for synchronisation. The data taking process was automatised with a Matlab application capable of controlling the scopes and performing online data analysis (see Fig. 6.67).

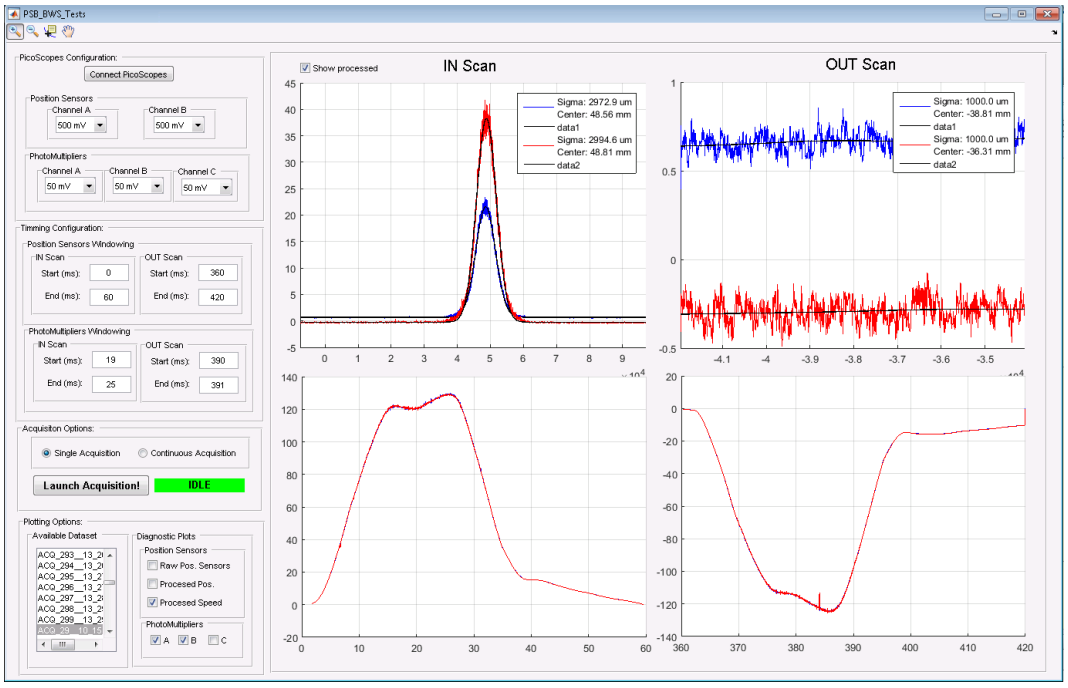

Figure 6.67 – Beam wire scanner testing application. The application is displaying processed beam profiles and scanner speeds for IN and OUT scans.

To emulate the TbT mode of the operational systems, the profiles were low-pass filtered at 500 KHz with a 5th order Butterworth filter applied on the digital data. Figure 6.68 shows a profile measurement with different filtering cut-off frequencies. During measurements, the PMT HV was fixed at 750V and its signal adapted through ND filter selection. The filters used during the campaign were 2, 5 and 20% transmittance.

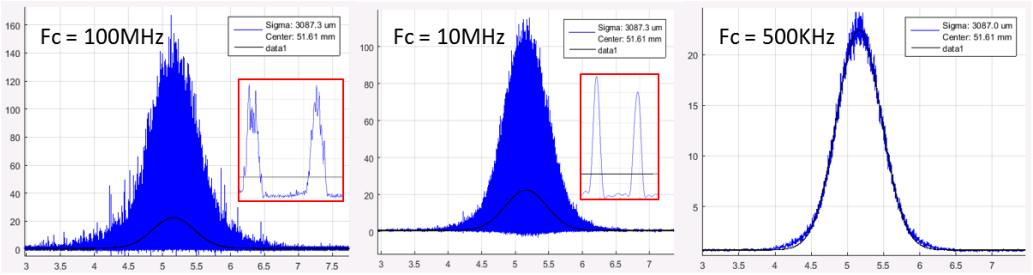

Figure 6.68 – PSB LHC25ns beam profile at 1.4GeV with prototype scanner. Different levels of filtering are applied to show the impact on the beam profile.

On the LHC25 beam, operational and prototype scanner performed scans over consecutive injections at 776 and 785ms of the cycle (1.4GeV flat top). The data taking was split on 5 periods to check for emittance blow-up induced by one scanner that could be potentially seen on the other (see Fig. 6.69). On the first and fifth periods only the LIU-BWS was operated, on the second and fourth periods both scanners worked at the same time, with operational and prototype scanning first respectively. The operational scanner measured alone during time-slot number 3.

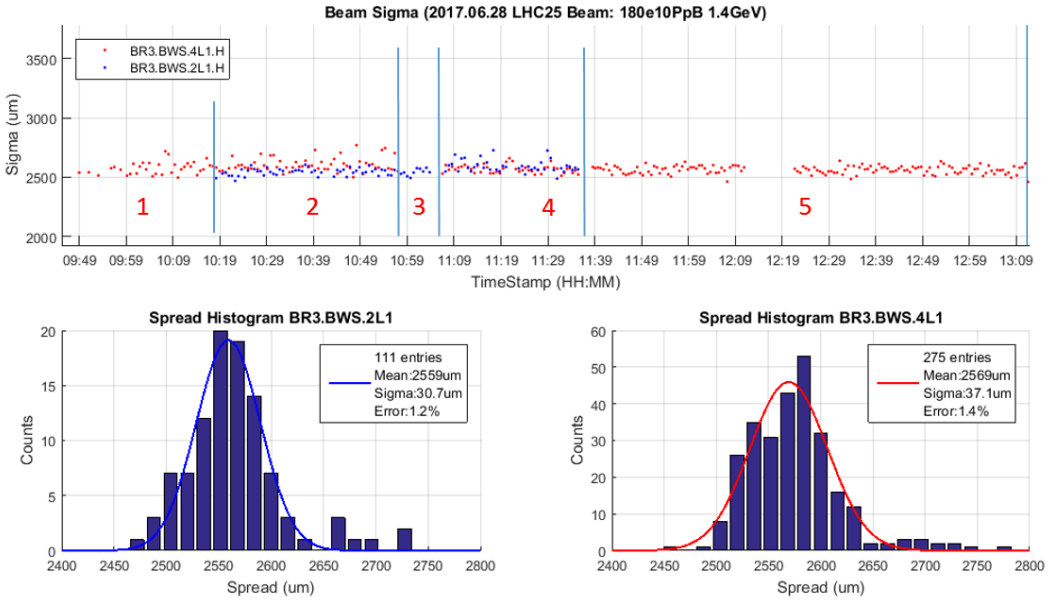

Figure 6.69 – Beam sigma values measured by prototype (BR3.BWS.4L1.H) and operational (BR3.BWS.2L1.H) scanners on PSB for a LHC25 beam at 1.4GeV with measurement spread histograms

The results shown on the 2nd and 4th time-slots shows what it seems emittance blow-up produced by the first scanner and seen on the second one. Some red dots show bigger beams than the rest on the second period, the situation is similar with the blue dots on the fourth period. Further studies are required to confirm and quantify this effect. Both scanners measured similar sigma values due to the close optics of their locations. Concerning the measurement spread that defines the scanner precision, both scanners shown ≈1.2 - 1.4% precision in beam width.

On the measurements during the ISOLDE cycle, in Fig. 6.70, the prototype scanner shown better overall performance with a sigma error determination ≈0.7%, the operational scanner leaded to ≈1.2% error. A comparative summary is provided in Table 6.12. These numbers must be considered carefully, successive scans were performed over different injected beams

and measurements are subject to shot-by-shot beam profile variations.

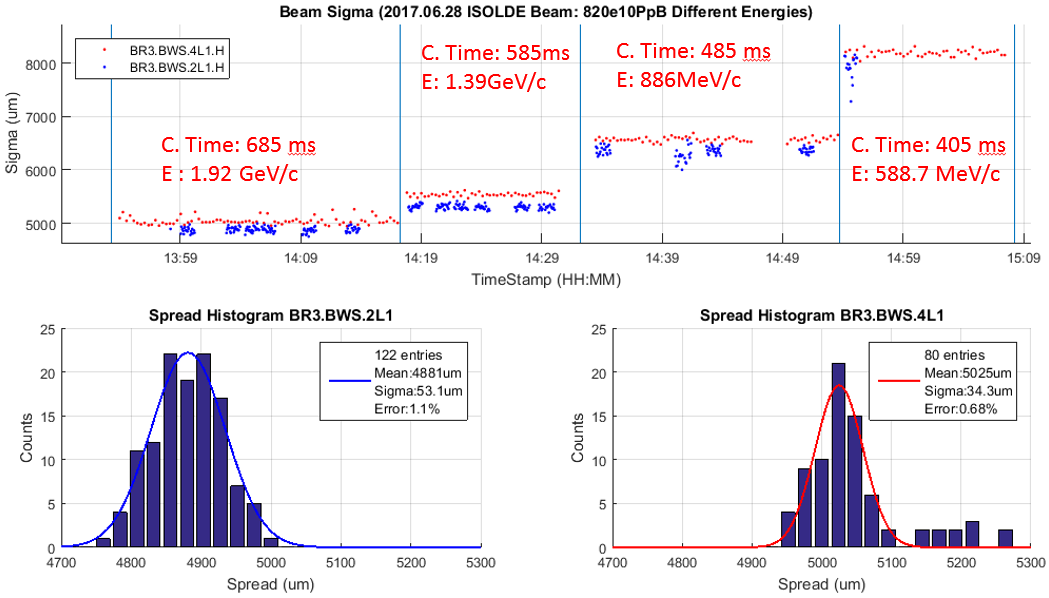

Figure 6.70 – Beam sigma values measured by prototype (BR3.BWS.4L1.H) and operational (BR3.BWS.2L1.H) scanners on PSB for an ISOLDE beam at different energies. Spread histograms correspond to the first period.

Table 6.12 – Measurement precision summary for operational (BR3.BWS.2L1) and prototype (BR3.BWS.4L1) scanners on PSB for LHC25 and ISOLDE beams

Beam Type	**Cycle Time (ms)**	**Momentum (GeV/c)**	**BR3.BWS.2L1**		**BR3.BWS.4L1**	
			Sigma (μm)	**Error (%)**	**Sigma (μm)**	**Error (%)**
LHC25	785	1.4	2559 ± 31	1.2	2569 ± 37	1.4
ISOLDE	685	1.92	4880 ± 53	1.1	5025 ± 34	0.7
	585	1.39	5302 ± 44	0.8	5538 ± 38	0.7
	485	0.86	6354 ± 88	1.4	6571 ± 46	0.7
	405	0.58	8021 ± 125	1.6	8245 ± 52	0.6

6.3.3.2. ICECAL V3 front-end acquisitions

The ICECAL V3 front-end prototype was automatically acquiring the quad-PMT detector signals during the previous campaign. The Figure 6.71 shows processed acquisitions on the four channels of the front-end, where each features a different dynamics. The ICECAL channels 1, 2, 3 and 4 are assigned to PMTs A, B, C and D respectively. The signal form the PMT with higher signal and no ADC saturation was used for the beam profile processing, in addition, a combination of different channels would be possible to enhance resolution on the Gaussian tails.

The ICECAL acquisitions were digitally low pass filtered (500 KHz) prior to a Gaussian fit for comparative measurements with operational systems.

Whereas the standard acquisition system required parameter tuning (ND filter change), the settings of the M-PMT were kept static during the campaign. The HV was fixed at 400 and 500 volts for the R7600 (central) and R9880 (satellite) PMTs, meaning an equivalent gain of 1e4. The ND filter used was T=20% at the beginning of the campaign (up to 12:55), to not reach ADC saturation in any ICECAL channel, no filter was used for the rest of the measurements. For comparison with the standard system, position information was not used.

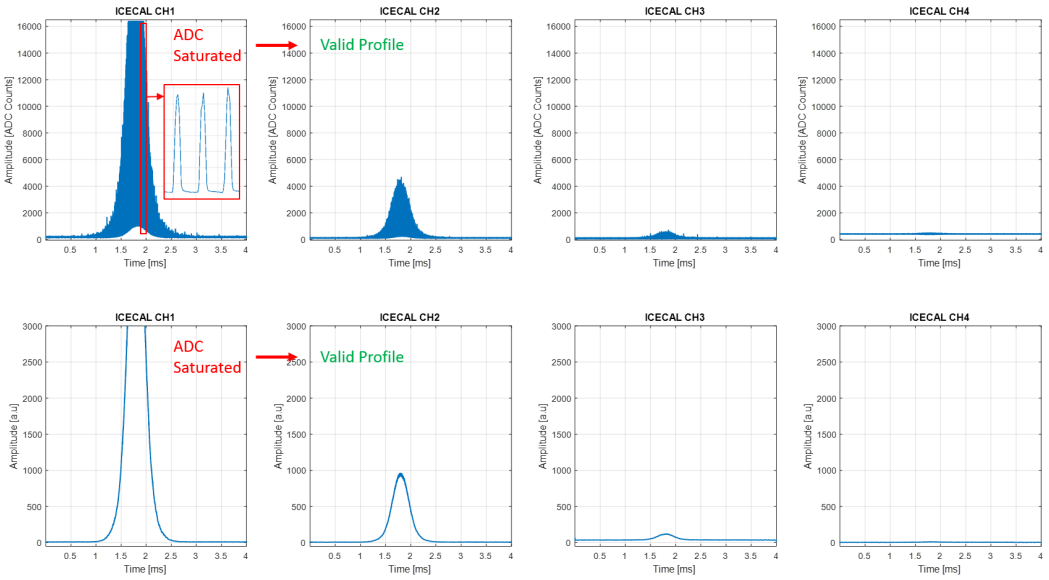

Figure 6.71 – Raw (top) and Processed (bottom) ICECAL V3 front-end acquisition from the quad-PMT detector system for a LHC25 beam at 1.4 GeV.

Gaussian fits on the profiles were performed on the temporal domain. The ICECAL Gaussian fit amplitudes, sigma values and estimated total charge delivered by the PMTs per scan were calculated. Figure 6.72 shows a graphical summary of the beam profile measurements taken by the M-PMT and ICECAL, data from standard system is presented with a track of changes and remarks on the measurements.

The standard system had to be adapted to respect the anode pulsed linearity (I_{pulse} <10mA) and avoid PMT base saturation. As shown on the magenta sigma values (especially during the LHC25 cycle), in some cases the PMT signal was too weak and had to be enhanced by changing to a lower attenuation filter. In other measurements, the light yield was too strong and the PMT base was discharged, showing an evident effect on the profile, "strong PMT saturation". Before being evident on the profile the PMT base saturation influences on the beam width measurement, "weak PMT saturation", this type of saturation is not trivial to identify without reference measurements or a proper PMT characterization.

A weak PMT saturation appears on the standard system around 15:19, measured beam profiles are systematically narrower than those from ICECAL. Note that the standard PMT base was not modified and its typical saturation at 800V appeared after delivering a charge of $\approx 0.4\mu$C (see Fig. 6.66, left). The central plot from Fig. 6.72 shows that this PMT (magenta) was delivering $> 0.1\mu$C during all the campaign, when the total charge of this system exceeds 0.4μC the measured profiles are distorted.

Due to the custom HV base and the working regime of the ICECAL inputs, its measurements are virtually free of PMT base saturation. Measurements within the ICECAL ADC scale featured a charge lower than 0.2μC. An ICECAL channel measurement only diverges from the rest when its ADC is saturated (see sigma values from Fig. 6.72, top, and ADC saturation limit, middle). The Gaussian amplitudes of the four ICECAL channels show about an order of magnitude difference. Since the gains of all PMT were equal, this was a direct effect of the received photon yield.

During the test campaign the amplitude of the PMTs signal varied up to 4 orders of magnitude, firstly due to the different characteristics of the beams (intensity and energy) and secondly due a HV sweep performed at the end measurements (from 15:25) to emulate the signal of higher intensity beams. Beam profiles under all circumstances could be properly determined with the ICECAL using a dynamic channel selection in post-processing (see Fig. 6.74). This approach is especially useful to avoid parameter tuning while performing scans

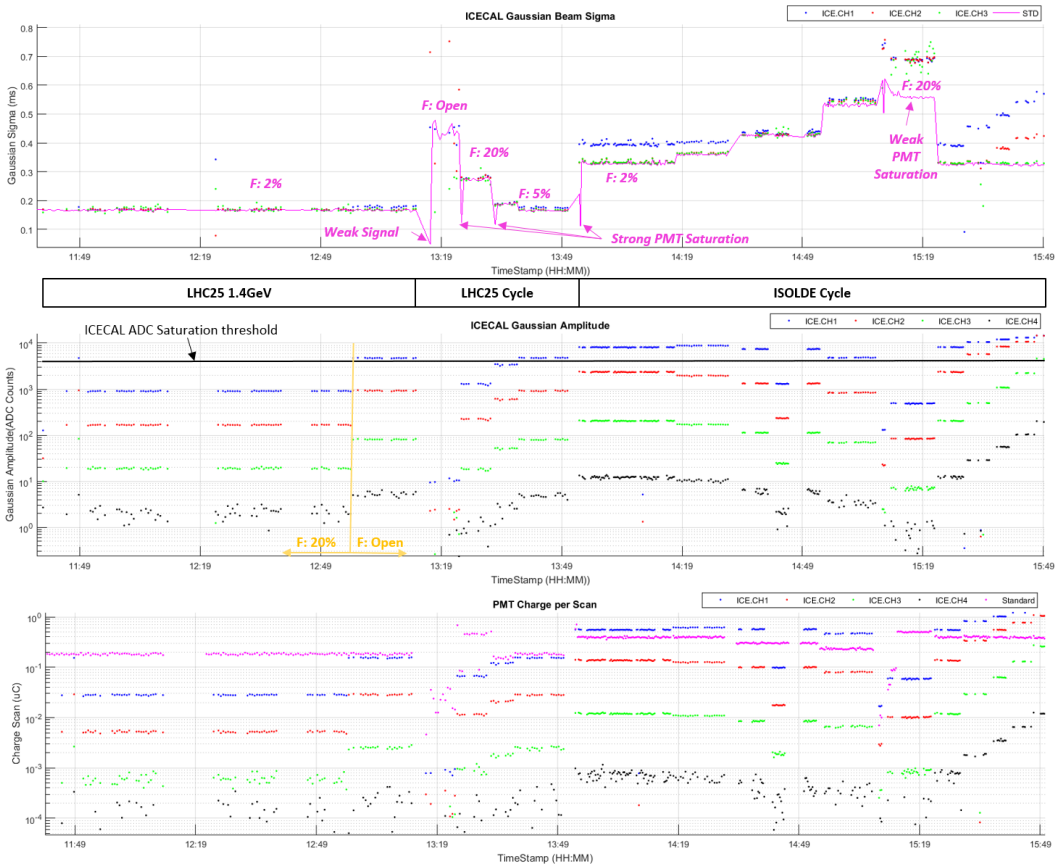

Figure 6.72 – Graphical summary of ICECAL measurements and comparison with standard acquisition system

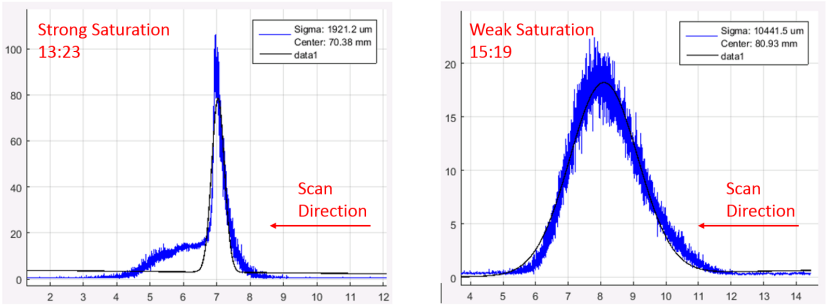

Figure 6.73 – PMT saturation observed on the standard system.

over the acceleration cycle. The signal amplitude during the LHC25ns cycle (300-750 ms) varied by a factor 500, whereas for the ISOLDE cycle (405-780 ms) the amplitude change was about a factor 20.

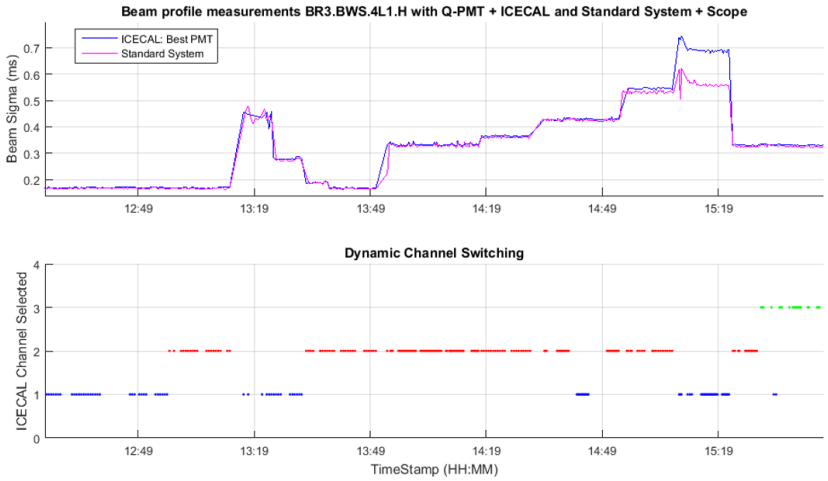

Figure 6.74 – Beam profiles determined by Standard system (with no strong saturation) and M-PMT with ICECAL readout. Dynamic ICECAL channel selection was applied to cover the beam dynamics.

Comparative profile measurements are shown in Fig.6.75 for the standard system, acquired on surface with a scope, and M-PMT system (CH2), acquired in the tunnel with the ICECAL FE. Both measurements correspond to the same scan and PMT type, configured in a different working point (Filter-PMT Gain). Both PMTs were operating on their linear range (Ip<10mA and Qo $< 0.4\mu$C).

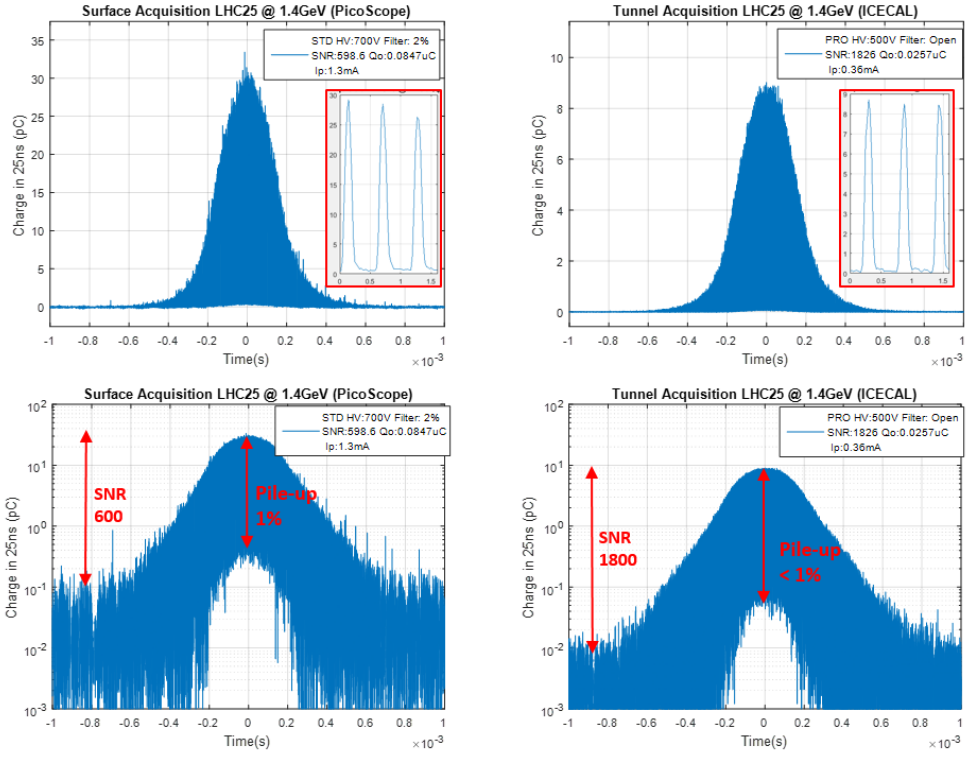

Figure 6.75 – Comparison of PSB beam profiles acquired on surface with standard system (left) and M-PMT acquired on tunnel with ICECAL Front-End (right) for a LHC25ns beam at 1.4GeV. Linear scale on top and logarithmic on bottom.

The equivalent charge noise (for 25ns buckets) for ICECAL was about 0.01pC, surface acquisition featured an order of magnitude higher charge noise (0.1pC). With a similar peak charge for both detectors, 10-30 pC, this effect leads to roughly an order of magnitude better SNR for acquisitions performed on the tunnel. With regard to the signals timing, the ICECAL profile featured faster pulses, with slightly shorter tails. The signal acquired on surface suffers from the inherent bandwidth reduction associated to the cable length. Despite the relaxed PSB bunch structure compared to other accelerators (single bunch with 200ns FWHM pulses and ≈600ns repetition period), some bunch pile-up can be observed on the profiles acquired on surface, note the baseline drift at the centre of the Gaussian on the logarithmic representation for both profiles. Same filtering and processing algorithm was applied in both traces on Fig. 6.75.

In addition, the SNR can be further enhanced with the use of clipped ADC channels for the Gausian tails. In the specific example shown on Fig. 6.76 SNR reaches up to 1e4 by combining CH1 and CH2 whereas only CH2 featured a SNR about 1e3. This is specially helpful for measuring the beam halo.

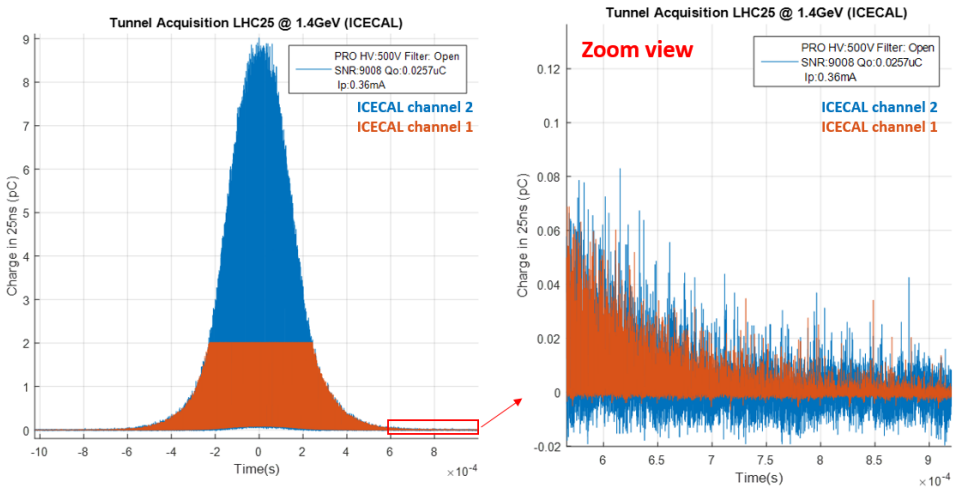

Figure 6.76 – PSB LHC25ns beam profile reconstructed by a combination of different acquisition channels.

6.3.4. Impact of scintillator geometry

Tests in section 6.3.3 resulted on a similar beam size precision for LIU-BWS prototype against an operational scanner. Given the high number of points per sigma (200-700), the relatively big beams (σ =2-5 mm) and the little incertitude on the position information for the prototype (≈11 µm), the dominant factor for the profile incertitude could either be related to shot-by-shot beam variations or to statistics on the secondaries crossing the detectors (as previously with the diamond detector).

An issue detected on the optical position sensor lead to the exchange of scanner and another measurement campaign was carried out on 29/09/2017. During the replacement of the scanner, the detector systems were upgraded with bigger scintillators featuring different geometry, the idea behind was to decrease the profiles amplitude uncertainty by increasing the detector area, thus allowing more particles to cross its surface. The 3x3 cm cylindrical scintillators were replaced by 10x10x1 cm square section scintillators, see Fig. 6.77.

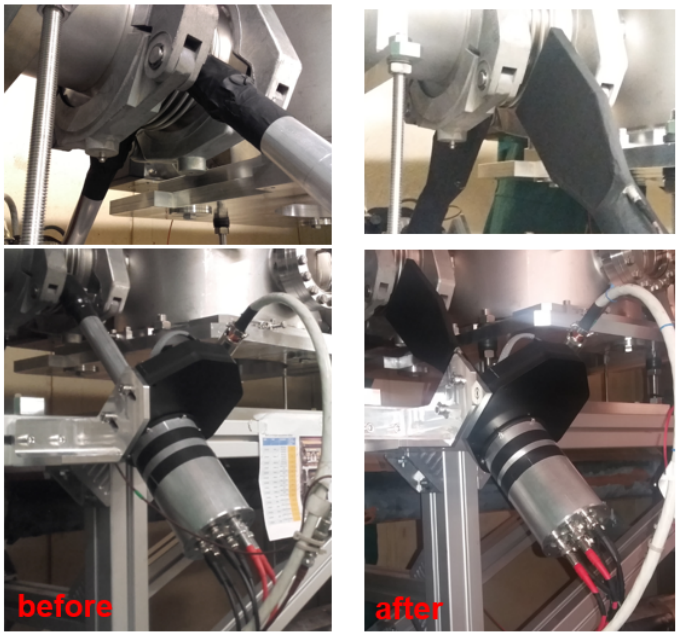

Figure 6.77 – Detector system before and after the scintillator change.

Comparative beam profile measurements under the same machine and PMT configurations (Beam: LHC25ns with 144e10p at 1.4 GeV, PMT: 700 V and 2 % ND filter) are shown on Fig. 6.78. The detector change resulted in a 30 % lower amplitude uncertainty which would correspond to about twice more particles crossing the detector surface.

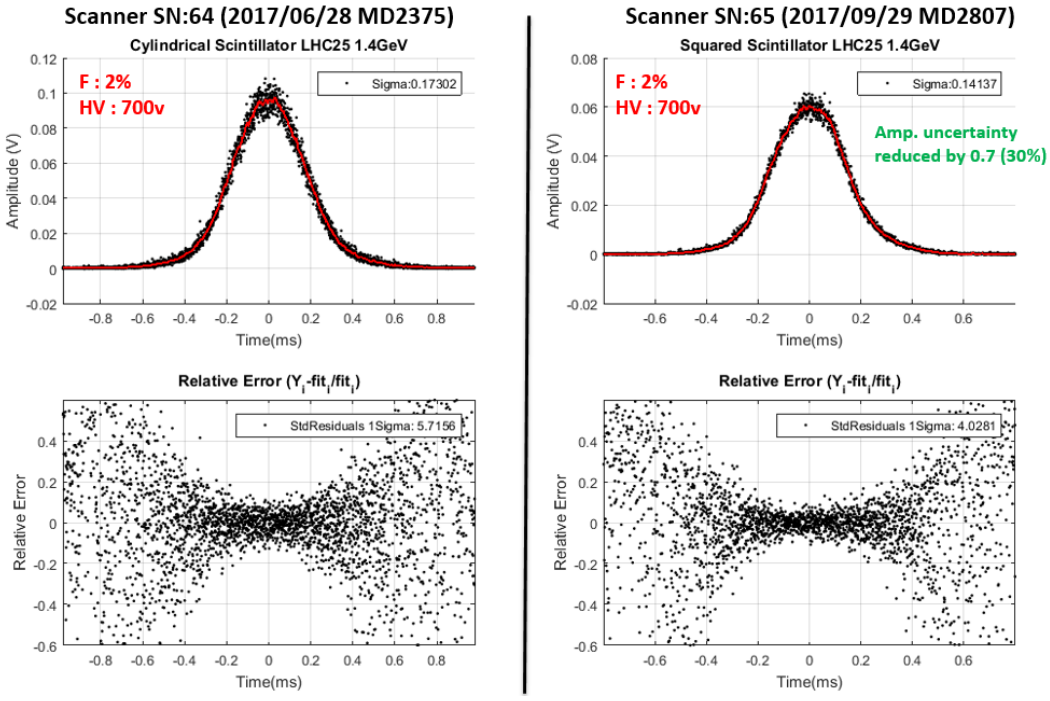

Figure 6.78 – Beam profiles under same beam and PMT configuration with different scintillator geometries. Cylindrical scintillator (left) versus squared scintillator (right).

The improved scintillator geometry, along with other mechanical and control improvements on the scanner leaded to a significant reduction on beam profile measurement uncertainty. On Fig. 6.79, it is shown that under the same circumstances the operational scanner is showing a consistent RMSe $\approx$ 1.6%, whereas the prototype scanner reduced this error from a RMSe

$\approx 1.6\%$ to about 1%.

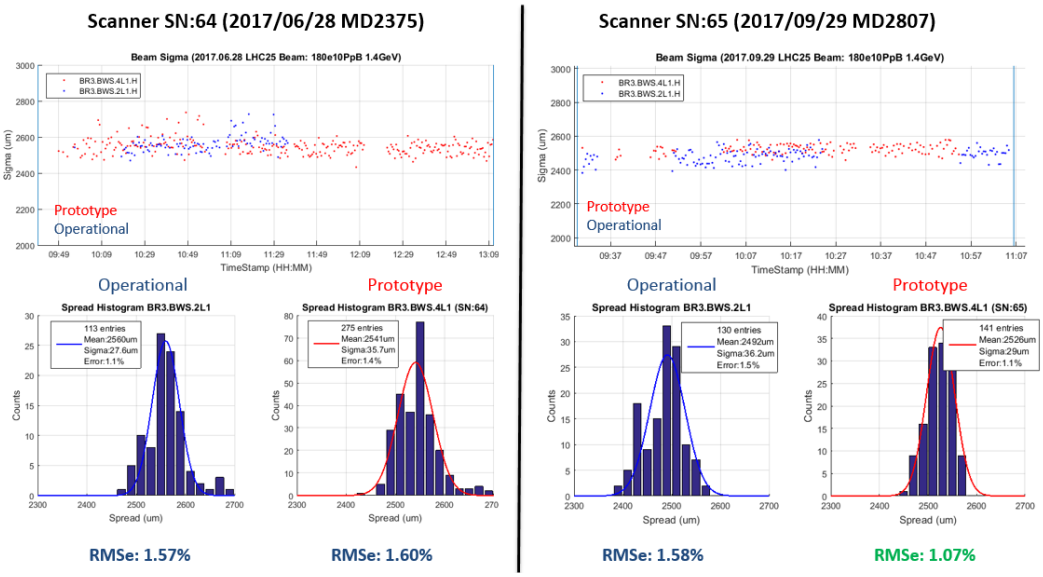

Figure 6.79 – Beam profile measurements for a LHC25 at 1.4 GeV for both measurement campagins.

To eliminate potential influence of shot-by-shot variations, the beam profile measurements were correlated to the intensity measured by a beam current transformers (BCT) on the same PSB ring. By analysing the residuals of a linear fit applied on each data-set, intensity dependence can be eliminated from both scanners. Figure 6.80 shows this process, a final precision of $\approx$ 1.4% is reached on operational scanners versus $\approx$ 0.9% for the LIU-BWS prototype.

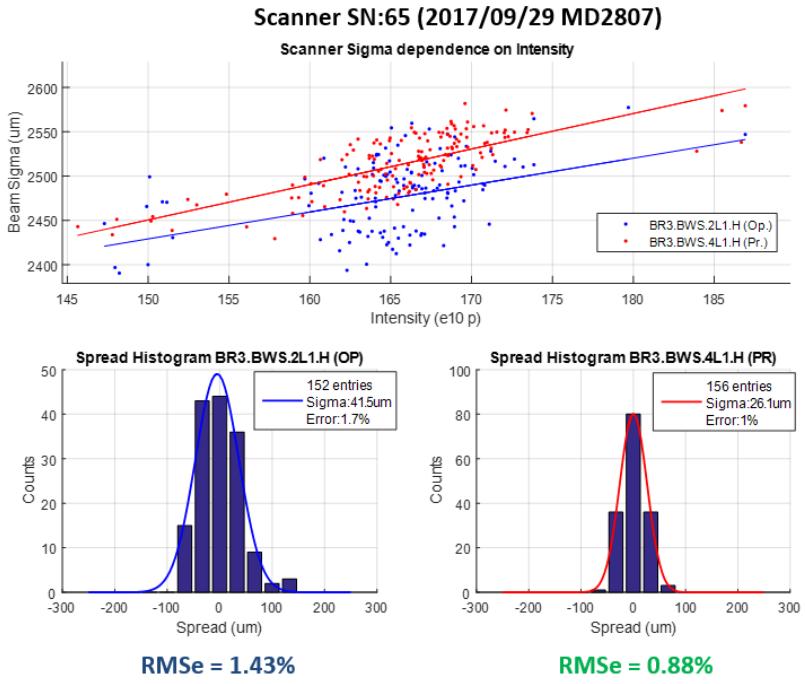

Figure 6.80 – Beam profile measurements for a LHC25 at 1.4 GeV correlated with their corresponding beam intensities.

The ICECAL front-end was also operated in parallel with the standard system. As previously, measurements were carried out at different moments of the cycle (beam energy) and

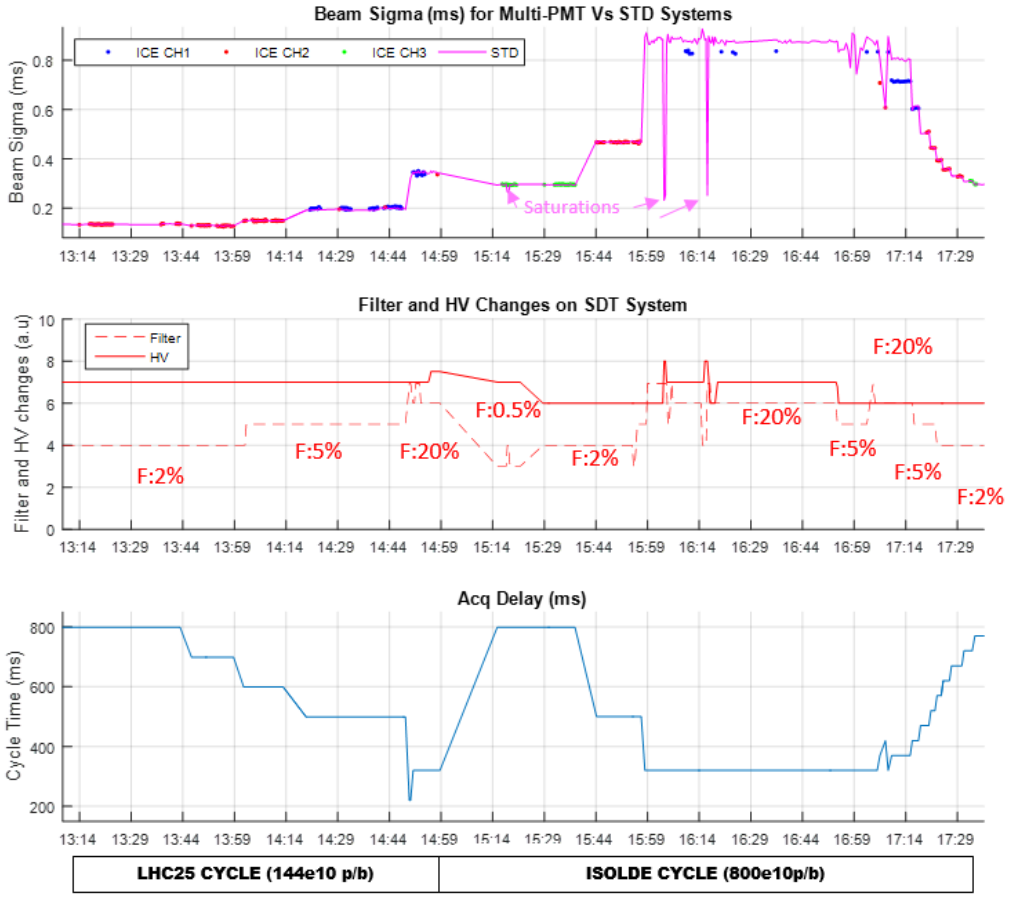

Figure 6.81 – Top: Beam profiles measured by standard and M-PMT + ICECAL Front-End. Middle: Filter and HV changes requied on standard systems. Bottom: Cycle time.

with different beam intensities (LHC25 and ISOLDE), the front-end featured a static configuration and dynamic channel selection was done in post-processing. The standard system required of many filter changes and high voltage adjustments to accommodate the PMT working point to the beam dynamics, see Fig. 6.81.

The beam profile measurements of both datasets were consistent with a disagreement $<$ 1%, demonstrating the feasibility of a M-PMT system for high dynamic range coverage.

Chapter 7

Conclusions and Outlook

7.1. Conclusions

This thesis covers the design of a bunch-by-bunch, low-noise and high dynamic range acquisition system for the detection of the secondary particles shower produced by beam wire scanners. In addition, solid state detectors based on poly-crystalline chemical vapour deposition (pCVD) diamond are firstly evaluated here for wire scanner applications. The project has been developed in the framework of the LHC Injectors Upgrade and aims to overcome the current acquisition limitations. Joint with the wire position determination uncertainty, the quality of the secondary shower acquisitions is a determinant factor that constraints the beam profile measurement precision of the upgraded instrument.

The performance and limitations of operational scanner systems at CERN were reviewed with special focus on its secondaries acquisition systems in Sec. 2.4. In addition to their operational complexity and reduced dynamics, the impact of long coaxial lines (CK50) in bunch-by-bunch beam profile determination was identified as one of the weak points of the current acquisition schema. A simulation model of the employed cable was used to quantify this effect under different scenarios, demonstrating that, for typical 25ns bunch structures, pile-up due to long cables (100-250m) could potentially induce beam profile errors $> 1\%$ (full discussion on Sec. 4.3).

A set of analyses and powerful simulations allowed scaling the required dynamic range for the upgraded detector and associated electronics. These analyses included, the study of the particle bunches density for different beams, and advanced particle physics simulations to characterise the secondary particles generated by a wire scan (Sec. 4.1 and Sec. 4.2). This highlighted the need to resolve up to 6 orders of magnitude, being the Proton Synchrotron Booster the most critical accelerator. The simulations provided comprehensive models of the secondary shower geometry, its main composition and the dose deposition around the beam pipe. Further simulations shown on Sec. 4.4 derived the beam profile uncertainty from the measurement conditions, essential information to determine the scanner and acquisition system specifications.

To fulfil the system requirements, the design proposed was a Front-End/Back-End (FE/BE) architecture based on standard beam instrumentation boards used at CERN (VFC and GEFE). Data transmission, FE control and synchronisation are performed through a 4.8Gb optical link running the CERN GBT protocol (Chapter 5). This architecture allows performing low-noise and high dynamic range acquisitions close to the detector in the tunnel, without the inherent bandwidth reduction imposed by long cables, thus ensuring bunch-by-bunch beam profile isolation. Two 40MHz integrator ASICs were selected to evaluate different acquisition strategies for wide dynamic range coverage, these were: ICECAL for multi-channel parallel acquisition and QIE10 for single-channel acquisition with logarithmic encoding. The early development state of the final boards leaded to the development of a proof-of-concept prototype based on rad-hard boards from CMS (Igloo2UMD as tunnel Front-End) and FPGA

development boards (for the surface Back-End). In addition, rad-tolerant mezzanine boards were designed and fabricated for the evaluation of both readout ASICs.

The FPGA firmware for the latency-optimised version of the GBT link was successfully implemented and tested for the first time with flash-based FPGAs. The LHC/SPS 40Mhz clock propagation and recovery technique implemented resulted in a recovered clock synchronised with the bunch-crossing with a deterministic phase and an uncertainty < 1.3ns, capable of maintaining synchronisation during the accelerator ramp.

Laboratory qualifications, shown on Section 6.1, fully characterised both front-end prototypes using the complete acquisition chain. QIE10 version demonstrated up to 5 orders of magnitude dynamics coverage (charge sensitivity of 3.2fC and saturation about 340pC) while keeping non-linearities bellow 5%. For the ICECAL version, each of its four channels featured 3 orders of magnitude dynamics with settable slopes (with 16fC sensitivity and 14pC saturation in its default configuration), non-linearities lied below 1% in any configuration.

Despite the fast response, excellent linearity and dynamic range that diamond detectors feature, the results of extensive beam tests campaigns on SPS concluded that their small available area ($1cm^2$) was a strong limitation for their application with BWS on the LHC injectors. Diamond profiles showed amplitude statistics, associated to the number of particles crossing its surface, which directly impacted on the beam profile determination uncertainty (Sec. 6.2.4). Statistical noise was especially dominant for SPS beams at injection energy (1×10^{11} protons per bunch at 26 GeV), where only $\approx 100 - 200$ particles per bunch crossed the detector at the Gaussian centre. The more intense secondary shower at 450 GeV (with $\approx 2000-5000$ crossing MIPs), significantly reduced the amplitude statistics and beam profiles, on this configuration profiles were comparable to those obtained with operational systems. These promising results suggest the application of such detectors on the LHC wire scanners with nominal proton beams. Studies with lead ions beams on SPS allowed recording profiles with diamond detectors. However the improvement with beam energy was not as remarkable as with protons, and statistical noise still remained an issue for 450 GeV Ion beams.

On this thesis, the mechanical performance of the upgraded BWS instruments was also studied and compared to operational scanners during the beam tests shown on Chapter 6. The LIU-BWS scanning at 20ms-1 on SPS with an AWAKE beam (1.1e11 at 400GeV) demonstrated a precision in the beam centroid $\approx$ 10 µm with a beam sigma uncertainty $\approx$ 4.2% using a diamond detector (with 1.1 points per sigma). On this configuration, linear scanners, at 1ms-1, showed uncertainties $\approx$ 30µm and $\approx$ 6% on centroid and beam sigma respectively (with 17 points per sigma). Measurements on SPS with a COAST beam (0.23e11 at 200GeV) resulted in LIU-BWS uncertainties of 48µm for beam centroid and $\approx$ 2.3% for beam profile (using scintillator-PMT readout), whereas linear scanners resulted in uncertainties of 94µm for centroid and $\approx$ 3% on beam profile. The required 1% beam size uncertainty specified for SPS can be reached by the LIU-BWS by reducing the scanner speed to increase the number of points per sigma of the measurement. Test results with the PSB LIU-BWS initially showed similar beam profile uncertainty compared to operational systems ($\approx$ 1.5%), with both operating at 20ms-1 (LIU-BWS) and 15ms-1 (Operational) and with a similar detector set-up, based on 3x3cm cylindrical scintillators. The beam profile measurement uncertainty was reduced for PSB LIU-BWS prototype to about 0.8% by using a bigger scintillator geometry, which demonstrated that, given the high number of points per sigma on PSB (200-700), the beam profile uncertainty on this specific accelerator was dominated by amplitude statistics.

Both remote readout schemas within the scope of this work (QIE10 and ICECAL based) were successfully evaluated on several test campaigns carried out in SPS and PSB accelerators. The QIE10 version used for pCVD diamond detector readout in tunnel, featured a significant noise reduction and much cleaner Gaussian tails when compared to surface acquisition. Simulations demonstrated that the constant 1% quantisation error of this ASIC could potentially influence profile measurement incertitude, especially for few points per sigma (<3). Nevertheless, this effect could not be practically verified given the diamonds statistical noise.

The QIE10 front-end demonstrated no performance degradation in terms of noise during 1.5 years of operation, which remained bellow 4fC (3 MIPS on diamond). The ICECAL front-end version was evaluated in the PSB tunnel with a novel detector schema based on a scintillator with multiple PMT for parallel readout. Such detector allowed to perform beam profile measurements with a single configuration for the PSB energy boundaries on different beam types. This configuration represents a significant improvement with respect to the existing systems, simplifying their operation and avoiding parameters settings for the different accelerator working points. In addition, the new detector configuration offered lower noise and redundant measurements with enhanced resolution, to properly resolve the far-tails of the beam profile distribution.

7.2. Outlook

The Multi-PMT (M-PMT) schema will be evaluated in the rest of the injectors (PS, SPS) after the End of the Year Technical Stop 2017 (EYETS2017). The initial evaluation will use long coaxial cables up to surface and fast digitisation (>500MSPS) allowing the application of baseline recovery algorithms during data processing. This novel detector configuration for beam wire scanner applications will work in a static configuration and aims to substitute the traditional filter wheel and HV adjustments required up to now during the scanners operation. New detector PCB boards and assemblies based on scintillators and M-PMT geometries are currently under construction for the BWS upgrade commissioning.

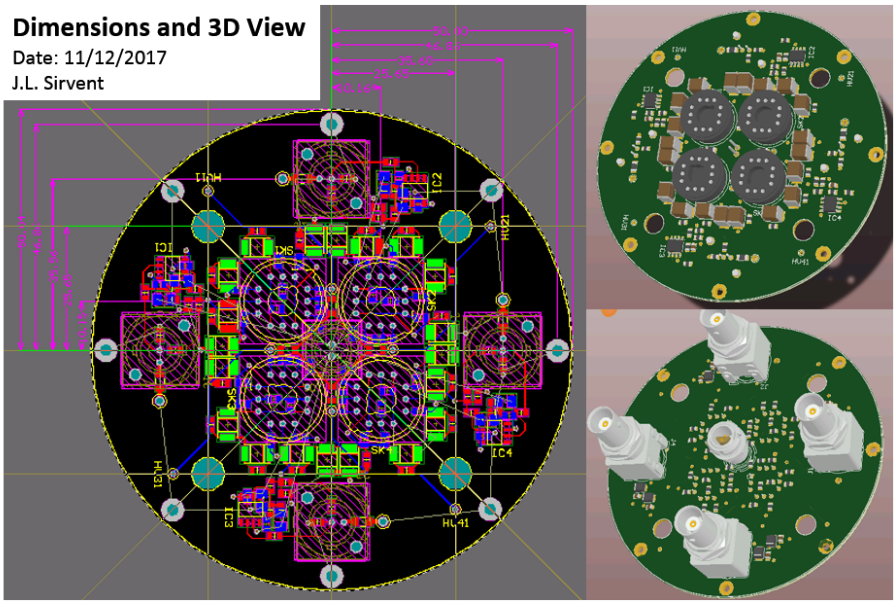

Figure 7.1 – Multi-PMT printed circuit board design.

On low energy accelerators, such as PS and PSB, commissioning electronics will be based on VFC boards with fast FMC ADC mezzanines. On these machines, ionising radiation can easily surpass 10kGy/year and compromise systems operation. Space constrains in some areas of these machines does not allow electronics shielding. Concerning LHC and SPS accelerators, where radiation levels are moderated ($\leq$ 1 kGy/year) and cable lengths much longer, remote acquisition systems as the evaluated on this work, can fully profit from close-detector acquisition.

Apéndice A

Appendix: Resumen en Español

El proyecto LHC Injectors Upgrade (LIU) tiene como objetivo incrementar la luminosidad del LHC doblando el brillo del haz de partículas a través de la construcción del nuevo LINAC4, el primer acelerador linear en la cadena del LHC. Con el fin de producir haces de baja emitancia y mayor intensidad para el High Luminosity LHC (HL-LHC), se requieren actualizaciones en toda la cadena de inyectores, incluyendo nueva instrumentación de diagnósticos de mayor precisión. En este contexto, una nueva generación de beam wire scanners (LIU-BWS) se encuentra en desarrollo para una medida precisa de la emitancia. Estos monitores obtienen el perfil transversal del haz cruzando un fino filamento de carbono (30um) a través del haz de partículas. El perfil del haz se obtiene a través de la correlación entre la intensidad de la lluvia de partículas secundarias producida por la interacción haz-filamento y la posición del hilo de carbono.

La operación de la actual generación de beam wire scanners (BWS) en el CERN es compleja y la precisión de su medida está parcialmente limitada por sus detectores de partículas secundarias y sistemas de adquisición. Estos detectores se basan en centelladores orgánicos, filtros de densidad neutra seleccionables y tubos foto-multiplicadores. Antes de cada medida se debe acomodar el punto de trabajo del detector en función de las condiciones del haz (intensidad, tamaño estimado y energía) para evitar saturar la electrónica de adquisición, localizada en superficie. En esta situación, muchas configuraciones implican una pobre relación señal ruido (SNR) y una resolución limitada, lo que afecta directamente a la fiabilidad de su medida. Además, la restricción en el ancho de banda, impuesto por los largos cables (hasta 250m) empleados para la transmisión de señal analógica, provoca el solape de los pulsos provenientes de cada bunch separados por 25ns, y compromete la medida del perfil de bunches individuales.

Esta tesis cubre el diseño de nuevos sistemas de adquisición de partículas secundarias para la nueva generación de BWS en el CERN. Este trabajo revisa los sistemas de adquisición operacionales para identificar sus limitaciones y muestra avanzadas simulaciones de física de partículas que caracterizan la lluvia de partículas secundarias alrededor del escáner en diferentes escenarios operacionales. Las simulaciones proporcionan una localización óptima para los nuevos detectores y, junto con un estudio de los haces empleados en cada acelerador, determinan un rango dinámico requerido de hasta 1e6 para la adquisición de la lluvia de secundarias.

El nuevo diseño investiga el uso de una innovadora tecnología para la detección de partículas basada en detectores de diamante poli-cristalino (pCVD), y propone el uso de sistemas de adquisición de alto rango dinámico en las inmediaciones de los detectores. Este nuevo esquema emplea ASICs integradores a 40Mhz para la digitalización de la señal del detector en el túnel. La información digital se transmite a través de un link óptico a 4.8Gbps hasta la electrónica de superficie. Se contemplan dos estrategias para cubrir un alto rango dinámico: un sistema mono-canal con codificación logarítmica o un sistema multi-canal con diferentes ganancias por canal. Prototipos de ambos esquemas han sido completamente desarrollados,

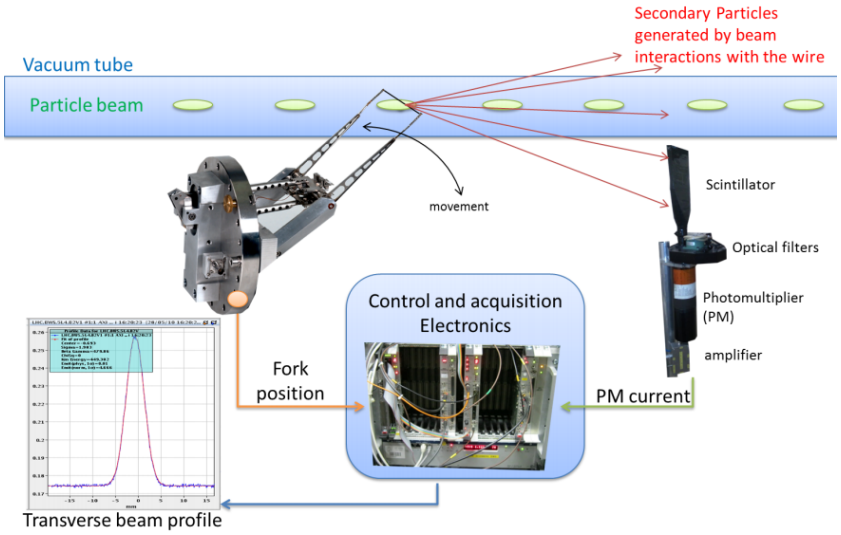

Figura A.1 – Principio de funcionamiento de un Wire Scanner.

caracterizados en laboratorio y evaluados en PSB y SPS con diferentes haces. El uso de estos sistemas no solo permite medidas de bajo ruido, sino que también evita el solape de la señal pulsada proveniente de cada bunch y simplifica significativamente la operación del escáner.

A.1. Beam wire scanners en el CERN y su actualización

Los beam wire scanners son una parte esencial de la instrumentación de diagnostico empleada diariamente por los operadores de los aceleradores del CERN. Estos son monitores interceptivos que determinan del perfil transversal del haz, medida necesaria para el cálculo de la emitancia. La emitancia es uno de los parámetros mas importantes de un haz de partículas, y tiene impacto directo en el cálculo de la luminosidad del LHC. La precisión y disponibilidad de estos instrumentos es fundamental, ya que también se emplean para la calibración de otros sistemas. Los wire scanners son capaces de obtener el perfil individual de cada bunch en aceleradores circulares, con una resolución espacial dependiente de la frecuencia de revolución del acelerador y la velocidad del escáner. En el caso de SPS y LHC, la separación entre bunches es de 25ns y su periodo de revolución es 23µs y 89µs respectivamente. El principio de funcionamiento de estos dispositivos se muestra esquemáticamente en la Fig.A.1.

En la actualidad se emplean diferentes diseños mecánicos optimizados para cada acelerador. Estos son conocidos como lineares, rotativos y rotativos rápidos, con velocidades de escaneo limitadas a 1, 6, y 15ms-1 respectivamente. En todos ellos se emplean fuelles para la transferencia de movimiento aire-vacío y potenciómetros para la lectura de la posición del escáner. La incertidumbre en la medida de posición es altamente susceptible a ruido en la lectura del potenciómetro y a juego mecánico de sus componentes, llegando en algunos casos a incertidumbres en el orden de 90-100µm [34] [23]. Una fractura por fatiga en uno de sus fuelles puede comprometer el vacío de los aceleradores.

Respecto a los sistemas operacionales de adquisición de secundarias, sus parámetros configurables dificultan la operación del escáner. Los largos cables empleados (hasta 250m) para la transmisión de señal implican su degradación en términos de ancho de banda (produciendo bunch pile-up), además de una reducción en la relación señal-ruido (SNR) debido a un entorno hostil (RF, EMI, lineas de potencia). En determinadas configuraciones, estos detectores sufren de un efecto conocido como "saturación de PMT", que limita la carga total extraída del PMT en cada medida y afecta directamente la determinación del perfil del haz.

En previsión a los haces destinados al High-Luminosity LHC (HL-LHC), el proyecto LHC Injectors Upgrade (LIU) contempla el reemplazo de sistemas obsoletos, el diseño de una nueva

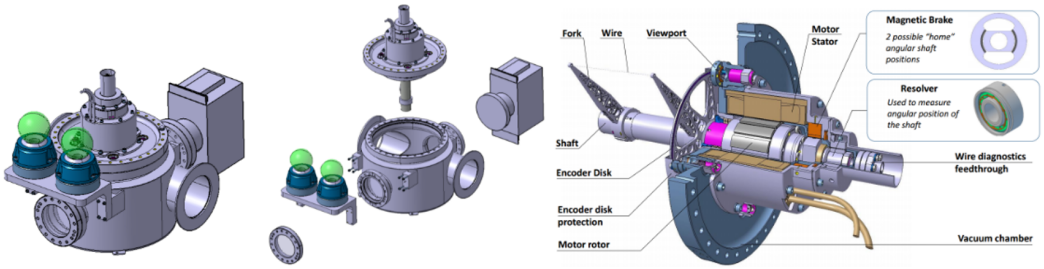

Figura A.2 – Esquemático de la nueva generación de BWS (LIU-BWS)

generación de wire scanners con menor incertidumbre en la medida del hilo y sistemas de adquisición de secundarias de alto rango dinámico. Con esta nueva generación se pretende una alta velocidad de escaneo para evitar la rotura del hilo en medidas de haces nominales con un gran número de bunches [20] y una incertidumbre menor de 5 % en la medida de la emitancia. La actualización de sistemas implica un nuevo diseño mecánico, electrónica de control, detectores de posición, detectores de secundarias y sistemas de adquisición.

La nueva generación (LIU-BWS) esta diseñada para una velocidad nominal de 20ms-1 y es mecánicamente compatible con todos los inyectores del CERN, ver Fig.A.2. Su principal característica es el uso de un solo eje para el montaje de todas las piezas móviles y la ausencia de interfaz mecánica para la transmisión de movimiento aire-vacío. El sistema está diseñado alrededor de un motor cuyo estátor se encuentra en el exterior de la cámara de vacío mientras que el rotor se encuentra en el interior. Una fina lamina de acero separa estas dos partes y preserva el vacío. Para el control del escáner, su posición se determina con un resolver. La posición precisa del hilo para la medida del perfil del haz se obtiene a través de un encoder incremental pasivo de fibra óptica, formado por un disco encoder instalado en el eje del escáner (en vacío) y dos las cabezas lectoras en el exterior de la cámara [41]. Tanto el diseño del instrumento como su perfil de movimiento están optimizados para evitar deformaciones mecánicas y vibraciones que puedan afectar a la precisión de su medida [22] [42]. Este sistema ha sido caracterizado en un banco de calibración, resultando en una exactitud de 10µm en la medida de la posición del hilo con una precisión de 6µm a su velocidad nominal [47].

Esta tesis cubre la investigación, diseño e implementación de nuevos detectores y sistemas de adquisición de partículas secundarias para la nueva generación LIU-BWS, con el objetivo de abordar las limitaciones de los sistemas existentes. Para ello se estudia la dinámica requerida por cada acelerador a través de simulaciones de física de partículas y las características de sus haces. Para evitar los efectos asociados a largos cables coaxiales, se propone el uso de sistemas de adquisición de alto rango dinámico en las proximidades del detector. Con el fin de evitar parámetros configurables, se contemplan diferentes tipos y arquitecturas de detectores: uno basado en centelladores con múltiples tubos fotomultiplicadores (M-PMT) y otro basado en detectores estado solido (diamante poli-cristalino pCVD). Por primera vez estos tipos de detectores se estudian de forma sistemática en condiciones operacionales para su aplicación con beam wire scanners. Este trabajo desarrolla y evalúa dos prototipos de sistemas de adquisición con digitalización en túnel, basada en Front-Ends resistentes a la radiación que emplean ASICs integradores a 40Mhz para la lectura de detectores y un link óptico basado en el estándar GBT para transmisión digital de datos. Estos innovadores esquemas demostraron facilitar la operación del escáner, un menor ruido y la ausencia de pile-up, lo que garantiza medidas fiables del perfil de bunches individuales.

Cuadro A.1 – Beam sigma and bunch densities summary for the BWS on the CERN accelerators.

Beam profiles and Bunch densities for the CERN accelerators at the Beam Wire Scanners location										
	σ_h **[mm]**		σ_v **[mm]**		**HD Bunch** [10^{11}/**mm**]		**ΔHD Bunch**	**VD Bunch** [10^{11}/**mm**]		**ΔVD Bunch**
Proton Synchrotron Booster (PSB)	1.57	13.5	1.2	9.0	0.01	16.82	1.6e3	0.01	26.43	2.6e3
Proton Synchrotron (PS)	0.8	13.0	0.5	8.8	0.01	8.53	8.5e2	0.01	16.54	1.6e3
Super Proton Synchrotron (SPS)	0.2	8.7	0.3	6.7	0.01	2.91	2.9e2	0.01	2.87	2.8e2
Large Hadron Collider (LHC)	0.16	1.19	0.22	1.79	0.031	4.752	1.5e2	0.022	3.403	1.5e2

A.2. Estimación del rango dinámico y consideraciones de diseño

Dinámica de los haces en los aceleradores:

La producción de partículas secundarias a partir de la interacción del haz con el hilo del escáner, para una energía determinada, es dependiente de la geometría e intensidad del haz de partículas. Bunches más intensos y estrechos (más densos) producirán más secundarias en una interacción que aquellos con menor intensidad y mas amplios. La dinámica de adquisición de secundarias basada en este concepto se ha estudiado para los aceleradores del CERN a través de la densidad de bunch, definida como:

$$HD_{Bunch} = \frac{N_b}{\sqrt{2\pi\sigma_h}}, VD_{Bunch} = \frac{N_b}{\sqrt{2\pi\sigma_v}} \tag{A.1}$$

donde N_b es el número de protones por bunch y $\sigma_{h/v}$ es su tamaño en un plano.

Además, la dimensión transversal de cualquier haz ($\sigma_{h/v}$), depende a su vez de su emitancia normalizada ($\epsilon*$), la óptica del acelerador para una localización en el determinada (β) y la energía del haz ($\gamma_L\beta_r$). Debido al fenómeno conocido como *Adiabatic Damping* los haces se estrechan al ganar energía. En el plano horizontal, su distribución depende también de la dispersión en energía ($(D\frac{dp}{p})^2$).

$$\sigma_h = \sqrt{\frac{\epsilon_h^*\beta_h}{\gamma_L\beta_r} + (D\frac{dp}{p})^2}, \qquad \sigma_v = \sqrt{\frac{\epsilon_v^*\beta_v}{\gamma_L\beta_r}} \tag{A.2}$$

Considerando todos estos efectos, y los haces típicos de cada acelerador, se ha determinado la máxima y mínima densidad de bunch para cada caso en la localización de los wire scanners operacionales (ver Tabla A.1).

Dado los diferentes haces, ciclos de aceleración y manipulaciones RF, hay una variación de cerca de 3 ordenes de magnitud para las densidades de bunch del PSB, mientras que para el caso del LHC esta variación es de aproximadamente 2 ordenes de magnitud. Además de características geométricas para estimar el rango dinámico requerido por el detector y sistema de adquisición, se debe considerar también la variación en la producción de secundarias asociada a la energía del haz primario en cada máquina, detallado en la sección siguiente.

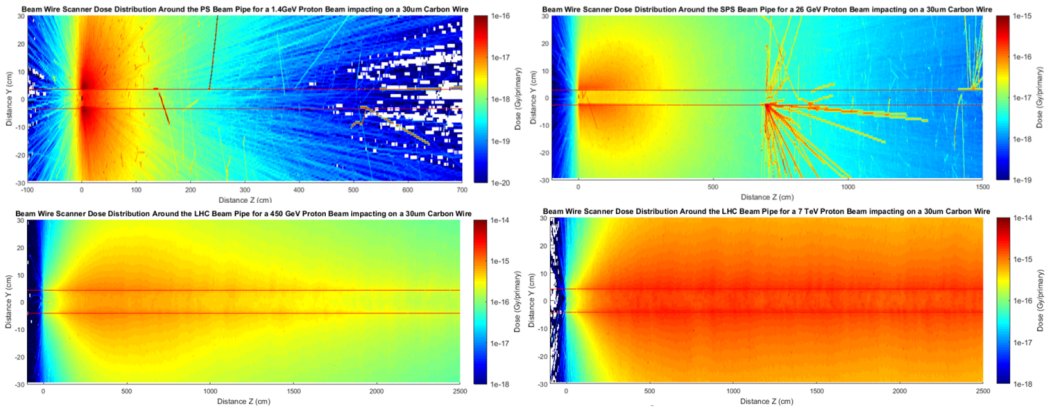

Figura A.3 – Simulaciones FLUKA mostrando energía depositada alrededor del punto de interacción con el escáner para los diferentes aceleradores del CERN y energías del haz. Las lineas horizontales rojas representan la cámara del acelerador.

Cuadro A.2 – Resumen numérico de simulaciones. Energía depositada por secundarias a diferentes energías del haz y distancias del punto de interacción.

BWS Secondaries dose deposition for CERN accelerators				
	Dose at 5cm (Gy/Primary)		**Dose at 15cm (Gy/Primary)**	
PSB	**100MeV**	**1.4GeV**	**100MeV**	**1.4GeV**
	8.46e-20	1.01e-16	1.49e-20	5.34e-17
	Dose at 10cm (Gy/Primary)		**Dose at 1m (Gy/Primary)**	
PS	**1.4GeV**	**26GeV**	**1.4GeV**	**16GeV**
	7.95e-17	1.70e-16	3.44e-18	1.60e-16
	Dose at 1m (Gy/Primary)		**Dose at 1m (Gy/Primary)**	
SPS	**26GeV**	**450GeV**	**26GeV**	**450GeV**
	1.82e-16	8.2e-16	5.18e-17	1.54e-15
	Dose at 3m (Gy/Primary)		**Dose at 7m (Gy/Primary)**	
LHC	**450GeV**	**7TeV**	**450GeV**	**7TeV**
	1.71e-15	3.32e-15	1.32e-15	3.43e-15

Simulaciones de lluvia de partículas secundarias:

La distribución geométrica de la lluvia secundarias producida por la interacción del haz con el hilo del escáner, así como su cantidad, está relacionada con la energía del haz y la sección y material del hilo [108]. Aquí se muestran simulaciones de física de partículas (FLUKA) para caracterizar la energía depositada alrededor del punto de interacción en cada uno de los aceleradores del CERN a diferentes energías. Los resultados se muestran normalizados por protón primario impactando en el hilo (ver Fig.A.3). La señal generada por el detector está íntimamente relacionada con la energía depositada en su volumen. De esta manera se puede estudiar el rango dinámico requerido para el sistema de adquisición solo dependiente de la energía del haz.

La Tabla A.2 muestra aproximadamente una variación en energía depositada de aproximadamente de 3 ordenes de magnitud para el caso de PSB, 2 ordenes de magnitud para PS, 1 orden de magnitud para SPS y aproximadamente un factor 2 para LHC. Esta dinámica, combinada con las estimaciones de la sección anterior determinan un rango dinámico requerido de aproximadamente 6 ordenes de magnitud, siendo el PSB la máquina más exigente.

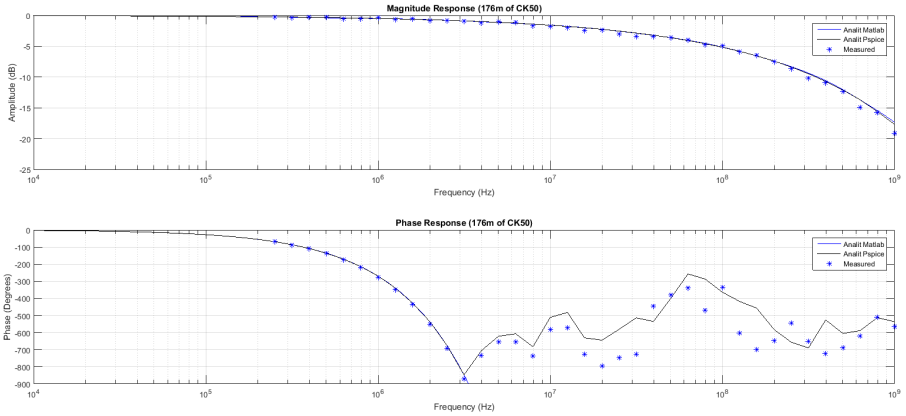

Figura A.4 – Diagrama Bode del modelo del cable (linea continua) y medidas (puntos).

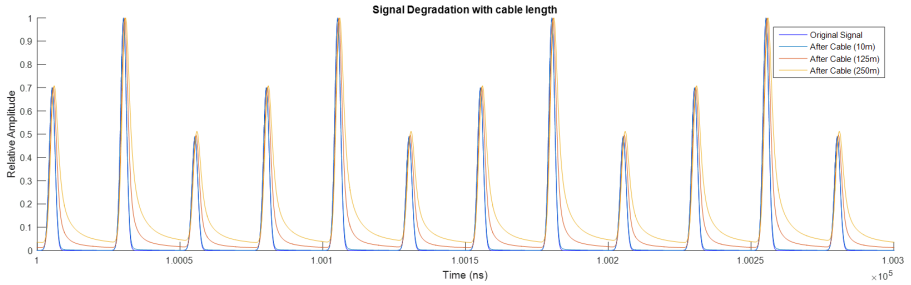

Figura A.5 – Simulación mostrando la señal de salida del modelo del cable para diferentes distancias con señales típicas de LHC/SPS (pulsos de 2ns FWHM separados por 25ns).

Degradación de señal en largos cables CK50 e impacto en perfiles:

La principal característica de los sistemas actuales es la transmisión de señal analógica a través de largos cables CK50. Su longitud alcanza hasta 250m en algunos sistemas. Para cuantificar como la degradación de la señal impacta en la medida del perfil del haz, se realizaron simulaciones con un detallado modelo analítico de este cable. La respuesta en frecuencia del modelo para 175m se muestra en Fig.A.4, su respuesta se aproxima correctamente a medidas realizadas para esa misma longitud.

En Fig.A.5 se aprecia como para señales típicas de detectores LHC/SPS, existe solape en pulsos consecutivos para distancias de cable mayores a 100m.

El error en la determinación del perfil de un bunch debido al solape con bunches previos se puede estimar simulando un haz de SPS, consistente de un tren de tres bunches consecutivos con diferentes anchuras (Fig.A.6). Usando el modelo del cable y reconstruyendo cada perfil a través de integrales alrededor de cada bunch (como se hace en sistemas operacionales), se puede determinar el error inducido en función de la similitud entre perfiles así como de la longitud del cable (ver Fig.A.7).

Este efecto, conocido como "bunch pile-up", puede llegar a producir fácilmente errores de hasta 2.5 % en trenes de bunches con perfiles relativamente similares (Sigma ratios 80 %) para longitudes de cable >200m, esto es inaceptable para los LIU-BWS.

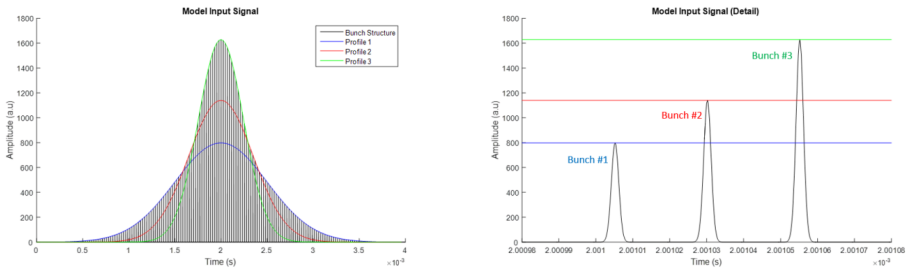

Figura A.6 – Señal de entrada al modelo del cable consistente en tres bunches separados por 25ns con un periodo de repetición de 23µs, zoom en la derecha.

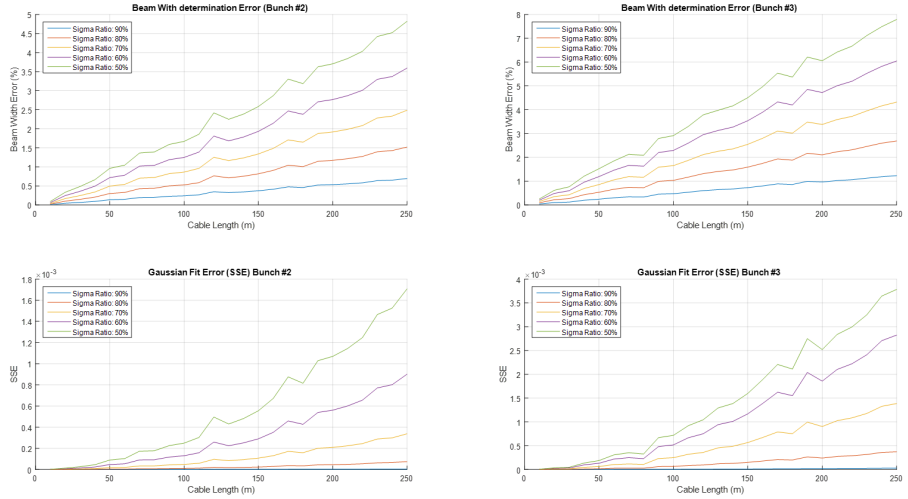

Figura A.7 – Error en la determinación del perfil (arriba), y error del ajuste Gausiano (abajo) para bunches 2 (izquierda) y 3 (derecha) en función de la distancia del cable y similitud de perfiles.

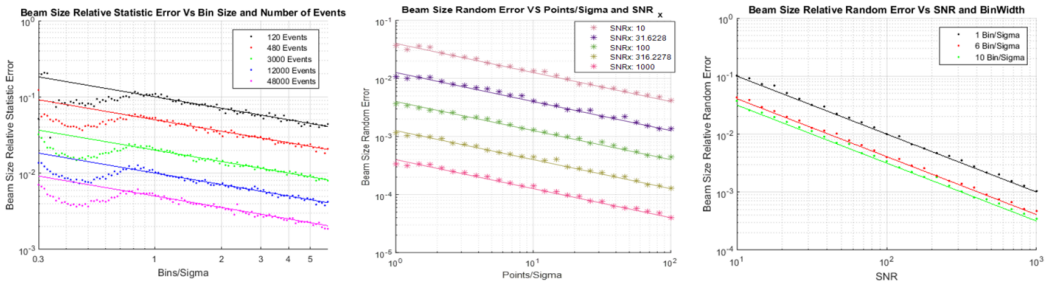

Figura A.8 – Error en la medida del perfil de bunches individuales debido a: el número de partículas cruzando el detector (izquierda), incertidumbre de la posición del hilo (centro) y ruido en la adquisición de partículas secundarias (derecha).

Fuentes de incertidumbre en la determinación el perfil del haz:

Una serie de análisis y simulaciones determinaron la manera en que la precisión del perfil Gausiano de bunches individuales viene condicionada por tres fuentes de incertidumbre principales:

- Número de interacciones por sigma: Determinado por la frecuencia de revolución del acelerador, el tamaño del haz y la velocidad del escáner. Esta unidad se expresa en puntos por sigma (PpS).
- Incertidumbre en el eje X: Es la incertidumbre en la medida de la posición del hilo, expresada en simulaciones en relación con el tamaño del haz como SNR_x.
- Incertidumbre en el eje Y: Incertidumbre asociada al sistema de lectura de partículas secundarias. Este componente está compuesto por dos contribuciones. La primera debido a ruido electrónico, expresado como SNR_y. La segunda relacionada con el error asociado al numero de eventos (N_{TE}). Cuando en una interacción hilo-bunch el promedio de partículas que cruza el detector es $\bar{x}$, su error asociado es $1/\sqrt{\bar{x}}$. En la detección media de 100 partículas, su error asociado en amplitud puede llegar hasta un 10 %.

Los resultados de las simulaciones se muestran en Fig.A.8 y permitieron la obtención de fórmulas analíticas (en líneas solidas), mostradas en Eq.A.3.

$$\epsilon(N_{\mathrm{TE}}, \mathrm{PpS}) = \frac{1{,}1}{\sqrt{N_{TE} PpS}} \ , \ \epsilon(\mathrm{SNR}_x, \mathrm{PpS}) = \frac{0{,}4}{\mathrm{SNR}_x \sqrt{PpS}} \ , \ \epsilon(\mathrm{SNR}_y, \mathrm{PpS}) = \frac{1}{\mathrm{SNR}_y \sqrt{PpS}} \tag{A.3}$$

La incertidumbre en la medida del perfil del haz viene determinada por la combinación de estos errores:

$$\epsilon_{\mathrm{beamWidth}} = \sqrt{\epsilon^2_{\mathrm{NTE}} + \epsilon^2_{\mathrm{SNRx}} + \epsilon^2_{\mathrm{SNRy}}} \tag{A.4}$$

De esta manera se pueden obtener las condiciones de medida necesarias para alcanzar una precisión determinada en el perfil de los diferentes bunches del haz. Como ejemplo, para la medida de un haz típico del LHC, sigma = 100um, con una incertidumbre menor de 1 %, la velocidad del escáner debe ser adaptada para medir más de 3 puntos por sigma y la incertidumbre en la medida de la posición del hilo debe ser menor de 4µm. Respecto al eje Y, SNR_y debe ser mayor de 100 y se requieren más de 10000 partículas cruzando el detector en el centro del perfil.

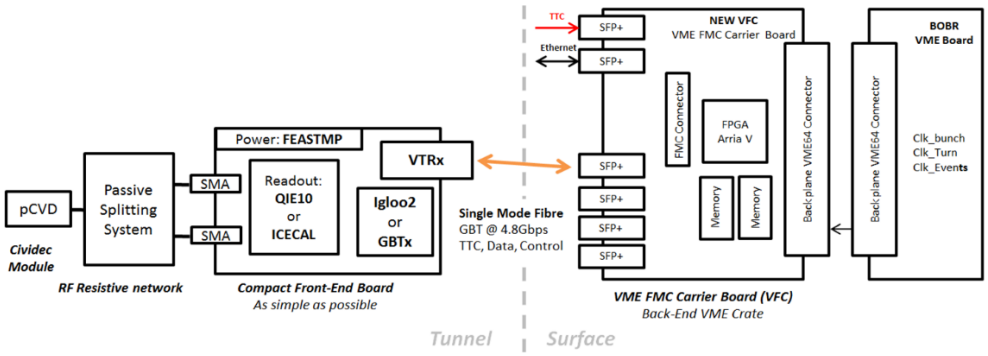

Figura A.9 – Arquitectura del sistema de adquisición de secundarias para la lectura de detectores de diamante pCVD.

A.3. Diseño del sistema de adquisición de partículas secundarias

Arquitectura del sistema:

Las medidas del escáner pueden quedar degradadas por el uso de largas lineas coaxiales (>100m) dando lugar a "bunch pile-up", esto degenera en el acople de perfiles de bunches consecutivos. Dada la rápida naturaleza de los detectores empleados (>250Mhz), el bajo ruido requerido y capacidad de detección de partículas individuales en detectores de diamante (1.6-3fC), se requiere de digitalización lo mas cercana posible al detector.

Esta tesis propone el uso de una arquitectura modular estandarizada en el grupo de instrumentación del CERN (BE-BI). Un front-end se encarga de digitalizar la señal en las proximidades del detector, en el túnel, posteriormente la información se transmite a través de link óptico digital a 4.8Gbps a un sistema back-End. En superficie los datos son almacenados y procesados. El sincronismo entre ambas partes del sistema, así como acciones de control, son posibles a través del link óptico bi-direccional, implementado con el protocolo GBT [140]. El front-end quedaría formado por una placa madre (GEFE [115]) resistente a la radiación, encargada de la gestión del link óptico, y una placa hija, responsable de la adquisición. La placa hija debe garantizar adquisiciones síncronas con los aceleradores, para proveer señales bunch a bunch, así como un alto rango dinámico para operar con los diferentes haces y energías de cada acelerador. Por otro lado, el back-end del sistema está compuesto por una placa VME multi-propósito diseñada en BE-BI (VFC-HD [114]). Esta configuración permite a un Back-End gestionar múltiples Front-Ends. La arquitectura propuesta se muestra en Fig.A.9.

ASICs de lectura:

Las rápidas señales de los detectores de diamante (o tubos foto-multiplicadores) (2-4ns FWHM), así como su periodo de repetición (25ns para SPS/LHC), sugiere como mejor estrategia en términos de compresión de datos y precisión de la medida, la integración de la señal en periodos de 25 ns. Digitalización directa implicaría frecuencias de conversión muy altas (>1 GSPS) para la adecuada reconstrucción de los pulsos o el uso de técnicas de ensanchamiento de pulso para frecuencias de adquisición mas bajas ($\approx$ 500MSPS) que podrían desembocar en bunch pile-up. Esto implicaría, además, la incorporación de lógica de compresión de datos en el Front-End. Un único link GBT, con un ancho de banda de 3.2 Gbps, no es suficiente para la transmisión directa de muestras ADC (650MSPS * 12bits = 7.8Gbps).

Esta tesis evalúa dos posibles esquemas de lectura para la cobertura de un alto rango dinámico, mono-canal logarítmico o multi-canal lineal, cada esquema se centra en uno de los

siguientes ASIC integradores:

- **QIE10:** Este ASIC [123], destinado para la lectura de tubos foto-multiplicadores en CMS, integra y digitaliza pulsos de corriente negativa con un periodo efectivo de 25ns. Esta función se realiza empleando 4 circuitos integradores operando en paralelo y en diferente fase. Cada circuito integrador requiere 100ns para procesar su integral de 25ns. Cada ASIC contiene un canal con un rango dinámico de 17 bits (sensibilidad 3.2fC y saturación 340pC), con codificación logarítmica en 8 bits (6 bits para mantisa y 2 de rango). Su comportamiento logarítmico se basa en la selección automática de 16 resoluciones (divididas en 4 rangos con 4 sub-rangos cada uno). Este esquema garantiza un error constante de cuantificación de 1 % en todo su rango dinámico. Su interfaz con lógica digital se realiza a través de 8 lineas DDR LVDS a 40Mbps, y otra linea LVDS de reloj. Su resistencia a la radiación está asegurada gracias a su proceso de fabricación (AMS 350nm SiGe BiCMOS). QIE10 ha sido caracterizado hasta TID = 2.5KGy [124].
- **ICECAL:** Destinado para lectura de tubos foto-multiplicadores en LHCb, este ASIC integrador consta de 4 canales analógicos con un rango dinámico de 12 bits cada uno (sensibilidad en 4fC y saturación alrededor de 16pC) [127]. Cada canal lo componen dos sub-canales con un ciclo de refresco de 50ns cada uno, gracias a su multiplexación el ASIC opera con un periodo efectivo de 25ns. Este ASIC ofrece una salida analógica diferencial, cuya amplitud es proporcional a la integral de la corriente de entrada en periodos de 25ns, que debe ser digitalizada con un ADC externo. Para operación en entornos radioactivos, ICECAL emplea el mismo proceso de fabricación que QIE10.

Prototipo de prueba de concepto:

En esta tesis se desarrollan dos prototipos para validar el concepto de lectura local del detector con transmisión digital a superficie. El temprano estado de desarrollo de las placas finales (GEFE y VFC-HD), y chipset asociado a la gestión el link óptico GBT (ASIC GBTx), motivó el desarrollo de una infraestructura propia para la implementación estos prototipos. En los sistemas desarrollados, el Front-End lo forman una placa madre 'Igloo2 UMD' (desarrollada por CMS), donde una FPGA Flash Igloo2 se encarga de la gestión del link óptico. La evaluación de ambos ASICs de lectura ha sido posible gracias al diseño de placas hijas compatibles y tolerantes a la radiación. El back-End del sistema está compuesto por un kit de desarrollo Igloo2, donde las adquisiciones son temporalmente almacenadas y posteriormente transmitidas a un ordenador para su análisis. Las diferentes placas para ambas versiones de Front-End, así como la implementación del Back-End se muestran en Fig.A.10 y Fig.A.11.

Gran parte de la complejidad de este prototipo reside en la implementación del link óptico para esta FPGA. Para que el Front-end realice adquisiciones síncronas con el acelerador (SPS/LHC 40Mhz) se necesita propagar este reloj de forma determinista desde el Back-end(BE) hasta el Front-End (FE) a través del link. Esto permite ubicar las ventanas de integración del FE siempre con la misma fase respecto al paso del bunch. De la misma manera, para la correcta identificación de cada bunch, los datos adquiridos deben llegar al BE con una latencia constante. Ambas condiciones implican la necesidad de un link óptico con latencia determinista en ambos lados y una única fuente de reloj, basada en los 40Mhz de cada acelerador.

Implementación del link óptico:

El link óptico GBT para esta especifica FPGA se realizó en colaboración con CMS HCAL. La implementación consistió en la migración y adaptación de código existente del proyecto GBT-FPGA [139] para Virtex 6 de Xilinx a Igloo2 de Microsemi, ambos modelos comparten similitudes en sus transceivers.

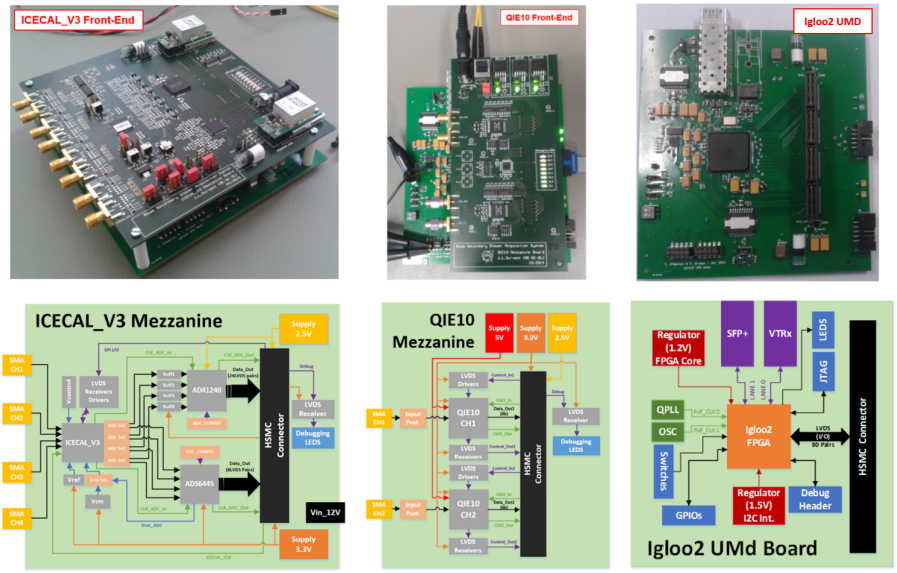

Figura A.10 – Placas desarrolladas para los dos los prototipos FE ICECAL y QIE10 (izquierda y centro respectivamente) y placa madre Igloo2 UMD (derecha) junto con sus correspondientes esquemáticos simplificados.

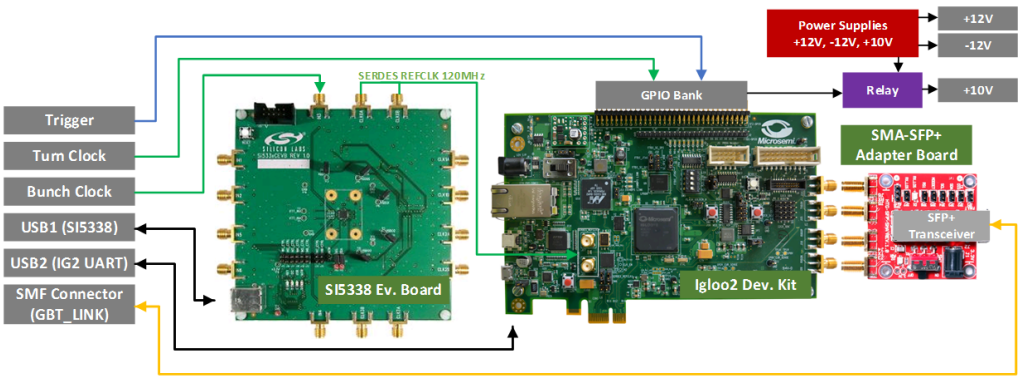

Figura A.11 – Esquemático del prototipo Back-end.

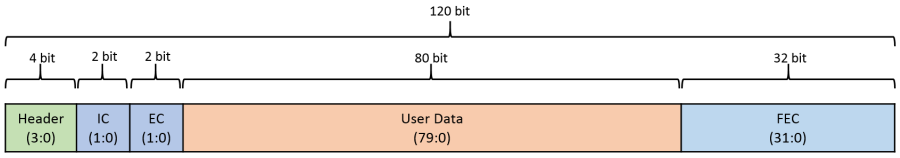

Figura A.12 – Estructura de un frame GBT.

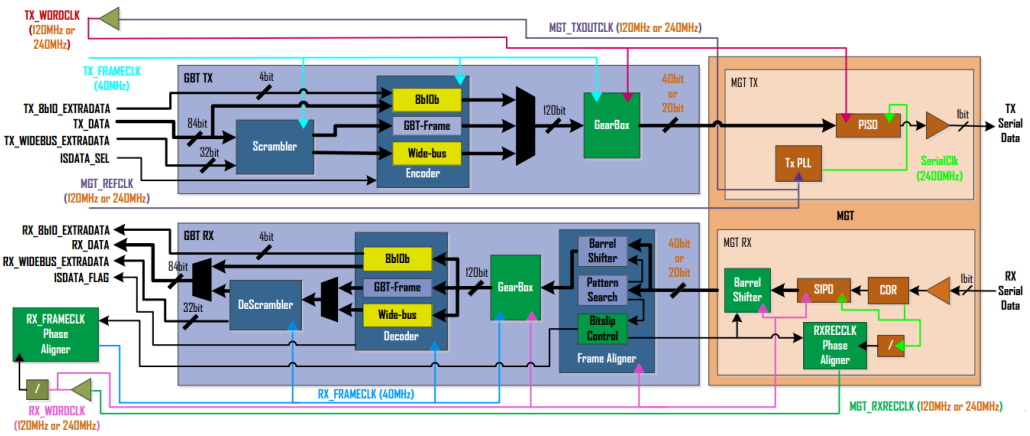

Figura A.13 – Esquemático del core GBT con componentes críticos para latencia determinista destacados en verde.

El protocolo GBT consiste en frames de 120 bits transmitidos cada 25ns (40Mhz), a una velocidad efectiva de 4.8Gbps, donde 3.2Gbps está dedicado exclusivamente para datos de usuario. El frame comprende bits de cabecera y de control (IC y EC) así como datos de usuario y un campo para detección y corrección de errores (FEC), ver Fig.A.12.

Esquemáticamente la implementación del protocolo GBT en FPGAs consta de los módulos mostrados en la Fig.A.13.

Tras una compleja migración, dado los limitados recursos de esta especifica FPGA (solo cuenta con 2 PLLs), la versión determinista del link GBT fue exitosamente implementada en ambos lados del link gracias a estrategias especificas de alineamiento de datos y reloj. Caracterizaciones en laboratorio determinaron una incertidumbre en latencia de datos, así como en la fase del reloj recuperado de 40Mhz, de unos 1.3ns tras cada reinicio del link. Este desplazamiento es sistemático y varia en función del desplazamiento en bits del frame para su correcto alineamiento (ver medidas en Fig.A.14).

De la misma manera se pudo comprobar en laboratorio la estabilidad del link durante la rampa de aceleración de SPS y LHC, donde las frecuencias de los relojes principales (40Mhz bunch clock) varían 800 y 2.5 ppm respectivamente. El link fue capaz de seguir estas variaciones y continuar sincronizado sin pérdida de datos.

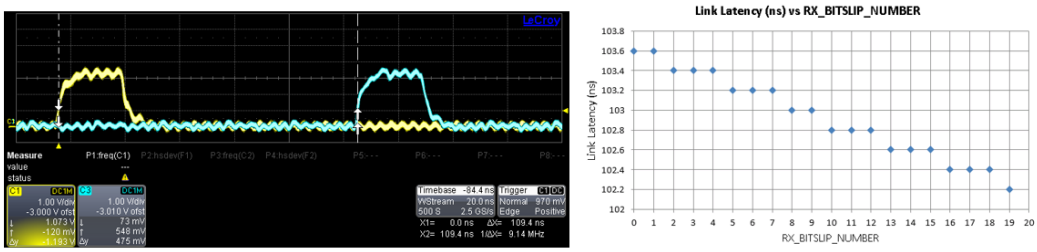

Figura A.14 – Estudios de la latencia del link GBT de latencia determinista en función del alineamiento del frame.

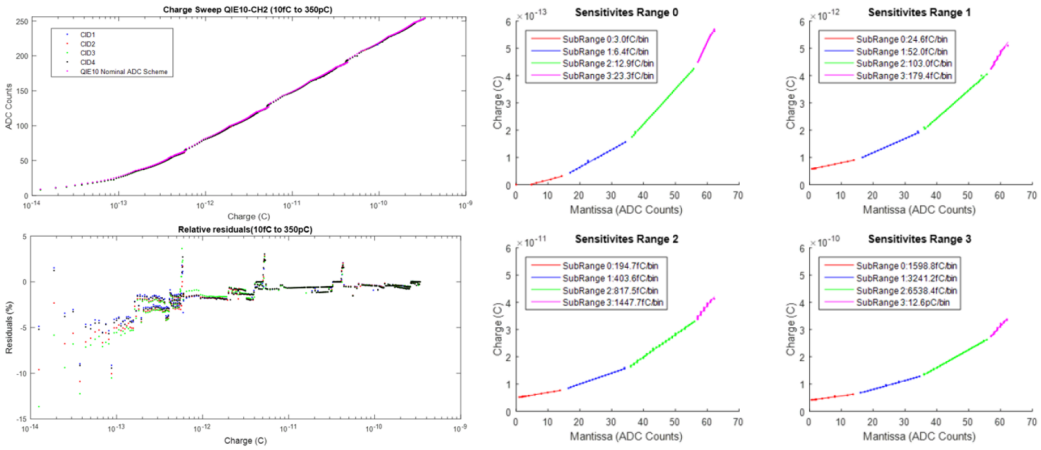

Figura A.15 – Estudios la respuesta (izquierda) y niveles de sensibilidad (derecha) de uno de los QIE10 del Front-End.

A.4. Evaluación en laboratorio y pruebas con haz

Test funcionales en laboratorio:

Ambas versiones del Front-End se probaron en laboratorio empleando la cadena de lectura completa, con transmisión de datos a través del link GBT, almacenamiento temporal en el Back-End y transmisión a un PC para su análisis.

La versión **QIE10** pudo demostrar la correcta cobertura de 5 ordenes de magnitud (3.2fc-340pC) en un barrido de carga con un generador de corriente DC de precisión. Ambos canales del Front-End mostraron un comportamiento similar y acorde a sus especificaciones. Las no-linealidades de su respuesta quedaron por debajo del 5 % y los 16 niveles de sensibilidad de su codificación logarítmica pudieron ser claramente identificados (ver Fig.A.15). No se apreció diferencia en sus 4 subcircuitos de integración.

La versión **ICECAL** con digitalización basada en AD6645 demostró un rango dinámico por canal de 3 ordenes de magnitud (12bits) con no-linealidades por debajo del 1 % (ver Fig. A.16). Para caracterizar su respuesta se empleó un generador de pulsos acoplado en AC, correctamente sincronizado con las ventanas de integración del ASIC. La sensibilidad del Front-End está limitada por un ruido de digitalización de 6 cuentas ADC, traducido en carga 10fC. La saturación del ASIC con la menor ganancia programable se alcanza alrededor de 30pC.

Estos resultados cualificaron ambos protoipos de FE para su posterior instalación en los aceleradores SPS y PSB.

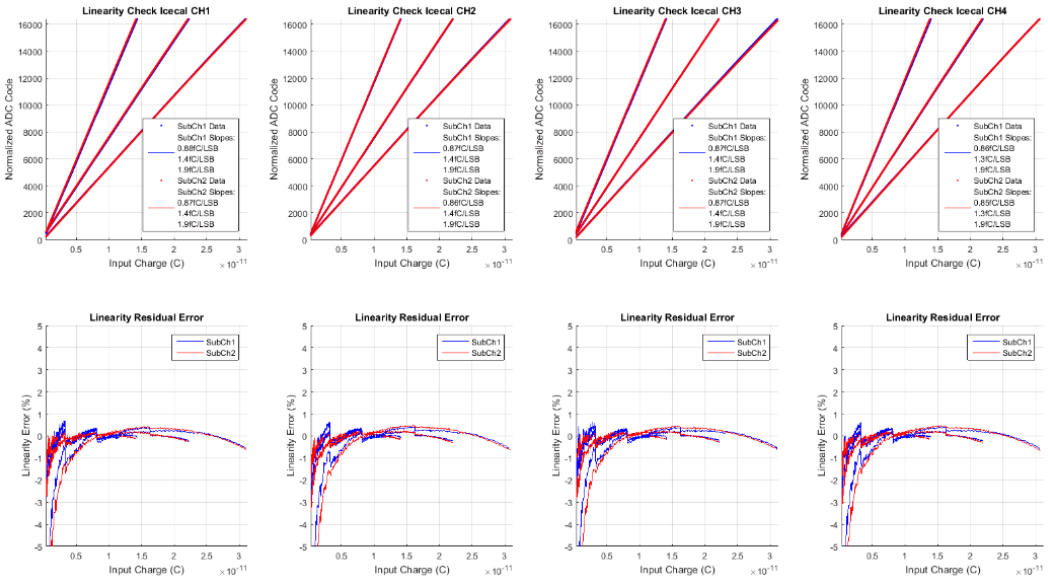

Figura A.16 – Estudios de linealidad del Font-End Icecal. Se muestra la respuesta de sus dos subcanales en diferente color para tres ganancias programables.

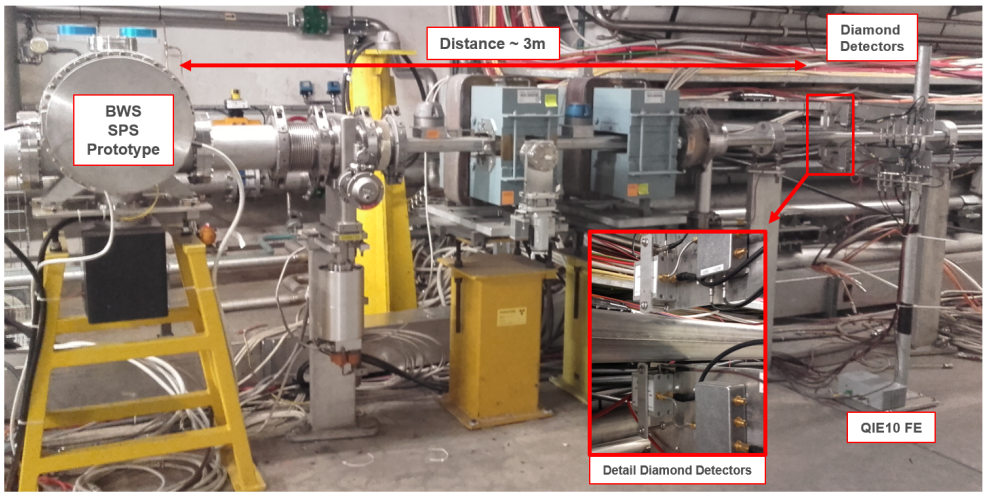

Figura A.17 – Instalación experimental en SPS.

Pruebas y resultados en SPS con detectores de diamante y Front-End QIE10:

El Front-End QIE10 evaluó para la lectura de detectores de diamante poli-cristalino (pCVD) gracias a una instalación experimental en SPS. Esta instalación consiste en 4 detectores de diamante y un sistema centellador-PMT estándar. La instalación se empleo con escáneres lineares y un prototipo LIU-BWS (ver Fig.A.17). Dos de los detectores de diamante se emplearon para digitalización en superficie (80m) y otros dos para digitalización en túnel con el FE QIE10.

Varias pruebas en diferentes configuraciones del haz con detectores de diamante determinaron que, a pesar de sus excelentes propiedades (linealidad, rango dinámico, rápida respuesta, resistencia a la radiación...) su pequeño tamaño ($1cm^2$) representa una gran limitación para su aplicación con BWS en SPS. Dada su reducida sección, muy pocas partículas secundarias cruzan el detector en haces de baja intensidad (LHCPILOT con 5e9 protones por bunch), o haces a energía de inyección 26GeV. En estas condiciones el perfil medido por el detector está dominado por factores estadísticos en el eje Y relacionados con el número de partículas detectado (ver Fig.A.18).

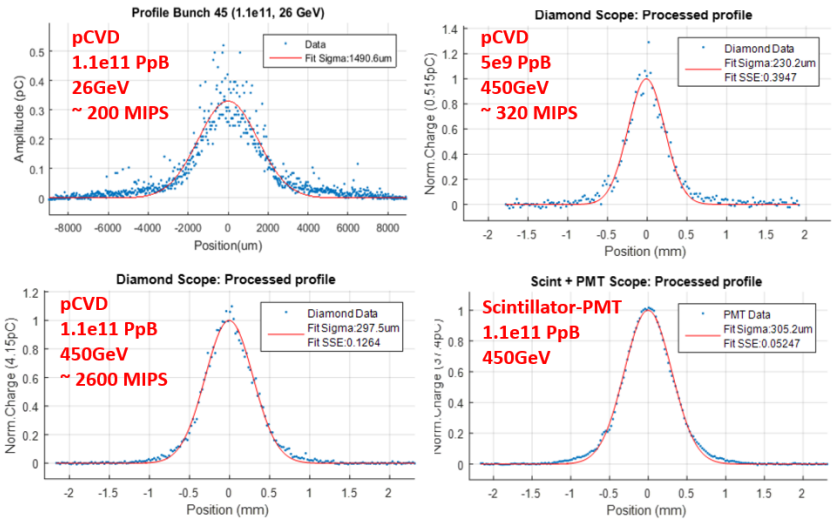

Figura A.18 – Perfiles medidos con detectores de diamante para diferentes intensidades y energías del haz, perfil medido con centellador para comparación.

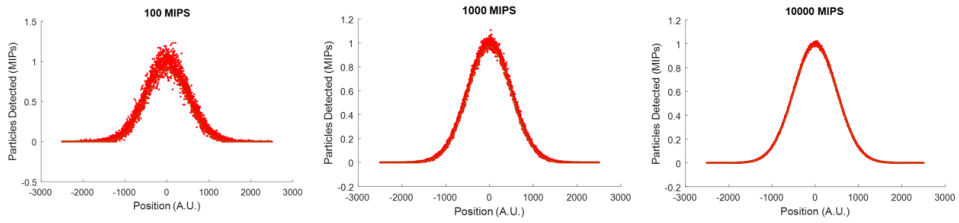

Figura A.19 – Simulación de perfiles para diferente número de partículas cruzando el detector en el centro de la distribución Gausiana.

Este efecto estadístico pudo ser confirmado por simulaciones (ver Fig.A.19). La figura A.20 muestra la evolución del tamaño de un haz COAST (un bunch con 0.2e11 partículas a 270 Gev) con el tiempo medido con dos escáneres, uno operacional lineal (azul) y LIU-BWS con adquisición basada en detectores de diamante (verde) y centellador + PMT (violeta). Se puede apreciar como para LIU-BWS la dispersión de la medida es significativamente mayor en con el uso con detectores de diamante, efecto directo de la incertidumbre en la amplitud del perfil.

Estas campañas también cualificaron y compararon la precisión del nuevo diseño respecto a sistemas operacionales. A pesar de un menor número de puntos por sigma, el nuevo sistema mejora en un factor 2 tanto en la precisión de la medida del perfil como de la localización de su centroide.

El FE QIE10 se pudo operar exitosamente y sus perfiles resultaron en un menor ruido, especialmente notable en las colas de las distribuciones, ver Fig.A.21 y Fig.A.22.

QIE10 demostró explotar las cualidades de los detectores de diamante, sin llegar a la saturación en ninguna de las configuraciones estudiadas. Además, durante 1.5 años de operación, no se observó degradación en su nivel de ruido, permaneciendo siempre cerca de la sensibilidad del ASIC (3-4fC).

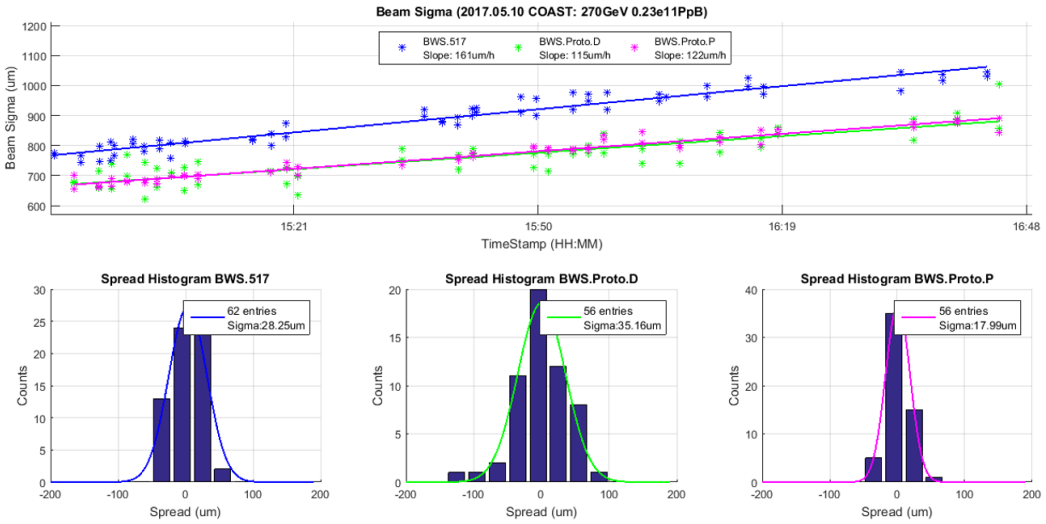

Figura A.20 – Evolución de la anchura del haz con el tiempo (arriba) e histograma de los residuos del fit linear (abajo) para escáner BWS517 (azul) y el prototipo LIU-BWS con detectores de diamante pCVD (verde) y centellador + PMT (violeta).

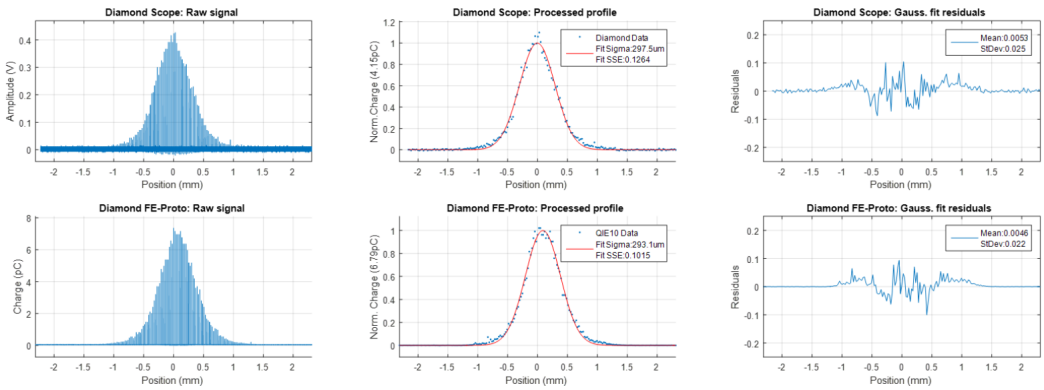

Figura A.21 – Perfiles con detectores de diamante para un haz LHC25 (1.1e11 PpB a 450GeV) adquiridos en superficie (arriba) y en túnel con el FE QIE10 (abajo)

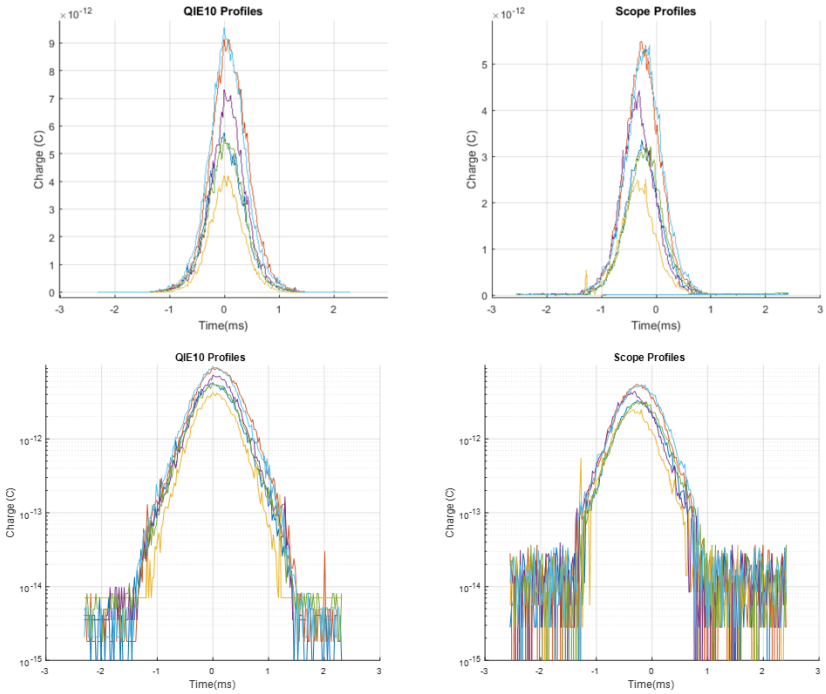

Figura A.22 – Comparación directa del perfil de un bunch adquirido con detectores de diamante en superficie (derecha) y por el FE QIE10 en el túnel (izquierda) para un haz LHC (1.1e11PpB a 450GeV). Medidas con representación lineal (arriba) y logarítmica (abajo).

Pruebas y resultados en PSB con detector Multi-PMT y Front-End ICECAL:

La instalación de un nuevo LIU-BWS en PSB permitió la evaluación del Front-End ICECAL junto con un nuevo detector basado en un sistema Multi-PMT. El objetivo es emplear los cuatro canales del Front-End para la lectura de PMTs. Estos PMTs reciben fotones de un mismo centellador y tienen diferentes tamaños de foto-cátodo y filtros para cubrir un alto rango dinámico dividido en 4 rangos lineales. Un sistema estándar (operacional) con digitalización en superficie actuó como sistema de referencia. La Fig.A.23 muestra la instalación del LIU-BWS junto con detalles de los detectores.

El FE ICECAL se encarga de la digitalización en paralelo de los cuatro detectores del M-PMT, posteriormente se selecciona off-line el primer canal no saturado para su procesamiento. De esta manera el sistema puede trabajar en una configuración fija y asegurar el correcto punto

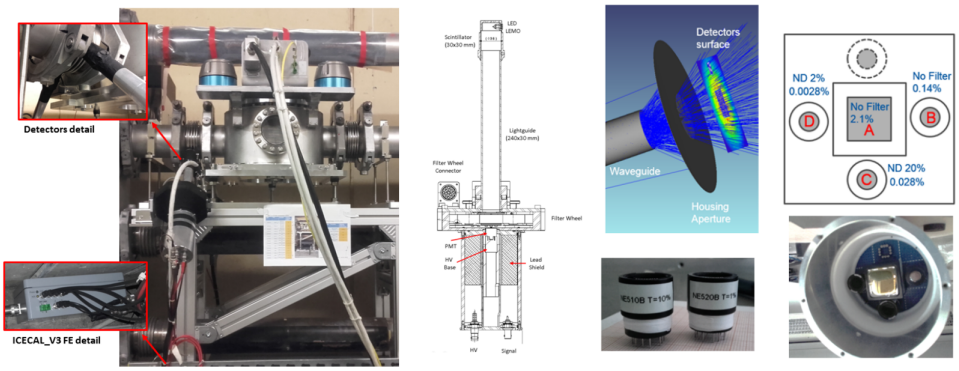

Figura A.23 – Instalación en PSB (izquierda) junto con detalles del detector completo estándar (centro) y configuración M-PMT (derecha).

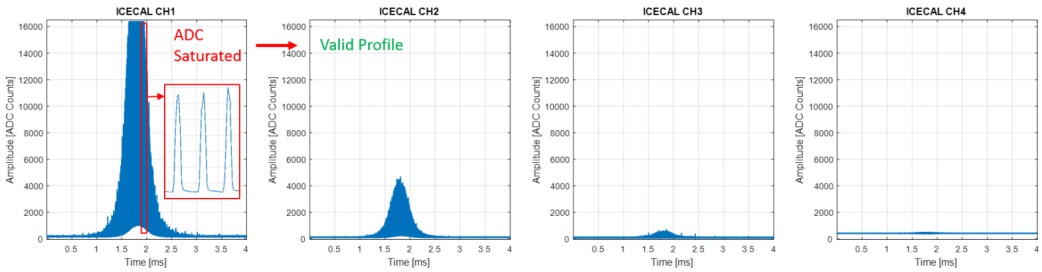

Figura A.24 – Adquisición de los 4 canales del FE ICECAL para un haz LHC25 a 1.4GeV en PSB.

de trabajo de al menos un PMT en cualquier configuración del acelerador.

El FE ICECAL y el detector M-PMT se evaluaron en campañas de medidas con diferentes tipos de haces y energías. La figura A.25 muestra como el nuevo sistema es capaz de trabajar en una única configuración durante una campaña de medidas con haces LHC25 (intensidad 144e10 protones por bunch) e ISOLDE (intensidad 800e10 protones por bunch) a lo largo de sus ciclos de aceleración. El sistema estándar necesita acomodar su punto de trabajo (filtro y ganancia del PMT) para mantener la señal en el rango de adquisición del osciloscopio y evitar la saturación de su base. La variación en amplitud del perfil Gausiano para un haz LHC25 durante su aceleración es de un factor 500, en el caso de ISOLDE es de un factor 20. La operación del sistema sin parámetros configurables representa una significativa mejora en la operación y fiabilidad del instrumento.

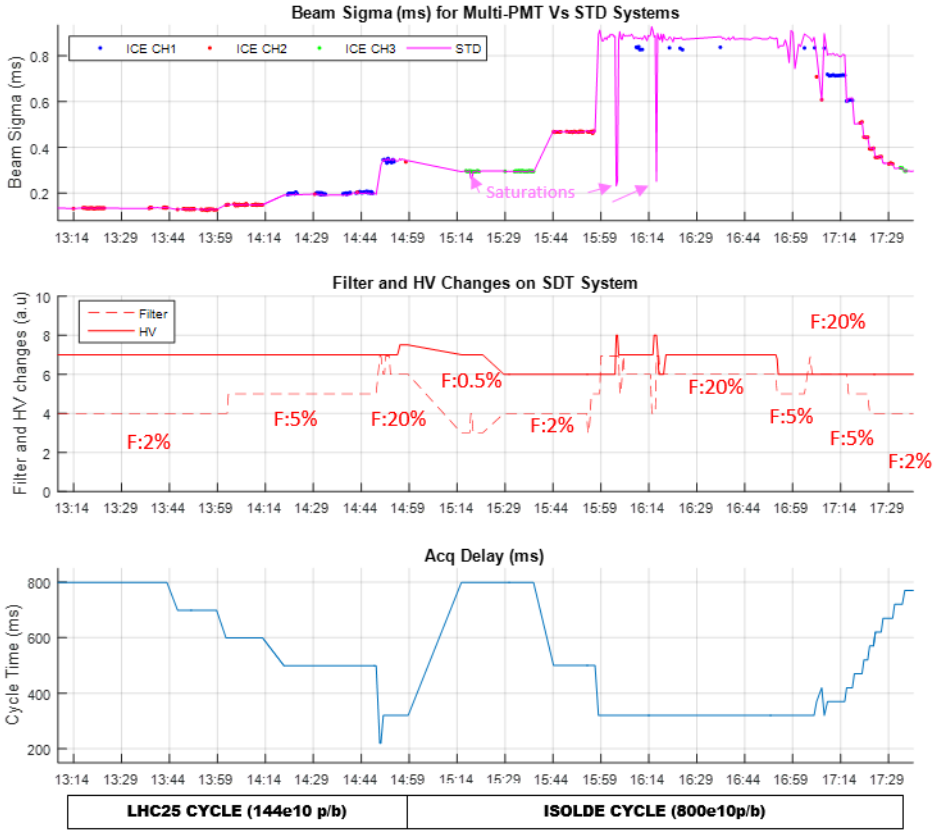

Figura A.25 – Arriba: Medidas del perfil del haz en el dominio temporal del FE ICECAL con selección dinámica de canal (puntos) y del sistema estándar (linea continua). Centro: Cambios en HV y filtro requeridos para sistema estándar. Abajo: Momento del ciclo donde se realiza la medida de ambos sistemas.

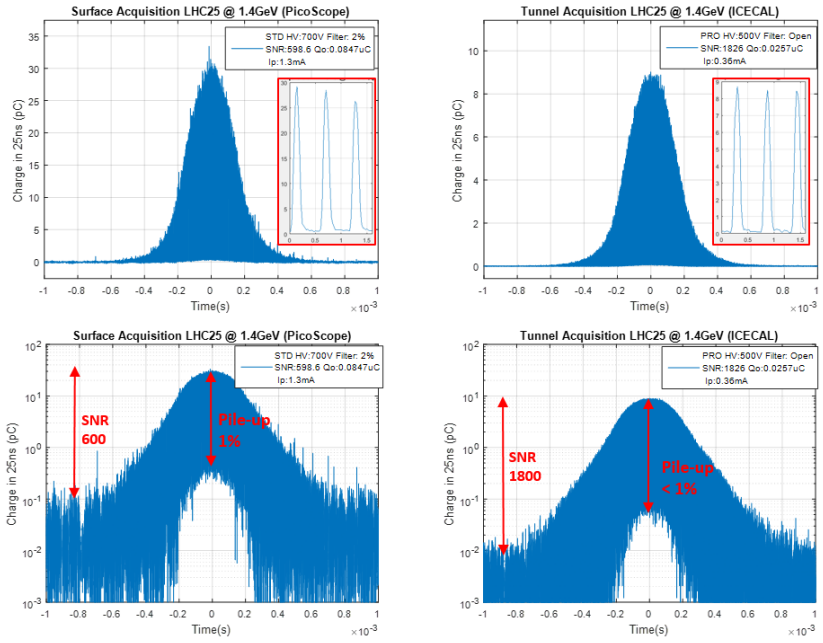

Figura A.26 – Perfiles de un haz LHC25 a 1.4GeV adquiridos en superficie (izquierda) y en túnel (derecha). Medidas con representación lineal (arriba) y logarítmica (abajo).

Las ventajas de adquisición cercana al detector en el caso de PSB se puede apreciar en Fig.A.26, donde se muestran las diferencias entre los dos sistemas de adquisición para una misma geometría de centellador y tipo de detector. Para comparación directa, la señal adquirida en superficie ha sido procesada mediante integraciones digitales en slots de 25ns, imitando el comportamiento de ICECAL.

El nivel de ruido en túnel (10fC, cerca de la sensibilidad del Front-End) es un orden de magnitud menor que en superficie (100fC). Aunque este efecto puede estar condicionado por la diferencia de resolución en ambos sistemas, supone a priori una significativa mejora en SNR. Respecto al ancho de banda se puede apreciar que, a pesar del relajado timming de PSB (pulsos 200ns FWHM separados por 600ns), en superficie se observa el efecto del cable con un pile-up cercano al 1 %. Este nuevo concepto, además de ofrecer redundancia en la medida del perfil, posibilita la combinación de canales para una mayor resolución (y por tanto SNR), empleando canales saturados para la lectura de la colas Gausianas.

En estas campañas se pudo comprobar la importancia de la geometría del centellador y su impacto en la precisión de la medida del instrumento. El prototipo LIU-BWS demostró una precisión de 1.6 %, similar a sistemas operacionales, en la medida de un haz LHC25 a 1.4GeV con centelladores operacionales (cilíndricos de altura 3cm y diámetro 3cm). Tras sustituir el centellador por uno de sección rectangular (10x10x1 cm) la precisión del instrumento alcanzó 1 % para las mismas condiciones.

A.5. Conclusiones

Esta tesis cubre el diseño de sistemas de adquisición bunch a bunch de alto rango dinámico para la detección de lluvias de partículas secundarias producidas por beam wire scanners. El proyecto se desarrolla en el marco del proyecto LHC Injectors Upgrade (LIU) y es una parte fundamental del diseño de una nueva generación de Beam Wire scanners. Junto con la incertidumbre en la medida de la posición del hilo, la relación señal ruido y resolución en la adquisición de secundarias definen la precisión de estos instrumentos.

El pile-up inducido por largas lineas de cable coaxial (CK50) en estructuras de 25ns y su impacto en la medida del perfil de bunch individuales se evaluó a través de simulaciones. Estos estudios demostraron que, en los sistemas operacionales, el error en la determinación

del perfil por pile-up puede llegar fácilmente al 1 % en distancias mayores de 100m. Además, simulaciones de física de partículas, junto con un estudio detallado de las características de diferentes haces, determinó la necesidad de un rango dinámico de adquisición de hasta 6 ordenes de magnitud.

Para satisfacer las especificaciones de LIU-BWS esta tesis evalúa un nuevos sistemas de detección, basados en detectores de diamante de estado solido (pCVD) y sistemas tradicionales basados en PMTs y centelleadores con varios canales y filtros. Los sistemas de adquisición de alto rango dinámico aquí desarrollados se basan en ASICs integradores a 40Mhz (QIE10 e ICECAL) para la lectura de detectores en la proximidad del detector y transmisión digital de datos a través de un link óptico. Estos prototipos emplean FPGAs Igloo2 donde el protocolo GBT con latencia determinista fue exitosamente implementado, la sincronización de las adquisiciones se garantiza propagando el reloj principal del acelerador a través del link óptico, algoritmos de recuperación y alineamiento de reloj (40Mhz) en el front-end permiten una incertidumbre en datos y fase $<$1.3ns y capacidad de transmisión sin interrupciones durante el ciclo de aceleración de SPS o LHC.

El Front-End QIE10 demostró en laboratorio la cobertura de 5 ordenes de magnitud con no-linearidades por debajo del 5 %. Su codificación logarítmica en 8 bits mantuvo un error de cuantificación del 1 % constante sobre toda su dinámica. La evaluación del front-end en condiciones operacionales para la lectura de detectores de diamante, en SPS, resulto en una reducción en ruido cercano a orden de magnitud comparado con adquisiciones en la superficie. Estudios sistemáticos sobre el uso de detectores de diamante pCVD en SPS determinaron que su reducida área (1cm2) es una fuerte limitación para su uso con wire scanners en este acelerador. En el caso de haces nominales (1e11PpB) a 26GeV únicamente 100-200 partículas cruzan el detector en el centro de la distribución Gausiana, lo que deriva en una incertidumbre en amplitud del 10 %. Este efecto se reduce drásticamente para haces nominales a 450GeV, donde 2000-5000 partículas cruzan el detector en el centro de la distribución, esto sugiere su aplicación en wire scanners en LHC.

El Front-End ICECAL demostró en laboratorio una cobertura de 3 ordenes de magnitud por canal para cualquier configuración de ganancia, sus no-linearidades permanecieron siempre por debajo del 1 %. La evaluación en PSB se realizó con un detector formado por varios PMT con diferentes filtros de densidad neutra y tamaños de foto-cátodo. El front-End ICECAL, junto con este detector permite la cobertura de 6 ordenes de magnitud. Gracias a la selección dinámica de canal, una configuración estática permite la medida de todo el ciclo de aceleración de haces LHC nominales y de alta intensidad (ISOLDE). Este diseño garantiza la ausencia de saturación de PMT en la dinámica de adquisición de ICECAL. Medidas comparativas en superficie demostraron una mejora significativa en SNR y la ausencia de bunch pile-up inducido por largos cables.

Bibliografía

[1] CERN. *The CERN accelerator complex.* https://cds.cern.ch/record/2197559 [Online; Accessed 11-November-2017]

[2] R. Bailey, P. Collier. *Standard Filling Schemes for Various LHC Operation Modes.* LHC-Project Note 323 Revised

[3] Cyclotron. (n.d.). *The American Heritage®Science Dictionary.* Retrieved September 18, 2017 from Dictionary.com website http://www.dictionary.com/browse/cyclotron

[4] F. Roncarolo. *Accuracy of the transverse emittance Measurements of the CERN Large Hadron Collider.* PhD. Thesis Ecole Polytechnique Federale de Lausanne (EPFL), 2005.

[5] S. Baird. *Accelerators for Pedestrians.* AB-Note-2007-014 OP, CERN. February 2017.

[6] S. Peggs, T. Satogata. *Introduction to Accelerator Dynamics.* Cambridge: Cambridge University Press. doi:10.1017/9781316459300

[7] H. Wiedelmann. *Particle accelerator physics.* vol. 1. Springer, 2003

[8] W. Herr and B. Muratori. *Concept of Luminosity.* CERN, Geneva, Switzerland, 2006.

[9] E. Bravin, G. Burtin, A.S. Fisher, A. Guerrero, A. Jeff, T. Lefèvre, A. Rabiller, F. Roncarolo. *First Beam Measurements with the LHC Synchrotron Light Monitors.* 1st International Particle Accelerator Conference, Kyoto, Japan, 23 - 28 May 2010. CERN-BE-2010-019

[10] G.Trad, E.Bravin, A. Goldblat, S.Mazzon, F.Roncarolo, T. Mitsuhashi. *Performance of the upgraded synchrotron radiation diagnostics at the LHC.* Proceedings of IPAC2016, Busan, Korea

[11] G. Trad. *Development and Optimisation of the SPS and LHC Beam Diagnostics.* PhD. Thesis, Laboratoire de Physique Subatomique et de Cosmologie (LPSC)/CERN, Grenoble, France, May 2015.

[12] M. Sapinski et al,. *The first experience with LHC beam gas ionization monitor.* Proceedings of IBIC2012, Tsukuba, Japan.

[13] J.W. Storey et al. *First results from the operation of a rest gas ionisation profile monitor based on a hybrid pixel detector.* Proceedings of IBIC2017, Grand Rapids, MI, USA.

[14] P.Hopchev et al.; *A beam gas vertex detector for beam size measurement in the LHC.* Proceedings of IPAC2014, Dresden, Germany

[15] A. Navarro. *Characterization and optimization of CERN Secondary Emission Monitors (SEM) used for beam diagnostics.* Bachelor Thesis, Universitat Politecnica de Catalunya.

[16] J.B. Lallement, A. Lombardi and P.A. Posocco. *Emittance reconstruction technique for the Linac4 high energy commissioning.* Technical report CERN, 2012. CERN-ATS-Note-2012-079 MD

[17] I. Ortega et al.; *A scintillating fibre beam profile monitor for the experimental areas of the SPS at CERN.* Journal of Physics Conference Series 763(1):012012 · October 2016

[18] R. Jones.*Introduction to LHC beam instrumentation: Beam Profile Measurements.* CERN Academic Lectures 2014.

[19] S.Burger, A.Boccardi, E.Bravin, A.Goldblatt, A.Ravni, F.Roncarolo and S.Sautier. *Turn by turn profile monitors for the CERN SPS and LHC.* Proceedings of IBIC2013, Oxford, UK

[20] M. Sapinski, B. Dehning, A. Guerrero, M. Meyer, T. Kroyer. *Carbon fiber damage in particle beam.* Proceedings of HB2010, Morschach, Switzerland.

[21] S.Burger, C. Carli, M. Ludwig, K Priestnall, U. Raich. *The PS Booster fast wire scanner.* Proceedings DIPAC 2003, Mainz, Germany. 2003. CERN-AB-2003-060-BDI.

[22] J. Herranz. *Minimisation of the wire position uncertainties of the new CERN vacuum wire scanner.* UPC PhD. Thesis, 2016.

[23] A. Guerrero, J. Koopman, A. Lokhovitskiy. *Fast wire scanner calibration.* Proceedings of DIPAC 2009. 25-27 May 2009, Basel, Switzerland. CERN-BE-2009-020 BI

[24] E. Piselli. *PSB Wire scanners in Operation.* Emittance Working Group meeting (13/08/2014)

[25] AB/BI. *VME64x Digital acquisition board for the LHC trajectory and closed orbit system.* Functional Specification. 2003. EDMS 410295.

[26] AB/BI. *IBMS An Individual Bunch Measurement System for LHC Beam Instrumentation.* Engineering Specification. 2005. EDMS 624344.

[27] G. Bohner et al. *Very front-end electronics for the LHCb preshower.*CERN, LHCb-2000-047, 2000.

[28] B. Dehning, E. Garcia, J. Koopman. *Distorsion and Noise Measurements on the IBMS.* Technical note, CERN 2007.

[29] CERN. *LHC Injectors Upgrade: Technical Design Report - Volume I: Protons.* ACC-2014-0337, 2014.

[30] M. Sapinski. *Beam Interaction with thin materials: heat dissipation, cooling phenomena and damage limits.* Proceedings Beam Instrumentation Workshop 2012.

[31] M. Sapinski. *LHC magnet quench test with beam loss generated by wire scan.* Proceedings of IPAC2011, San Sebastian, Spain 4-9 Sept 2011.

[32] F. Roncarolo, B. Dehning, C. Fischer, J. Koopman. *Accuracy of the SPS transverse emittance monitors.* Proceedings of DIPAC 2005, Lyon, France.

[33] M. Kuhn. *Transverse emittance measurement and preservation at LHC.* PhD. Thesis University of Hamburg, 2016.

[34] G. Baud, B. Dehning, J. Emery, J-J. Gras, A. Guerrero, E. Piselli. *Performance assessment of wire scanners at CERN.* Proceedings of IBIC2013, Oxford, UK, 16-19 September 2013. CERN-ACC-2013-0308

[35] M. Kuhn et al,. *LHC Emittance preservation during the 2012 run.* LHC Beam Operation Workshop. Evian 2012.

[36] P. Blondel. *Rapport d'estage.* CERN, Geneve, 2012.

[37] J. Emery. *BWS Photomultiplier Saturation: Hardware Knowledge.* CERN Emittance working group meeting 26/06/2012.

[38] E.Piselli, L. Timeo, J. Emery. *LHC Photomultiplier Studies.* CERN Emittance working group meeting 25/02/2015.

[39] J. Emery. *Beam Wire Scanner Control, monitoring and Supplies part.* Engineering Specification. EDMS 1318827. CERN, 2015.

[40] C. Grosjean. *Motorisation d'un scanner du CERN.* Haute Ecole Specialisee de Suisse Occidentale (HES-SO), Bachelor Thesis 2014.

[41] J.L. Sirvent. *Design of an optical fibre based angular position sensor for wire scanners complying with ultra-high vacuum, high temperature and radiation conditions for the CERN's accelerators.* Master Thesis, University Miguel Hernandez, Elche, Spain, 2012.

[42] S. Samuelsson. *Mechanical optimisation of a high-precision fast wire scanner at CERN.* Master Thesis Chalmers University of Technology, 2013.

[43] R.Veness et al,. *Experience from the Construction of a New Fast Wire Scanner Prototype for the CERN-SPS and its Optimization for Installation in the CERN-PS Booster.*IBIC2015, International Beam Instrumentation Conference 2015. 13-17 September 2015. Melbourne (Australia).

[44] J.L. Sirvent. *Position sensor and secondary particle shower acquisition.* 9th. DITANET workshop, 2013.

[45] J.L. Sirvent. *Optical Position Sensors.* Review of the PSB Beam Wire Scanner Prototype design, 2016.

[46] T. Watanabe, H. Fujimoto, T. Masuda. *Self-calibratable rotary encoder.*Journal of Physics: Conference Series, National Metrology Institute of Japan, Tsukuba, Japan, 2005.

[47] J.L. Sirvent et al,. *Performance Assessment of Pre-Series Fast Beam Wire Scanner Prototypes for the Upgrade of the CERN LHC Injector Complex.* IBIC 2017 International Beam Instrumentation Conference, 20-24 August 2017 Grand Rapids, Michigan (USA).

[48] L.Garcia. *Performance assesment of pre-series beam wire scanner prototypes for the LHC injectors upgrade.* Master Thesis, Institut d'optique ParisTech, Université de Bordeaux.

[49] Particle Data Group.*Review of Particle Physics.* Chin. Phys. C 38 (2014) 090001.

[50] C. Grupen and B. Schwartz. *Particle Detectors.* Cambridge University Press, 2008.

[51] G.G. Knoll. *Radiation detection and measurement.* 4th Edition, Wiley, 2010.

[52] Eljen Technology. *Plastic Scintillators Catalogue.* Eljen, 2016.

[53] J. Birks. *The Theory and Practrice of Scintillation Counting.* Pergamon Press, Oxford, 1967.

[54] R. Craun and D. Smith. *Analysis of response data for several organic scintillators.* Nuclear Instruments and Methods, vol. 80, no. 2, pp. 239-244, 1970.

[55] Z. Li. *Properties of plastic scintillators after irradiation.* Nuclear Instruments and Methods, vol. 552, no. 3, pp. 449-455, 2005.

[56] Y. Protopopov and V. Vasil'chenko. *Radiation damage in plastic scintillators and optical fibers.* Nuclear Instruments and Methods, vol. 4, no. 4, pp. 496-500, 1995.

[57] S. Afanasiev and S. Borzakov. *Experimental study of the plastic scintillator damage caused by radiation on IREN at JINR.* CMS Note - 2014/003, Geneva (Switzerland), 2014.

[58] W. Leo. *Techniques for Nuclear and Particle Physics Experiments.* Springer-Verlag, 1993.

[59] Saint Gobain Crystals. *Scintillation materials and assemblies catalog.*

[60] K. Ianakiev, B. Alexandrov and M. Browne. *Temperature behavior of NaI(TI) scintillator detectors.* Nuclear Instruments and Methods in Physics research A, vol. 607, no. 2, pp. 432-438, 2009.

[61] J. Jelley. *Cerenkov Radiation and its applications.* Pergamon Press, 1958.

[62] C. Ambrosio. *Commisioning of the LHCb RICH detectors* Nuclear Instruments and Methods in Physics, vol. 595, no. 1, pp. 36-39, 2008.

[63] S.Ecklund and C. Field. *A fast luminosity monitor system for PEP II.* Nuclear Instruments and Methods in Physics, vol. 463, no. 1-2, pp. 68-76, 2001.

[64] M. Shiozawa. *Reconstruction algorithms in the Super-Kamiokande large water Cherenkov detector.* Nuclear Instruments and Methods in Physics Research, vol. 433, no. 1-2, pp. 240-246, 1999.

[65] J. Gubeli and P. Evtushenko. *Cherenkov converter for large dynamic range, high sensitivity detectors for use on wire scanners.*Proceedings of IBIC2015, Melbourne (Australia), 2015.

[66] M. Kastriotou, S. Dobert, E. B. Holzer, E. Nebot del Busto, F. Tecker and C. Welsch. *A versatile beam loss monitoring system for CLIC.* Proceedings of IPAC2016, Busan (Korea), 2016.

[67] Hamamatsu. *Photomultiplier Tubes: Basics and applications.* Hamamatsu Photonics, 2007.

[68] R. DeSalvo. *Why people like the Hybrid PhodoDiode.* Nuclear Instruments and Methods in Physics Research A, vol. 387, pp. 92-97, 1997.

[69] F. Bachmair *CVD Diamond Sensors in Detectors for High Energy Physics.* PhD. thesis, Institute for Particle Physics, Department of Physics, ETH Zurich, 2016.

[70] A. Owens and A. Peacock. *Compound Semiconductor radiation detectors.* Nucl. Instr. and Meth., vol. A531, pp. 18-37, 2004.

[71] Hyperphysics. *The PN Junction.* Department of physics and Astronomy, Georgia State University, 2017.

[72] M. Mikestikova, Z. Kotek and J. Stastny. *Evaluation of Bulk and Surface Radiation Damage of Silicon Sensors for the ATLAS upgrade.* 23rd International Workshop on Vertex Detectors, Macha Lake, The Czech Republic, 2014.

[73] The RD42 Collaboration. *CVD diamond detectors for ionizing radiation.* Nuclear Instruments and Methods in Physics Research, vol. A 435, pp. 194 - 201, 1999.

[74] P. May, *Diamond thin films: a 21st-century material.* Philosophical Transactions of the Royal Society A, vol. 358, no. 1766, 2000.

[75] M. Schwander and K. Partes. *A review of diamond synthesis by CVD processes.* Diamond and Related Materials, vol. 20, p. 1287 - 1301, 2011.

[76] F. Bachmair. *Diamond sensors for future high energy experiments.* Nuclear Instruments and Methods in Physics Research A, vol. 831, p. 370 - 377, 2016.

[77] H. Kagan. *Recent advances in diamond detector development.* Nuclear Instruments and Methods in Physics Research A, vol. 541, p. 221 - 227, 2005.

[78] E.Griesmayer and B. Dehning. *Diamonds for Beam Instrumentation.* Presentation and proceedings for TIPP2011 - Technology and Instrumentation in Particle Pysics 2011. Physics Procedia 37 (2012) 1997 – 2004

[79] M. Marinelli, E. Milani, A. Paoletti, A. Tucciarone, G. Verona, M. Angelone and M. Pillon. *Systematic study of pre-irradiation effects in high efficiency CVD diamond nuclear particle detectors.* Nuclear Instruments and Methods in Physics Research, vol. A 476, p. 701 - 705, 2002.

[80] J. Fernandez.*Development of a Beam Condition Monitor system for the Experimantal Areas of the LHC using CVD Diamond.* PhD. thesis, Universitat Politecnica de Catalunya, 2004.

[81] F. Kassel, M. Guthoff, A. Dabrowski and W. de Boer. *Description of radiation damage in diamond sensors using an effective defect model.* arXiv:1705.09324v1 [physics.ins-det], 2017.

[82] M. Guthoff. *Performance and perspectives of the diamond ased Beam Condition Monitor for beam loss monitoring at CMS.* International Conference on Technology and Instrumentation in Particle Physics 2014, Amsterdam, Netherlands, 2014.

[83] M. Guthoff, W. de Boer and S. Muller. *Simulation of beam induced lattice defects of diamond detectors using FLUKA.* Nuclear Instruments and Methods in Physics Research A, vol. 735, pp. 223-228, 2014.

[84] The RD42 Collaboration. *CVD Sensors for Charged Particle Detection.* Diamond and Related Materials, vol. 10, pp. 1778-1782, 2001.

[85] C. Bauer. *Radiation hardness studies of CVD diamond detectors.* Nuclear Instruments and Methods in Physics Research A, vol. 367, no. 1, pp. 2007 - 2011, 1995.

[86] The RD42 Collaboration. *Depelopment of Diamond Tracking Detectors for High Luminosity Experiments at the LHC: Status Report.* CERN/LHCC 2007-002, Geneve (Switzerland), 2007.

[87] S. Schnetzer. *Tracking with CVD diamond radiation sensors at high luminosity colliders.* IEEE Transactions on Nuclear Science, vol. 46, no. 3, pp. 193-200, 1999.

[88] W. Trischuk. *Recent Advances in Diamond Detectors.* Department of Physics, University of Toronto, Toronto, ON, M5S 1A7, Canada, 2008.

[89] C. Ilgner, M. Domke, M. Lieng, M. Nedos, J. Sauerbrey, S. Schleich, B. Spaan, K. Warda and J. Wishahi. *The Beam Conditions Monitor of the LHCb Experiment.* IEEE Transactions on Nuclear Science, 2009.

[90] V. Cindro, et al. *The ATLAS Beam Conditions Monitor.* Journal of Instrumentation, vol. 3, 2008.

[91] E. Castro, et al. *The CMS Beam Conditions and Radiation Monitoring System.* Technology and Instrumentation in Particle Physics , Chicago (USA), 2011.

[92] K.K. and Gan. *Diamond Particle Detector Systems in High Energy Physics.* in Technology and Instrumentation in Particle Physics, Amsterdam (Netherlands), 2014

[93] E. Effinger, B. Dehning, T. Baer, R. Schmidt, H. Frais-Kolbl, E. Griesmayer and P. Kavrigin. *A Prototype Readout System for the Diamond Beam Loss Monitors at LHC.* International Beam Instrumentaion Conference (IBIC), Oxford (UK), 2013.

[94] F. Burkart, W. Wartmann, B. Dehning, E. Effinger, M. Fraser, B. Goddart, V. Kain, O. Stein and E. Griesmayer. *Beam Losses at CERN's PS and SPS Measured with Diamond Particle Detectors.* International Particle Accelerator Conference (IPAC), Busan (Korea), 2016.

[95] C. Kurfurst. *Cryogenic Beam Loss Monitoring for the LHC.* CERN-THESIS-2013-232, Viena (Austria), 2013.

[96] J. Bol, E. Berdermann, W. deBoer, W. Grigoriev, F. Hauler and L. Jungermann. *Beam Monitors for TESLA Based on Diamond Strip Detectors.* IEEE Transactions on nuclear science, vol. 51, no. 6, pp. 2999-3005, 2004.

[97] S. Liu. et al. *In Vacuum diamond sensor scanner for beam halo measurements in the beam line at the KEK Accelerator Test Facility.* Nuclear Instruments and Methods in Physics Research A, vol. 832, pp. 231-242, 2016.

[98] T. Zhou, W. Ding, M. Gaowei, G. DeGeronimo, J. Boron, J. Smedley and E. Muller. *Pixelated transmission-mode diamond X-ray detector.* Journal of Synchrotron Radiation, vol. 22, pp. 1396-1402, 2015.

[99] J. Smedley, A. Heroux, J. Keister, M. Gaowei, E. Muller, J. Bohon, K. Attenkofer and J. Distel. *Diamond X-ray beam position monitors.* Particle Accelerator Conference, New York (USA), 2011.

[100] C. Bidaut and F. Chapuiss. *PSB Operation Space: Beam Docs 2016.* CERN, 2016. [Online]. Available: https://wikis.cern.ch/display/PSBOP/Beam+Docs+2016.

[101] C. Kittel and M. Delrieux *PS Operations Space: Beam Doc 2015.* CERN, 2016. [Online]. Available: https://wikis.cern.ch/display/PSOP/Beam+Doc+2015.

[102] O. Berring. *CERN Accelerator Optics.* CERN, 2016. [Online]. Available: http://cern-accelerators-optics.web.cern.ch/cern-accelerators-optics/.

[103] CERN. *The LHC design report.* CERN, Geneve (Switzerland), 2004.

[104] R. Steerenberg. *Beams from Injectors in 2016.* LHC Performance Workshop, Chamonix, 2016.

[105] R. Bruce. *LHC Machine configuration in the 2016 proton run.* in LHC Performance Workshop, Chamonix 2016, Chamonix, 2016.

[106] H. Bartosik. *Operational Beams fot the LHC.* in LHC Performance workshop, Chamonix, 2014.

[107] H. Bartosik. *Can we ever reach che HL-LHC requirements with the injectors?.* in Review of LHC and Injector Upgrade Plans Workshop (RLIUP), Centre de Convention, Archamps, 2013.

[108] P. Elmfors. *Wire Scanners in low energy Accelerators.* Nucl.Instrum.Meth, vol. A396, pp. 13-22, 1997.

[109] A. Ferrari, P. R. Sala, A. Fasso, J. Ranft. *FLUKA: a multi-particle transport code.* CERN 2005-10, INFN/TC-05/11, SLAC-R-773, 2005.

[110] A. Lechner. *LHC beam wire scanner: dose and particle spectra in the vicinity of the beam pipe.* Fluka Team Internal Report, 2013.

[111] John A. Buck and William H. Hayt (2000).Engineering Electromagnetics. 6th Edition. Mc. Graw Hill.

[112] Murray Thompson (1999). Transmission lines. Physics 623 notes.

[113] Draka. *02Y(St)C(St)H 4.2/11.5AF (CK50).*Coaxial according to CERN specification 461 REV. 6

[114] A. Boccardi, M. Barros, T. Levens, B. Szuk, W. Vigano and C. Zamantas. *A modular approach to acquisition systems for the future CERN Beam Instrumentation developments.* Vols. Proceedings of ICALEPCS2015, Melbourne, Australia, 2015.

[115] M. Barros, A. Boccardi, C. Donat, J. Gonzalez, T. Lefevre, T. Levens and B. Szuk. *The Giga Bit Transceiver based Expandable Front-End (GEFE) - a new radiation tolerant acquisition system for beam instrumentation.* Journal of Instrumentation, vol. 2016 JINST 11 C02062, 2016.

[116] J. Gonzalez, T. Botey, C. Delplano and J. Savioz. *Development of a high dynamic range beam position measurement system using logarithmic amplifiers for the SPS at CERN.* Proceedings of IBIC 2013, Oxford, UK, 2013.

[117] I. Brunner, F. Jaquenod, J. Trummer and H. Vincke. *High-level dosimetry results for the CERN high-energy accelerators: Annual report for 2007 and 2008.* CERN-DGS-2012-026-RP-TN, EDMS Id: 1213583, 2012.

[118] I. Brunner, F. Jaquenod, J. Trummer and H. Vincke. *High-level dosimetry results for the CERN high-energy accelerators: Annual report for 2009-2010.* CERN-DGS-2012-027-RP-TN, EDMS Id: 1213585, 2012.

[119] J. Saraiva and M. Brugger. *Radiation levels at CERN's injectors and their impact on electronic equipment.* AccApp13 - Eleventh International Topical Meeting on Nuclear Applications of Accelerators, Bruges, Belgium, 2013.

[120] C. Collaboration. *CMS Technical Design Report for the Phase 1 Upgrade of the Hadron Calorimeter.* CERN-LHCC-2012-015, CMS-TDR-010, Geneve (Switzerland), 2012.

[121] G. Usai. *Upgrade of the ATLAS Tile Calorimeter for the High Luminosity LHC.* ATL-TILECAL-PROC-2015-009, Geneve (Switzerland), 2015.

[122] T. Zimmerman. *QIE10P5 Specifications.* Fermilab, 2012.

[123] A. Baumbaugh, L. Dal Monte, G. Drake, J. Freeman, D. Hare, H. Hernandez, E. Hughes, S. Los, D. Mendez and J. Proudfoot. *QIE10: a new front-end custom integrated circuit for high rate experiments.* JINST, vol. 2014 JINST 9 C01062, 2014.

[124] J. Hirschauer. *QIE Radiation Testing.* HCAL Phase 1 Upgrades Meeting (13/02/2014), 2014.

[125] E. Picatoste. *LHCb Calorimeter electronics upgrade.* vol. Proceedings of CHEF 2013, 2013.

[126] G. Bohner and e. al. *Very front-end electronics for the LHCb preshower.* CERN LHCb-2000-047, 2000.

[127] E. Picatoste, C. Bigbeder-Beau, O. Duarte, L. Garrido, D. Gascon, E. Grauges, J. Lefrancois, F. Machefert, J. Mauricio and X. Vilasis. *Low noise 4-channel front end ASIC with on-chip DLL for the upgrade of the LHCb calorimeter.* vol. 2015 JINST 10 C04017, 2015.

[128] M. Wirthlin. *Using FPGAs in a Radiation Environment.* ATLAS CMS Electronics Workshop for LHC updates (ACES2014), Geneve (Switzerland), 2014.

[129] T. Grassi. *FPGA Use within the detector volume.* ECFA High Luminosity LHC Experiments Workshop, Aix-Les-Bains, 2014.

[130] D. Dsilva, J. Wang, N. Rezzak and N. Jat. *Neutron SEE testing of the 65nm SmartFustion2 flash-based FPGA.* IEEE Radiation Effects Data Workshop (REDW), 2015.

[131] Microsemi. *Understanding Single Event Effects (SEEs) in FPGAs.* Microsemi, 2011.

[132] C. Poivey, M. Grandjean and F. Guerre. *Radiation Characterization of Microsemi ProASIC3 Flash FPGA Family.* IEEE Radiation Effects Data Workshop (REDW) , 2011.

[133] R. Mountain, B. Gui, J. Wang and M. Artuso. *FPGA Irradiation @ NPTC-MGH.* LHCb FPGA Irradiations (16/11/2010), Geneve (Switzerland), 2010.

[134] A. Whitbeck and J. Hirschauer. *The CMS central hadron calorimeter DAQ system upgrade.* Topical Workshop on Electronics for Particle Physics (TWEPP2014) , Aix en Provence (France), 2014.

[135] S. Groadhouse, T. Grassi and T. O'Bannon. *The CMS HCAL FEE Control Module.* Topical Workshop on Electronics for Particle Physics (TWEPP2014), Aix-En-Provence (France), 2014.

[136] A. Finkel, J. Mans and J. Turkewitz. *Ratiation Testing of an Igloo2 FPGA.* University of Minnesota, Minnesota, 2014.

[137] J. Mariano. *ngCCM IGLOO2 Mezzanine irradiation tests at Unversity of Maryland.* University of Maryland, Maryland, 2015.

[138] Y. Sano, Y. Horii, M. Ikeno, T. Kawaguchi, K. Mizukoshi, O. Sasaki, K. Shukutani and M. Tomoto. *Application of flash-based field-programmable gate arrays in high energy physics.* Topical Workshop on Electronics for Particle Physics (TWEPP2016), Karlsruhe (Germany), 2016.

[139] S. Baron and J. Mendez. *GBT-FPGA User Guide.* EP-ESE-BE, Geneve (Switzerland), 2016.

[140] M. Barros and S. Baron. *The GBT-FPGA Project (One unified core for multiple users).* Fourth Common ATLAS CMS Electronics Workshop for LHC Upgrades (ACES2014), Geneve (Switzerland), 2014.

[141] Microsemi. *IGLOO2 FPGA Evaluation Kit: User Guide.* Microsemi.

[142] Microsemi. *IGLOO2 FPGA High Speed Serial Interfaces: User guide.* Microsemi.

[143] G. Di Mattia. *Test del funzionamento e della resistenza alle radiazione del l'elettronica per il trigger di primo livello dell' esperimento ATLAS.* Universita degli Studi di Roma La Sapenza, 2003.

[144] J. Albertone, T. Bogey, C. Delplano and J. Gonzelez. *Logarithmic Amplifiers, ADC drivers and Voltage Regulators: Radiation Test Report at PSI-PIF.* CERN, Geneve, 2013.

[145] CERN. *FEASTMP Datasheet: Radiation and magnetic field tolerant 10W DC/DC converter module.*

[146] P. Oser and G. Spiezia. *Radiation Test Report VMO1200 / MCP1824 / UCC3895.* Paul Scherrer Institute Proton Irradiation Facility (EDMS 1404940), 2014.

[147] J. Gilmore, J. Haley, V. Khotilovich, J. Roe and A. Safonov. *Very forward muon trigger and data acquisition electronics for CMS: design and radiation.* vol. 2013 JINST 8 C02040, 2013.

[148] K. Kloukinas, S. Bonacini and A. Marchioro. *Characterization and production testing of a quad 12 bit 40 Ms/sec A/D converter with automatic digital range selection for calorimetry.* 11th Workshop on Electronics for LHC and Future Experiments, Heidelberg, Germany, 12 - 16 Sep 2005, pp.241-245, 2005.

[149] H. Takai, J. Kierstead, H. Chen, K. Chen, F. Lanni and S. Rescia. *Characterization of COTS ADC radiation properties for ATLAS LAr calorimeter readout upgrade.* in Topical Workshop on Electronics for Particle Physics 2013 (TWEPP2013), Perugia, Italy, September 23-27, 2013, 2013.